



Universiteit Utrecht

The Nature of Acid Sites in Fluid Catalytic Cracking Catalysts

A Probe Molecule Based Research on the Exact Structure and Nature of Acid Sites

Master Research Thesis by Iris E. Teune Bsc.

Supervisors: Marjolein E.Z. Velthoen Msc.

Prof. Dr. In. Bert M. Weckhuysen

Dr. Gareth Whiting

*Department of Inorganic Chemistry and Catalysis
Debye Institute Utrecht University*

Abstract

The majority of the world's gasoline is produced with the Fluid Catalytic Cracking (FCC) process, in which heavy gas oil (HGO) or vacuum gas oil (VGO) is cracked into smaller hydrocarbons. Every day around 2300 metric tons of FCC catalyst is produced.^[1,2] The FCC catalyst used for this cracking contains three components: clay, binder and zeolite. The binder is a physical mixture of silica and alumina. Along with the clay, a natural source of kaolinite, this forms the active matrix. The active matrix is responsible for the pre-cracking of the crude oil, which is said to be Lewis acid catalysed.^[1,2] The mechanism through which the pre-cracking occurs is however still not clear, nor is the true origin of the acid sites responsible for this pre-cracking.^[2-6] The zeolite is said to be the component which is responsible for most of the cracking, due to its shape selectivity and high concentration of Brønsted acid sites.^[2,7,8] The nature of this Brønsted acid site has been investigated extensively, and is quite well understood. Though it is said that the zeolite is the active component in the FCC catalyst, a true understanding of the nature of all the acid sites in the FCC, and the complete cracking mechanism, is still lacking.

In this master thesis the true origin and structure of all the acid sites, present in the FCC catalyst, is elucidated. The acidity is determined of both the individual and mixed components, with respect to the FCC. The acidity was studied with pyridine and CO based FT-Infrared measurements. Additionally, ¹H-NMR was employed to detect the different protons in the samples. The structure of the acid sites is investigated with ²⁷Al MAS and ²⁷Al MQ-MAS NMR spectroscopy. Correlations between the proximity of different surface hydroxyl groups and aluminium structures are obtained with {¹H-²⁷Al} CP and {²⁷Al-¹H} CP NMR spectroscopy.

In this research we show that the zeolite is indeed the component which contributes the most to the overall acidity of the FCC catalyst. Here we show that a higher aluminium content results in an increased concentration of Lewis acid sites and medium Brønsted acid sites. The increase in medium Brønsted acid sites was correlated to a decreased electronegativity of the tetrahedral aluminium species. The formation of the Lewis acid sites is associated with the formation of penta-coordinated Extra Framework Aluminium (EFAL) species. Furthermore, we show that the aluminium center of the aluminol groups and Brønsted acid sites can act as a Lewis acid site.

Additionally, we show that the binder is the component which contributes most to the acidity of the active matrix. The binder contains mostly Lewis acid sites, which suggests that the pre-cracking is Lewis acid catalysed. Furthermore, it is shown that the binder contains medium Brønsted acid sites which form due to the interaction between silica and alumina. The Brønsted acid sites were associated with the formation of a tetrahedrally coordinated aluminium species.

Moreover, a correlation between the OH bands in the infrared spectra are correlated to the proton peaks in the ¹H-NMR spectra. We thereby show that ¹H-NMR is a useful technique to analyse the change in the amount and acidity of the Brønsted acid sites.

Additionally, it was shown that heating of the FCC catalyst resulted in a structural collapse of the binder and clay. Furthermore, heating of the samples generated penta-coordinated type aluminium, which were therefore ascribed exclusively to EF aluminium species. Moreover, prolonged heating resulted in an increased amount of Lewis acid sites and a decreased amount of Brønsted acid sites. This was associated with an increased heterogeneity around the aluminium nuclei.

Content

Abstract	2
Chapter 1. Introduction	8
1.1 Fluid Catalytic Cracking.....	8
1.2 The Fluid Catalytic Cracking Catalyst	8
1.3 The Zeolite.....	9
1.4 The Active Matrix.....	10
1.5 Aim and Approach.....	11
Chapter 2. Theory	12
2.1 The Fluid Catalytic Cracking Process	12
2.2 The Cracking Mechanism.....	13
2.3 The Origin of Brønsted and Lewis Acid Sites.....	14
2.4 Characterization Techniques	15
2.4.1 Nuclear Magnetic Resonance	15
2.4.2 Probe Molecule-based Infrared Spectroscopy.....	21
Chapter 3. Experimental	26
3.1 Samples.....	26
3.2 Characterization Techniques	27
Results and Discussion.....	28
Chapter 4. The Effect of the Si/Al Ratio in Zeolite HY	30
4.1 Acidity	30
4.2 Structure.....	36
4.3 Summary and Conclusion.....	38
Chapter 5. Interactions Between Alumina and Silica	40
5.1 Acidity	40
5.2 Structure.....	45
5.3 Summary and Conclusions	48
Chapter 6. Single Components.....	50
6.1 Acidity	50
6.2 Structure.....	56
6.3 Cross-Polarization Experiments	59
6.3.1 $\{^{27}\text{Al} - ^1\text{H}\}$ Cross Polarization	59
6.3.2 $\{^1\text{H} - ^{27}\text{Al}\}$ Cross Polarization.....	60

6.4	Summary and Conclusion.....	62
Chapter 7.	Mixed components	64
7.1	Binder-Zeolite.....	64
7.1.1	Acidity.....	64
7.1.2	Structure	68
7.1.3	Summary and Conclusion	70
7.2	Binder-Clay.....	71
7.2.1	Acidity.....	71
7.2.2	Structure	75
7.2.3	Summary and Conclusion	77
7.3	FCC versus mixed components	78
7.3.1	Acidity.....	78
7.3.2	Structure	82
7.3.3	Summary and Conclusion	84
Chapter 8.	The Effect of Heating	86
8.1	Acidity	86
8.2	Structure.....	88
8.3	Summary and Conclusion.....	91
Chapter 9.	Conclusions	92
Chapter 10.	Outlook and Recommendations.....	94
Chapter 11.	Acknowledgements.....	96
Chapter 12.	Bibliography	98
Appendix	104
13.1	FCC model component.....	105
13.1.1	Acidity.....	105
13.1.2	Structure	107
13.2	Single Components.....	108
13.2.1	XRD	108
13.2.2	²⁷ Al MQ-MAS NMR Spectrum	113
13.2.3	TEM Single Components.....	114
13.3	Clay and Zeolite.....	116
14.3.1	Acidity.....	116
13.3.2	Structure	118

13.4	Effect of heat treatment on individual components.....	119
13.5	^{27}Al -NMR spectra of the zeolites	122
13.6	FT-IR spectra low crystalline boehmite	125
13.6.1	High and low crystalline boehmite.....	125
13.6.2	Washed and not washed clay.....	125
13.7	^1H -NMR Spectra.....	126

Chapter 1. Introduction

With increasing attention for the effects of global warming, governments all over the world have been trying to prevent, minimize, and control the environmental changes.^[1] Global agreements, like the clean air act of 2004 and the Paris climate agreement, help by drawing up rules which dictate that the emission of greenhouse gasses must be diminished.^[9,10] This can be accomplished by improving on currently used processes and by finding alternative energy sources. With the depletion of fossil fuels, the demand for alternative energy sources is growing.^[2,11–14] Alternatives like hydrogen powered cars, biofuels and solar cells are already in use, but are still lacking the same efficiency compared to fossil fuels.^[11] To make the transition from fossil fuel based technology to alternative energy sources, improvement of the currently used processes is necessary.

1.1 Fluid Catalytic Cracking

One of the most widely applied processes in the fossil fuel industry is the Fluid Catalytic Cracking (FCC) process. In this process, heavy gas oil (HGO) or vacuum gas oil (VGO) is heated with a catalyst which selectively cracks the large hydrocarbons into smaller fractions, like gasoline and diesel.^[2] Every day around 2300 metric tons of catalyst is produced for the FCC process.^[2] The mechanism through which the cracking occurs, is discussed in paragraph 2.2. To improve the FCC process, a complete understanding of the catalytic cracking mechanism is required. In order to accomplish this, the origin and amount of all the acid sites present in the FCC catalyst must be elucidated.^[2,15]

1.2 The Fluid Catalytic Cracking Catalyst

Ever since the early 1960 and 1970, synthetic crystalline microporous aluminosilicates have been used for the cracking of oil, nowadays better known as zeolites.^[2] The FCC catalyst which is currently used, consist primarily of three components: zeolites, clay and binder, as shown in Figure 1. These three components consist mainly of a mix of alumina and silica.^[2]

The zeolite is a mesoporous crystalline solid, which consist of tetrahedrally coordinated silica in which some silicon atoms are substituted by aluminium.^[2,8,15–26] In the FCC catalyst, most often zeolite HY or ZSM-5 is used, due to their thermal stability, shape selectivity, and high concentration of acid sites.^[2,27] The origin of the acid sites in the zeolite is discussed in paragraph 1.3. The second component is a clay, which is added as a filler, to increase both the heat capacity and the mechanical stability.^[2,28–30] Various types of clay like kaolinite, bentonite, and attapulgite are used in the production of FCC catalysts.^[28] The clay consist of a mixture of alumina, silica, and counter ions like magnesium or potassium.^[31–33] The third component in a FCC catalyst particle is a binder, which is a physical mixture of an alumina and silica. The binder is added to bind the zeolite and clay together, to form a mechanically stable FCC catalyst particle.^[2] The introduction of the binder also produces meso- and macropores, which allows larger molecules to access the catalytically active sites.^[28,29] The mix of binder and clay is referred to as the active matrix, which is responsible for pre-cracking of the VGO.^[34,27] The origin of the acid sites is discussed in paragraph 1.4.

The catalytic activity, acidity and structure of the three individual components has been studied extensively. However, very little research focusses on the interaction between the components, to the best of our knowledge. Only in recent research by Whiting et al., the interaction of the zeolite with an alumina and a clay has been studied.^[28,29] In their research, an increase in acidity was found, upon mixing of the zeolite with alumina.^[28,29] This illustrates that the combination of the different components can lead to changes in acidity and cracking activity.

1.3 The Zeolite

In literature, it is often stated that the zeolite is the main active component in the FCC catalyst, due to its shape selectivity and high concentration of Brønsted acid sites.^[2,8] Due to the high concentration of acid sites, a tuneable pore size, and tuneable shape, the origin and structure of acid sites in zeolites has been studied extensively and are therefore quite well understood.^[16,24,35]

The zeolite consists of a crystalline, tetrahedral silica framework in which some silicon atoms are substituted by aluminium.^[2,8,15–26] Since aluminium is a trivalent cation, the substitution of silicon by aluminium induces a partial negative charge in the silicon framework.^[8,26] This negative charge can subsequently be compensated by the uptake of a proton, resulting in the formation of a Brønsted acid site, as shown in Figure 2.^[25,26] The strength of this Brønsted acid site depends on the amount of aluminium incorporated in the framework: A high aluminium concentration results in a high concentration of Brønsted acid sites of medium acid strength.^[23,36,37] A lower concentration of aluminium results in a lower concentration of Brønsted acid sites, but with an increased acid strength.^[23,36,37] Though this theory is often postulated, there is no conclusive evidence which proves this theory, to the best of our knowledge.

Although the structure of the zeolite is quite stable, prolonged heating of the zeolite results in aluminium migration.^[21,38,39] In the work of Deng et al., it was reported that prolonged heating of the zeolite resulted in the formation of penta- coordinated, distorted tetrahedral, and octahedral aluminium coordinations, at the cost of the tetrahedral framework aluminium.^[40–44] These new aluminium coordinations are ascribed to the

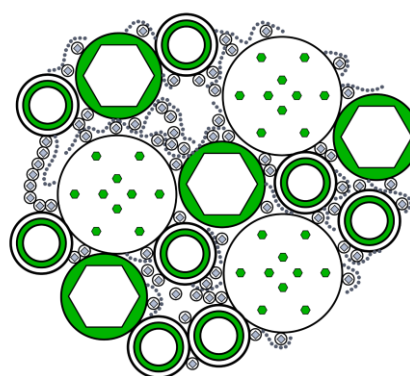
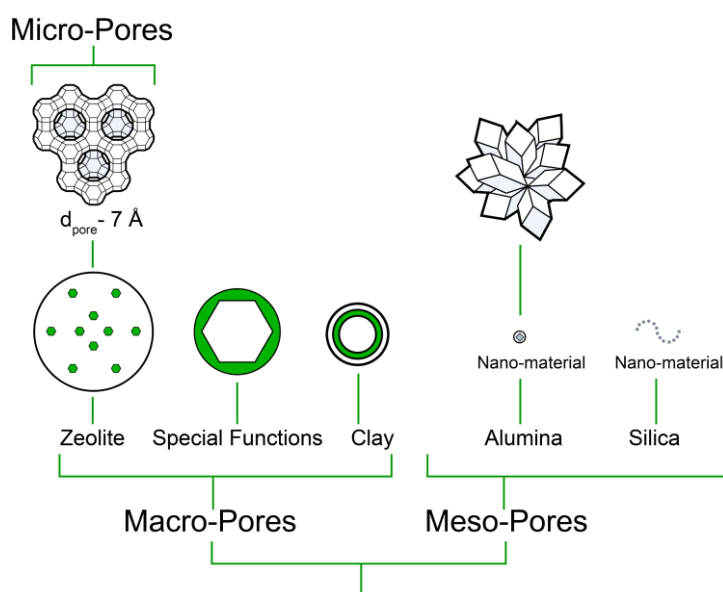


Figure 1 Schematic representation of the chemical and structural components of a FCC catalyst. Image copied from reference ^[2]

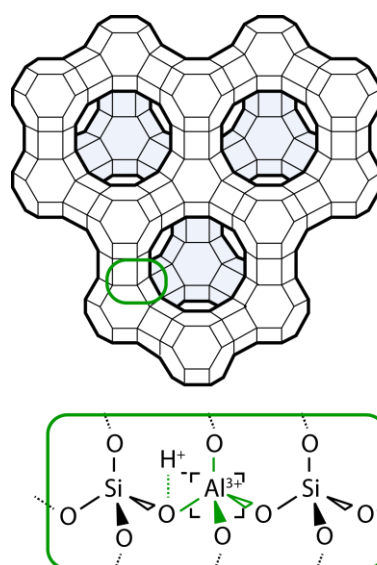


Figure 2 Schematic representation of the Brønsted acid site in a zeolite HY. ^[8,27,39]

formation of Extra Framework aluminium (EFAl) species, since these aluminium species are no longer located in the silica framework. The formation of the EFAl species is often associated with the formation of Lewis acid sites.^[8,21,44,45] The formation of EFAl species has been studied extensively, but a complete understanding of their structure, acidic character, and catalytic properties is still lacking.^[23,37]

1.4 The Active Matrix

As mentioned in section 1.2, the combination of clay and binder forms the active matrix, which is responsible for the pre-cracking of the oil.^[2] The pre-cracking is partially due to thermal cracking, but is also postulated to be Lewis acid catalysed.^[2]

The binder is a mix of crystalline alumina and amorphous silica. Alumina has several structures, which depend on the temperature treatment of the alumina precursor.^[46] The acidic character of alumina is generally ascribed to coordinatively unsaturated Al^{3+} ions, which can act as a Lewis acid site.^[23,47,48] In the work of Corma et al. it was shown that pure alumina contained primarily medium Lewis acid sites which showed a low cracking activity for the cracking of n-heptane.^[19,49] Pure silica contains only non-acidic surface hydroxyl groups and does not possess any intrinsic acidity.^[15,50] When silica and alumina are combined and heated, condensation of the surface hydroxyl groups of the two components can occur.^[15] This results in the formation of a Brønsted acid site at the interface of the silica and alumina. Overall, different acidities have been found for different silica-alumina mixtures, depending on the preparation and temperatures used to produce the silica-alumina mixtures.^[15,51,52]

The clay consists of the natural mineral kaolinite ($Al_2O_3 \cdot 2SiO_2 \cdot 2H_2O$).^[2,53] Kaolinite consists of layered alumina and silica sheets. After heating the kaolinite to temperatures around 550 °C, the structure changes from a crystalline structure into an amorphous structure, known as metakaolin.^[30,54-57] The metakaolin contains Brønsted and Lewis acid sites, which are formed due to the dehydroxylation of the kaolinite.^[30] In cracking reactions, kaolinite was shown to have a low activity, and seemed to be solely used for the stabilization of the FCC catalyst.^[30]

1.5 Aim and Approach

As described in paragraph 1.3 and 1.4, all the different components consist of alumina and silica. Changes in the acidity and activity have already been reported, upon mixing of the zeolite with alumina.^[28,29] This suggests that the clay, zeolite and binder can interact and possibly form new acid sites. The changes in acidity are most often correlated to a change in the environment around the aluminium nuclei.^[20,23,37,39,43,58] In order to obtain a complete understanding of the cracking mechanism, both the acidic contribution of the individual components and the combinations of the components must be elucidated.

For this research the main question we want to answer is: What is the structure-acidity correlation in the FCC catalyst and its individual components? This question can subsequently be split in sub-questions, which are discussed in the following chapters:

Chapter 4: How does the acidity and aluminium structure of zeolite HY change, with increasing aluminium concentration?

Chapter 5: How does the acidity and aluminium structure change, upon mixing of alumina with silica in the binder?

Chapter 6: What is the acidic and structural contribution of all the individual components to the acidity and structure the FCC catalyst?

Chapter 7: How does the acidity and aluminium structure change, upon mixing of the individual components?

Chapter 8: What structural and acidic changes occur, upon heating the FCC catalyst to temperatures present in the riser reactor (~538 °C)?

To answer these questions, we will investigate: a FCC catalyst of which the composition is known, the individual components of the FCC catalyst, and physical mixtures of two components.

The acidity was determined with CO and pyridine based infrared (FT-IR) spectroscopy. Additionally, magic angle- nuclear magnetic resonance (MAS-NMR) was used, to study the environment around the aluminium nuclei in a 1D-, and 2D multiple quantum- MAS NMR experiment. (²⁷Al MAS-NMR and ²⁷Al MQ-MAS NMR). Furthermore, proton MAS-NMR (¹H MAS-NMR) was used to study the different protons in the samples.

Chapter 2. Theory

In chapter 1, a general explanation was provided of the Fluid Catalytic Cracking (FCC) process and the contribution of the different components. In this chapter, a more in-depth description will be given of the FCC process, the cracking mechanism and the origin of the different acid sites in the FCC catalyst. Subsequently, the theory of Nuclear Magnetic Resonance (NMR) spectroscopy and FT-Infrared (FT-IR) spectroscopy will be explained in paragraph 2.4.1.

2.1 The Fluid Catalytic Cracking Process

As mentioned in section 1.1, the oil refinery industry uses the Fluid Catalytic Cracking (FCC) process to crack large hydrocarbons in the crude oil into smaller fractions.^[2] Figure 3 provides a schematic representation of the cracking process. At the bottom of the reactor, a mix of fresh and used catalyst is mixed with the Vacuum Gas Oil (VGO) or Heavy Gas Oil (HGO) fraction of the crude oil. Both the catalyst and the feedstock are pre-heated to approximately 530 °C.^[2] During the cracking of the oil, gaseous products are formed, which cause the feedstock and FCC catalyst to rise in the reactor. Due to the rapid rising in the reactor, the contact time between the FCC catalyst and the feedstock is in the order of seconds.^[2] At the top of the riser, the catalyst and the products are separated, using steam.

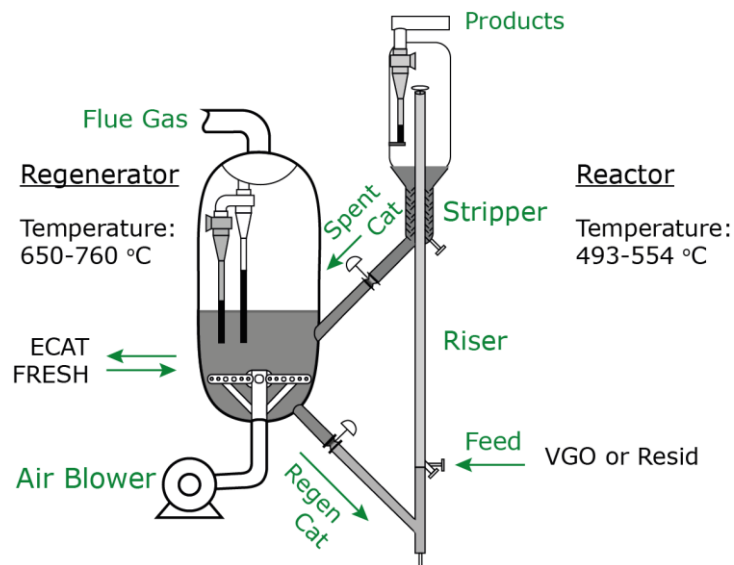


Figure 3 Schematic representation of the fluid catalytic cracking process, showing the riser reactor and regenerator with the appropriate temperatures. Figure copied from reference.^[2]

During the cracking of the oil, cyclic hydrocarbons are formed, known as coke.^[1,2,34,38] The coke blocks the pores in the FCC catalyst, which makes the acid sites inaccessible for the feedstock. To maintain a high cracking activity the catalyst is subjected to a regeneration cycle. During the regeneration cycle, the coke is burned off at approximately 760 °C. Due to the steaming conditions in the stripper and the high temperature in the regenerator, dealumination of the FCC catalyst occurs.^[22,24,59,60] Additionally, the VGO and HGO feedstock contains impurities like metals, and hetero-atoms such as sulfur and nitrogen. These impurities cause poisoning of the catalyst. As a result, the FCC catalyst gradually deactivates during each cycle.^{[61,62][1,2,24,34,38]} To maintain a high conversion rate, without continuously replacing the used catalyst with fresh catalyst, a mix of fresh and used catalyst is used, also known as an equilibrium catalyst or E-cat. The FCC is designed to be as effective and selective as possible, by taking the following properties into account^[2,27,38]:

- Activity: The FCC catalyst must have a high activity, which is accomplished by the incorporation of the acidic zeolite Y, which contains a high concentration of Brønsted acid sites.

An excessive amount of acid sites would however lead to the production of substantial amounts of gas and coke. An optimal activity therefore depends on the balance of the different acid sites and the amount of catalyst used in the process.^[63]

- **Selectivity:** The FCC catalyst must have a good selectivity for the desired products, to minimize the formation of unwanted side-products.^[38] This is realized, by making the pores shape selective for the desired products or the transition state of the reactants.
- **Lifetime:** The deactivation of the catalyst must be as slow as possible. Metal traps, a balanced acidity and shape selective pores help to minimize the metal poisoning and coke formation.^[38]
- **Stability:** The FCC catalyst particles must be able to withstand the harsh conditions in the riser reactor and regenerator, both thermally and mechanically.^[2]
- **Accessibility:** due to a very short contact time between the feedstock and catalyst, it is crucial that the active sites are accessible for the molecules. The introduction of micro-, meso- and macro-pores makes active sites more accessible.^[2]
- **Fluidizability:** the FCC particles must have the appropriate size to be fluidized. The fluidization of the FCC catalyst helps the rising of the catalyst with the oil, resulting in an optimal contact time between the catalyst and the feed-stock. ^[2]

2.2 The Cracking Mechanism

As mentioned in paragraph 1.4, the cracking of hydrocarbons is ascribed to both thermal cracking and acid catalysed cracking. Combining the results and findings of several papers and reviews, the most accepted and most commonly used mechanism is the cracking mechanism as depicted in Figure 4. ^[1,3,6,19,20,34,64,65]

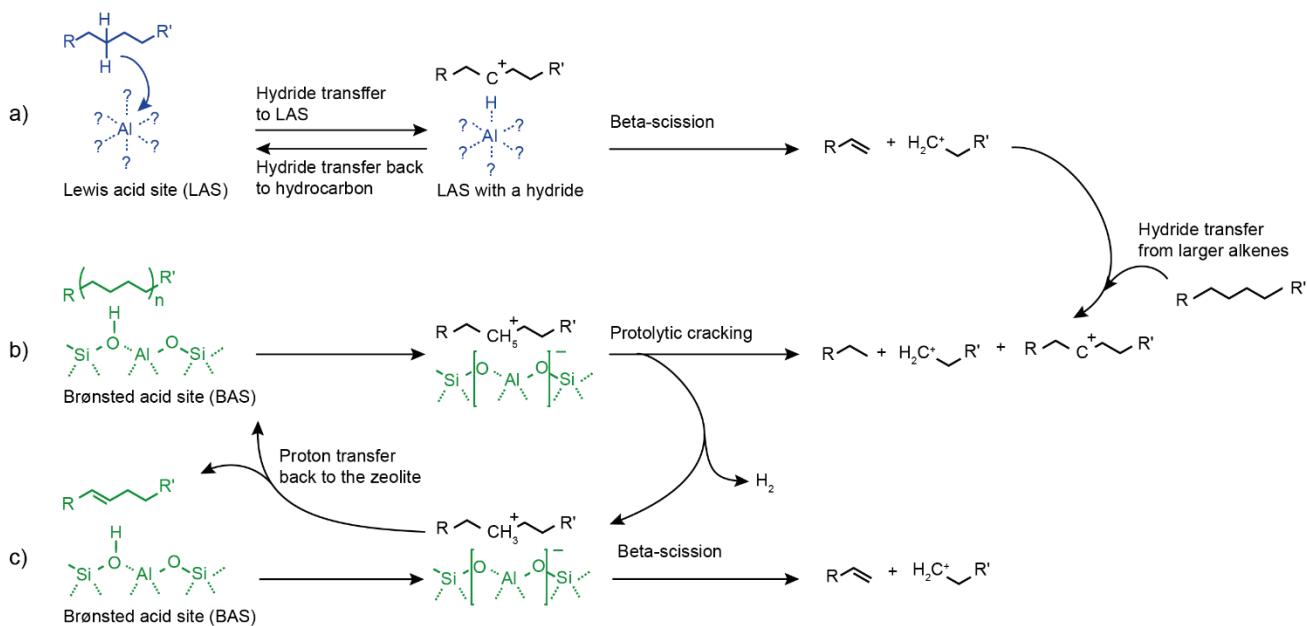


Figure 4 Schematic representation of the cracking mechanism, catalysed by a Lewis (a) or Brønsted acid site (b,c). ^[1,3,6,19,20,34,64,65]

The Brønsted acid site (BAS) catalysed mechanism (Figure 4b) involves the transfer of a proton, from the acid site, to an alkane, thereby creating a carbonium ion. The latter can transform to a carbenium ion through the loss of hydrogen or through protolytic cracking. The carbenium ion can subsequently undergo β -scission and form an alkene and an alkane. ^[2,19,27,64,65]

As shown in Figure 4a, the Lewis acid site (LAS) can abstract a hydride ion (H^-) from the alkane, generating a carbenium ion. The carbenium ion can subsequently undergo β -scission, as depicted in Figure 4c. The formed carbenium ion can also subtract a hydride from larger alkanes, recreating a new carbenium ion (Figure 4a).^[3,19,20,22,66]

2.3 The Origin of Brønsted and Lewis Acid Sites

As described in section 1.3, the origin of the Brønsted acid site in zeolites is very well understood. The substitution of a silicon atom with aluminium results in a negative charge in the silica framework.^[8,26] This negative charge can subsequently be compensated by the uptake of a proton, resulting in the formation of a Brønsted acid site, as shown in Figure 2.^[2,8,15–26] Brønsted acid sites also appear in physical mixtures of alumina and silica. Mixing of silica and alumina can result in bond formation between the silica and the alumina, which generates a Brønsted acid site.^[15] Zeolites and silica-alumina mixtures also contains Lewis acids sites, as described in paragraph 1.3 and 1.4. The exact origin and structure of the Lewis acid sites is however not completely understood.

In various papers, it is proposed that the Lewis acid sites originate from extra-framework aluminium (EFAl) species.^[8,21,44,45] It has also been postulated that the Lewis acid sites originate from trigonal coordinated aluminium within the framework.^[8,67] Octahedral, tetrahedral, trigonal and penta-coordinated aluminium has been found in different zeolites and silica-alumina samples.^[68] Numerous researches focussed on identifying the exact coordination of the EF aluminium species, but, to the best of our knowledge, no explanation was provided why these structures were Lewis acidic. Overall, it is proven that the addition of both framework and non-framework alumina results in the formation of Lewis acid sites.^[25,69] In order to understand how an aluminium can act as a Lewis acid the following considerations have to be taken into account:

The origin of the different Lewis acid sites most often involves the presence of Al^{3+} ion with different groups attached to it.^[23,37,41–43] The electronical configuration of an Al^{3+} ion is $[Ne]3s^03p^0$. The empty 2s and 3p orbitals can subsequently hybridization to form four empty sp^3 orbitals, favouring a tetrahedral coordination.^[25] Due to the three plus charge, aluminium is able to accommodate three negative charges in three of the four empty sp^3 orbitals. The additional empty orbital could however still accept electrons, which subsequently results in a net negative charge in the complex. In literature, octahedral and penta-coordinated aluminium species are also postulated to act as a Lewis acid site. Therefore, it can be assumed that aluminium has the same characteristics as a d-metal, which can form organo-metallic complex. The attached groups could then be considered to serve as ligands, which are coordinated to the aluminium.^[25,69] This model is confirmed with DFT calculations in the work of Li et al.^[43,44,70] In their work they show that the different aluminium coordinations are formed due to coordination of EFAl species to the framework, or due to coordination of water. The oxygen atoms in the framework are coordinated to the aluminium, without the formation of covalent bonds. As a result, a peak affiliated with octahedrally coordinated aluminium is observed in the ^{27}Al MAS-NMR spectra.^[43,44]

In order to understand the strength and origin of the different acid sites, it is important to elucidate the structure around the aluminium nuclei.

2.4 Characterization Techniques

To investigate the structural changes upon mixing of the different component in the FCC, the coordination around the aluminium is studied with nuclear magnetic resonance (NMR) spectroscopy. To confirm that the structural changes did not only occur around the aluminium nuclei, changes in the crystallinity and morphology were determined using X-Ray diffraction (XRD) and transmission electron microscopy (TEM) measurements. To determine the acidity of the samples, both pyridine and CO based FT- Infrared Spectroscopy (FT-IR) was used. The physical principles of NMR and the different NMR techniques will be discussed in paragraph 2.4.1. The physical principles behind probe-molecule based FT-IR measurements will be discussed in section 2.3.2

2.4.1 Nuclear Magnetic Resonance

In this paragraph, the principles of Nuclear Magnetic Resonance spectroscopy will be explained. First the physical principles and interactions between nuclei will be reviewed. Additionally, the different NMR techniques, which are used in this thesis, are explained.

2.4.1.1 Physical Principles

NMR stands for Nuclear Magnetic Resonance. In a NMR experiment, the change of the net magnetization of the studied nucleus is investigated. How this net magnetization changes, is characteristic for the magnetic field applied and chemical environment around the nucleus. A NMR experiment consists of four basic steps: First an external magnetic field is applied, followed by a radio frequency (RF) pulse perpendicular to the direction of the external magnetic field as shown in Figure 5A. The change of the net magnetization of the nuclei is subsequently measured and the signal is transformed with a Fourier transformation to obtain the spectrum, characteristic for the environment around the nucleus. ^[16,35,71-76]

All nuclei possess a spin, and when an external magnetic field is applied, they precess around the magnetic field at a particular frequency, known as the Larmor frequency, ν_L . The Larmor frequency is different for each element, which enables us to look at specific changes around one type of nucleus. Since nuclei consist of protons, they possess a nuclear charge. Movement of a charge results in the formation of a magnetic moment, according to Ampère's law. The rotation of the nuclei therefore creates a magnetic moment $\mu = \mathbf{P} \cdot \gamma$, where \mathbf{P} is the angular momentum and γ the gyromagnetic ratio of the nucleus. The magnetic moment μ is susceptible to an external magnetic field. Thus, when the nuclei are placed in an external magnetic field, the nuclei will orient their spin in the same direction as the external magnetic field, if γ is positive. The alignment of the nuclear spin with respect to the external magnetic field causes a separation in energy between the different spin states, due to the quantization of the magnetic moment: $\mathbf{P} = \hbar \sqrt{I(I+1)}$ where I is the angular momentum quantum number. The energy of the different spin states is given by $E = m \cdot \gamma \cdot \hbar \cdot B_0$ and therefore depends on the strength of the magnetic field, as shown in Figure 5A. The different spin states created due to this quantization are also called Zeeman levels. The difference in energy between the Zeeman levels depends on the strength of the external magnetic field: A stronger external magnetic field results in a larger energy separation, as shown in Figure 5A. ^[16,35,71-76] Most nuclei in the periodic table contain an angular momentum which is higher than $\frac{1}{2}$, which result in quadrupolar interactions, which are discussed in paragraph 2.4.1.2.4. ^[16,35,71-76] For the explanation of the physical principles, a system with $I = \frac{1}{2}$ will be used.

Due to the different energy of the different spin states, occupation of the spin states with a low energy is thermodynamically more favourable. The distribution of the nuclear spins over the spin states, is given by Boltzmann statistics $\frac{N_\beta}{N_\alpha} = e^{-\Delta E/k_B T}$. At room temperature the Boltzmann statistics tells us that there

is a population difference of approximately 1 in 10^5 for protons. Though this difference in population is very low, the difference results in a tiny net magnetization, due to overpopulation of one of the two spin states, as depicted in Figure 5 B. The Boltzmann statistics also show that the distribution depends on the temperature and is therefore slightly tuneable: Cooling the system results in a larger population difference and therefore a stronger NMR signal can be obtained. [16,35,71–76]

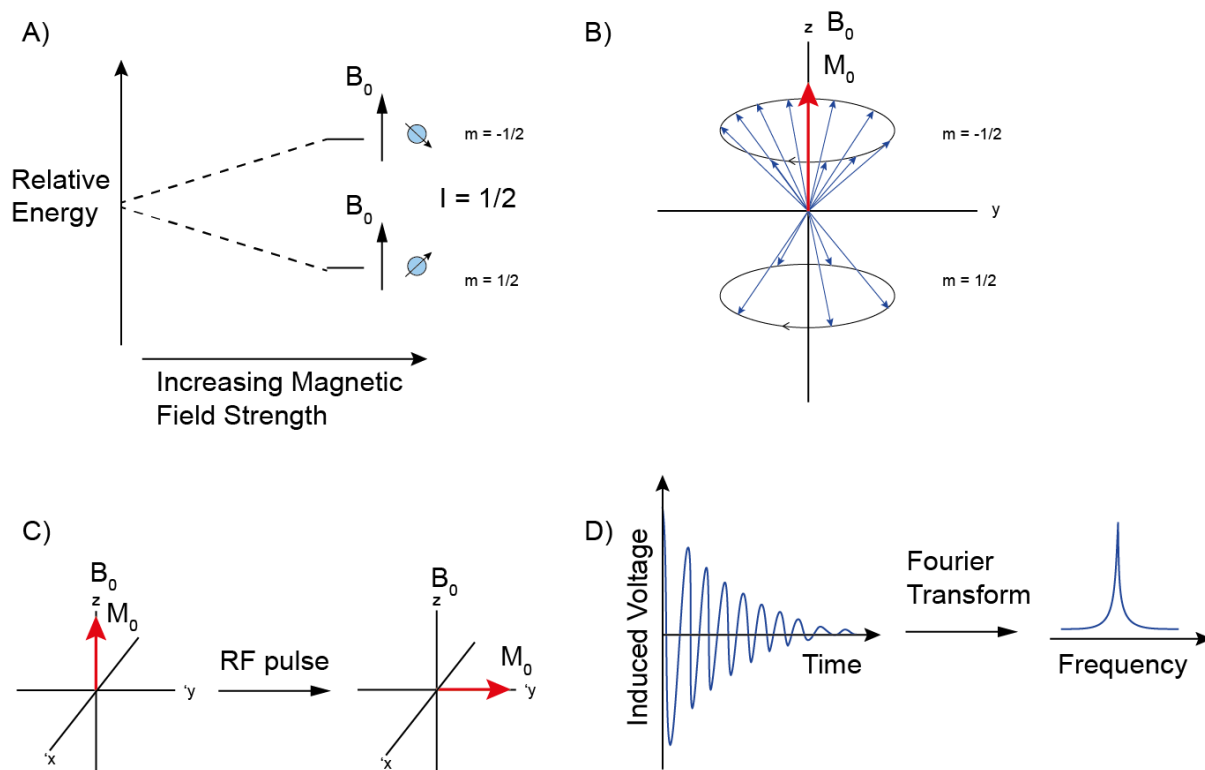


Figure 5 A) Schematic representation of the splitting in energy between two different spin states of a nucleus with spin $1/2$. A stronger magnetic field results in a larger splitting between the spin states. B) Schematic representation of the difference in spin population, which results in a net magnetization M_0 . C) The change of the net magnetization after a RF pulse is applied. The 'x and 'y axis represent the rotational axes. D) Schematic representation of the NMR signal. [73,79]

The energy difference between the spin states can be overcome by applying a RF pulse to excite the nuclei to a different spin state. For this excitation the energy of the RF pulse must equal the energy difference between the Zeeman levels, $\Delta E = \gamma \hbar B_0 = \nu_1 \hbar$. The frequency of the pulse must therefore match the precession frequency of the nuclei, $\nu_L = \nu_1 = \left| \frac{\gamma}{2\pi} \right| B_0$, hence the term Nuclear Magnetic Resonance: The frequencies of the pulse must resonate with the frequency of the nuclei. [16,35,71–76]

When this energy difference is overcome, the spin population will be altered, causing the net magnetization to change direction as shown in Figure 5C. The angle over which the net magnetization will change depends on the strength of the RF pulse. The change of the net magnetization induces an alternating current in the receiver coil. The alternating current is the signal detected in an NMR experiment (Figure 5D). Since the nuclei precess with the Larmor frequency, the signal looks like a sinusoidal which decays exponentially over time, as shown in Figure 5D. The signal decays, due to relaxation of the nuclei back to their original spin states. The time it takes for all the nuclei to relax back to their original spin state is called the T_1 or longitudinal relaxation time. The signal, detected in the time domain, can subsequently be transformed into the frequency domain with a Fourier transformation, to obtain the spectrum. [16,35,71–76]

From the spectrum the resonance frequencies of the nuclei can be obtained. In NMR there is however no absolute value for the resonance frequencies, since the measured frequencies are dependent on the magnetic field strength B_0 . Therefore, a relative scale is used, whereby the frequency difference between the resonance signal of the sample and a reference compound is measured. The difference frequency also depends on the magnetic field strength. To correct for this, the frequency difference is divided by the resonance frequency of the reference compound: $\delta_{sample} = \frac{\nu_{sample} - \nu_{reference}}{\nu_{reference}}$.^[76] The obtained value is defined as the chemical shift.

2.4.1.2 Interactions

In this section the different interactions between nuclei are explained. These interactions are all present in solids and liquids.

2.4.1.2.1 Chemical Shielding

One of the most dominant interactions in liquids and solids, is the chemical shielding $B_{eff} = (1 - \sigma)B_0$, in which σ is the chemical shielding constant. The shielding constant is a measure of the electron density around a nucleus, which shield the nucleus from the magnetic field.

When two nuclei with different dipole moments are in close proximity, the nucleus with the higher dipole moment withdraws electron density from the neighbouring nucleus. The effective electronic shielding, provided by the electrons, is therefore decreased for the nucleus with the lower dipole moment. The difference in electronic shielding is measured by the chemical shielding constant. A higher chemical shielding constant then results in a decrease of the effective magnetic field, experienced by the nucleus. This subsequently results in a change of the resonance frequency: $\Delta E = \gamma \hbar B_{eff} = \nu_1 h$. When this formula is combined with the chemical shielding, a new resonance condition is obtained $\nu_1 = \left| \frac{\gamma}{2\pi} \right| (1 - \sigma)B_0$. This new resonance condition illustrates that a high/low chemical shielding results in a high/low chemical shift.^[16,35,71-76] The difference in chemical shift is therefore a measure of the difference in electronic shielding of the nuclei and thereby gives information about the local environment around a nucleus.

2.4.1.2.2 Indirect Spin-spin Coupling

The principal source of spin-spin coupling in molecules is an indirect interaction, mediated by electrons involved in chemical bonding. When nuclei of the same element are attached to neighbouring atoms, their magnetic moments can interfere. This coupling of nuclear magnetic moments causes a slight difference in energy, which can be detected. This results in splitting of the peaks in the NMR spectrum. The coupling pattern which arises has the same intensity as

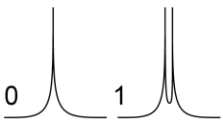
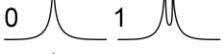

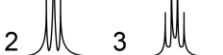
Number of indirect neighbouring nuclei	Coupling pattern	Spectrum
0	1	
1	1 1	
2	1 2 1	
3	1 3 3 1	

Figure 6 From left to right: Number of neighbouring nuclei; Pascal triangle which gives the relative intensities of the peaks; Obtained NMR spectra with the number of neighbouring nuclei.

given by the Pascal triangle as shown in Figure 6. This indirect spin-spin coupling is more often referred to as the J coupling. The energy difference between the peaks is called the scalar coupling constant J. Coupling between chemically equivalent nuclei cannot be observed. For example: A proton spectrum of

benzene will show only one peak, since all protons are chemically identical. This type of coupling is visible both in liquids and solids.^[16,35,71–76]

2.4.1.2.3 Direct Spin-spin Coupling

This interaction is most often referred to as the dipolar coupling. The dipolar coupling is an interaction between the dipolar nuclear magnetic moments of two nuclei. Since each nucleus has a spin, a small magnetic field is generated by the nucleus. The interaction of the generated magnetic field with the neighbouring nucleus results in a slight change in effective magnetic field experienced by the neighbouring nucleus. The change in the magnetic field subsequently results in a change in the chemical shift. This causes broadening of the peaks in the NMR spectrum. With the right software, the proximity between two nuclei can be estimated, based on this interaction. This interaction is averaged in liquids, due to the rapid motion of the molecules. In solids the heteronuclear dipolar coupling can be averaged by rapid rotation around the magic angle, which is discussed in paragraph 2.4.1.3.1.^[16,35,71–76]

2.4.1.2.4 Quadrupolar interaction

As mentioned in paragraph 2.4.1.1, most nuclei in the periodic system have a nuclear spin which is larger than $\frac{1}{2}$. This results in an additional interaction: the quadrupolar coupling. Due to this spin $> \frac{1}{2}$, the nucleus has a quadrupole moment which couples to the inhomogeneous local electric field gradients (EFG).^[78] This means that the electrons are not symmetrically distributed around the nucleus, but take the shape of an ellipse, as shown in Figure 7.^[79]

Due to the elliptical distribution of the electrons around the nucleus, the effective magnetic field becomes directionally dependent. This results in a change in the energy separation between the Zeeman levels. To what extent the Zeeman levels change depends on the EFG, which on its turn depends on the chemical environment and symmetry around the nucleus.^[80] The quadrupolar coupling (QC) contains two components: the first and second order quadrupolar coupling. The first order QC only shifts the Zeeman levels symmetrically with respect to each other. The central transition (between $m = \frac{1}{2}$ and $m = -\frac{1}{2}$) is not affected by this interaction. The second order QC results in an asymmetric shift of the Zeeman levels, which does change the position of the central transition, as shown in Figure 8. Since the central transition is the only transition which is exclusively affected by the second order QC, excitation of the central transition results in relatively sharp peaks which contains information about the strength of the second order QC. The first order QC can be averaged with spinning around the magic angle, which is explained in paragraph 2.3.1.3.1. The second order QC cannot be averaged however, which results in slight

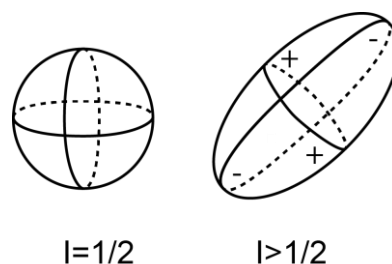


Figure 7 A schematic representation of the electron distribution around a nucleus with $I = \frac{1}{2}$ and $I > \frac{1}{2}$.^[79]

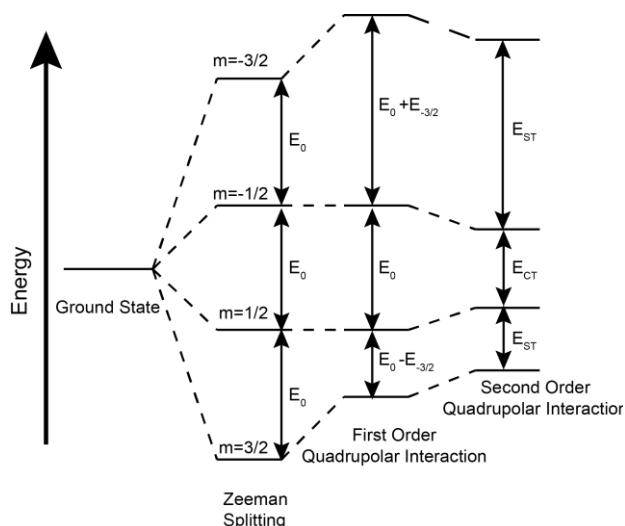


Figure 8 Splitting of the Zeeman levels due to the quadrupolar interaction. Image copied from reference.^[80]

differences between the spin states. These minor differences in energy result in broadening of the peaks in the NMR spectrum. The peaks get more broadened with increasing distortion around the nucleus, due to an increased QC. The broadening of the peaks in the spectra is therefore also a measure of the distortion around the nuclei.^[35,79,80]

2.4.1.3 Advanced NMR techniques

2.4.1.3.1 Magic Angle Spinning

MAS stands for Magic Angle Spinning, which refers to the rapid rotation of the sample, while keeping the sample tilted around the magic angle (about 54.7°). Spinning around the magic angle helps with the spatial averaging and it removes the following interactions: the chemical shift anisotropy, the heteronuclear dipolar interactions and the second rank elements of the second order quadrupolar interaction. This overall results in more defined and sharper peaks in the spectrum. For quadrupolar nuclei, the second order quadrupolar interaction is, however, not completely cancelled and, therefore, still causes broadening of the peaks in the NMR spectrum. This technique is primarily used for solid samples, since the signal is largely affected by the intermolecular interactions, which are averaged in liquids, due to the rapid movement of the molecules.^[16,35,71–76]

2.4.1.3.2 ²⁷Al MQ-MAS

MQ-MAS stands for Multiple Quantum Magic Angle Spinning, where multiple quantum refers to the fact that the nucleus possesses multiple quantum spin states. MQ-MAS is a 2D pulse sequence that correlates the isotropic chemical shift in one dimension to the anisotropic chemical shift in the second dimension. The pulse sequence of an MQ-MAS experiment is shown in Figure 9.^[78,79] The isotropic chemical shift still contains information about the second order quadrupolar interaction, whereas the anisotropic chemical shift is primarily affected by the chemical shielding. Plotting the anisotropic versus the isotropic chemical shift results in a 2D spectrum in which the coordination is plotted versus the distortion of that specific coordination. The broadening along the isotropic dimension therefore gives an indication of the strength of the second order quadrupolar coupling, and therefore about the level of distortion around the aluminium nucleus.^[35,79,80]

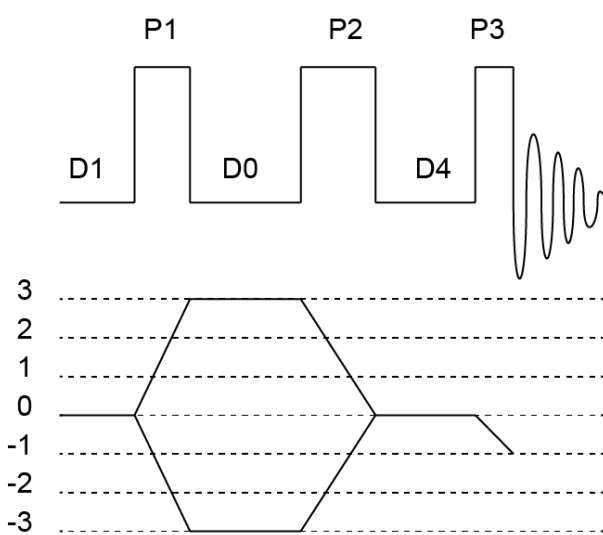


Figure 9 Schematic representation of a MQ-MAS pulse sequence (above) and the spin states (below). P1 is the excitation pulse followed by P2 the conversion pulse. P3 is the 90-degree selective pulse.^[35,79,80]

2.4.1.3.3 CP and HETCOR

In this section, the very basic principles of coupled NMR techniques are explained, to get a general impression about what sort of information can be obtained from these techniques. An in-depth explanation of the techniques is beyond the scope of this thesis.

Using the effect of heteronuclear coupling, coupled NMR techniques can be used to get more information about the proximity of different nuclei. In a Cross Polarization (CP) experiment, the polarization is transferred from one nucleus to another in close proximity. In order to do that, the Hartmann-Hahn condition has to be fulfilled: $\gamma_S B_{1S} = \gamma_I B_{1I}$ in which S and I represent the spins of the

two different nuclei. The Hartmann-Hahn condition states that the spin states of two different nuclei must have the exact same ‘position’ of the spin states, in order for the spins to be coupled. This is illustrated in Figure 10. This is accomplished by spin-locking the two different spins. If this condition is fulfilled, the spin population of one nucleus can be transferred to a different nucleus. This results in an enhanced signal of the nuclei which are close to the nuclei of which the spin population is transferred.^[35,81]

Another powerful method for analysing heteronuclear connectivities is the HETeronuclear CORrelation (HETCOR) experiment. This experiment is similar to a CP experiment, but instead of a 1D spectrum, a 2D spectrum is obtained in which the enhances signals appear as cross-peaks in the NMR spectra. Thus, when two nuclei are in close proximity, a cross-peak appears in the NMR spectrum. It can therefore directly be deduced which nuclei are in close proximity to each other, by looking at the cross-peaks.

When quadrupolar nuclei are investigated, it is useful to combine MQ-MAS and HETCOR techniques, in a so-called MQ-HETCOR experiment. In a MQ-HETCOR, first the MQ-MAS pulse sequence is used and subsequently a CP experiment is performed.^[72] The difference between a normal HETCOR and a MQ-HETCOR is the decreased broadening of the peaks, due to the MQ-MAS experiment. Since the MAS-NMR spectrum of a quadrupolar nucleus still contains broadening due to the second order quadrupolar coupling, the peaks are very broad. As mentioned in section 2.4.1.3.2, the MQ-MAS experiment separates this broadening from the anisotropic chemical shift. The enhanced MQ-HETCOR cross-peaks are therefore also separated from their anisotropic chemical shift.

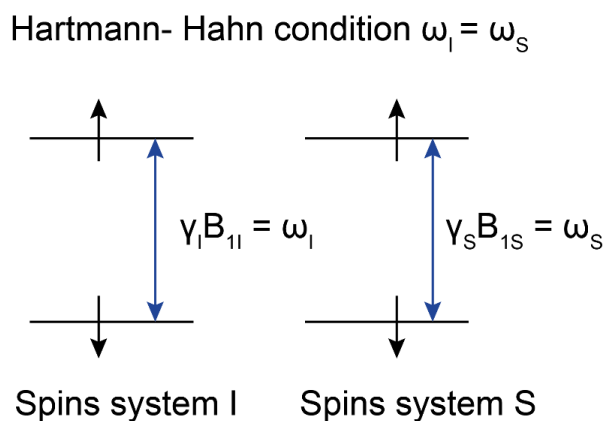


Figure 10 Schematic representation of the Hartmann-Hahn condition, showing the resonance condition of two nuclei.

2.4.2 Probe Molecule-based Infrared Spectroscopy

As described in paragraph 1.5, probe molecule based infrared spectroscopy (FT-IR) is used, to study the acidity of the samples. Probe molecules are used since they can provide information about the strength and origin of the different acid sites. The probe molecule is chosen in such a way that it can interact with the acid site without reacting. Due to the interaction of the probe molecule with the acid site, the frequency of the probe molecule changes.^[36,82] The change in the frequency can subsequently be detected with FT-IR spectroscopy. In order for a probe molecule to be a good probe molecule it has to meet certain requirements.^[82,83] The probe molecule:

- Cannot react with the sample
- Must inform on the nature of the acid site: It must distinguish the difference between a Lewis- and a Brønsted acid site.
- Must have a vibrational frequency which appears in a suitable zone: If overlap between multiple vibrations occurs, the distinction of the acid sites is more difficult.
- Must be small enough to access the acid sites

For this research, both pyridine (Py) and carbon monoxide (CO) are used as probe molecules. Pyridine is slightly larger and has a higher basicity, compared to CO.^[82-84] This makes pyridine a better probe molecule for strong acid sites and CO a good probe molecule to probe medium acid sites. CO is a smaller molecule compared to pyridine, which makes it more suitable to detect acid sites which are not accessible to pyridine. In the following two sections, the interactions between different acid sites and CO and pyridine are discussed. In paragraph 2.4.2.3, characteristic OH vibrations of silica, alumina and zeolite HY are discussed.

2.4.2.1 CO as probe molecule

CO has a high sensitivity for both Brønsted and Lewis acid sites and is often used to probe the acidity of the sample. In order to use CO as a probe molecule, the sample has to be cooled to $-189\text{ }^{\circ}\text{C}$ with liquid nitrogen. At this temperature, CO is inert and can adsorb on the different acid sites. In the experiment, an increasing amount of CO is pulsed onto the sample. To determine the acid strength, the change in the CO stretching frequency is studied. In Figure 11, three different interactions are shown between CO and a metal. The sigma donor interaction is the most dominant interaction between CO and the surface (interaction 1 in Figure 11). An increasing electron withdrawing character of the surface results in more sigma donation of the CO. This subsequently results in stabilization of the CO bond and therefore an increase in the stretching frequency. The shift in the CO stretching frequency is therefore an indication of strength of the acid site to which the CO coordinates.^[48,85]

Since a Lewis acid site is defined as an electron acceptor, the interaction between CO and a Lewis acid site results in a band formation between $2240 - 2180\text{ cm}^{-1}$, where an increase in acid strength results in a shift to higher wavenumbers.^[82,83,86] A Brønsted acid site is defined as a proton donor, in which case the proton is electron deficient.^[26] The electron withdrawing properties of a Brønsted acid site are therefore less, compared to a Lewis acid site. The CO stretching frequency of a Brønsted acid site is therefore less compared to when CO is interacting with a Lewis acid site.^[25,26] The interaction of CO with a Brønsted acid site typically results in a band between $2180 - 2160\text{ cm}^{-1}$.^[82,83,86]

Bands affiliated with CO on a non-acidic surface hydroxyl groups are found between $2160 - 2145\text{ cm}^{-1}$. In order to see if the surface is saturated with CO, the band around $2145 - 2140\text{ cm}^{-1}$ is used as a reference. The band around $2145 - 2140\text{ cm}^{-1}$ is ascribed to liquid-like CO, or physisorbed CO.^[23,36,82] Upon increased loading of CO on the surface, the acid sites will be occupied first. Increasing loading of CO

subsequently results in a shift of the bands to lower wavenumbers due to dipole-dipole interactions between the CO molecules.

Sometimes, bands below 2140 cm^{-1} are observed. These bands form due to interaction of metal ions with the CO, as described by interaction of type 2 and 3 in Figure 11. Both interactions result in a decrease of the CO stretching frequency.^[69]

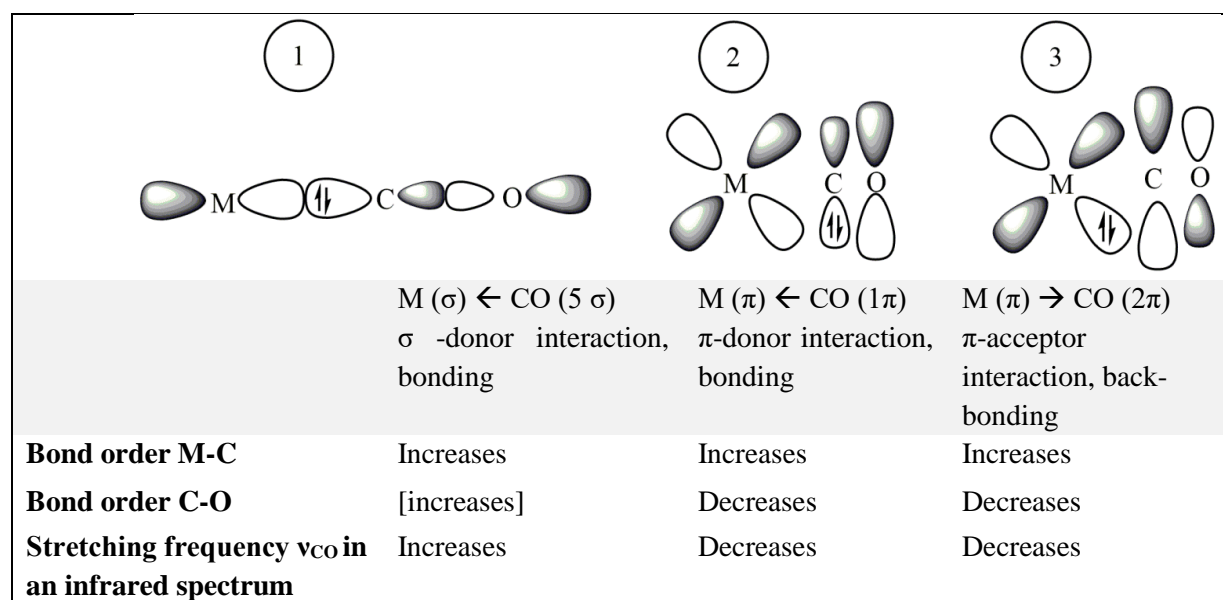


Figure 11 Schematic representation of the interaction of CO with a material (M).^[87] The first interaction involves sigma donation of the antibonding 5 sigma orbital of the CO to the metal. The second interaction involves pi donation of the 1 pi non-bonding orbital of the CO to the metal. The third interaction is pi donation of the metal in the 2 pi bonding orbital of the CO.

2.4.2.2 Pyridine as probe molecule

Pyridine is a probe molecule which is also often used to probe Lewis and Brønsted acidity. The lone pair of the nitrogen does not participate in the aromaticity of the pyridine and can therefore easily be donated, which leads to the strong basicity of pyridine. The high basicity of the pyridine makes it a suitable probe molecule to probe strong acid sites.

In pyridine based FT-IR spectroscopy, the change of the ring vibration is studied. Pyridine has four vibrational modes as shown in Figure 12. Each mode has a specific frequency and therefore appears as a different band in the FT-IR spectrum. These vibrational modes of pyridine appear around $1400\text{-}1650\text{ cm}^{-1}$ in the infrared spectra.^[83,88]

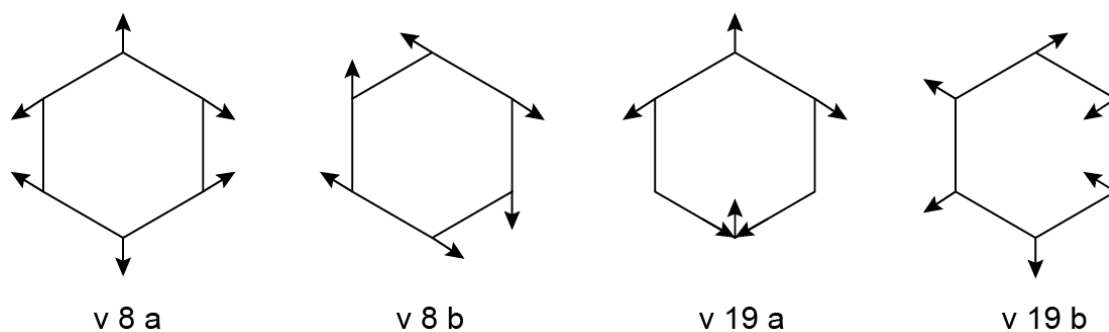


Figure 12 Schematic representation of the different vibrational modes of pyridine, copied from reference^[82,88]

When pyridine is adsorbed, the electrons located on the nitrogen interact with the surface. This interaction is similar to the sigma donation of CO (interaction 1 in Figure 11). Due to the decreased electron density of the nitrogen, the frequency of the vibrational modes is slightly changed. The frequency of the vibrational modes, upon adsorption on different acid sites, are tabulated in Table 1. The 8a and 19b vibrational modes are the most sensitive to changes in acidity and are therefore often used to determine the different acid sites in the sample.

Like CO, the adsorption of pyridine on a stronger acid site results in a shift towards higher wavenumbers. The shift is however less pronounced compared to CO. Therefore, temperature programmed desorption (TPD) is performed, after loading the samples with pyridine. The temperature is gradually increased, to promote desorption of the pyridine. This way, the physisorbed pyridine is removed and the pyridine on strong acid sites remain attached.

Table 1 Vibrational modes of pyridine attached to different acid sites with the corresponding wavenumber [82,89,90]

Vibration	Physisorbed (cm ⁻¹)	H-bonded (cm ⁻¹)	Coordinated to Lewis acid site (cm ⁻¹)	Pyridinium (cm ⁻¹)
8a	1585	1580-1600	1600-1630	1630-1640
8b	1570	1575-1580	1575-1580	1610-1640
19a	1478	1475-1485	1490-1500	1485-1495
19b	1438	1440-1450	1445-1455	1500-1540

2.4.2.3 OH vibrational region in FT-IR

As described in paragraph 2.3, Brønsted acid sites are attached to an aluminium with a localized negative charge. The electron withdrawing character of the aluminium subsequently affect the strength of the OH bond. The change in the strength of the OH bond can be detected with FT-IR. In this paragraph the characteristic OH vibrations of silica, alumina and zeolites will be discussed.

Silanol groups give rise to a band at 3745 cm⁻¹. [21,36,58,91] Hydroxyl groups attached to framework alumina shows multiple bands between 3790-3750 cm⁻¹. Extra-Framework (EF) type aluminol groups give rise to multiple bands around 3690-3670 cm⁻¹. [15,48,58,83,89,92-95] Figure 13 shows the different positions of the Brønsted acid sites in a zeolite HY. OH groups positioned at the 1 or 4 position result in a band around 3625 cm⁻¹, also referred to as OH groups in a super cage, or the high-frequency (HF) band. OH groups at the 2 or 3 position result in a band around 3545 cm⁻¹ and is referred to as OH groups in a sodalite cage, or the low-frequency (LF) band. Both bands are characteristic for zeolite HY type Brønsted acid sites. [23,36,37,48,58,91,95-98] The difference in band

position of the HF and LF band is ascribed to the confinement of the OH groups: the OH groups in the sodalite cage are more confined, which results in a lower vibrational frequency. The HF and LF band

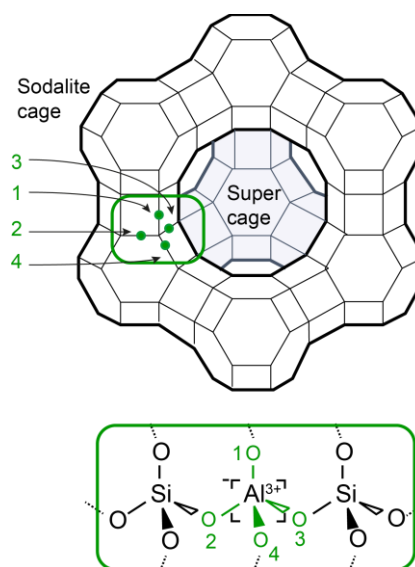


Figure 13 Structure of zeolite HY, displaying the position of possible acidic OH groups. [23] The numbers 1-4 indicate the positions where a Brønsted acid site can be located.

can also shift, due to a change in acidity: A stronger Brønsted acid site has a weaker OH bond and thus results in a lower vibrational frequency.^[36] This shift to lower wavenumbers is referred to as a red shift.

The acidic character of the different OH vibrations can be determined by observing which OH vibration is consumed upon probing the samples with either CO or pyridine. The band position in the CO (2500-2250 cm^{-1}) or pyridine (1700-1350 cm^{-1}) vibrational region can subsequently be used to differentiate the acidic character of the OH group.

Chapter 3. Experimental

3.1 Samples

The following samples were provided by Albemarle®:

FCC catalyst: This FCC catalyst contains 30 weight percent of the three individual components and contains no additional components with special functions. The FCC catalyst consists of the binder component, a zeolite HY with a Si/Al ratio of approximately 7, clay, which is a washed kaolin. In this thesis, the terms FCC or FCC catalyst are used to refer to this sample.

Zeolite HY: Three samples of zeolite HY were provided, with a different Si/Al ratio of 30, 11 and 7. The zeolites are proton exchanged to remove ammonium counter ions and to create Brønsted acid sites. In this thesis, the zeolite with a Si/Al ratio of 7 is referred to as zeolite.

Binder: The binder is a mix of both amorphous silica and two types of boehmite: high crystalline and low crystalline.

Clay: The clay consists of the mineral kaolinite. Two types of clay were provided: washed and not washed. In this thesis, both samples are referred to as clay, since no differences were found in the crystallinity or acidity, as shown in Appendix 13.6.2.

Binder-zeolite mix: This is a physical mixture in which 50 weight percent of binder was mixed with zeolite HY Si/Al 7.

Binder- clay mix: This is a physical mixture in which 50 weight percent of binder was mixed with clay.

Alumina: This is an amorphous alumina, prepared from AlCl_3 with temperature treatments.

Silica: This is an amorphous silica.

Boehmite: Two types of boehmite were provided: high crystalline and low crystalline boehmite. Both samples were kept in a container with an aqueous solution. Approximately 2 grams of high crystalline boehmite and 5 grams of low crystalline boehmite was dried at 60 °C overnight.

All the samples were calcined and spray-dried by Albemarle®. The samples are approximately 5 years old and have been kept in a dark and dry place.

3.1.2 Heat treatment

The samples were heated to 538-550 °C to imitate the temperature present in the riser reactor of the FCC process, as described in paragraph 2.1. The samples were heated in a quartz calcination tube in an oven, with a continuous nitrogen flow of 100 ml/min. The samples were subsequently transferred to a glovebox, to make sure the samples were not exposed to air or moisture.

3.2 Characterization Techniques

3.2.1 Infrared Measurements

The infrared (FT-IR) measurements were performed on a Perkin Elmer System 2000 with a DTGS detector and a resolution of 4 cm^{-1} with 32 scans per spectrum. Approximately 15 mg of sample was pressed into a thin wafer and placed in the CO/pyridine cell.

For the CO measurements the sample was heated with $10\text{ }^{\circ}\text{C}/\text{min}$ to $550\text{ }^{\circ}\text{C}$ under a dynamic high vacuum. The samples were kept at $550\text{ }^{\circ}\text{C}$ for one hour, after which the sample was cooled to room temperature. Subsequently, the sample was cooled with liquid nitrogen to $-188\text{ }^{\circ}\text{C}$. The samples were then loaded with increasing amounts of CO. This was done by building a pressure of CO in the pump system, while keeping the valve to the cell closed. Subsequently, the CO was used to pulse the system, by opening the valve to the cell. In this way the system was pulsed with increasing pressure of CO, to gradually saturate the surface. The surface was saturated when the intensity of the band around 2140 cm^{-1} , ascribed to liquid like CO, increased faster compared to the bands around 2155 cm^{-1} , ascribed to CO attached to non-acidic groups and the Lewis and Brønsted acid sites were saturated. [36,82,99,100]

For the pyridine measurements the sample was heated with $10\text{ }^{\circ}\text{C}/\text{min}$ to $550\text{ }^{\circ}\text{C}$ under a dynamic high vacuum. The sample was kept at $550\text{ }^{\circ}\text{C}$ for one hour, after which the sample was cooled to room temperature. The sample was then exposed to approximately 22 mbar of pyridine vapour for 30 min., after which a vacuum was applied for 45 min., to remove all the physisorbed pyridine. Subsequently temperature programmed desorption (TPD) was performed, by heating the sample with $5\text{ }^{\circ}\text{C}/\text{min}$ to $550\text{ }^{\circ}\text{C}$ to remove all the pyridine.

3.2.2 NMR measurements

NMR measurements were performed on a Bruker 500 MHz spectrometer of 11.7 Tesla. The samples were spun with 18 kHz. $\text{Al}(\text{NO}_3)_3$ was used as a reference for the ^{27}Al NMR measurements. A 3.2 mm probe was used on a double channel with a 120-205 MHz filter. The MQ-MAS spectra were recorded with a zero-quantum filtered MQ-MAS pulse sequence. The rotor was exposed to air during the measurements.

For the NMR measurements, the samples were put in a 3.2 mm zirconia rotor with an air tight Teflon cap. The samples which were subjected to a heat treatment were filled in the glovebox to minimize the exposure to air and were then transported in a sealed Eppendorf tube to the spectrometer. To check whether the rotor was air tight, a ^1H -NMR spectrum was measured before and after the experiment, of some samples.

3.2.3 XRD measurements

X-ray powder diffraction (XRD) measurements were performed on a Bruker AXS Advance D8 apparatus, equipped with Co $K\alpha$ radiation, operating at 45 kV and 30 mA. The diffractograms were collected between $10\text{--}80\text{ }^{\circ}$ or $20\text{--}80\text{ }^{\circ}$ respectively with different increments, depending on the sample. The samples were prepared outside of the diffractometer. It was assumed that the crystallinity of the sample would not change upon exposure to air.

3.2.4 TEM measurements

TEM measurements were performed on a FEI TalosTM F200X device. The FCC particles were first casted in a wax, and subsequently microtomed. The microtomed samples, along with the single components, were deposited on a TEM grid.

Results and Discussion

As mentioned in paragraph 1.5, the results and discussion are divided over 5 chapters. In these chapters the changes in acid strength, ratio between Lewis and Brønsted acid sites, and aluminium structure, are studied. First, the effect of different silicon to aluminium ratios in zeolite HY is discussed in chapter 4. In chapter 5, the interaction between silica and alumina in the binder is studied. The structure-acidity correlations of chapter 4 and 5 are further used in chapter 6, to elucidate the acidic and structural contribution of the single components, with respect to the FCC catalyst. The interactions between two different components are subsequently studied in chapter 7 and subsequently compared to the FCC. In chapter 8, the effect of different heat treatments on the acidity and aluminium structure of the FCC catalyst is investigated. The obtained structure-acidity correlations are then summarized and discussed in chapter 9.

Chapter 4. The Effect of the Si/Al Ratio in Zeolite HY

In this chapter, the acidity and aluminium structures of zeolite HY with different silicon-aluminium (Si/Al) ratios will be discussed. As described in paragraph 1.3 and 2.2, the substitution of a Si^{4+} ion by an Al^{3+} ion in the tetrahedral silica framework results in a negative charge. The negative charge of the framework is compensated by the uptake of a counter ion like a proton. The uptake of a proton results in the formation of a Brønsted acid site.^[2,8,15-24] The ratio of the silicon to aluminium (Si/Al ratio) determines the relative strength and concentration of the Brønsted acid sites.^[23,36,37] A low Si/Al ratio results in a high concentration of Brønsted acid sites, but with a medium acid strength. A high Si/Al ratio results in a lowered concentration of Brønsted acid sites, but with high acid strength, due to a more localized negative charge.^[37,101] For the fabrication of a FCC catalyst, a zeolite with a Si/Al ratio of approximately 7 is often used, because of the thermal stability and high cracking activity of this zeolite.^[2,27]

The acidity was determined with CO and pyridine based infrared (FT-IR) spectroscopy. Additionally, magic angle- nuclear magnetic resonance (MAS-NMR) spectroscopy was used, to study the environment around the aluminium nuclei in a 1D-, and 2D multiple quantum- MAS NMR experiment. (^{27}Al MAS-NMR and ^{27}Al MQ-MAS NMR). Furthermore, proton MAS-NMR (^1H MAS-NMR) spectroscopy was used to study the different protons in the samples.

4.1 Acidity

For the FT-IR measurements, the samples were heated to 550 °C for one hour under high vacuum and cooled down, while kept under vacuum, as described in paragraph 3.2.1. All spectra were corrected for the weight of the wafer.

In Figure 14, the FT-IR spectra of zeolites HY with different Si/Al ratios are shown. As described in paragraph 2.4.2, the shift of the CO stretching vibration and the pyridine ring vibrations are characteristic for the acid type and acid strength, to which the CO or pyridine is attached.^[8,16,36,48,82,83,86] Since all spectra are corrected for the weight of the wafer, the intensity of the bands can be compared for different samples, which gives information about the relative amount of the acid sites in the samples. The FT-IR spectra of the OH vibrational region (4000-3000 cm^{-1}) are shown in Figure 14a and 14b. The acidic character of the different OH vibrations can be determined, by observing which OH vibration is consumed upon probing the samples with either CO or pyridine. The band position in the CO (2500-2250 cm^{-1}) or pyridine (1700-1350 cm^{-1}) vibrational region, can subsequently be used to differentiate the acidic character of the OH group. The FT-IR measurements in Figure 14a and 14c are performed at -188 °C. This results in very defined bands in the OH vibrational region which are slight blue shifted, compared to the OH vibrations in Figure 14b which are taken at room-temperature.^[16,48]

In Figure 14c, an increase in the aluminium concentration results in an increase of the band at 2164 cm^{-1} which is attributed to CO interacting with medium Brønsted acid sites.^[82,83,86] The increase of the band at 2164 cm^{-1} appears to be accompanied by the increase of the band around 3600 cm^{-1} , in Figure 14a. The increase of the band at 3600 cm^{-1} could therefore be correlated to the increase in medium Brønsted acid sites. Moreover, the band at 2179 cm^{-1} does not appear to decrease with increasing aluminium concentration. This band is associated with CO on a strong Brønsted acid site.^[82,83,86] Literature states that an increased aluminium concentration results in a decrease of the amount of strong Brønsted acid sites.^[8] Therefore, it can be assumed that the band at 2165 cm^{-1} overlaps with the band at 2179 cm^{-1} . This gives the impression that the band at 2179 cm^{-1} does not decrease with increasing aluminium concentration. Yet, the band at 2179 cm^{-1} does show that the formation of strong Brønsted acid sites is not inhibited by incorporation of more aluminium into the zeolite framework.

Furthermore, an increased intensity of the bands at 2229 and 2195 cm^{-1} is observed, with increasing aluminium concentration. These bands are attributed to CO interacting with Lewis acid sites. [15,23,50,52,96] This shows that the amount of Lewis acid sites increases with increasing aluminium concentration, which has also been observed in literature. [8,16,102]

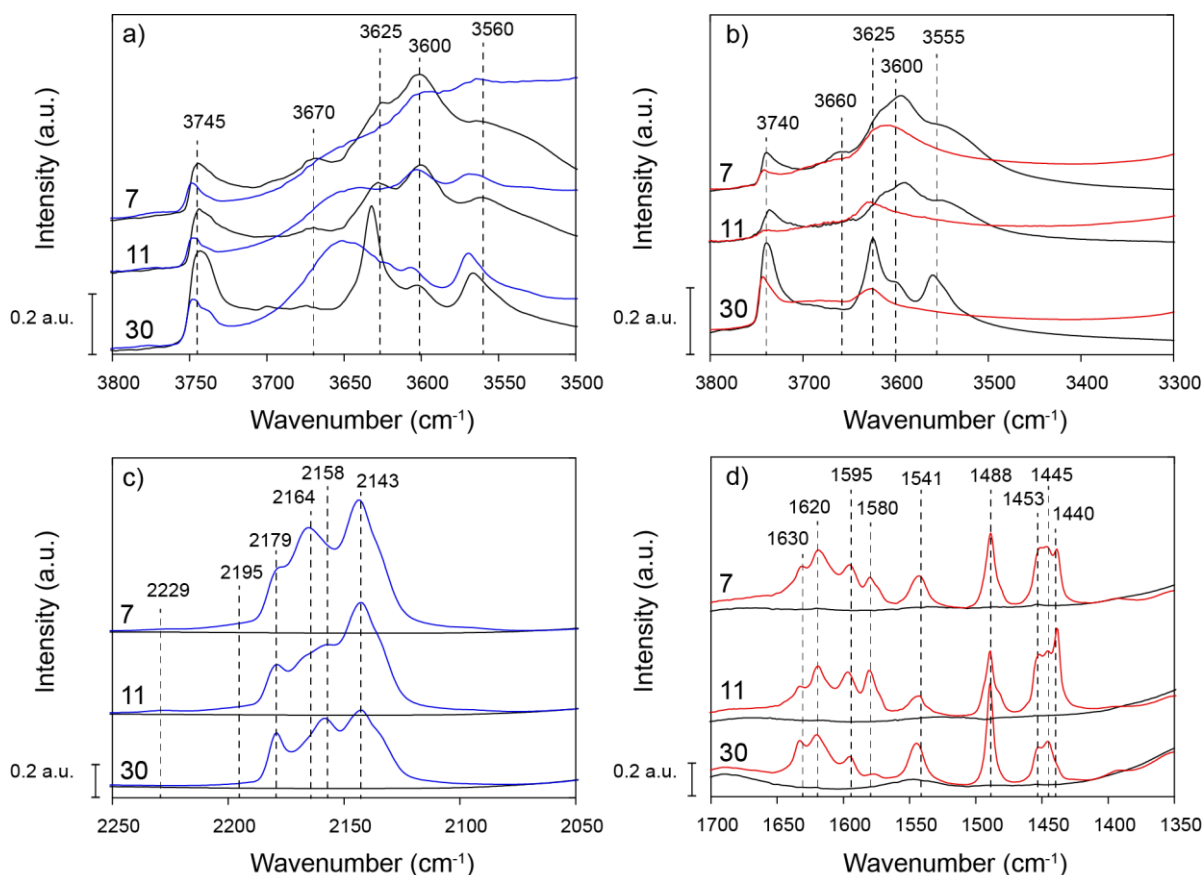


Figure 14 FT-IR spectra of zeolite HY with a Si/Al ratio of 7, 11, and 30 respectively. a)- c) OH vibrational region and CO vibrational region before (black) and after maximal loading with CO (blue) b)- d) OH vibrational region and pyridine vibrational region before (black) and after exposed to pyridine vapour for 30 min. (red)

In the pyridine ring vibrational region (Figure 14d), no significant decrease or increase of the bands attributed to pyridine on Brønsted acid sites (1630 and 1541 cm^{-1}) can be observed, with increasing aluminium concentration. [36,82,91] This shows that the increase in the amount of medium Brønsted acid sites, observed with CO FT-IR, is not confirmed by the pyridine FT-IR measurement. Furthermore, a small increase in the intensity of the bands at 1595 and 1445 cm^{-1} can be observed with increasing aluminium concentration. These two bands are attributed to pyridine hydrogen bonded to non-acidic hydroxyl groups. [23,36,50,82,89,103] Since pyridine is a stronger base compared to CO, the interaction between a very weak Brønsted acid site and pyridine could result in the formation of a band attributed to non-acidic groups, due to the insensitivity to the small change in acidity. [25] This means that the increase of the bands at 1595 and 1445 cm^{-1} might partially originate from pyridine interacting with a medium Brønsted acid site. In Figure 14d, an increase in aluminium concentration results in an increased intensity of the band at 1620 and 1453 cm^{-1} . These bands are attributed to pyridine on a Lewis acid site. [22,23,50,82,89,93,98] As observed with CO FT-IR, this confirms that the amount of Lewis acid sites increases with increasing aluminium concentration.

In Figure 14b, the bands at 3600 and 3555 cm^{-1} are predominantly consumed, upon loading with pyridine. These bands are affiliated with pyridine on a medium Brønsted acid site and a Brønsted acid 31

in a sodalite cage respectively.^[36] This contrasts with Figure 14a, which shows primarily consumption of the band at 3625 cm⁻¹ upon loading with CO. The band at 3625 cm⁻¹ is attributed to Brønsted acid sites in super cages.^[23,36,37,48,58,91,95-98] The difference in basicity of the CO and pyridine could therefore also result in different interactions of the pyridine and CO with different acidic groups, which subsequently results in different consumptions of the different OH bands in Figure 14a and 14b. Alternatively, the difference in consumption could also be affiliated with a difference in accessibility, since pyridine is larger compared to CO.^[82] However, this assumption is debilitated by the fact that the sodalite cage is the smallest cage in the zeolite.^[66] The consumption of this peak upon loading with pyridine therefore shows that this OH group is accessible.

To study the change in strong acid sites, the FT-IR spectra of the samples after minimal CO loading and remaining pyridine loading at 550 °C are shown in Figure 15. The first CO loading is experimentally found to give rise to bands associated with the strongest acid sites present in the samples. The FT-IR spectra in Figure 15d show the bands of the residual pyridine, which is still attached to acid sites after heating the sample to 550 °C, and are, therefore, associated with the strongest acid sites.

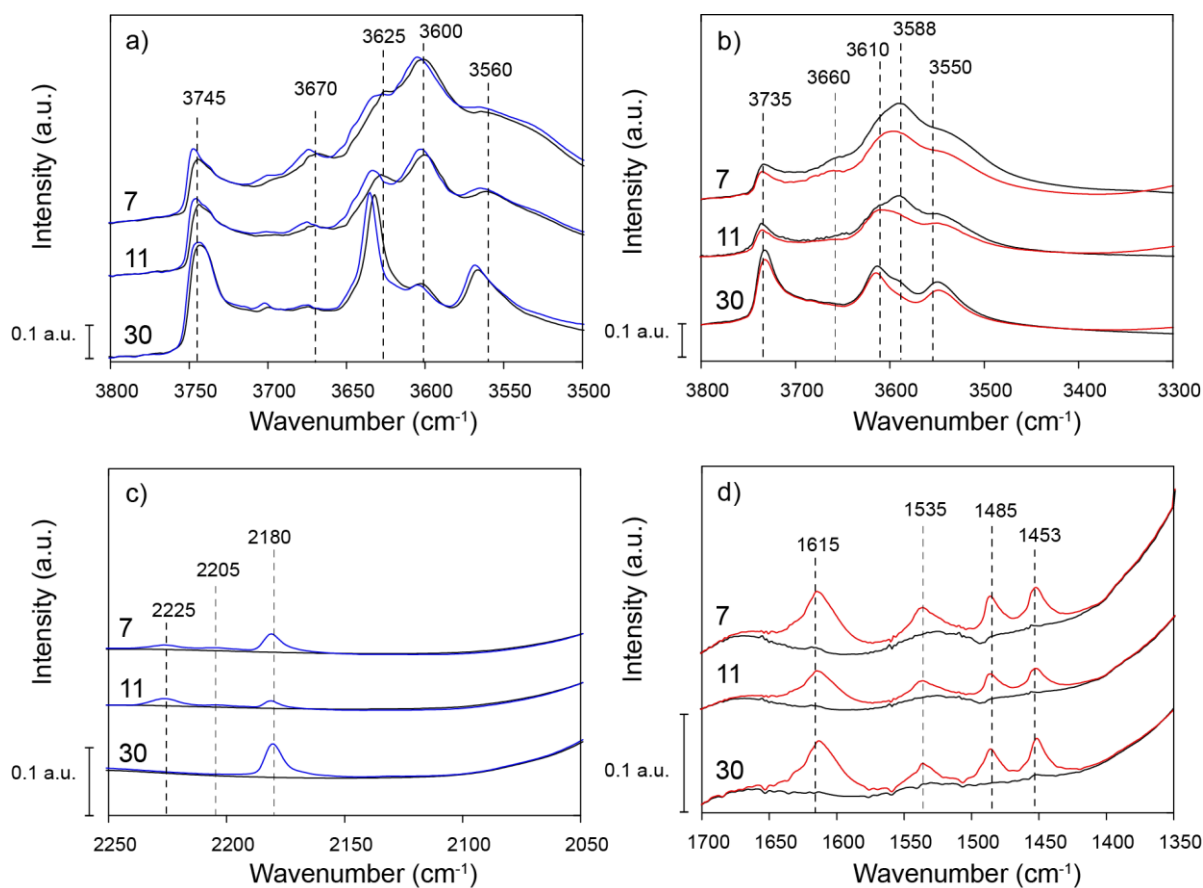


Figure 15 FT-IR spectra of zeolite HY with a Si/Al ratio of 7, 11, and 30 respectively. a)- c) OH vibrational region and CO vibrational region before (black) and after minimal loading with CO (blue). b)- d) OH vibrational region and pyridine vibrational region under vacuum at 550 °C (black) and after being exposed to pyridine vapour for 30 min. and heated to 550 °C (red) as described in paragraph 3.2.1.

As shown in the CO vibrational region (figure 15c), an increased aluminium content results in an increased intensity of the bands associated with CO on a Lewis acid site (2230 and 2205 cm⁻¹).^[15,23,48,50,93,97] The bands are shifted to higher wavenumbers, compared to the bands in Figure 15c. This is due to a decreased CO loading, as described in paragraph 2.4.2.^[82] The formation of these bands is accompanied by a shift to higher wavenumbers of the OH vibrations between 3750-3500 cm⁻¹ (Figure

15a), for all three samples. These OH bands are attributed to aluminol species (3670 cm^{-1}) and Brønsted OH (3625 , 3600 and 3560 cm^{-1}) vibrations.^[16,36] As explained in paragraph 2.4.2, this indicates that the OH bond strengthens due to the adsorption of CO. It is therefore postulated that the aluminium center to which the Brønsted acid site and aluminol group is attached, can act as a Lewis acid site, to which the CO can coordinate. As a result, electrons are donated to the Al-OH bond, which results in strengthening of the OH bond.^[16,48] This suggests that an increase in Brønsted acidic sites and aluminol groups could also result in more Lewis acid sites.

In Figure 15d, a minimal increase of the bands ascribed to pyridine on strong Brønsted acid sites (1630 and 1535 cm^{-1}) is observed, with increasing aluminium concentration.^[15,36,82,91,93,98] The bands affiliated with pyridine on a Lewis acid site (1615 and 1453 cm^{-1}) also show little to no increase in intensity with increasing aluminium concentration.^[22,23,50,82,89,93,98] The bands are shifted to lower wavenumbers, due to the increased temperature, as described in paragraph 2.4.2. Based on these results it can be concluded that an increase in aluminium content does not result in an increase in the amount of strong Lewis or Brønsted acid sites. The increased intensity of the band at 1453 cm^{-1} (Figure 14d) can therefore only be ascribed to an increase in the amount of the medium Lewis acid sites, with increasing aluminium concentration. In Figure 15b, a clear consumption the band at 3588 cm^{-1} can be observed, whereas the intensity of the band at 3610 cm^{-1} is almost completely restored. It can therefore be assumed that the band at 3588 cm^{-1} is the origin of the remaining strong Brønsted acid sites.

Based on the CO FT-IR measurements, it is postulated that the increased band at 3600 cm^{-1} is the origin of the increased concentration of medium Brønsted acid sites (Figure 14a and 14c). Based on the pyridine FT-IR measurements, the band was associated with strong Brønsted acid sites (Figure 15b and 15d). To get a better understanding about the nature of all the OH vibrations, $^1\text{H-NMR}$ was employed to detect changes in acidity by comparing the chemical shift of the proton in the $^1\text{H-NMR}$ measurement with the IR bands in the OH vibrational region ($4000\text{-}3000\text{ cm}^{-1}$). The $^1\text{H-NMR}$ spectra are not corrected for the weight of the samples, but equal volume amounts were used. Differences in intensity of similar bands between the samples can therefore not be assigned to a change in the amount, since differences in sample density result in a changed amount of hydroxyl groups. Differences in peak ratios can however be used to get a better idea about the ratio of different protons within a sample.

In Figure 16, the FT-IR spectra of the OH vibrational region (a) and corresponding $^1\text{H-NMR}$ spectrum (b) of the zeolites with a Si/Al ratio of 7 and 30 are shown. In the $^1\text{H-NMR}$ spectrum of zeolite Si/Al 30, three Brønsted peaks at 4.0, 3.6 and 2.9 ppm can be observed. A shift towards higher ppm values indicates a more electronegative environment around the proton.^[104] This subsequently indicates an increased Brønsted acid strength, but could also be affiliated with an increase in the confinement.^[16,35,36,71-76,96,105] The peaks at 4.0 and 3.6 ppm are attributed to Brønsted acid sites in a sodalite cage and in a super cage respectively.^[40,43,81,106] The peaks at 4.0 and 3.6 ppm can therefore be correlated to the bands at 3560 cm^{-1} and 3625 cm^{-1} in the FT-IR spectrum, since these bands are also affiliated with Brønsted acid sites in a sodalite cage and in a super cage respectively.^[23,36,37,48,58,91,95-98] The sodalite cage is the smallest cage of the zeolite.^[66] The high shift in the $^1\text{H-NMR}$ spectrum can therefore be affiliated with the increased confinement of the Brønsted acid site. The peak at 2.9 ppm is often ascribed to Extra-Framework (EF) aluminol groups.^[105-107] In $^1\text{H-NMR}$ spectrum of zeolite Si/Al 7, two peaks are observed at 4.0 and 2.9 ppm. A significant increase of the peaks at 2.9 and 2.2 ppm can be observed, with increasing aluminium content. The high intensity of the peak at 2.9 ppm and absence of the peak at 3.6 ppm in zeolite Si/Al 7 suggests that the peak at 3.6 ppm might be lying underneath the peak at 2.9 ppm. This is also confirmed by the $\{^{27}\text{Al-}^1\text{H}\}$ CP NMR results of chapter 6.

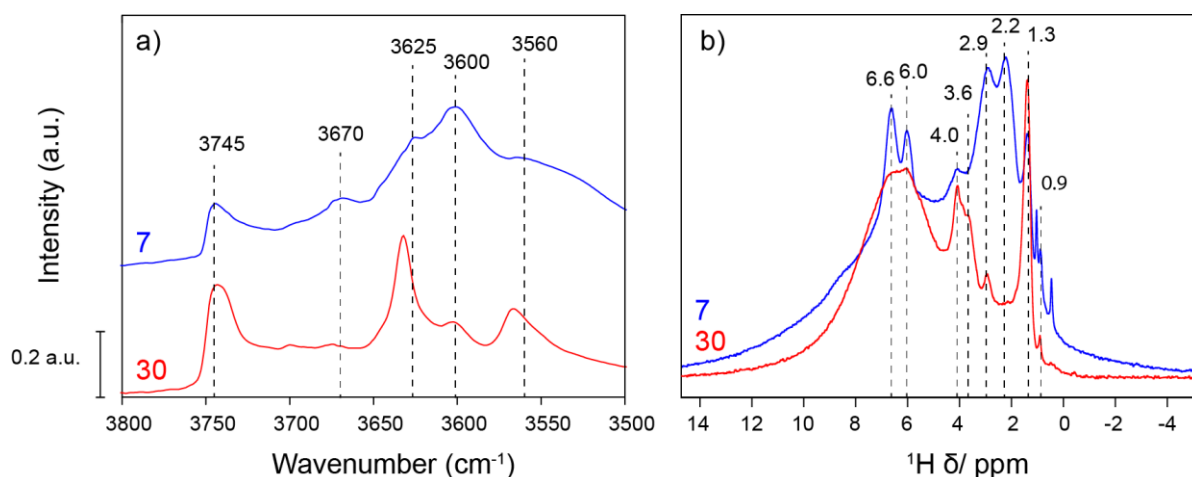


Figure 16 a) FT-IR spectrum of the OH vibrational region under vacuum at $-188\text{ }^{\circ}\text{C}$ and b) $^1\text{H-NMR}$ spectrum of zeolite HY with a Si/Al ratio of 7 and, 30 respectively

The increased intensity of the peak at 2.9 ppm with increasing aluminium concentration appears to be accompanied by an increase of the band at 3600 cm^{-1} (Figure 16a). Based on the lowered shift of the peak at 2.9 ppm, compared to the two Brønsted acid sites at 3.6 and 4.0, this peak is ascribed to medium Brønsted acid sites. This confirms the CO FT-IR measurement.

Based on literature and the relative intensity of the OH vibrations in Figure 16a, a correlation between the shift in the $^1\text{H-NMR}$ could be made and the OH vibrations in the IR spectra, which are tabulated in Table 2. Using the correlations in Table 2 and the FT-IR measurements in Figure 14 and Figure 15, the peak at 2.9 can be attributed to medium Brønsted acid sites in the zeolite framework. [23,36,37,96,108–110]

The peak at 2.2 ppm is attributed to non-acidic aluminol groups in literature. [104,111] The large increase of the peak at 2.2 ppm is therefore possibly correlated to the band at 3670 cm^{-1} respectively. Both are often ascribed to Extra-Framework (EF) aluminol groups in literature, which shows that an increased aluminium concentration in zeolites also results in more EF aluminium species. [41,108] This has been observed in literature as well. [8,16,102] In Figure 11a and c, a blue shift of the aluminol and Brønsted OH bands was observed, upon loading with CO. This was accompanied by the formation of bands affiliated with CO on a Lewis acid site. This showed that CO can interact with the aluminium center to which the aluminol and Brønsted acid sites are attached. An increase in aluminol groups and Brønsted acid sites could therefore result in an increased concentration of Lewis acidic aluminium species. The increase of the peak at 2.2 ppm might therefore be related to the increase in the amount of Lewis acid sites.

Based on literature, the peak at 6 ppm is affiliated with water on Lewis acid sites. [43,106,112] In the $^1\text{H-NMR}$ spectrum of zeolite Si/Al 7, the peak at 6 ppm appears more intense, compared to the peak at 4.0 ppm. The ratio of these peaks in zeolite Si/Al 30 appears to be lowered, indicating that an increase in aluminium content results in an increase of the amount of water adsorbed on a Lewis acid site. Based on this increase and Figure 15c, it can be concluded that an increase in the amount of medium Brønsted acid sites and a slight increase of the amount of Lewis acid sites occurs upon increasing the concentration of aluminium.

Table 2 Correlation between the chemical shift in $^1\text{H-NMR}$ and the wavenumber in FT-IR.

Wavenumber (cm^{-1})	Chemical shift (ppm)	Assignment	References
/4000-3650	0.9	<i>Non-acidic silanol groups and aluminol groups</i>	[113]
3745	1.3	<i>Silanol groups</i>	[96,107,109]
3670, 3690	2.2 ppm	<i>Non-acidic aluminol groups</i>	[107] and the $\{^{27}\text{Al-}^1\text{H}\}$ CP experiment in chapter 6
3625	3.6	<i>Bridging OH groups in a super cage</i>	[96,109]
3600	2.9	<i>Bridging OH groups in a super cage</i>	<i>Experimentally found</i>
3560	4.0	<i>Bridging OH groups in a sodalite cage</i>	[96,109]
-	6.0	<i>Water on a Lewis acid site</i>	[43,106,112]
-	6.6	<i>NH_4^+ ions present in the zeolite</i>	[113]

4.2 Structure

The increase of aluminium concentration resulted in an increased amount of medium Brønsted acid sites, Lewis acid sites, and aluminol groups. This suggests an increase in the amount of EF aluminium species.^[8,16,102] To see if this hypothesis is correct, the samples were measured with aluminium- magic angle NMR spectroscopy (²⁷Al MAS-NMR). All the samples were heated to 538 °C for one hour under a nitrogen flow of 100 mL/min, as described in paragraph 3.2.2. The ²⁷Al MAS-NMR spectra are not corrected for the weight of the samples, but equal volume amounts were used. Differences in intensity of similar peaks between the samples can therefore not directly be assigned to a change in the amount, since differences in sample density result in a changed absolute amount of aluminium. Differences in peak ratios can however be used to get a better idea about the ratio of different aluminium coordinations within a sample.

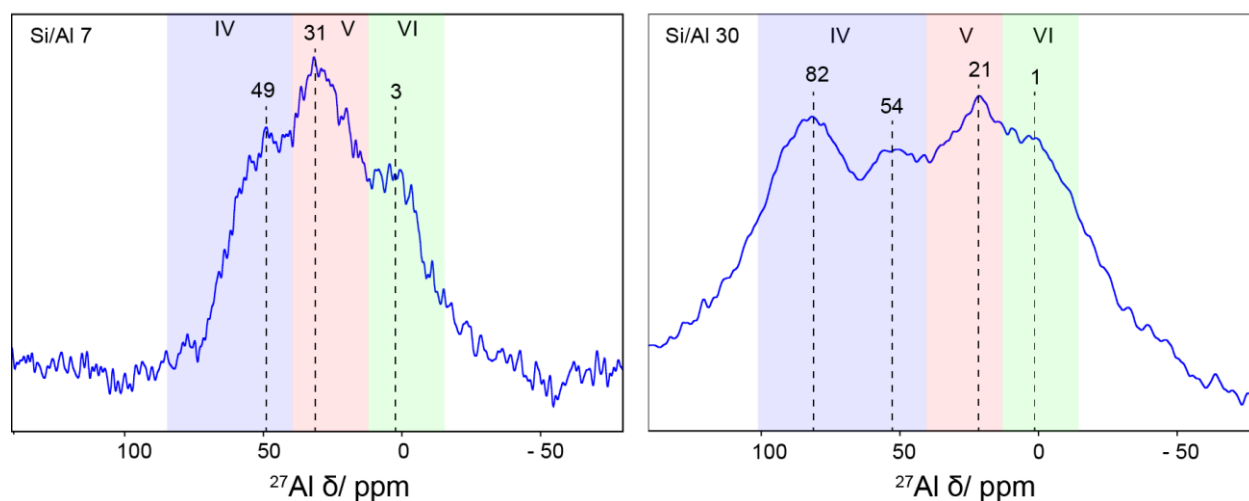


Figure 17 ²⁷Al MAS spectra of zeolite HY with a Si/Al ratio of 7 (left) and 30 (right). The shaded regions indicate the tetrahedral (IV), penta- coordinated (V) and octahedral (VI) aluminium coordinations respectively. * Zeolite Si/Al 30 was recorded with a very high number of scans, resulting in a low noise level compared to Zeolite Si/Al 7.

Figure 17 depicts ²⁷Al NMR spectra of zeolite Si/Al 7 and 30. Three distinct regions can be distinguished in the ²⁷Al MAS spectra: 0-30 ppm, 20-50 ppm and 40-90 ppm, which are ascribed to octahedral, penta-coordinated and tetrahedral aluminium coordinations respectively.^[35,41,114,115] The peak around 20-50 ppm is also attributed to trigonal or distorted tetrahedral aluminium, but will henceforth be referred to as the penta-coordinated aluminium coordination, since this is most often used in literature.^[116] In the spectrum of zeolite Si/Al 30 there is an additional tetrahedral peak around 90 ppm, which is attributed to anionic tetrahedral aluminium species like [AlCl₄]⁻.^[117,118] The presence of this peak is ascribed to residual starting material of the zeolite synthesis.

In zeolite HY Si/Al 30, the peak attributed to a tetrahedral aluminium coordination appears at 54 ppm, whereas zeolite HY Si/Al shows a peak at 49 ppm. The peak from the tetrahedral aluminium thus appears to shift towards higher ppm values with decreasing aluminium concentrations. A shift towards higher ppm values indicates a more electronegative environment around the aluminium nucleus.^[35,76] The decreased aluminium concentration could therefore result in localization of the negative charge, which is induced by the substitution of silicon by aluminium.^[8,26] The incorporation of more aluminium thus results in stabilization of this negative charge and thereby in a shift towards lower ppm values. This effect is confirmed by literature.^[16,35,71-76] The stabilization of the negative charge, additionally, results in a less electron withdrawing character of the aluminium, thereby decreasing the Brønsted acid strength

of the bridging SiOHAl group.^[37,101] The shift of the tetrahedral coordination towards lower ppm values with increasing aluminium concentration can therefore be correlated to the increase in the concentration of medium Brønsted acid sites.

In Figure 17a, the peak at 31 ppm appears to have an increased intensity, compared to the peak at 21 ppm in Figure 1b. These peaks are attributed to a penta-coordinated aluminium and associated with Extra-Framework (EF) type aluminium species.^[18,119] This confirms the increased amount of EF aluminium species with increasing aluminium concentration. The peak at 2.2 ppm (Figure 17b) is affiliated with aluminol groups attached to EF-aluminium species.^[107] The increase of the pentahedral aluminium species with increasing aluminium content could therefore be coupled to the increase of the peak at 2.2 ppm. The peak at 3 ppm, ascribed to octahedrally coordinated aluminium, does not appear more intense in Figure 17a compared to the peak at 1 ppm in Figure 17b.^[35] The octahedral coordination is also ascribed to EF-aluminium species, since only tetrahedral aluminium is present in the zeolite framework.^[8,37,43,120] Unfortunately, due to the strong broadening of the peaks caused by the second order quadrupolar coupling constant, distinction of the different aluminium coordinations is difficult. Changes in the distortion around the aluminium nuclei can therefore not be distinguished.

4.3 Summary and Conclusion

It was observed in paragraph 4.2 that an increase in aluminium content in zeolite HY resulted in the formation of medium Brønsted and both strong and medium Lewis acid sites, according to the CO-based FT-IR measurements. The increased concentration did not inhibit the formation of some strong Brønsted acid sites, which was confirmed with CO and pyridine based FT-IR measurements. The formation of Lewis acidic bands in the CO vibrational region resulted in a blue shift of the aluminol and Brønsted acidic OH vibrations. This indicated that the aluminium center of the aluminol and Brønsted acid sites can act as a Lewis acid site, to which the CO can coordinate. The pyridine-based FT-IR measurements showed an increase in the amount of medium Lewis acid sites and non-acidic hydroxyl groups with increasing aluminium content. In the OH vibrational region ($4000\text{-}3000\text{ cm}^{-1}$) an increase of the band at 3600 cm^{-1} was observed with increasing aluminium content. The pyridine and CO based FT-IR measurements were not conclusive on the acidic nature of this OH band: The pyridine FT-IR measurement showed consumption of the band at 3600 cm^{-1} after heating the sample to $550\text{ }^{\circ}\text{C}$. This suggested that the band could be affiliated with strong Brønsted acid sites. In the CO based measurements an increase in the amount of medium Brønsted acid sites appeared to be correlated to the increase of the band at 3600 cm^{-1} . This indicates that the band at 3600 cm^{-1} can be affiliated with medium Brønsted acid sites.

Using $^1\text{H-NMR}$, a correlation between the OH vibration and the shift in $^1\text{H-NMR}$ was established. Based on this correlation the band at 3600 cm^{-1} was correlated to a peak at 2.9 ppm, which was subsequently associated medium Brønsted acid sites. An additional increase of the peak at 2.2 ppm with increasing aluminium concentration was observed. This was attributed to an increased amount of aluminol groups, which gave rise to a band at $3670\text{-}3690\text{ cm}^{-1}$ in the FT-IR spectrum. [15,48,58,83,89,92–95]

In the $^{27}\text{Al MAS-NMR}$ spectra, a shift of the peak attributed to tetrahedrally coordinated aluminium towards lower ppm values with increasing aluminium concentration was observed. This was correlated to spreading of the negative charge induced by the incorporation of aluminium into the silicon framework. The shift was subsequently correlated to the increased amount of medium Brønsted acid sites. Additionally, an increased intensity of the peak attributed to penta-coordinated aluminium was observed with increasing aluminium content. Since a penta-coordination is exclusively ascribed to Extra-Framework aluminium species, this increase could be correlated to an increase in the amount of Lewis acid sites with increasing aluminium concentration. Finally, the increased amount of aluminol groups was attributed to the formation of octahedrally coordinated aluminium species.

To conclude: the shift towards lower ppm values of the peak attributed to tetrahedrally coordinated aluminium in the $^{27}\text{Al MAS-NMR}$ spectrum is correlated to the formation of medium Brønsted acid sites. The penta-coordinated aluminium is possibly the origin of the Lewis acid sites and the octahedral aluminium coordination is accompanied by the formation of additional aluminol groups.

Chapter 5. Interactions Between Alumina and Silica

In this chapter, the acidity and aluminium structures of the binder, and the alumina in the binder, will be discussed. As described in paragraph 1.4, pure alumina contains Lewis acid sites, which are proposed to originate primarily from tetrahedral and octahedral Extra Framework (EF) Al^{3+} ions.^[19,48] When alumina is mixed with silica, new Brønsted and Lewis acid sites are formed.^[48,58,121–123] The binder used in the model FCC catalyst is a physical mixture of silica and two types of boehmite: high crystalline and low crystalline boehmite. To study the interaction of these components, both the acidity and structure of the binder, high crystalline boehmite, and silica were studied. The crystalline structure of boehmite is known to transform to γ -alumina, upon heating the boehmite to 500 °C for a prolonged period of time.^[92,124–127] An additional alumina was studied, to test whether the acidic and structural properties of the heated boehmite were comparable to an amorphous alumina. In this chapter, the heated boehmite will be referred to as boehmite, although the boehmite has transformed to an amorphous alumina due to the temperature treatment. (see Appendix 13.2.1). The acidity of the low crystalline boehmite was also measured with CO based infrared spectroscopy, but the acidity of the sample did not differ from the high crystalline boehmite, as is shown in Appendix 13.6.1 The high crystalline boehmite was therefore used to study the change in acidity and aluminium coordination, upon mixing with silica.

The acidity was determined with CO and pyridine based infrared (FT-IR) spectroscopy. Additionally, magic angle- nuclear magnetic resonance (MAS-NMR) spectroscopy was used, to study the environment around the aluminium nuclei in a 1D-, and 2D multiple quantum- MAS NMR experiment. (^{27}Al MAS-NMR and ^{27}Al MQ-MAS NMR). Furthermore, proton MAS-NMR (^1H MAS-NMR) spectroscopy was used to study the different protons in the samples.

5.1 Acidity

For the FT-IR measurement, the samples were heated to 550 °C for one hour under high vacuum, and cooled down, while kept under vacuum, as described in paragraph 3.2.1. All spectra were corrected for the weight of the wafer.

In Figure 18, the FT-IR spectra of the binder and the individual components are depicted. As described in paragraph 2.4.2, the band positions of the CO stretching vibration and the pyridine ring vibrations are characteristic for the acid type and acid strength, to which the CO or pyridine is attached.^[8,16,36,48,82,83,86] Since the spectra are corrected for the weight of the wafer, the intensity of the bands can be compared, which gives information about the amount of the different acid sites in the samples. The FT-IR measurements in Figure 18a and 18c are performed at -188 °C. This results in very defined bands in the OH vibrational region which are slight blue shifted, compared to the OH vibrations in Figure 18b which are taken at room-temperature.^[16,48]

In Figure 18c and 18d, both the CO vibrational region (2250-2050 cm^{-1}) and pyridine ring vibrational region (1700-1350 cm^{-1}) are shown. In Figure 18c, the formation of a band at 2230 cm^{-1} , attributed to CO on a strong Lewis acid site, can be observed in the binder.^[15,23,48,50,93,97] This band is absent in the other three samples, which suggests that the strong Lewis acid site forms due to the interaction between the silica and boehmite in the binder. A broad band stretching from 2195 to 2180 cm^{-1} can be observed in the binder, boehmite, and alumina sample (Figure 18c). This band is affiliated with CO on medium Lewis acid sites.^[15,23,48,50,93,97] This illustrates that different alumina types all contain medium Lewis acid sites. The shift of the band at 2195 to 2180 cm^{-1} in the alumina is due to an increased CO loading on the Lewis acid site, which results in a red shift of the band. Bands which are affiliated with CO on a Lewis acid site have a lower extinction coefficient, which results in a lower intensity, compared to CO on Brønsted acid sites. In the boehmite, an intense band at 2164 cm^{-1} is ascribed to CO on weak Brønsted

acid sites.^[36,48,82,83,86] The silica contains primarily a band at 2158, which is attributed to CO on non-acidic surface hydroxyl groups.^[23,36,82] In the binder, a band around 2175 cm⁻¹ can be observed. This band is attributed to medium Brønsted acid sites.^[36,48,82,83,86] Since both the silica and the boehmite contain no band at 2175 cm⁻¹, the formation of the band in the binder could indicate that Brønsted acid sites have formed due to the mixing of the boehmite with the silica.

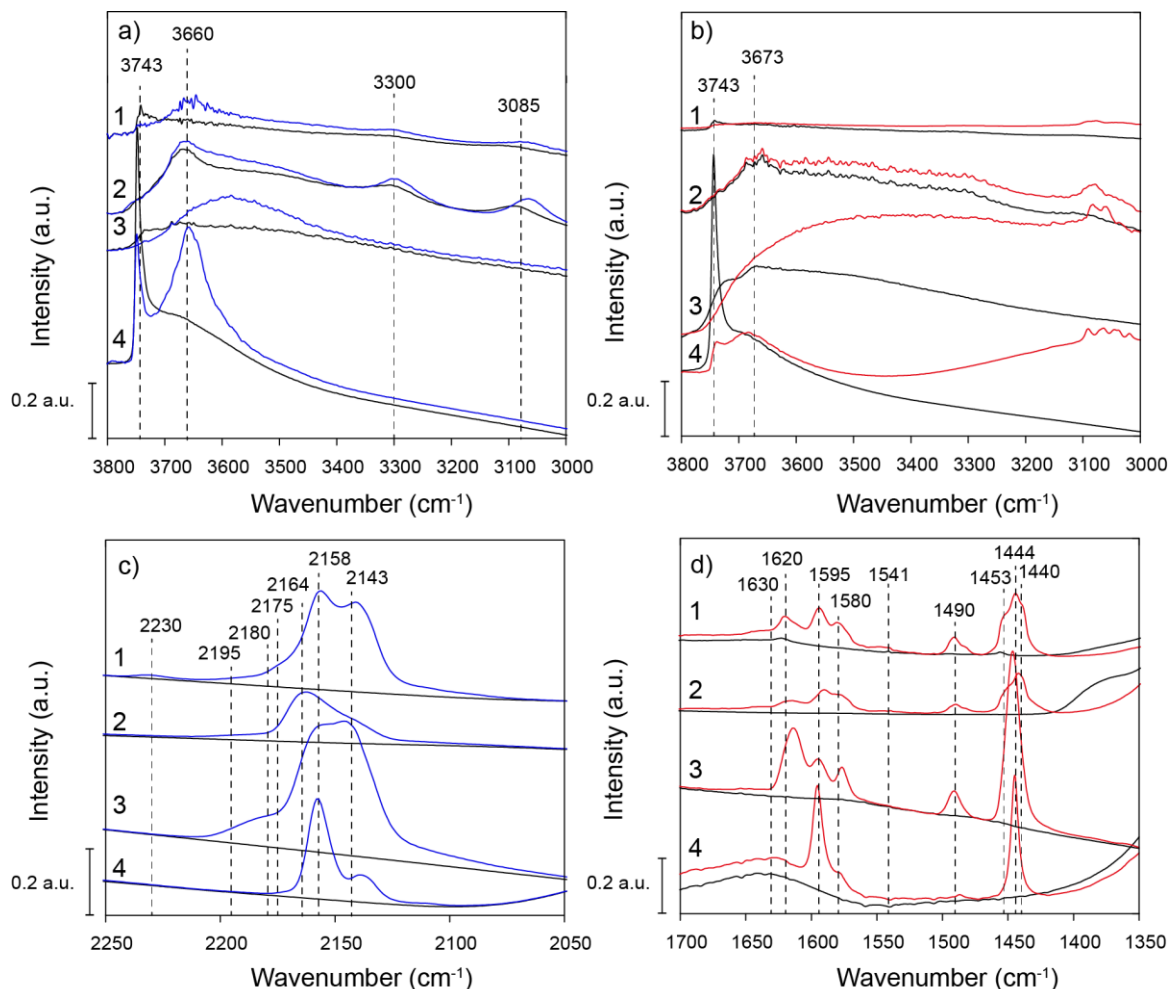


Figure 18 FT-IR spectra of 1. Binder 2. Boehmite 3. Alumina 4. Silica. a)- c) OH vibrational region and CO vibrational region before (black) and after maximal loading with CO(blue) b- d) OH vibrational region and pyridine vibrational region before (black) and after exposed to pyridine vapour for 30 min. (red)

In the OH vibrational region (4000-3000 cm⁻¹), in Figure 18a and 18b, the binder and silica show primarily consumption of the band at 3743 cm⁻¹. This band is attributed to non-acidic silanol groups.^[21,36,58,91] A small consumption of this band is also observed in the alumina, due to a slight silica contamination. In Figure 18a, the boehmite contains three bands at 3660, 3300 and 3085 cm⁻¹. Bands around 3680-3660 cm⁻¹ are reported to originate from aluminol groups attached to Extra-Framework aluminium (EFAl) groups, as described in paragraph 2.4.2.^[128] These EFAl species are often proposed to be Lewis acidic.^[23,30,44] No clear consumption of the band at 3660 cm⁻¹ is however observed, in the boehmite, binder or alumina, in Figure 18a and 18b. This could indicate that the interaction of CO with a Lewis acid site does not result in a decrease of the hydroxyl groups attached to the Lewis acid site. The bands around 3300 cm⁻¹ and 3085 cm⁻¹, in Figure 18a, are attributed to OH stretching vibrations, characteristic for highly crystalline boehmite.^[46] The presence of these bands suggests that the structure

of the boehmite is still partially preserved, even though it is known to change in structure upon heating. Both OH vibrational regions show similar consumption of the OH bands, which indicates that both the CO and pyridine interact in a similar way with the surface hydroxyl groups.

In the pyridine ring vibrational region (1700-1350 cm^{-1}), in Figure 18d, the silica contains two bands which are affiliated with pyridine hydrogen bonded to non-acidic surface hydroxyl groups (1595 and 1444 cm^{-1}).^[23,36,50,82,89,103] This confirms the absence of acidic surface groups in silica as shown by the CO FT-IR measurements. The binder shows an increased intensity of the bands at 1620 and 1453 cm^{-1} , with respect to the boehmite. These bands are attributed to pyridine on a Lewis acid site, which suggests that the combination of silica and boehmite results in the formation of additional Lewis acid sites.^[22,23,50,82,89,93,98] Additionally, the binder shows a slightly increased intensity of the bands affiliated with pyridine on a Brønsted acid site (1630 and 1541 cm^{-1}) compared to the boehmite.^[15,36,82,91,93,98] This proves that the combination of silica and boehmite results in the formation of medium Brønsted acid sites, as was postulated by the CO FT-IR measurements in Figure 18c. The alumina shows two intense bands at 1615 and 1450 cm^{-1} . These bands are shifted to lower wavenumbers with respect to the bands at 1620 and 1453 cm^{-1} , which are attributed to pyridine on a Lewis acid site.^[22,23,50,82,89,93,98] The shift to lower wavenumbers is attributed to a less electron withdrawing character of the acid sites, as described in paragraph 2.4.2.^[36] The bands at 1615 and 1450 cm^{-1} can therefore be attributed to pyridine on medium Lewis acid sites.

To determine whether the origin of the Lewis acid sites is comparable to the Lewis acid sites in the zeolites, described in chapter 4, the strongest acid sites were studied. Figure 19 depicts the FT-IR spectra of the samples after minimal CO loading and remaining pyridine at 550 °C. The first CO loading is experimentally to give rise to bands which are associated with the strongest acid sites in the samples. The FT-IR spectra in Figure 19d show the residual pyridine which is still attached to acid sites after heating the sample to 550 °C and are therefore associated with the strongest acid sites.

In the CO vibrational region (Figure 19c), a band at 2228 cm^{-1} can be observed in the FT-IR spectrum of the binder. This band is attributed to CO on a strong Lewis acid site.^[15,23,48,50,93,97] The boehmite, alumina and silica contain no band around 2228 cm^{-1} , which indicates that the strong Lewis acid site originates from the interaction between the silica and boehmite. The binder and alumina both contain a band at 2205 cm^{-1} , which is attributed to CO on medium Lewis acid sites.^[15,23,48,50,93,97] The silica contains primarily non-acidic surface groups, based on the band at 2158 cm^{-1} , associated with CO on a non-acidic hydroxyl group.^[23,36,82] A small band at 2172 cm^{-1} can be observed in the silica. This band is attributed to medium Brønsted acid sites, which are originate from vicinal silanol groups.^[90]

In the OH vibrational region (Figure 19a), no clear consumption or shift of the band at 3660 cm^{-1} can be observed for all the samples. In the FT-IR spectrum of the boehmite, the bands at 3300 and 3085 cm^{-1} appear to increase in intensity and shift to lower wavenumbers. This is accompanied with the formation of a band at 2205 with negligible intensity (Figure 19c), which is associated with CO on a medium Lewis acid site.^[15,23,48,50,93,97] The electron donating interaction of the CO with the Lewis acid site should result in a decrease of the aluminium electronegativity, and therefore stabilization of the OH group, attached to this aluminium. The origin of the red shift of the bands at 3300 and 3085 cm^{-1} is therefore possibly not related to Lewis acid sites.

In Figure 19d, the pyridine ring vibrational region (1700-1350 cm^{-1}) is shown. In the binder and boehmite, two bands at 1616 and 1451 cm^{-1} can be observed. The position of the bands shifts to lower wavenumbers, upon heating the sample. These bands are therefore attributed to pyridine on a strong Lewis acid site.^[22,23,50,82,89,93,98] The intensity of these two bands seems slightly higher in the binder,

thereby confirming the formation of strong Lewis acid sites upon mixing of silica and boehmite. In the spectrum of the binder, no bands affiliated with Brønsted acid sites are observed (1630 and 1548 cm^{-1}). [15,36,82,91,93,98] This confirms that mixing of silica and boehmite results in the formation of medium Brønsted acid sites. In the OH vibrational region (Figure 19b), no bands appeared to be consumed. The decreased intensity of the FT-IR spectrum of the alumina (Figure 19b) is due to a difference in temperature. In paragraph 4.1, it was shown that the aluminium center of Brønsted acid sites and aluminol groups, could act as a Lewis acid site, to which CO could coordinate. This resulted in a shift towards higher wavenumber of the aluminol and Brønsted acid bands. Both in Figure 19a and 19b, no positive shift or consumption of the OH vibrations can be observed in the binder, boehmite, or alumina. This suggests that the origin of the Lewis acid sites in these samples is different from the origin of the Lewis acid sites in the zeolite.

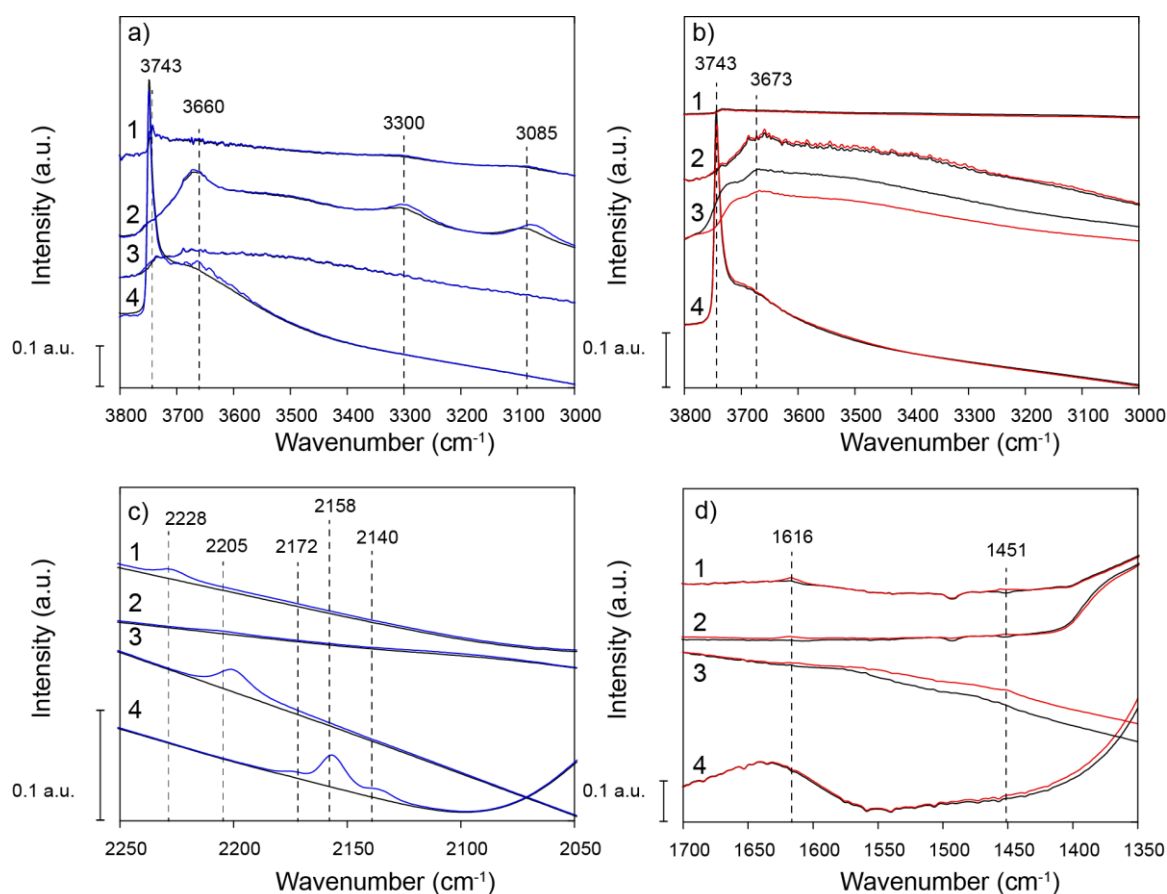


Figure 19 FT-IR spectra of 1. Binder 2. Boehmite 3. Alumina 4. Silica. a)- c) OH vibrational region and CO vibrational region before (black) and after minimal loading with CO(blue). b- d) OH vibrational region and pyridine vibrational region under vacuum at 550 550 °C (black) and after being exposed to pyridine vapour for 30 min. and heated to 550 °C (red) as described in paragraph 3.2.1.

To get a better understanding about the origin of the Lewis acid site, $^1\text{H-NMR}$ was employed to detect changes in acidity, by comparing the chemical shift of the proton in the $^1\text{H-NMR}$ measurement with the IR bands in the OH vibrational region (4000-3000 cm^{-1}) In Figure 20, the OH vibrational region of the FT-IR spectra (a) is shown with the corresponding $^1\text{H-NMR}$ spectrum (b). The $^1\text{H-NMR}$ spectra are not corrected for the weight of the samples, but equal volume amounts were used. Differences in intensity of similar peaks between the samples can therefore not be assigned to a change in the amount, since

differences in sample density result in a changed amount of hydroxyl groups. Differences in peak ratios can however be used to get a better idea about the ratio of different protons within a sample.

As show in Figure 20, the samples contain fairly broad bands in both the FT-IR spectra and the $^1\text{H-NMR}$ spectra. This is caused by hydrogen bonding between the different surface hydroxyl groups.^[16,22,35,36,71–76,93,102] This makes it difficult to distinguish the different groups. All three the samples show a broad peak around 2.2 ppm in the $^1\text{H-NMR}$ spectrum (Figure 20b). This peak is attributed to EF aluminol groups, which give rise a band at 3670–3690 cm^{-1} in the FT-IR spectra (Figure 20a).^[15,48,58,83,89,92–95] In chapter 4 it was postulated that an increase of these aluminol groups could be correlated to an increased amount of Lewis acid sites. The peaks at 2.2 ppm in Figure 20b, are very broad, which makes it difficult to compare the samples. In the $^1\text{H-NMR}$ spectra of the binder, a slight peak formation around 3.3 ppm can be observed, which is associated with Brønsted acid sites.^[40,41,43,81,105,106,112,113,129] In the $^1\text{H-NMR}$ spectrum of the boehmite, a peak at -0.2 ppm can be observed. In the binder, the same peak appears at -0.7 ppm with a decreased intensity. Since this peak is not visible in the $^1\text{H-NMR}$ spectrum of the alumina, it could be correlated to the characteristic bands at 3305 and 3088 cm^{-1} in the FT-IR spectrum of the boehmite and binder.^[46] The diminished intensity of these OH bands in the binder confirms the correlation (Figure 20a). All three samples contain a peak at 6 ppm, which is affiliated with water on Lewis acid site.^[40,41,71,112,114] The intensity of this peak appears to be the most intense in the alumina and binder, which is in agreement with the relative amount of Lewis acid sites in these samples.

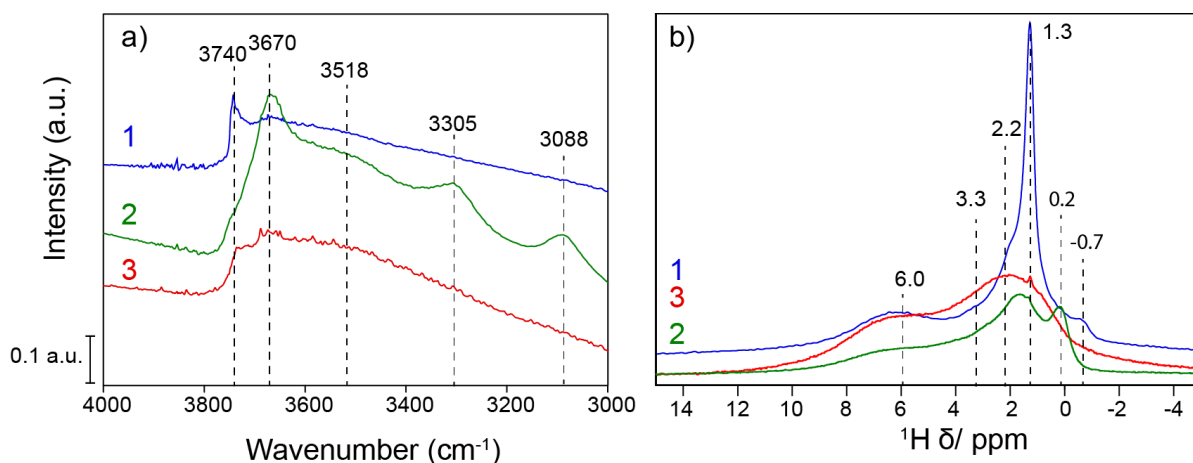


Figure 20 a) FT-IR spectrum of the OH vibrational region under vacuum at -188 °C and b) $^1\text{H-NMR}$ spectrum of 1. Binder 2. Boehmite 3. Alumina

Based on these results, it can be concluded that the mixing of silica and boehmite results in the formation of medium Brønsted acid sites and strong Lewis acid sites. Due to very broad peaks in the $^1\text{H-NMR}$, no conclusive evidence was found which could correlate the increase in the amount of Lewis acid sites to a clear peak in the $^1\text{H-NMR}$ spectrum.

5.2 Structure

The mixing of silica and boehmite resulted in the formation of medium Brønsted acid sites and strong Lewis acid sites. To understand the changes in acidity, the samples were measured with ^{27}Al MQ-MAS and ^{27}Al MAS NMR spectroscopy. All the samples were heated to 538 °C for one hour under a nitrogen flow of 100 mL/min, as described in paragraph 3.2.2. The ^{27}Al MAS- and ^{27}Al MQ-MAS NMR spectra are not corrected for the weight of the samples, but equal volume amounts were used. Differences in intensity of similar peaks between the samples can therefore not directly be assigned to a change in the amount, since differences in sample density result in a changed absolute amount of aluminium. Differences in peak ratios can however be used to get a better idea about the ratio of different aluminium coordinations within a sample.

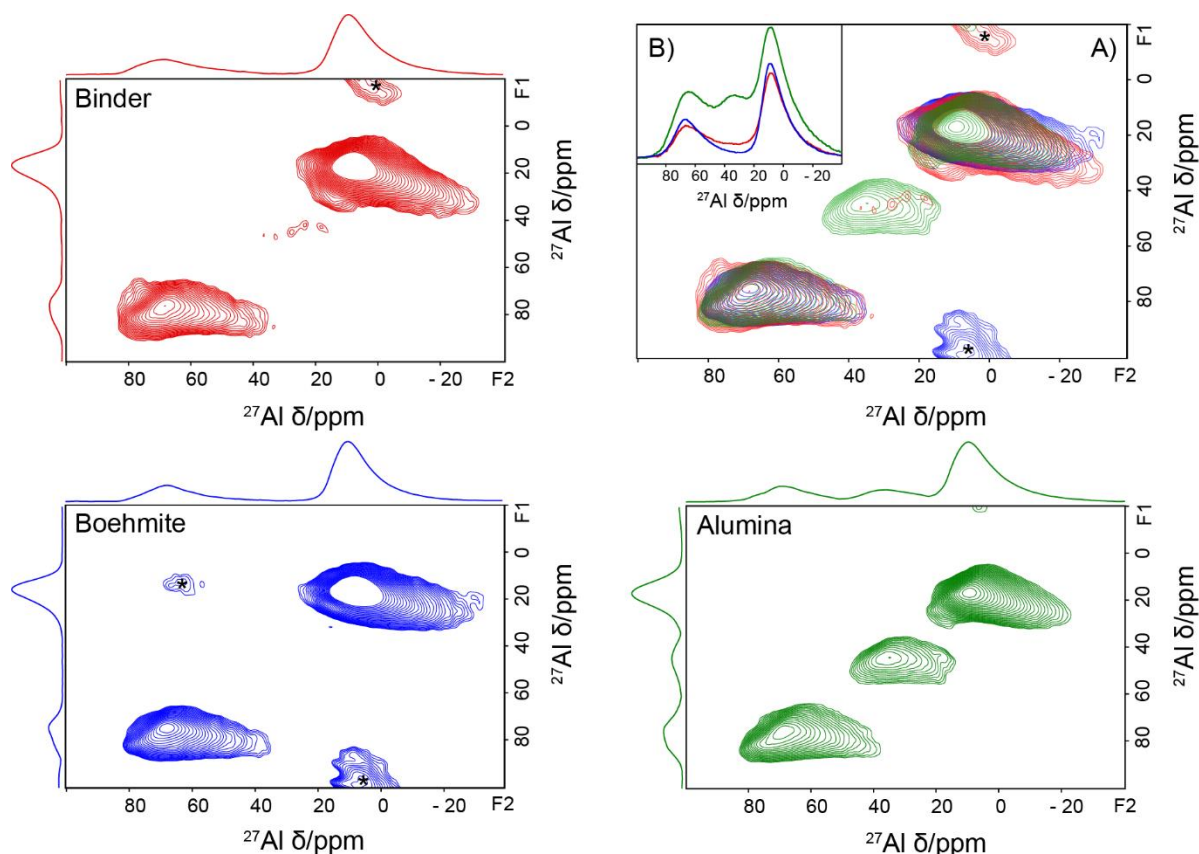


Figure 21 ^{27}Al MQ-MAS of the binder and individual components with the projections on the F1 and F2 axis. In the top right an overlay of the ^{27}Al MQ-MAS (A) is shown along with an overlay of the ^{27}Al MAS spectrum (B). Red: Binder, Blue: Boehmite, Green: Alumina. The *asterisk indicates spinning side-bands and are therefore not considered to be real peaks.

As explained in paragraph 2.4.1, in MQ-MAS NMR spectra, the F1 axis depicts the isotropic chemical shift and the F2 axis shows the anisotropic chemical shift. The peak position along the F1 axis thus gives information about the coordination of the aluminium nucleus. The anisotropic chemical shift in the F2 direction is largely affected by the second order quadrupolar coupling. A broadening along the F2 direction thus provides information about the strength of the quadrupolar coupling constant and therefore about the symmetry and environment around the aluminium nucleus.^[35,41,79,80,114,115] The broadening is therefore an effect of heterogeneity in the groups attached to the oxygens surrounding the aluminium, which is referred to as the second coordination sphere. The same regions can be defined in the ^{27}Al MQ-MAS spectra as in the ^{27}Al MAS spectra: 0-30 ppm, 20-50 ppm and 40-90 ppm, which are ascribed to octahedral, penta- coordinated and tetrahedral aluminium coordinations respectively.^[35,41,114,115]

In Figure 21, the ^{27}Al MQ-MAS NMR spectra of the binder, boehmite, and alumina, are shown, along with an overlay of the ^{27}Al -MAS NMR spectra. As shown in in Figure 21A, the samples contain very similar peaks in the octahedral region (0-30 ppm).^[43,98,130,131] In the ^{27}Al MQ-MAS NMR spectra of the binder and alumina, a peak at 35,30 ppm (F1,F2) appears. As described in paragraph 2.4.1, a shift towards higher ppm values indicates a more electronegative environment.^[16,35,71–76] The new aluminium coordination would therefore be slightly more electronegative and could therefore function as a Lewis acid site.

The boehmite contained overall very little Lewis acid sites, as was shown with the pyridine and CO FT-IR measurements. It is thus expected that the concentration of Lewis acidic aluminium coordinations is low in the boehmite. As shown in Figure 21A and 21B, the boehmite does not contain penta-coordinated aluminium species. The Lewis acidity could therefore originate from an octahedral aluminium coordination. It could therefore be postulated that the slight elongation at 35,30 ppm (F1,F2) originates from a peak which partially lies underneath the large octahedral peak. The Lewis acidic character of the boehmite could then originate from this octahedral peak, lying underneath the large octahedral peak.

Both the binder and alumina contain penta-coordinated aluminium species (40 ppm), as shown in the ^{27}Al MAS-NMR spectrum in Figure 21B.^[8,22,43,98,131] The penta-coordinated aluminium of the binder is however not clearly visible in the ^{27}Al MQ-MAS NMR spectrum. This could be due to a very large diversity of different groups around the aluminium nucleus, which results in a signal which is too low in intensity, due to the large broadening in the F2 direction. Therefore, if a quadrupolar coupling is too strong, the species are no longer detectable and are therefore 'NMR invisible'. Octahedral and penta-coordinated aluminium coordinations are often ascribed to EF aluminium species with Lewis acidic character.^[37,40,42,43,110] The increased amount of strong Lewis acid sites could therefore be correlated to the formation of the very distorted penta-coordinated aluminium species in the binder.

The ^{27}Al MAS-NMR and ^{27}Al MQ-MAS NMR spectrum of the alumina, both display a high intensity of the peak, affiliated with penta-coordinated aluminium. In paragraph 5.1 it was shown that alumina contained a high concentration of medium Lewis acid sites, based on CO and pyridine FT-IR measurements. The high concentration of medium Lewis acid sites in the alumina could therefore be correlated to the high concentration of penta-coordinated aluminium species. The symmetrical shape of the peak in the ^{27}Al MQ-MAS NMR spectrum indicates a homogeneous environment around the aluminium nucleus.^[35,131] The strength of the Lewis acidity could therefore be associated with the increased homogeneity around the aluminium nucleus.

As shown in Figure 21A, the peak in the tetrahedral region (40-90 ppm) is almost identical for all the samples. The large tetrahedral peak at 75,70 ppm (F1,F2) is affiliated with a tetrahedral alumina framework, which forms upon heating of boehmite.^[92,126,132] The binder is the only sample which contains a small additional peak around 70,75 ppm in the F1,F2 direction. As described in paragraph 2.3, the origin of Brønsted acid sites in mixtures of silica and alumina, is due to condensation of the surface hydroxyl groups.^[15,51,93] The coordination of the aluminium is postulated to be tetrahedral, just as in the zeolite.^[93] Combined with the increase in the amount of medium Brønsted acid sites, the formation of the peak at 70,75 ppm could be the origin of the medium Brønsted acid sites.

To confirm that the formation of the slightly Brønsted acidic peak in the binder could be an effect of silica-alumina bond formation, a ^{29}Si -MAS NMR spectrum was taken of the binder before and after heating, as shown in Figure 22. The heating of the binder is expected to result in condensation of the surface hydroxyl groups, which would subsequently result in the formation of silica-alumina bonds.

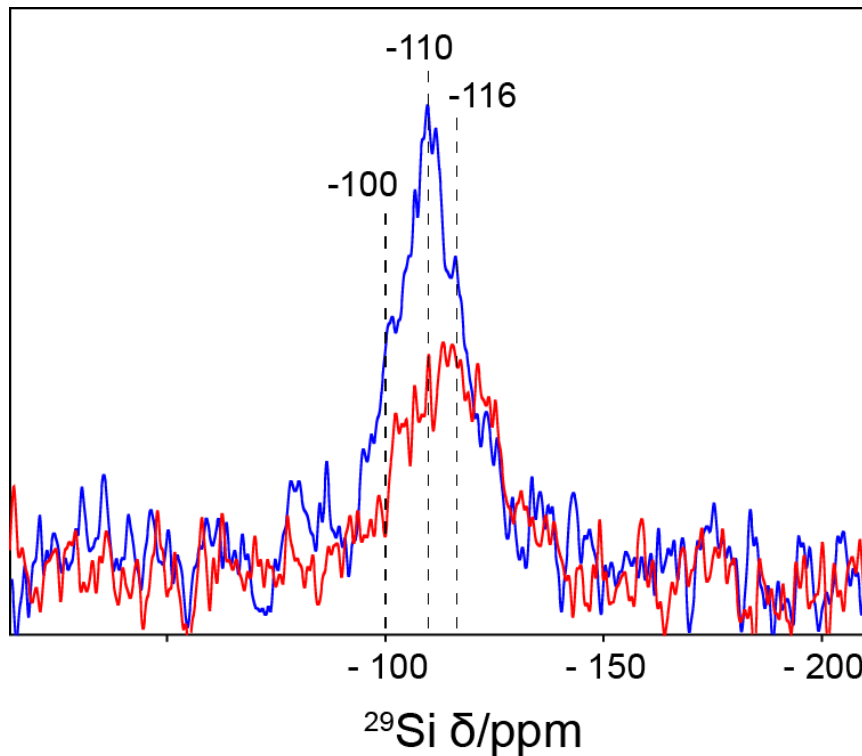


Figure 22 ^{29}Si -NMR of binder *before heating (red)* and *after heating (blue)*

Three different shifts are distinguished in a silicon NMR spectrum: $\text{Si}(\text{OSi})_4$, $\text{Si}(\text{OSi})_3\text{OAl}$ and $\text{Si}(\text{OSi})_2(\text{OAl})_2$, which give rise to three peaks at -107, -101 and -95 ppm respectively.^[133] In Figure 22 an enhanced signal at -110 and -100 ppm can be observed. This could indicate the formation of silica islands, along with the bond formation between silica and alumina. Another possibility, is the changes in the crystallography, which results in shifts of chemically equivalent silicon nuclei.^[100] The increased signal does however not result in a decreased signal in the silicon spectrum of the not-heated binder. This suggests that the peaks could be too broad to be detected. Due to the low resolution, more experiments and a higher resolution are required to study the changes in the environment around the silicon nuclei.

5.3 Summary and Conclusions

In paragraph 4.1, it was shown that the combination of boehmite and silica in the binder resulted in the formation of strong Lewis acid sites and medium Brønsted acid sites, based on the CO based FT-IR measurements. The pyridine-based FT-IR measurements confirmed the formation of medium Brønsted acid sites and showed an increase in the amount of strong Lewis acid sites in the binder with respect to the boehmite. The formation of medium Brønsted acid sites was postulated to originate from condensation between the surface hydroxyl groups on the silica and boehmite. The formation of Lewis acidic bands in the CO and pyridine vibrational region did not result in consumption or shift of the bands in the OH vibrational region. This suggests that the origin of the Lewis acid sites is different from the origin of the Lewis acid sites in the zeolites (Chapter 4).

Using $^1\text{H-NMR}$ spectroscopy, no peak could clearly be correlated to the increase in Lewis acid site. The bands were very broad, which was associated to hydrogen-bonded aluminol groups.^[16,22,35,36,71–76,93,102] A slight increase of the peak around 3 ppm in the $^1\text{H-NMR}$ spectrum was attributed to the formation of Brønsted acidic OH groups. This was confirmed by the increase in the amount of medium Brønsted acid sites in the binder, with CO and pyridine based FT-IR measurements. The binder, boehmite, and alumina contained a broad band at 6 ppm, which is affiliated with water on a Lewis acid site.^[40,41,71,112,114]

Based on the $^{27}\text{Al MQ-MAS}$ spectra, it was shown that the combination of boehmite with silica resulted in the formation of penta-coordinated aluminium species in the binder. The penta-coordinated aluminium species were not clearly visible in the $^{27}\text{Al MQ-MAS}$ NMR spectra, which was affiliated with a very distorted environment around the aluminium nucleus. The formation of this coordination was subsequently correlated to the increase in the amount of strong Lewis acid sites in the binder. In the $^{27}\text{Al MQ-MAS}$ NMR spectrum of the aluminium, an intense and symmetrical peak at 40,35 ppm (F1,F2) could be observed. This peak was affiliated with penta-coordinated aluminium with a very homogenous environment. This peak was correlated to the high concentration of medium Lewis acid sites in the alumina. The increased homogeneity of the penta-coordinated aluminium species was subsequently correlated to a decrease in Lewis acid strength. Formation of an additional peak at 35,30 ppm (F1,F2) was observed in the $^{27}\text{Al MQ-MAS}$ NMR spectrum of the binder and alumina. It was postulated that this peak partially lies underneath the intense octahedral peak at 0,20 ppm and was therefore postulated to be the origin of the medium Lewis acid sites in the binder, boehmite and alumina. In the $^{27}\text{Al MQ-MAS}$ NMR spectrum of the binder, a new tetrahedral aluminium peak at 70,75 ppm (F1,F2) was observed. This peak was correlated to the formation of medium Brønsted acid sites in the binder, upon mixing of the boehmite and silica.

In the $^{29}\text{Si MAS-NMR}$ spectrum, an increase of the peaks at -109 and -101 ppm was observed, for the heated binder, with respect to the not-heated binder. The increased peak at -101 ppm is affiliated with the formation of silica-alumina bonds, and therefore proves the bond formation between the boehmite and silica in the binder.^[133] However, due to a very low intensity, the correlation is not unambiguous. A higher resolution is therefore required.

To conclude: mixing of silica and boehmite in the binder, result in the formation of medium Brønsted acid sites, which is ascribed to bond formation between the silica and boehmite. Additionally, strong Lewis acid sites form in the binder, which is associated with the formation of very distorted penta-coordinated aluminium species. Furthermore, the high concentration of penta-coordinated aluminium in the alumina is ascribed to the high concentration of Lewis acid sites. It is therefore concluded that de strength of the Lewis acidity depends on the heterogeneity of the penta-coordinated aluminium species. The medium Lewis acidity in the boehmite, alumina and binder is ascribed to an octahedral aluminium coordination, which appears at 35,30 ppm (F1,F2) in the $^{27}\text{Al MQ-MAS}$ NMR spectrum.^[43,98,130,131]

Chapter 6. Single Components

In this chapter the acidic and structural contribution of the individual components with respect to the FCC catalyst are discussed. As described in paragraph 3.1, the FCC catalyst contains 30 weight percent of each component. For the nuclear magnetic resonance (NMR) measurements, a not-washed clay was used. In appendix 13.6.2, it is proved that both the not-washed and washed clay have the same acidity and structure. It is therefore assumed that the NMR spectra of the not-washed clay are representable for the washed clay.

The acidity was determined with CO and pyridine based infrared (FT-IR) spectroscopy. Additionally, magic angle- nuclear magnetic resonance (MAS-NMR) spectroscopy was used, to study the environment around the aluminium nuclei in a 1D-, and 2D multiple quantum- MAS NMR experiment. (^{27}Al MAS-NMR and ^{27}Al MQ-MAS NMR). Furthermore, proton MAS-NMR (^1H MAS-NMR) spectroscopy was used to study the different protons in the samples.

6.1 Acidity

For the FT-IR measurement, the samples were heated to 550 °C for one hour under high vacuum, and cooled down, while kept under vacuum, as described in paragraph 3.2.1. All spectra were corrected for the weight of the wafer.

In Figure 23 the FT-IR spectra of the FCC catalyst and the individual components is depicted. As described in paragraph 2.4.2, the band positions of the CO stretching vibration and the pyridine ring vibrations are characteristic for the acid type and acid strength, to which the CO or pyridine is attached.^[8,16,36,48,82,83,86] Since the spectra are corrected for the weight of the wafer, the intensity of the bands can be compared, which gives information about the amount of the different acid sites in the samples. The FT-IR measurements in Figure 23a and 23c are performed at -188 °C. This results in very defined bands in the OH vibrational region which are slight blue shifted, compared to the OH vibrations in Figure 23b which are taken at room-temperature.^[16,48]

As depicted in Figure 23a, the clay has four very distinct bands, in the OH vibrational region at 3700, 3675, 3660 and 3620 cm^{-1} .^[94,134-136] In the work of Farmer et al., the first three bands are ascribed to one single vibration. The vibration appears as three bands in the OH vibrational region, due to dipole-dipole interactions.^[94,134] Upon loading with CO or pyridine (Figure 23a and 23b), the bands 3700, 3675 and 3660 cm^{-1} shift towards higher wavenumbers and the band at 3620 cm^{-1} shifts to lower wavenumbers. The origin of the shift has also not been reported or observed in literature, but could possibly due to the interaction of the CO and pyridine with the dipole moment of the OH groups.^[94,134] In Figure 23a and 23b, a small band around 3600 cm^{-1} can be observed, in the FT-IR spectrum of the clay. This band is affiliated with medium Brønsted acid sites, in chapter 4. In the CO vibrational region (Figure 23c), this is confirmed by the formation of a band at 2165 cm^{-1} . This bands is attributed to CO on a weak Brønsted acid site.^[82,83,86] In the pyridine ring vibrational region (Figure 23d), a band at 1489 cm^{-1} can be observed, which is associated with pyridine on a Brønsted acid site or on a Lewis acid site.^[36,82] The bands attributed to pyridine on Brønsted acid sites (1630 and 1540 cm^{-1}) are however not visible.^[15,36,82,91,93,98] This could be due to a decreased accessibility of this group. Furthermore, a very low intensity of the bands affiliated with pyridine on Lewis acid sites (1620 and 1455 cm^{-1}) can be observed.^[22,23,50,82,89,93,98] According to the pyridine FT-IR measurements, the clay must therefore contain a very minimal amount of Lewis acid sites. The absence of a band in the CO vibrational region, affiliated with CO on a Lewis acid site, could then be ascribed to the low extinction coefficient.^[82] The shift of the peaks at 3700, 3675, 3660 and 3625 cm^{-1} might therefore be related to Lewis acid sites. Both in the pyridine and CO vibrational region, the intensity of the bands, affiliated with physisorbed CO (2143 cm^{-1}) or pyridine

(1580 and 1440 cm^{-1}) are very low. This indicates that the sample is probably very dense, which results in a minimal uptake of the CO or pyridine. The impenetrable behaviour of the clay has been reported in literature as well and therefore supports this claim.^[28]

The absence of acid sites in the clay could indicate that the binder is the component responsible for the pre-cracking and could therefore be the active component in the active matrix. Since the binder contains primarily Lewis acid sites, the pre-cracking is most likely Lewis acid catalysed.

As described in chapter 4, zeolite HY Si/Al 7 contains a high concentration of medium Brønsted acid sites, which was associated with the band at 3600 cm^{-1} in the OH vibrational region (Figure 23a). The bands at 3625 and 3545 cm^{-1} were subsequently affiliated with strong Brønsted acid sites.^[23,36,37,48,58,91,95–98] Additionally, the zeolite contained both strong and weak medium Lewis acid sites, which were affiliated with the formation of Extra-Framework (EF) aluminium species.

As shown in chapter 5, the binder contains primarily strong and medium Lewis acid sites and medium Brønsted acid sites. The Brønsted acid sites were shown to originate from the interaction between silica and boehmite. The strong Lewis acid sites were ascribed to the formation of very distorted penta-coordinated aluminium species.

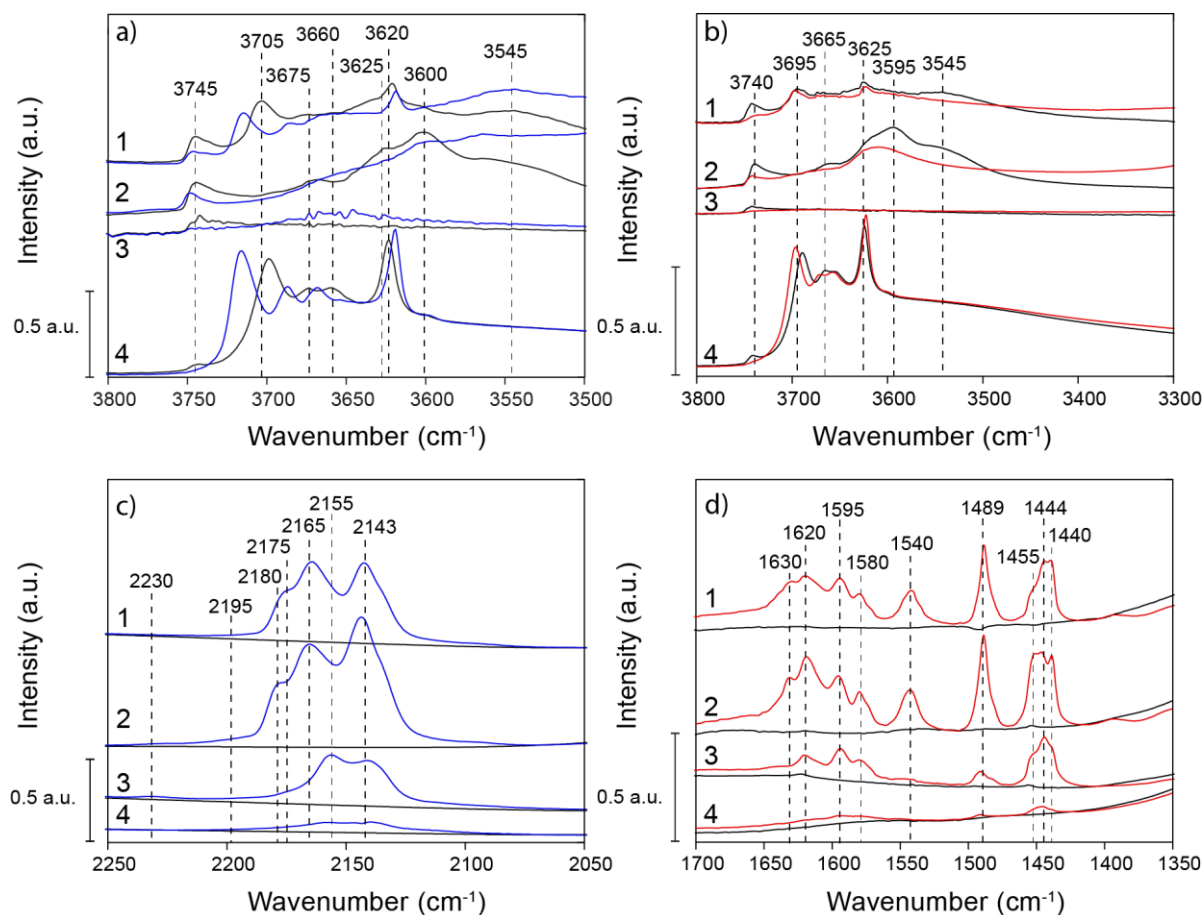


Figure 23 FT-IR spectra of 1. FCC catalyst 2. Zeolite HY Si/Al 7 3. Binder 4. Clay. a)- c) OH vibrational region and CO vibrational region before (black) and after maximal loading with CO(blue) b- d) OH vibrational region and pyridine vibrational region before (black) and after exposed to pyridine vapour for 30 min. (red)

As shown in Figure 23c the bands in the CO vibrational region of the FCC catalyst appear to be similar to the bands in the zeolite FT-IR spectrum. This shows that the acidity in the FCC catalyst originates

primarily from the zeolite. The overall intensity of all the bands is however decreased in the FCC FT-IR spectrum. This is accompanied by a decreased intensity of all the bands in the OH vibrational region (Figure 23a). The diminishing of the acidity, could be due to the incorporation of the clay, which contains little to no acid sites, thereby decreasing the overall acidity of the FCC catalyst. In Figure 23c, a shift of the band at 2180 to 2175 cm^{-1} can be observed, in the FCC. The band at 2180 cm^{-1} is affiliated with CO on a strong Brønsted acid site, whereas the band at 2175 cm^{-1} is attributed to CO on a medium Brønsted acid site.^[36,48,82,83,86] This suggests that mixing of the components results in a decreased acid strength of the strong Brønsted acid sites. Additionally, the intensity of the band at 2165 cm^{-1} appears to have decreased more in the FCC catalyst, compared to the band at 2180 cm^{-1} . This is confirmed by a decreased intensity of the band at 3600 cm^{-1} (Figure 23a), compared to the zeolite. The band at 3600 cm^{-1} is attributed to medium Brønsted acid sites, based on the results of chapter 4. This diminishing of the bands at 3600 and 2164 cm^{-1} thereby confirm the correlation from chapter 4. Additionally, in figure 23c, the intensity of the band at 2155 cm^{-1} appears to have decreased the most in the FCC. This band is affiliated with CO on non-acidic hydroxyl groups. The decrease of this band is noteworthy, since both the zeolite and the binder contain an intense band around 2155 cm^{-1} . The decreased intensity could indicate or removal of the surface groups or that the non-acidic groups are no longer accessible. Furthermore, a decreased intensity of the bands at 2195 and 2230 cm^{-1} can be observed, in the FCC. These bands are assigned to CO on a medium or strong Lewis acid site respectively.^[15,23,48,50,93,97] This indicates that the overall amount of Lewis acid sites decreases, upon mixing of the components.

In the pyridine vibrational region (Figure 23d), almost all the bands in the FCC have the same intensity as the bands in the zeolite, except for the bands at 1620 and 1455 cm^{-1} . These bands are attributed to pyridine on a Lewis acid site.^[22,23,50,82,89,93,98] The decreased intensity of these bands confirms the decreased amount of the Lewis acid sites, which was postulated, based on the CO FT-IR measurement (Figure 23c). The intensity of the bands affiliated with pyridine on a Brønsted acidic (1630 and 1540 cm^{-1}) appear to have decreased slightly in the FT-IR spectrum of the FCC, compared to the zeolite.^[15,36,82,91,93,98] The decreased intensity of the peak at 3595 cm^{-1} could therefore be correlated to the decreased amount of the Brønsted acid sites in the FCC. It is however remarkable that the decrease in the amount of Brønsted acid sites is very minimal. The bands at 1595 and 1444 cm^{-1} don't appear to have a decreased intensity, compared to the bands in the FT-IR spectrum of the zeolite. These bands are affiliated with pyridine hydrogen bonded to non-acidic hydroxyl groups.^[23,36,50,82,89,103] The decreased intensity of the band at 2155 cm^{-1} in Figure 23c is therefore not confirmed by the pyridine FT-IR measurements.

Based on these results it can be concluded that the amount of Lewis acid sites decreases upon mixing of the different components. Additionally, it can be suggested that mixing of the components might result in an enhanced Brønsted acidity.

To confirm these findings, the strongest acid sites were studied. Figure 24 depicts the FT-IR spectra of the samples after minimal CO loading and remaining pyridine at 550 °C. The first CO loading is experimentally to give rise to bands which are associated with the strongest acid sites in the samples. The FT-IR spectra in Figure 24d show the residual pyridine which is still attached to acid sites after heating the sample to 550 °C and are therefore associated with the strongest acid sites.

In the OH vibrational region (Figure 24a) of the FCC catalyst, a very minimal blue shift of the bands between 3725-3600 cm^{-1} can be observed, upon loading the sample with CO. This is accompanied by the formation of a band at 2230 and 2200 cm^{-1} , which is affiliated with CO on a strong and medium Lewis acid site respectively.^[15,23,48,50,93,97] This blue shift is not observed in the FT-IR spectrum of the FCC in Figure 24b, but an overall consumption of almost all the bands between 3725-3500 cm^{-1} can be

observed. In the pyridine ring vibrational region (Figure 24d), bands associated with pyridine on a Lewis acid sites (1620 cm^{-1}) or on a Brønsted acid sites (1540 cm^{-1}) can be observed.^[22,23,50,82,89,93,98] Additionally, a band affiliated with pyridine on both Brønsted and Lewis acid sites (1489 cm^{-1}) can be observed.^[36,82] The intensity of the bands at 1540 and 1489 cm^{-1} is compared to the intensity of these bands in the zeolite. This shows that there is a minimal decrease in the amount of strong Brønsted acid sites upon mixing of the components in the FCC. In Figure 24d, the band at 1455 cm^{-1} is absent in the FCC catalyst, and the band at 1620 cm^{-1} has a decreased intensity, compared to the zeolite. Both bands are associated with pyridine on a Lewis acid site, which thereby confirms that mixing of the components results in a decrease in the amount of Lewis acid sites.

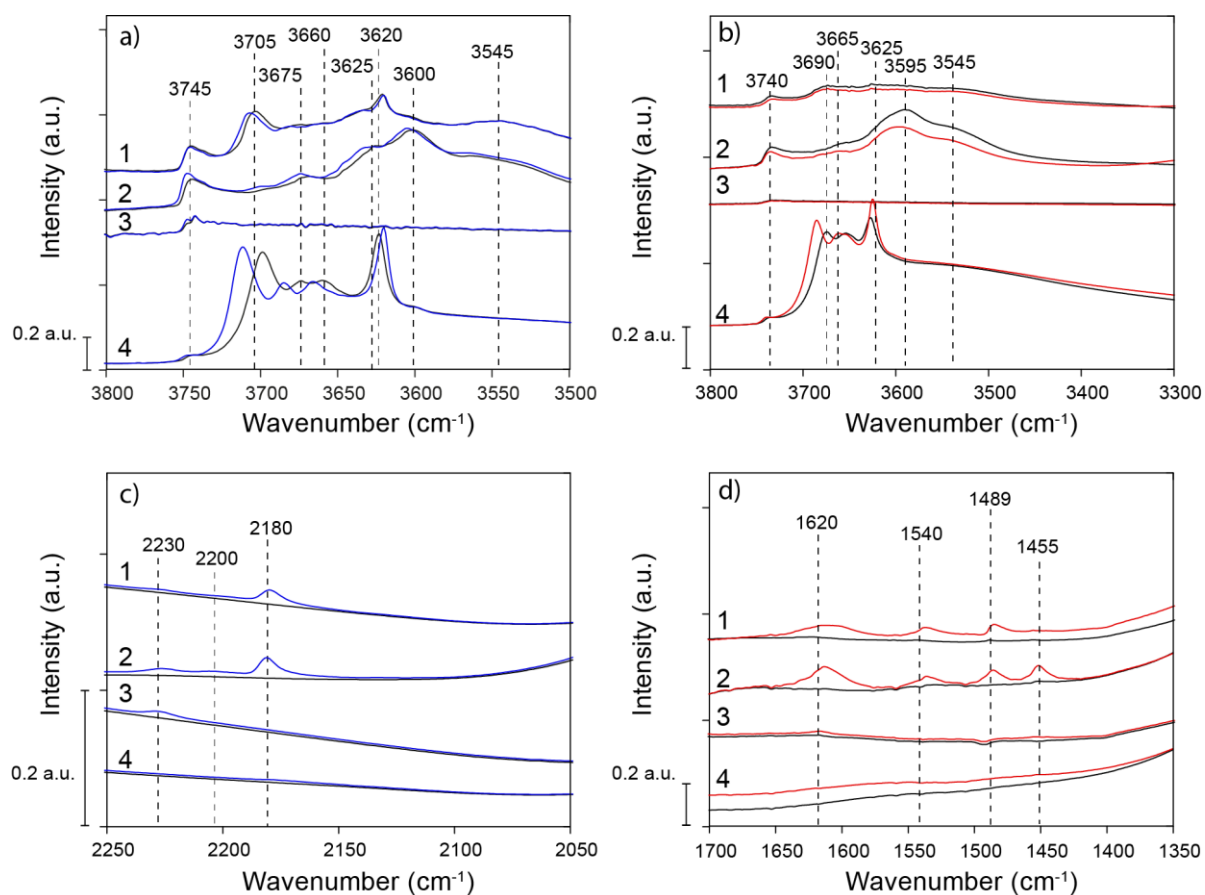


Figure 24 FT-IR spectra of 1. FCC catalyst 2. Zeolite HY Si/Al 7.3. Binder 4. Clay. a)- c) OH vibrational region and CO vibrational region before (black) and after minimal loading with CO(blue). b- d) OH vibrational region and pyridine vibrational region under vacuum at $550\text{ }^{\circ}\text{C}$ (black) and after being exposed to pyridine vapour for 30 min. and heated to $550\text{ }^{\circ}\text{C}$ (red) as described in paragraph 3.2.1.

In the OH vibrational region of the zeolite (Figure 2a), the OH bands between $3725\text{-}3600\text{ cm}^{-1}$ show a stronger blue shift, upon loading with CO, compared to the FCC catalyst. The stronger blue shift indicates a more stabilizing interaction between the CO and the aluminium, which could be an indication of stronger Lewis acid sites. Another explanation for the stronger blue shift is the accessibility of the OH groups: Due to confinement, the OH vibrations are hindered and thereby cannot shift to higher wavenumbers. In the OH vibrational region of the clay (Figure 24a), the bands at 3705 , 3675 , 3660 and 3620 cm^{-1} show the same shift upon loading with CO and pyridine as in Figure 23a and 23b. In the CO and pyridine vibrational region in Figure 24c and 24d, there is however no clear formation of a band. This could mean that the extinction coefficient is very low, or that the groups are non-acidic.

Overall the decrease in the concentration of Lewis acid sites upon mixing of the single components is confirmed. The pyridine FT-IR measurements showed no decrease of the amount of strong Brønsted acid sites. Both the CO and pyridine based FT-IR measurements showed that the clay contained no strong acid sites.

To get a better understanding about the decreased concentration of the Lewis acid sites, and the preservation of the Brønsted acidity, $^1\text{H-NMR}$ was employed to detect changes in acidity, by comparing the chemical shift of the proton in the $^1\text{H-NMR}$ measurement with the IR bands in the OH vibrational region ($4000\text{-}3000\text{ cm}^{-1}$) in the FT-IR spectra. In Figure 25 the OH vibrational region (a) of the samples is shown with their $^1\text{H-NMR}$ spectrum (b). The $^1\text{H-NMR}$ spectra are not corrected for the weight of the samples, but equal volume amounts were used. Differences in intensity of similar peaks between the samples can therefore not be assigned to a change in the amount, since differences in sample density result in a changed amount of hydroxyl groups. Differences in peak ratios can however be used to get a better idea about the ratio of different protons within a sample.

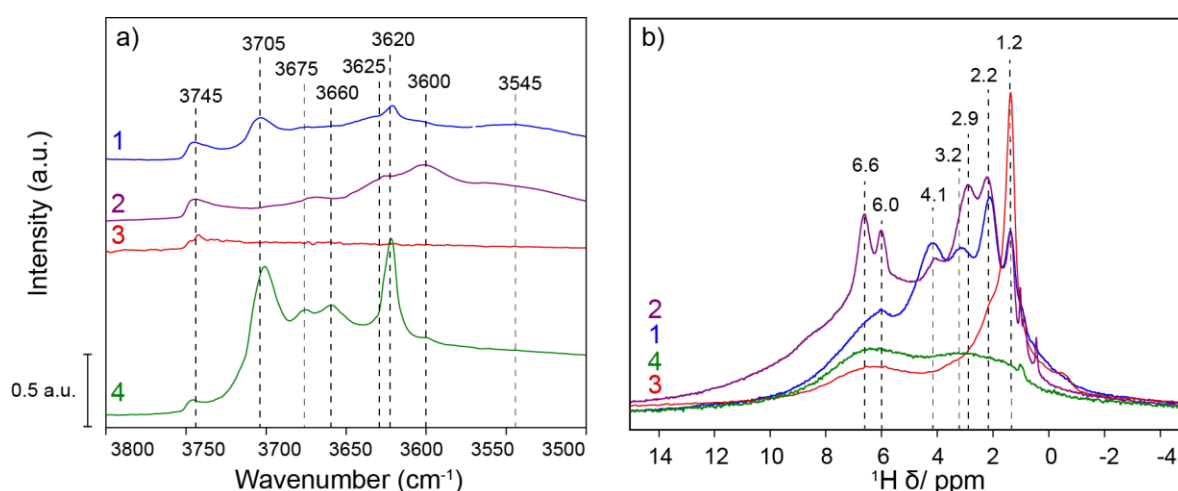


Figure 25 a) FT-IR spectrum of the OH vibrational region under vacuum at $-188\text{ }^\circ\text{C}$ and b) $^1\text{H-NMR}$ spectrum of 1. FCC catalyst 2. Zeolite HY Si/Al 7 3. Binder* 4. Clay * The intensity of the binder in the $^1\text{H-NMR}$ spectrum is divided by 2.

Figure 25 displays the FT-IR spectra of the OH vibrational region (a) and the corresponding $^1\text{H-NMR}$ spectra (b) of the FCC and the individual components. Based on the correlations described in Table 2, the peak around 3600 cm^{-1} is ascribed to the peak around 2.9 ppm , which is attributed to medium Brønsted acid sites.^[23,36,37,96,108–110] In the $^1\text{H-NMR}$ spectrum of the FCC, the peak at 2.9 ppm appears to have shifted to 3.2 ppm . This is accompanied by a large decrease in intensity of the band at 3600 cm^{-1} . The band at 3625 cm^{-1} is affiliated with a peak at 3.6 ppm and ascribed to strong Brønsted acid sites located in a super cage.^[23,36,37,48,58,91,95–98] The shift of the peak at 2.9 ppm to 3.2 ppm could therefore be explained by a relatively higher contribution of the peak at 3.6 ppm which was postulated to lie underneath the peak at 2.9 ppm , as described in chapter 4. The decreased intensity of the peak at 3.2 ppm therefore confirms that mixing of the components results in an overall decrease of the amount of Brønsted acid sites, located in the super cage. In the $^1\text{H-NMR}$ spectrum of the FCC, the peak at 4.1 ppm has an increased intensity, compared to the peak at 3.2 ppm . The peak at 4.1 ppm is attributed to Brønsted acid sites in sodalite cages and coupled to the band at 3545 cm^{-1} .^[96,109] The small decrease of the peak at 4.1 ppm shows that mixing of the components does not result in a decreased amount of Brønsted acid sites in a sodalite cage. The sodalite cages are the smallest cages in the zeolite, which results in confinement of the Brønsted acid site.^[66] The conservation of this Brønsted acid sites could therefore be correlate to the inaccessibility of the Brønsted acid site.

As described in the work of Farmer et al., the appearance of the four OH bands in the clay (3700, 3675, 3660, 3620 cm^{-1}) are due to strong dipole-dipole interactions between the OH vibrations.^[94,134] In Figure 25b no defined peak can be observed in the $^1\text{H-NMR}$ spectrum of the clay. This is caused by the strong dipole-dipole interactions between the OH groups, which results in broadening of the peaks in the $^1\text{H-NMR}$, as described in paragraph 2.4.1.^[16,22,35,36,71–76,93,102] The broad peak which stretches from 4 to 0 ppm is therefore associated with the characteristic OH vibrations in the FT-IR spectrum.

In Figure 25b, the peak at 6 ppm appears to have a decreased intensity in the FCC, compared to the zeolite. This peak is affiliated with water adsorbed on a Lewis acid site.^[40,41,71,112,114] The decreased intensity of this band thereby confirms the decreased concentration of the Lewis acid sites in the FCC catalyst, compared to the single components.

Based on these results, a new correlation between the OH vibration and shift in the $^1\text{H-NMR}$ was made as shown in Table 3.^[23,36,40,91,94,96,104,109,129,137]

Table 3 Correlation between the chemical shift in $^1\text{H-NMR}$ and the wavenumber in FT-IR.

Wavenumber (cm^{-1})	Chemical shift (ppm)	Assignment	References
3745	1.2	Silanol groups	[96,107,109]
3700, 3675, 3660, 3620	Broad peak stretching from 4-0 ppm	Aluminol groups characteristic for kaolinite, which appear as four peaks due to dipole-dipole interactions in the OH vibrational region in the FT-IR spectrum. Due to the dipole-dipole interactions, the $^1\text{H-NMR}$ shows a very broad peak.	[94,134]
3675, 3660	2.2 ppm	Non-acidic aluminol groups	[107] and the $\{^{27}\text{Al-}^1\text{H}\}$ CP experiment in paragraph 6.3.1
3625	3.4	Bridging OH groups in a super cage	[96,109]
3600	2.9	Bridging OH groups in a super cage	Experimentally found
3545	4.1	Bridging OH groups in a sodalite cage	[96,109]
-	6.0	Water on a Lewis acid site	[43,106,112]
-	6.6	NH_4^+ ions present in the zeolite	[113]

Based on this correlation it can be concluded that mixing of the components results in a decreased amount of Lewis acid sites in the FCC and a decrease in the amount of Brønsted acid sites in the super cages. The amount of Brønsted acid sites in the sodalite cages appears to remain unaffected by the mixing of the components.

6.2 Structure

To understand the decrease in the amount of Lewis and Brønsted acid sites in the FCC, the samples were measured with ^{27}Al MQ-MAS and ^{27}Al MAS NMR spectroscopy. All the samples were heated to 538 °C for one hour under a nitrogen flow of 100 mL/min, as described in paragraph 3.2.2. The ^{27}Al MAS- and ^{27}Al MQ-MAS NMR spectra are not corrected for the weight of the samples, but equal volume amounts were used. Differences in intensity of similar peaks between the samples can therefore not directly be assigned to a change in the amount, since differences in sample density result in a changed absolute amount of aluminium. Differences in peak ratios can however be used to get a better idea about the ratio of different aluminium coordinations within a sample.

As explained in paragraph 2.4.1, in MQ-MAS NMR spectra the peak position along the F1 axis is only affected by the chemical shift isotropy, which gives information about the coordination of the aluminium nucleus. The anisotropic chemical shift in the F2 direction is largely affected by the second order quadrupolar coupling.^[35,79,80] A broadening along the F2 direction thus provides information about the strength of the quadrupolar coupling constant, and therefore about the symmetry and environment around the aluminium nucleus.^[35,41,79,80,114,115] As described in paragraph 2.4.1, three regions can be distinguished in the ^{27}Al MQ-MAS NMR spectra: 0-30 ppm, 20-50 ppm and 40-90 ppm, which are ascribed to octahedral, penta-coordinated and tetrahedral aluminium coordinations respectively.^[35,41,114,115]

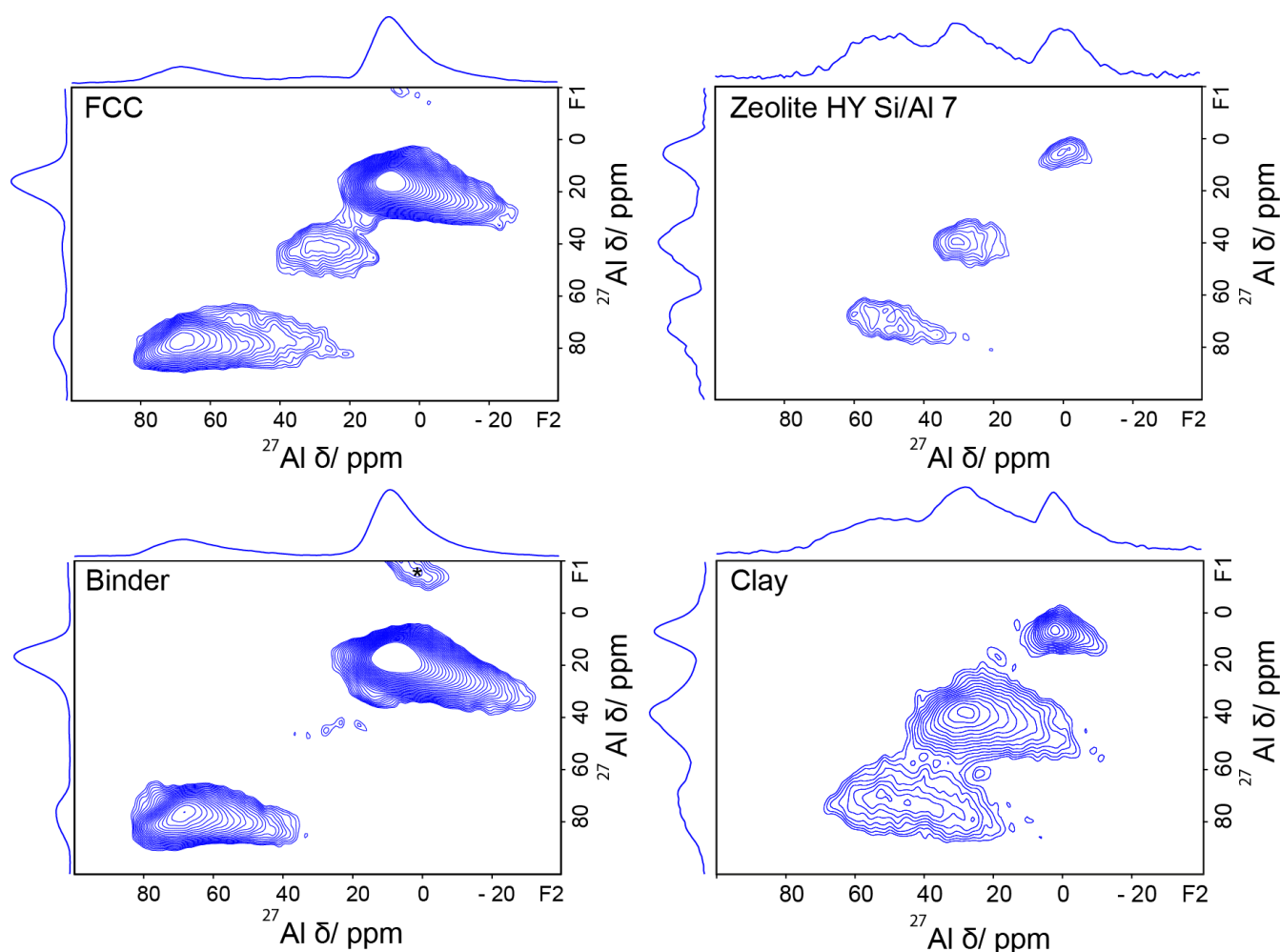


Figure 26 ^{27}Al MQ-MAS spectra of the single components and the FCC catalyst, with the projections on the F1 and F2 axis. The *asterisk indicates spinning side-bands and are therefore not considered to be real peaks.

Figure 26 shows the ^{27}Al MQ-MAS NMR spectra of the individual components and the FCC catalyst. In the ^{27}Al MQ-MAS NMR spectrum of zeolite HY Si/Al 7, three peaks can be observed. As described in chapter 4, the Brønsted acidity originates from tetrahedrally coordinated aluminium, which gives rise to a peak around 70 ppm, in the F1 direction. The two other two peaks were ascribed to penta-coordinated (40 ppm) and octahedrally coordinated (10 ppm) aluminium species.^[43,98,130,131] Both the penta- and octahedral aluminium coordinations are ascribed to Extra-Framework (EF) aluminium species.^[2,8,15–24] In the work of Deng et al. similar aluminium coordinations have been obtained, upon heating of a zeolite HY.^[43,44] Based on these results, and the results in chapter 4, the penta-coordinated aluminium species is associated with the presence of Lewis acid sites in the zeolite.

As shown in chapter 5, the binder contained medium and strong Lewis acid sites, which were affiliated with the formation of penta- and octahedrally coordinated aluminium species, at 35,30 ppm (F1,F2) and 45,35 ppm (F1,F2) respectively. The penta-coordinated aluminium was not clearly visible in the ^{27}Al MQ-MAS NMR spectrum, which was probably due to a large heterogeneity around the aluminium nucleus.^[35,131] The small peak at 70,75 ppm (F1,F2) was attributed to the medium Brønsted acid sites in the binder in chapter 5. The large tetrahedral peak at 75,70 ppm (F1,F2) was affiliated with the formation of a tetrahedral alumina framework.^[92,126,132]

The ^{27}Al MQ-MAS NMR spectrum of the clay, the peaks affiliated with tetrahedrally (70 ppm) and penta-coordinated (40 ppm) aluminium, are strongly broadened along the F2 direction. As described in paragraph 2.4.1, this indicates that the second coordination sphere of the aluminium nuclei is very distorted.^[35,79,80] This suggests that these coordinations originate from EF aluminium species. The peak affiliated with octahedrally coordinated aluminium (10 ppm), has a very symmetrical shape. This indicates that the aluminium has a very symmetrical second coordination sphere.^[35,79,80] The octahedral coordination can therefore be affiliated with framework aluminium with a very symmetrical structure.

In the ^{27}Al MQ-MAS NMR spectrum of the FCC, the peak associated with octahedrally coordinated aluminium (10 ppm) appears to be comparable to the peak in the ^{27}Al MQ-MAS NMR spectrum of the binder. This peak was associated with non-acidic aluminium species. In chapter 5, the peak at 30,35 ppm (F1,F2) was attributed to medium Lewis acid sites. As shown in paragraph 6.1, the FCC contains little to no Lewis acid sites. The appearance of this peak in the FCC therefore contradicts the assignment, made in chapter 5. In both chapter 4 and 5, the peak affiliated with penta-coordinated aluminium was correlated to a change in the Lewis acidity. As shown in Figure 27A, the FCC contains a high concentration of penta-coordinated aluminium. However, the FT-IR measurements in paragraph 6.1 showed that the FCC catalyst contained a low concentration of Lewis acid sites. This suggests that the penta-coordinated aluminium is not the origin of the Lewis acidity. Another possibility is that the Lewis acid sites are no longer accessible, due to the mixing.

In the tetrahedral region (70 ppm), the peak in the FCC catalyst appears to contain both the tetrahedral aluminium coordinations from the binder and the zeolite. The peak at 75,70 ppm (F1,F2) in the binder appears to have vanished in the ^{27}Al MQ-MAS NMR spectrum of the FCC catalyst. This peak was affiliated with the medium Brønsted acid sites in the binder. As described in paragraph 6.1, mixing of the components does result in a decreased amount of the medium Brønsted acid sites in the FCC catalyst. This confirms the correlation between the peak at 75,70 ppm (F1,F2) and the medium Brønsted acidic character of the binder.

To compare the aluminium coordinations of the single components with the FCC catalyst, an overlay of the ^{27}Al MQ-MAS and the ^{27}Al MAS -NMR spectra are shown in Figure 27.

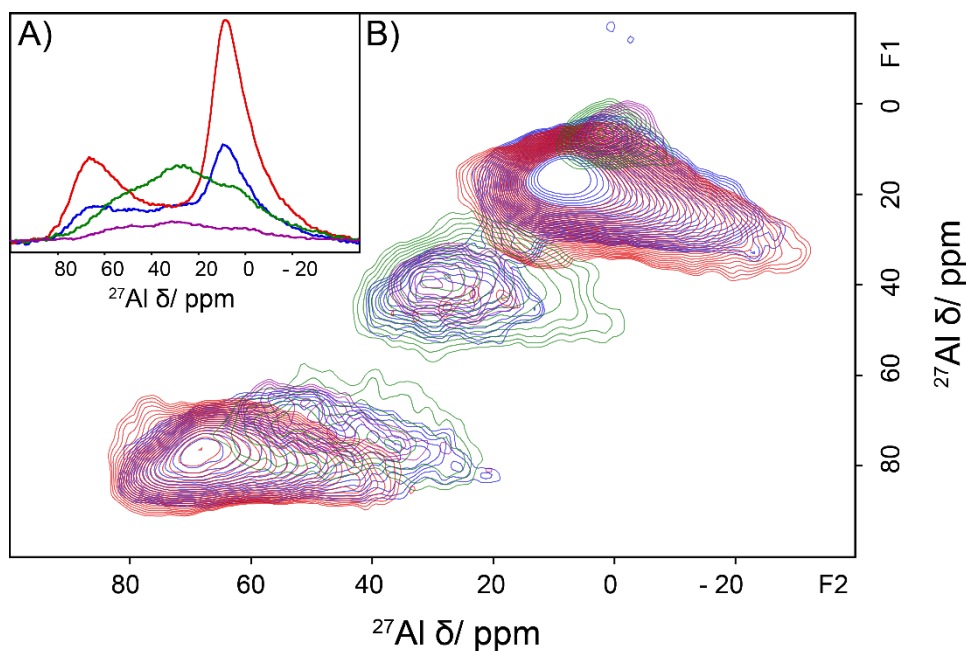


Figure 27 A) one-pulse ^{27}Al MAS spectrum B) ^{27}Al MQ-MAS spectrum. Blue: FCC catalyst, Red: Binder, Purple: Zeolite HY Si/Al 7, Green: Clay.

As shown in the ^{27}Al MAS-NMR spectra, the aluminium coordination of the zeolite is similar to the structure of the kaolin. The ^{27}Al MQ-MAS NMR spectra of the zeolite and the clay are however not identical: The peaks affiliated with tetrahedrally and penta-coordinated aluminium species are more broadened along the F2 direction in the clay, compared to the zeolite. This shows that the aluminium coordinations in the clay are more distorted in the second coordination sphere.^[35,79,80] The large heterogeneity could be an effect of confinement of the aluminium species. The similarity of the aluminium coordinations would suggest a similar acidity of the kaolin, compared to the zeolite. However, the FT-IR measurements in paragraph 6.1 showed that the clay contained little to no acid sites. It was postulated that the acid sites were not accessible in the clay, based on the low concentration of physisorbed CO and pyridine in Figure 23. Based on Figure 27, it can therefore be postulated that the clay does contain acid sites, but they are not accessible.

In Figure 27, the ^{27}Al MAS-NMR spectrum of the FCC appears to be a summation of all the single components, which is confirmed in the ^{27}Al MQ-MAS NMR spectrum. In the ^{27}Al MQ-MAS NMR spectrum of the FCC, a decrease of the broadening along the F2 directions of all the aluminium coordinations can be observed. This suggests that all aluminium coordinations have obtained a more homogeneous environment, upon mixing of the individual components. It can therefore be argued that a decrease in heterogeneity results in an overall decrease in the amount of acid sites, as was observed in paragraph 6.1.

Based on these results it can be concluded that mixing of the individual components results in a more homogeneous environment around the different aluminium species. The stabilizing interaction between the components could subsequently be linked to the decreased amount of Lewis acid sites. This suggests that the Lewis acid sites are located on the surface of the individual components, which has also been postulated in literature.^[21] The large distortion around the aluminium nuclei in the clay could be attributed to confinement of the aluminium species. This was confirmed by the low amount of physisorbed CO and pyridine, in paragraph 6.1. The decrease amount of medium Brønsted acid sites could partially be attributed to the vanishing of the peak at 75,70 ppm (F1,F2), in the FCC catalyst.

6.3 Cross-Polarization Experiments

To get a better understanding of the structure and the origin of the different acid sites and surface groups, a cross polarization (CP) MAS-NMR spectroscopy was employed. As described in paragraph 2.4.1, in a CP-MAS NMR experiment the polarization of one nucleus is transferred to another nucleus. The resulting spectrum gives an enhanced signal for the nuclei which are in close proximity. The enhanced intensity thereby gives information about the proximity of two different nuclei and could thus be used to study the proximity of protons to aluminium. In a $\{^{27}\text{Al}-^1\text{H}\}$ CP MAS-NMR experiment, a ^1H -NMR spectrum is obtained in which the signal of the protons in close proximity to an aluminium nucleus is enhanced. In a $\{^1\text{H}-^{27}\text{Al}\}$ CP experiment an ^{27}Al MAS spectrum is obtained, which gives an enhanced aluminium signal of the coordinations which are in close proximity to a proton. The experiments are optimized in such a way that the overall intensity is the highest. The polarization transfer of a proton - aluminium pair could thus have an optimal condition in the $\{^1\text{H}-^{27}\text{Al}\}$ CP experiment, but not in a $\{^{27}\text{Al}-^1\text{H}\}$ CP experiment. The enhancements can thus be used as a guideline to correlate the different aluminium coordinations to the different protons, but an enhanced signal in the $\{^1\text{H}-^{27}\text{Al}\}$ CP experiment does not have to result in an enhancement in a $\{^{27}\text{Al}-^1\text{H}\}$ CP for the same H-Al pair.

The FCC was measured after heated it to 538 °C for one hour, under a nitrogen flow of 100 mL/min, as described in paragraph 3.2.2.

6.3.1 $\{^{27}\text{Al}-^1\text{H}\}$ Cross Polarization

In Figure 28 the $\{^{27}\text{Al}-^1\text{H}\}$ CP spectrum of the FCC is shown with an overlay of the original ^1H -NMR spectrum. The spectra are normalized with respect to the peak at 2.1 ppm, to distinguish the peaks which are not as strongly enhanced. The high intensity of the peak at 2.1 ppm in the $\{^{27}\text{Al}-^1\text{H}\}$ CP NMR spectrum indicating that this peak is most likely due to aluminol groups. Furthermore, two shoulders can be observed at 2.9 and 3.3 ppm, which confirms that the peak at 3.3 ppm lies underneath the peak at 2.9 ppm. This confirms the assignment of the ^1H -NMR shift and OH vibration in the FT-IR spectra, tabulated in Table 3.

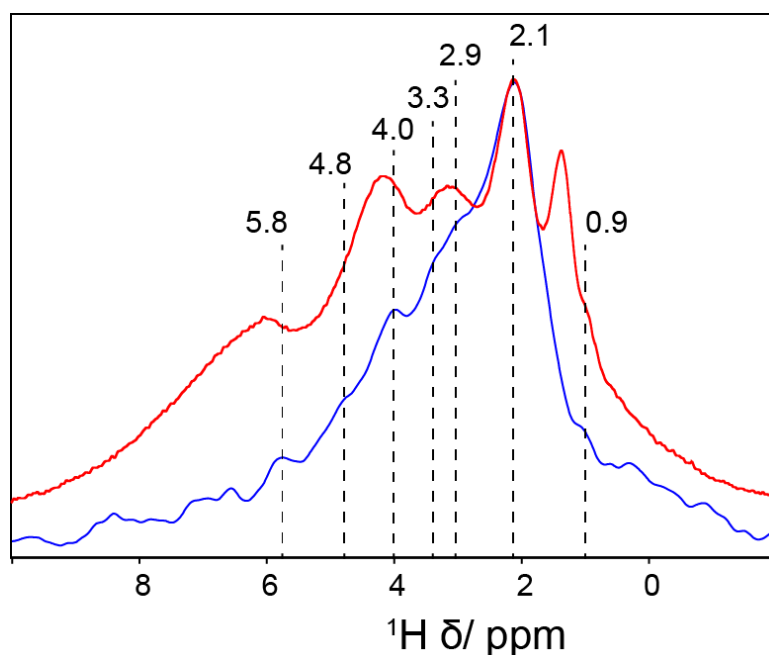


Figure 28 $\{^{27}\text{Al}-^1\text{H}\}$ CP of the FCC (blue) compared to the ^1H -NMR spectrum of the normal FCC (red) normalized with respect to the peak at 2.2 ppm

The stronger decrease of the peaks towards higher wavenumbers indicates that the polarization transfer of the proton and aluminium is less successful. This could be due to the confinement of the protons, or due to an increased acidity of the protons. Confinement of the protons results in a larger chemical shift, due to electron withdrawal of the groups, confining the proton. An enhanced Brønsted acidity results in a decreased shielding of the proton and thereby an increase in the energy difference between the Zeeman levels. This makes the proton less prone to a successful transfer of polarization.^[35,72,81]

The peak at 6 ppm is almost completely vanished in the $\{^{27}\text{Al}-^1\text{H}\}$ CP NMR spectrum, which could indicate that the protons are not close to an aluminium nucleus, or the transfer was unsuccessful. This makes the correlation of the peak at 6 ppm with water on a Lewis acid site doubtful.^[40,41,71,112,114] The large diminishing could therefore originate from water which is confined in small pores and therefore does not interact with any specific aluminium coordination.

6.3.2 $\{^1\text{H}-^{27}\text{Al}\}$ Cross Polarization

In Figure 29 the $\{^1\text{H}-^{27}\text{Al}\}$ CP of the FCC is shown with an overlay of the original ^{27}Al MAS spectrum. The spectrum is normalized with respect to the peak at 5 ppm. A large enhancement of the peak around 60 ppm can be observed in the $\{^1\text{H}-^{27}\text{Al}\}$ CP NMR spectrum. Additionally, the intensity of the peak at 65-70 ppm appears to be decreased in the $\{^1\text{H}-^{27}\text{Al}\}$ CP NMR spectrum. The peak at 65-70 ppm can be linked to the tetrahedral coordination of the binder, based on Figure 27A, whereas the peak at 60 ppm is originating from the zeolite and clay.

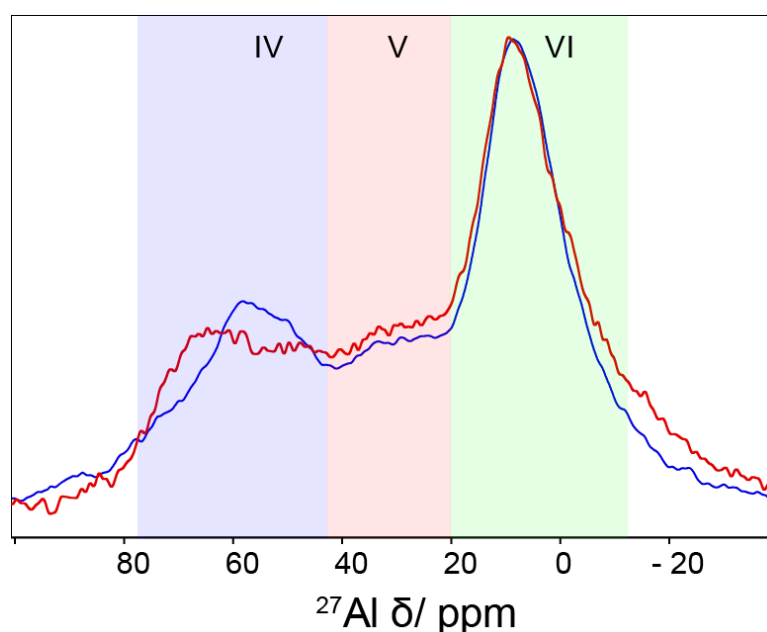


Figure 29 $\{^1\text{H}-^{27}\text{Al}\}$ CP of the FCC (blue) compared to the ^{27}Al MAS NMR spectrum of the normal FCC (red) normalized with respect to the octahedral peak. The shaded regions indicate the tetrahedral (IV), penta-coordinated (V) and octahedral (VI) aluminium coordinations respectively.

Based on the enhanced signal of the peak at 2.2 ppm in Figure 28, it can be postulated that the enhanced peak at 60 ppm originates from these protons. However, the two peaks cannot directly be correlated, since the enhancement of the signal depends partially on the optimization. As shown in Figure 28, the peaks affiliated with Brønsted acid sites (2.9, 3.3 and 4.0 ppm) are also reasonably enhanced. Additionally, in chapter 4, the peak at 60 ppm was ascribed to Brønsted acid sites. Therefore, it can be postulated that the peak at 60 ppm originates from tetrahedral aluminium which is in close proximity to Brønsted acidic protons.

The large diminishing of the peak at 65-70 ppm is attributed to tetrahedral aluminium originating from the binder. In literature, the formation of tetrahedral aluminium is affiliated with the formation of an alumina framework. ^[92,126,132] The decrease in intensity could therefore be affiliated with the formation of a tetrahedral alumina framework in which there are few protons present.

In the $\{^1\text{H}-^{27}\text{Al}\}$ CP NMR spectrum, the ratio in intensity of the peak at 5 ppm peak with respect to the peak at 35 ppm is very similar to the ratio of these peaks in the ^{27}Al MAS-NMR spectrum. In the work of Feng Deng, the peak at 2.2 ppm was affiliated with EF aluminol groups, which were attached to octahedrally and penta- coordinated EFAl species. The similar intensity of the peaks at 5 ppm and 30 ppm is therefore probably due to the close proximity of the non-acidic aluminol groups at 2.2 ppm. ^[40,41,43,44,103]

6.4 Summary and Conclusion

Based on the FT-IR measurement in paragraph 6.1, it was concluded that the overall acidity of the FCC originated primarily from the zeolite. Additionally, mixing of the single components resulted in a decrease of the concentration Lewis acid sites. Furthermore, mixing of the single components resulted in a decreased concentration of the medium Brønsted acid sites. This was confirmed by a decreased intensity of the peak at 2.9 ppm in the ^1H -NMR spectrum of the FCC catalyst, which is associated with medium Brønsted acid sites. Little decrease in the concentration of the strong Brønsted acid sites was observed in the FCC catalyst. In the ^1H -NMR spectrum, the peak affiliated with Brønsted acid sites in sodalite cages did not appear to decrease in intensity upon mixing of the single components. The minimal decrease of these protons was attributed to the shielding of the proton by the small sodalite cage. Additionally, it was observed that the clay contained almost no acid sites or physisorbed CO or pyridine. This was subsequently attributed to the inaccessibility of the acid sites of the clay. It was therefore concluded that the binder is most likely the active component responsible for the pre-cracking.

In the ^{27}Al MQ-MAS NMR spectrum of the FCC, a decreased elongation in the F2 direction was observed, compared to the single components. This was postulated to be correlated to a more homogenous environment around the aluminium nuclei. The increased homogeneity was subsequently associated with the decreased concentration of the Lewis acid sites and medium Brønsted acid sites, due to the interactions of the components. The increased homogeneity was coupled to a less electron withdrawing character of the aluminium species and therefore a decrease in the acid strength. In the ^{27}Al MAS-NMR spectrum, the aluminium coordinations in the zeolite appeared to be comparable to the aluminium coordinations of clay. In the ^{27}Al MQ-MAS NMR spectrum the peaks affiliated with tetrahedrally and pentahedral-aluminium appeared to be more distorted in the clay. This was ascribed to confinement of the aluminium species. The confinement of the aluminium species in the clay confirmed the inaccessibility of the acid sites, which was postulated in paragraph 6.1.

With the $\{^{27}\text{Al}-^1\text{H}\}$ CP experiment in 6.4 it was shown that the peak at 2.2 ppm in the ^1H -NMR spectrum can be attributed to aluminol groups. The formation of two peaks at 2.9 and 3.3 ppm confirmed the presence of two different Brønsted acid sites in super cages. The protons affiliated with more confined Brønsted acid sites showed a decreased signal in the $\{^{27}\text{Al}-^1\text{H}\}$ CP NMR spectrum, which was attributed to a less successful transfer of polarization, caused by confinement of the different protons. A large decreased intensity of the peak at 6 ppm was observed in the $\{^{27}\text{Al}-^1\text{H}\}$ CP NMR spectrum. This peak is affiliated with water on a Lewis acid site.^[40,41,71,112,114] The large diminishing was partially ascribed to a possibly unsuccessful cross-polarization. The peak was also postulated to originate from water, confined in small pores.

In the $\{^1\text{H}-^{27}\text{Al}\}$ CP experiment a large increase of the tetrahedral coordination, originating from the zeolite, was observed. This peak was postulated to originate from aluminium close to Brønsted acid sites in the zeolite. The conservation of the octahedral and penta-coordinated aluminium peaks was affiliated with the attachment of Extra-Framework aluminol groups, which appeared at 2.2 ppm in the $\{^{27}\text{Al}-^1\text{H}\}$ CP NMR spectrum. Furthermore, a decreased intensity of the tetrahedral coordination at 65-70 ppm was observed. This coordination was associated with the tetrahedral aluminium which originated from the binder. The decreased intensity was correlated to the formation of a tetrahedral alumina framework.

To conclude: The acidity of the FCC catalyst originated primarily from the acid sites in the zeolite. Mixing of all the components resulted in a decreased concentration of Lewis and Brønsted acid sites. Tetrahedral aluminium is responsible for the formation of Brønsted acid sites. The Brønsted acid sites, which are located in sodalite cages, are not affected by mixing with other components. An increase in homogeneity around the penta-coordinated aluminium nuclei results in a decrease in the amount of the strong Lewis acid sites. Both the penta-coordinated and octahedrally coordinated aluminium species are EFAl species. The incorporation of clay resulted in a decreased concentration of acid sites. Additionally, the incorporation of clay results in blockage of the pores.

Chapter 7. Mixed components

In this chapter the interactions between two individual components will be discussed. As observed in chapter 6, mixing of the single components in the FCC catalyst led to a decrease in the amount of Lewis acid sites and a decrease in the amount of the medium Brønsted acid sites. However, in the work of Whiting et al. an enhanced reactivity was found when zeolite ZSM-5 was mixed with silica and alumina, indicating that binder and zeolite could interact.^[28,29,138] Therefore, a mix of binder-zeolite HY Si/Al 7 and a mix of binder-clay was analysed to detect possible changes in acidity and aluminium coordination, to distinguish possible interactions between the components.

7.1 Binder-Zeolite

First a mix of binder with zeolite HY Si/Al 7 was investigated, to test whether mixing of the zeolite with the binder would result in an enhanced acidity, as reported in literature.^[28,29,138]

The acidity was determined with CO and pyridine based infrared (FT-IR) spectroscopy. Additionally, magic angle- nuclear magnetic resonance (MAS-NMR) spectroscopy was used, to study the environment around the aluminium nuclei in a 1D-, and 2D multiple quantum- MAS NMR experiment. (²⁷Al MAS-NMR and ²⁷Al MQ-MAS NMR). Furthermore, proton MAS-NMR (¹H MAS-NMR) was used to study the different protons in the samples.

7.1.1 Acidity

For the FT-IR measurements, the samples were heated to 550 °C for one hour under high vacuum and cooled down, while kept under vacuum, as described in paragraph 3.2.1. All spectra were corrected for the weight of the wafer.

In Figure 30, the FT-IR spectra of the binder-zeolite mix with respect to the binder and zeolite HY Si/Al 7 is depicted. As described in paragraph 2.4.2, the band positions of the CO stretching vibration and the pyridine ring vibrations are characteristic for the acid type and acid strength, to which the CO or pyridine is attached.^[8,16,36,48,82,83,86] Since the spectra are corrected for the weight of the wafer, the intensity of the bands can be compared, which gives information about the amount of the different acid sites in the samples. The FT-IR measurements in Figure 30a and 30c are performed at -188 °C. This results in very defined bands in the OH vibrational region which are slight blue shifted, compared to the OH vibrations in Figure 30b which are taken at room-temperature.^[16,48]

In the CO vibrational region of the binder-zeolite mix (Figure 30c), a decrease in the intensity of the band at 2158 cm⁻¹ can be observed. This band is ascribed to CO on non-acidic hydroxyl groups.^[23,36,82] The decrease in non-acidic groups is due to the incorporation of the binder, which has a lower intensity of the band at 2158, compared to the zeolite. This results in an overall decrease of the non-acidic groups in the mix of zeolite and binder. Moreover, a decrease of the bands at 2230 and 2195 cm⁻¹, can be observed in the zeolite-binder mix. These bands are associated with CO on a strong and medium Lewis acid site respectively.^[15,23,48,50,93,97] This suggests that mixing of the binder and the zeolite results in a decrease in the amount of Lewis acid sites. Additionally, the band at 2180 cm⁻¹ is shifted to 2175 cm⁻¹ in the zeolite-binder mix. This band is associated with CO on a strong Brønsted acid site.^[36,48,82,83,86] The shift to lower wavenumbers indicates a slight decrease in the Brønsted acid strength, upon mixing of the binder and zeolite. In Figure 30c, the band at 2164 cm⁻¹ has an almost identical intensity in the binder-zeolite mix, compared to the zeolite. This band is affiliated with CO on a medium Brønsted acid site.^[36,48,82,83,86] In the OH vibrational regions (Figure 30a and 30b), the band at 3600 cm⁻¹ has a decreased intensity in the binder-zeolite mix, with respect to the zeolite. This band is affiliated with medium Brønsted acid sites in chapter 4. The decrease in intensity of the band at 3600 cm⁻¹ is therefore not accompanied by a decrease in the amount of medium Brønsted acid sites.

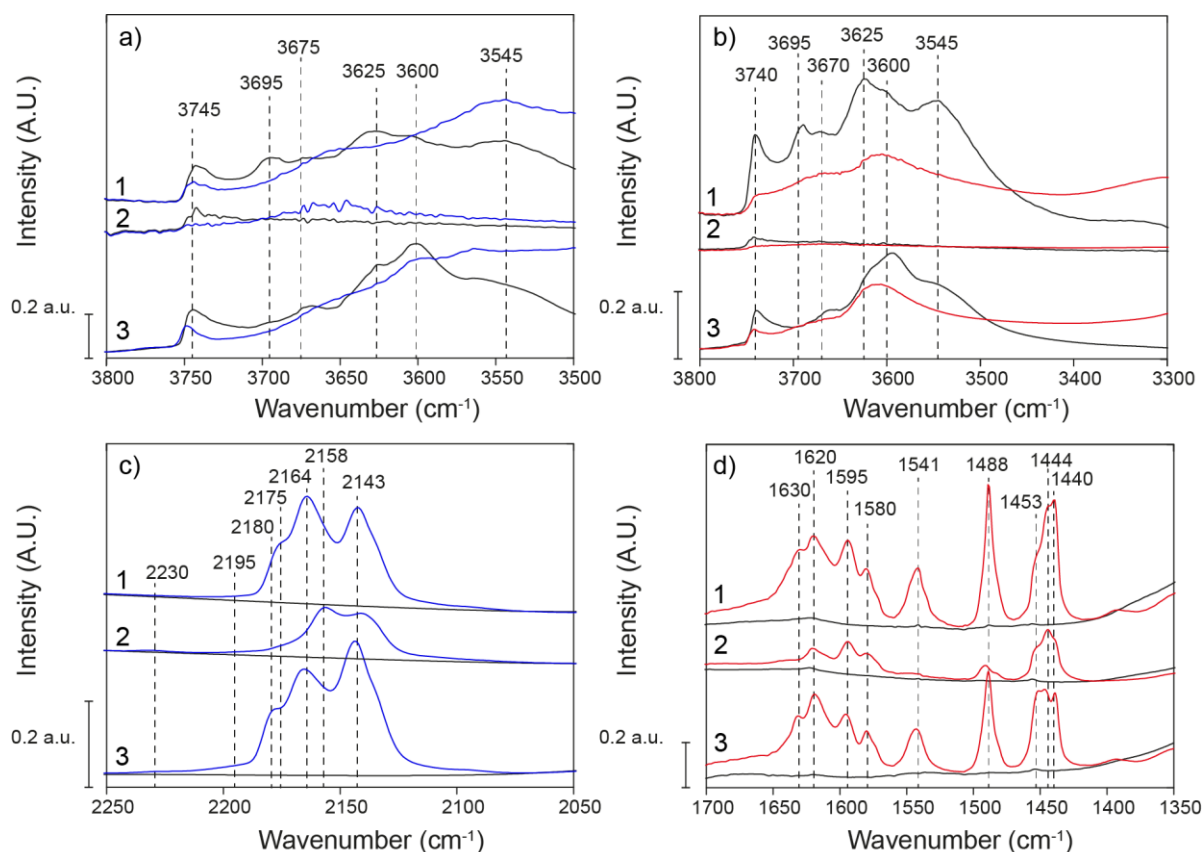


Figure 30 FT-IR spectra of 1. Binder-zeolite mix* 2. Binder 3. Zeolite HY Si/Al 7. a)- c) OH vibrational region and CO vibrational region before (black) and after maximal loading with CO(blue) b- d) OH vibrational region and pyridine vibrational region before (black) and after exposed to pyridine vapour for 30 min. (red)* The intensity of the binder-zeolite mix in the pyridine based measurements is divided by 2.

In the pyridine vibrational region (Figure 30d), the bands affiliated with pyridine on a Lewis acid site (1620 and 1453 cm^{-1}) have a decreased intensity in the FT-IR spectrum of the zeolite-binder mix, compared to the bands in the FT-IR spectrum of the zeolite.^[22,23,50,82,89,93,98] This confirms that mixing of two components results in a decreased amount of Lewis acid sites. The bands associated with pyridine on a Brønsted acid site (1630 and 1541 cm^{-1}) show no clear decrease in intensity, which suggests that the concentration Brønsted acid sites in the zeolite-binder mix is similar to the concentration of Brønsted acid sites in the zeolite.^[15,36,82,91,93,98] This shows that mixing of the binder and zeolite results in an increased concentration of Brønsted acid sites. Moreover, in Figure 30d an increased intensity of the band at 1488 cm^{-1} can be observed, which is attributed to pyridine on a Brønsted acid site and to pyridine on a Lewis acid site.^[22,23,50,82,89,93,98] Since the amount of Lewis acid site has decreased, the increased intensity could only originate from an increase in the amount of Brønsted acid sites. The high intensity of the zeolite-binder mix in the pyridine measurements might however be due to an overcompensation of the detector, due to a very thin wafer.

To confirm that the Lewis acidity decreased upon mixing, the strongest acid sites were studied. Figure 31 depicts the FT-IR spectra of the samples after minimal CO loading and remaining pyridine at 550 °C. The first CO loading is experimentally to give rise to bands which are associated with the strongest acid sites in the samples. The FT-IR spectra in Figure 31d show the residual pyridine which is still attached to acid sites after heating the sample to 550 °C and are therefore associated with the strongest acid sites.

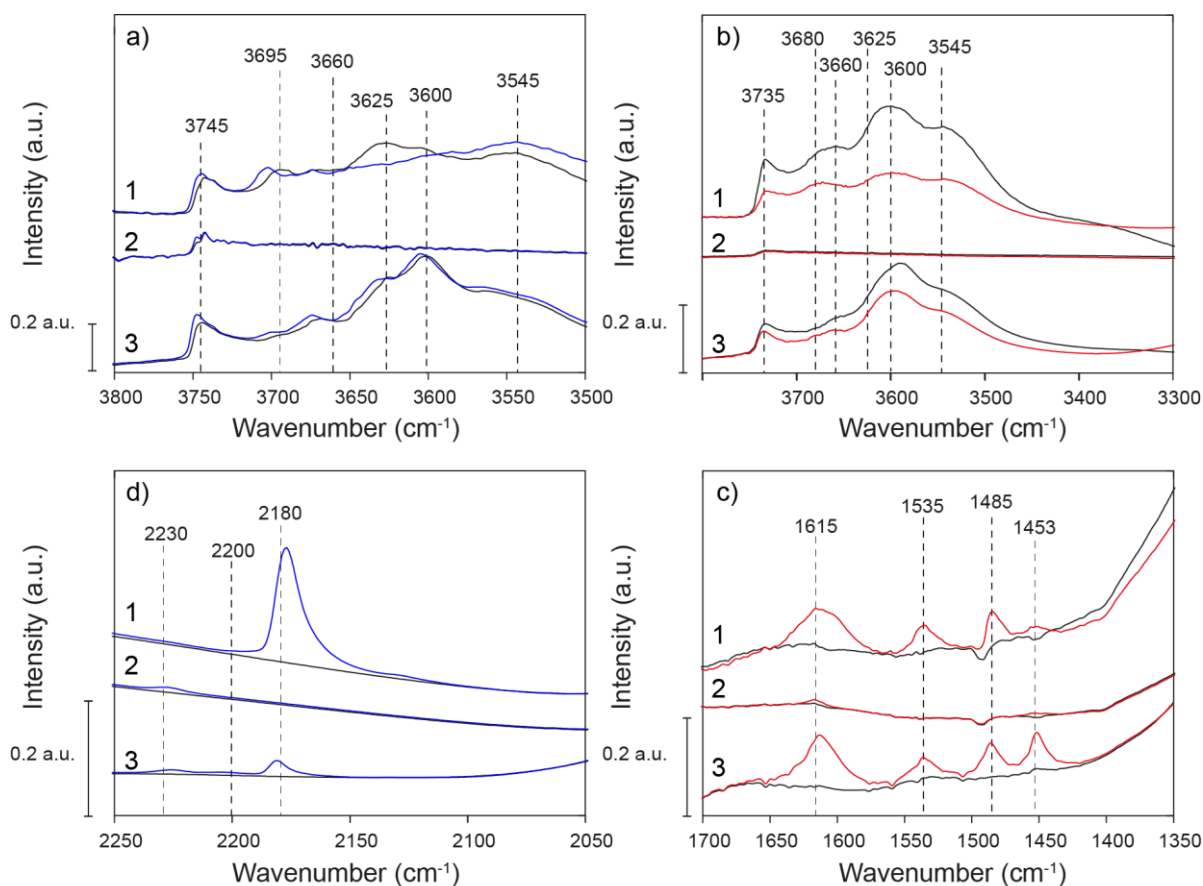


Figure 31 FT-IR spectra of 1. Binder-zeolite mix* 2. Binder 3. Zeolite HY Si/Al 7. a)- c) OH vibrational region and CO vibrational region before (black) and after minimal loading with CO(blue). b- d) OH vibrational region and pyridine vibrational region under vacuum at 550 550 °C (black) and after being exposed to pyridine vapour for 30 min. and heated to 550 °C (red) as described in paragraph 3.2.1.* The intensity of the binder-zeolite mix in the pyridine based measurements is divided by 2.

In Figure 31c, a decreased intensity of the bands affiliated with CO on a Lewis acid site (2230 and 2200 cm^{-1}) can be observed in the FT-IR spectra of the binder-zeolite mix, with respect to the binder and zeolite. [15,23,48,50,93,97] This is confirmed by the decrease of the bands associated with pyridine on a Lewis acid site (1615 and 1453 cm^{-1}) in Figure 31d. [22,23,50,82,89,93,98]

In the OH vibrational region (Figure 31b), a consumption of all the OH vibrational bands between 4000-3400 cm^{-1} can be observed in the spectrum of the zeolite-binder mix and for the zeolite, upon loading with pyridine. Overall the band at 3600 cm^{-1} appears to have the lowest intensity and could therefore be correlated to the residual Lewis and Brønsted acid sites. In Figure 31a, a blue shift of the bands between 3700-3550 cm^{-1} can be observed in the FT-IR spectrum of the zeolite. This is accompanied by the formation of bands at 2230-2200 cm^{-1} in the CO vibrational region, which are affiliated with CO on strong and medium Lewis acid sites. [15,23,48,50,93,97] In Figure 31a, only a blue shift can be observed for the bands at 3700-3650 cm^{-1} , in the zeolite-binder mix. This is accompanied by the formation of a band at 2200 cm^{-1} . This band is associated with CO on a medium Lewis acid site. The shift of the OH bands to higher wavenumbers can therefore be associated to an interaction of CO with the aluminium center of the Brønsted acid sites. The consumption of the OH vibrations in Figure 31b can thus be explained by the interaction of pyridine with the Lewis acidic origin of the Brønsted acid sites.

In Figure 31d, the binder shows a very low intensity of the bands associated with pyridine on a Lewis acid site (1615, 1453 cm^{-1}). [22,23,50,82,89,93,98] In Figure 31c, the low concentration of Lewis acid sites is

confirmed by the low intensity of the band at 2230 cm^{-1} , which is affiliated to CO on a strong Lewis acid site. [15,23,48,50,93,97] The binder therefore does not appear to contribute to the strong acid sites in the binder-zeolite mix. The residual strong acid sites in the binder-zeolite mix can therefore be ascribed to the contribution of the zeolite. Overall, the decrease in the amount of Lewis acid sites upon mixing suggests that the Lewis acid sites are located on the outer surface of the zeolite and binder. This is confirmed by literature.^[21]

To study the increase in the amount of Brønsted acid sites, $^1\text{H-NMR}$ was employed to detect changes in the concentration of hydroxyl groups, by comparing the chemical shift of the proton in the $^1\text{H-NMR}$ measurement with the IR bands in the OH vibrational region ($4000\text{-}3000\text{ cm}^{-1}$). In Figure 32, the OH vibrational region of the FT-IR spectra (a) is shown with the corresponding $^1\text{H-NMR}$ spectrum (b). The $^1\text{H-NMR}$ spectra are not corrected for the weight of the samples, but equal volume amounts were used. Differences in intensity of similar peaks between the samples can therefore not be assigned to a change in the amount, since differences in sample density result in a changed amount of hydroxyl groups. Differences in peak ratios can however be used to get a better idea about the ratio of different protons within a sample.

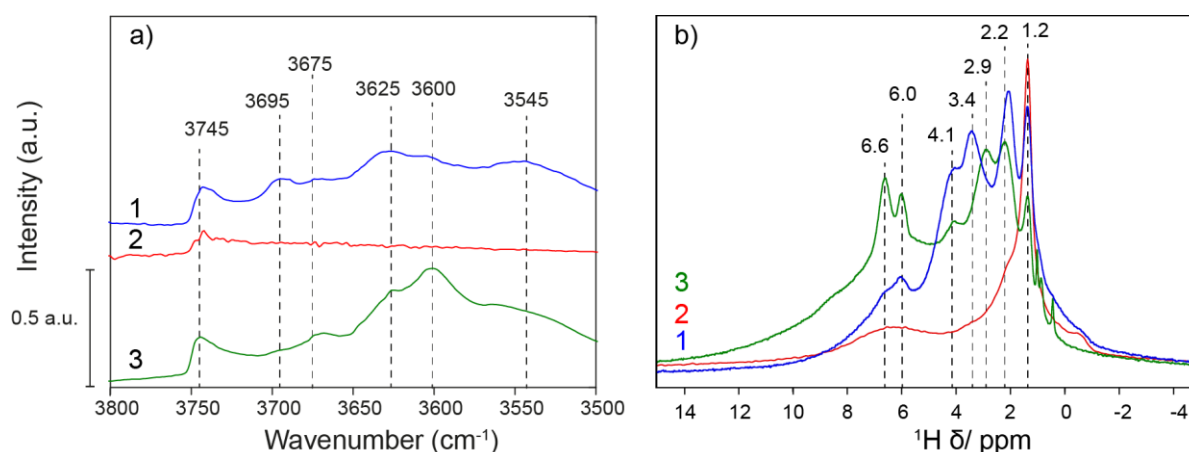


Figure 32 a) FT-IR spectrum of the OH vibrational region under vacuum at $-188\text{ }^\circ\text{C}$ and b) $^1\text{H-NMR}$ spectrum of 1. Binder-zeolite mix 2. Binder* 3. Zeolite * The intensity of the binder in the $^1\text{H-NMR}$ spectrum is divided by 2.

The $^1\text{H-NMR}$ spectrum of the binder-zeolite mix, a shift of the peak at 2.9 ppm to 3.4 ppm can be observed. This is accompanied by a decrease of the peak at 3600 cm^{-1} in the OH vibrational region (Figure 32a), which is associated with the peak at 2.9 ppm in the $^1\text{H-NMR}$ spectrum. This peak is associated with medium Brønsted acid sites, based on the results in chapter 4 and 6. The shift of the peak at 2.9 to 3.4 ppm is ascribed to the peak at 3.6 ppm, which lies underneath the peak at 2.9 ppm, as shown in chapter 4 and chapter 6. The peak at 3.6 ppm is subsequently correlated to the band at 3625 cm^{-1} in the OH vibrational region (Figure 32a) and affiliated with strong Brønsted acid sites in a super cage. Upon comparison of the $^1\text{H-NMR}$ spectrum of the binder-zeolite mix with the zeolite, an increase of the peak at 4.1 ppm with respect to the peak at 3.4 ppm can be observed. The peak at 4.1 ppm is affiliated with strong Brønsted acid sites in sodalite cages.^[96,109] This suggests that upon mixing the concentration of medium and strong Brønsted acid sites does not decrease. This is confirmed by the FT-IR measurements, which showed little to no decrease of the Brønsted acid sites in the binder-zeolite mix. The decrease of the band at 3600 cm^{-1} (Figure 32a) could therefore be affiliated to confinement of the OH groups, which results in a shift towards higher ppm values in the $^1\text{H-NMR}$ spectrum and broadening of the band in the FT-IR spectrum. Moreover, a decreased intensity of the peak at 6 ppm, in the $^1\text{H-NMR}$ spectrum of the zeolite-binder mix confirms the diminishing of the amount of Lewis acid sites.

7.1.2 Structure

Mixing of the zeolite and binder resulted in a decrease of the Lewis acidity and perseverance of the Brønsted acidity. As described in chapter 6, a decrease in the amount of Lewis acidity was accompanied by an increased homogeneity around the aluminium nuclei. This suggested that Extra-Framework aluminium species were stabilized, upon mixing of the individual components, which resulted in a decrease in the Lewis acid strength. To see if this hypothesis is true for the binder-zeolite mix, the aluminium coordination in both the mixed sample as the individual components was studied with ^{27}Al MQ-MAS and ^{27}Al MAS NMR spectroscopy. All the samples were heated to 538 °C for one hour under a nitrogen flow of 100 mL/min, as described in paragraph 3.2.2. The ^{27}Al MAS- and ^{27}Al MQ-MAS NMR spectra are not corrected for the weight of the samples, but equal volume amounts were used. Differences in intensity of similar peaks between the samples can therefore not directly be assigned to a change in the amount, since differences in sample density result in a changed absolute amount of aluminium. Differences in peak ratios can however be used to get a better idea about the ratio of different aluminium coordinations within a sample.

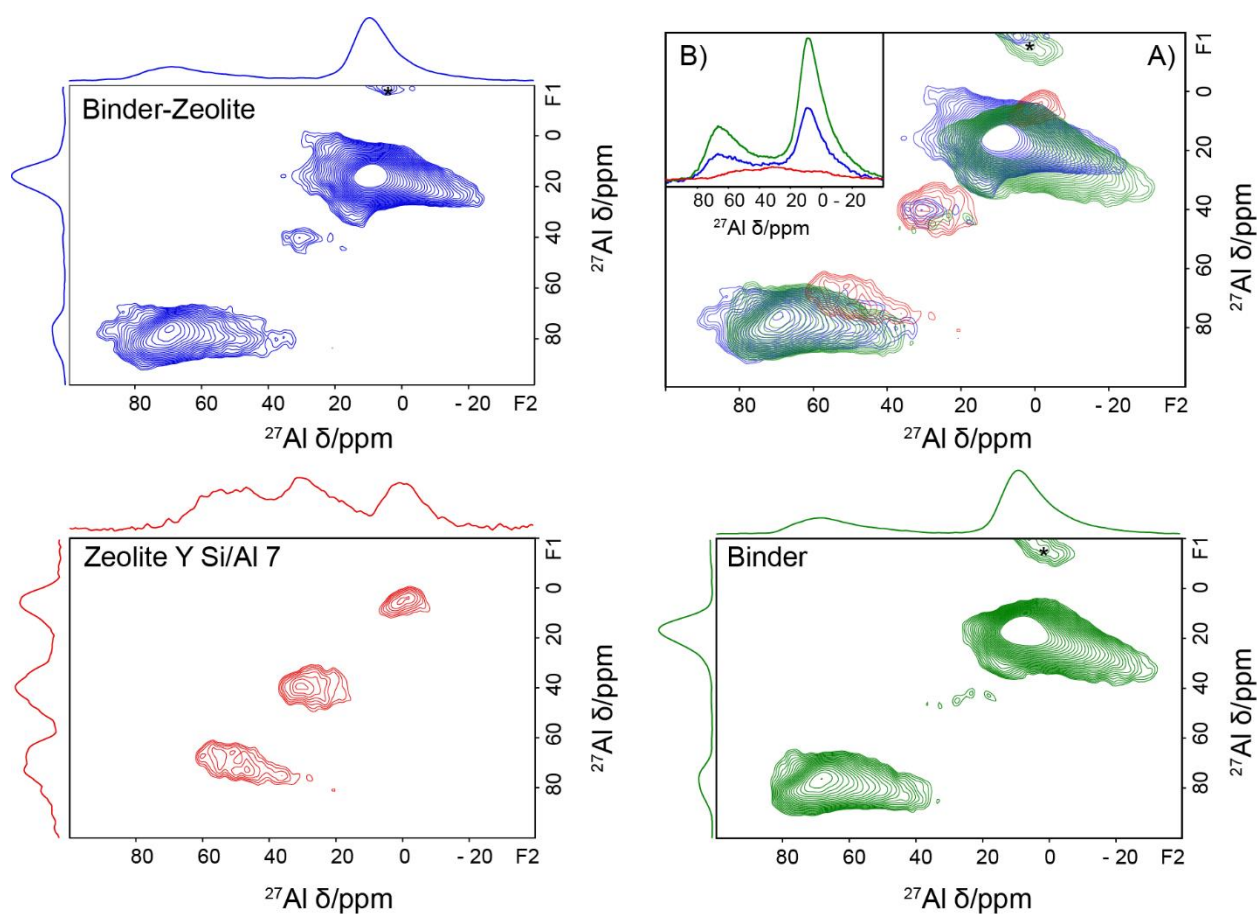


Figure 33 ^{27}Al MQ-MAS of the binder-zeolite mix and individual components with the projections on the F1 and F2 axis. In the top right an overlay of the ^{27}Al MQ-MAS (A) is shown along with an overlay of the ^{27}Al MAS (B) spectrum. Blue: Binder-zeolite, Red: Zeolite HY Si/Al 7, Green: Binder. The *asterisk indicates spinning sidebands and are therefore not considered to be real peaks.

As explained in paragraph 2.4.1, in MQ-MAS NMR spectra, the F1 axis depicts the isotropic chemical shift, where the F2 axis shows the anisotropic chemical shift. The peak position along the F1 axis, therefore, gives information about the coordination of the aluminium nucleus. The peak in the F2 direction is largely affected by the second order quadrupolar coupling. A broadening along the F2 direction thus provides information about the strength of the quadrupolar coupling constant, and

therefore about the symmetry and environment around the aluminium nucleus. [35,41,114,115] As described in paragraph 2.4.1, three regions can be distinguished in the ^{27}Al MQ-MAS NMR spectra: 0-30 ppm, 20-50 ppm and 40-90 ppm, which are ascribed to octahedral, penta- coordinated and tetrahedral aluminium coordinations respectively. [35,41,114,115]

Figure 33 shows the ^{27}Al MQ-MAS and ^{27}Al MAS- NMR spectra of the samples. In the ^{27}Al MAS-NMR spectrum (Figure 33B), the binder-zeolite mix spectrum appears to contain all the different aluminium structures from the zeolite and binder. However, the ^{27}Al MQ-MAS NMR spectrum of the binder-zeolite mix shows large structural changes in both the octahedral (10 ppm) and tetrahedral (70 ppm) region. [43,98,130,131] The peak at 70,70 ppm (F1,F2) in the ^{27}Al MQ-MAS NMR spectrum of the zeolite does not reappear in the aluminium coordination of the binder-zeolite mix. This peak was affiliated with tetrahedral aluminium, which is responsible for the generation of the Brønsted acid sites. [2,8,15-26] In the ^{27}Al MQ-MAS NMR spectrum of the zeolite-binder, a new peak seems to form around 70,80 ppm (F1,F2). The shift in the F1 direction of this new peak is similar to the peak position of the tetrahedral aluminium in the zeolite. This new peak was affiliated with the formation of medium Brønsted acid sites in the binder, in chapter 5. The incorporation of the binder could interfere with the Brønsted acid sites in the zeolite. The shift of the peak to higher ppm values in the F2 direction indicate a more electronegative environment and could be affiliated with a more confined environment of the aluminium. This could confirm the shift of the peak at 3.3 ppm in the ^1H -NMR spectrum (Figure 32b) and the decrease of the band at 3600 cm^{-1} in the OH vibrational region (Figure 32a). Additionally, confinement of the Brønsted acid sites could also explain the decreased interaction of the CO with the aluminium to which the Brønsted acid sites are attached. This is confirmed by the decreased blue shift of the OH vibrations in Figure 32a. Overall, the preservation of the tetrahedral coordination can be correlated to the conservation of most of the Brønsted acid sites.

In the ^{27}Al MQ-MAS NMR spectrum of the binder-zeolite a peak at 35,30 ppm (F1,F2) can be observed. This peak is also visible in the ^{27}Al MQ-MAS NMR spectrum of the binder. In chapter 5, this peak was affiliated with medium Lewis acid sites. The conservation of this peak could therefore be correlated to the residual Lewis acid sites in the binder-zeolite mix. In the penta- coordinated region (40 ppm), a decrease in the broadening along the F2 direction can be observed in the binder-zeolite spectrum, compared to the zeolite. However, in the ^{27}Al MAS-NMR spectrum, the peak affiliated with penta-coordination aluminium has a similar intensity in the binder-zeolite mix compared to the zeolite. This suggests that mixing of the binder and zeolite results in a more homogeneous environment around the penta-coordinated aluminium species but does not result in a large decrease in the concentration. In chapter 4 and 5 this peak was affiliated with strong Lewis acid sites. It can therefore be assumed that the increased homogeneity of the penta- coordinated aluminium coordination could be the origin of the decrease in the amount of the strong Lewis acid sites.

In the ^{27}Al MQ-MAS NMR spectrum of the zeolite-binder mix, the broad peak at 0 to -20 ppm along the F2 direction appears to have shifted to lower ppm values in the F1 direction compared to the binder. The shift to lower ppm values in the F1 direction indicates a less electronegative environment around the aluminium nucleus and could therefore be affiliated with the decrease in the amount of medium Lewis acid sites. Additionally, the peak at 10,0 ppm (F1,F2) in the zeolite ^{27}Al MQ-MAS NMR spectrum appears to have vanished in the spectrum of the binder-zeolite mix. In literature, octahedral and penta-coordinated aluminium species in the zeolite are often ascribed to Lewis acidic EFAl groups. [37,40,42,43,110] The disappearance of this peak in the binder-zeolite mix can therefore be affiliated with the decrease in Lewis acid site concentration.

7.1.3 Summary and Conclusion

In paragraph 7.1.1, it was shown that mixing of the binder and zeolite resulted in a decreased concentration of strong and medium Lewis acid sites. The Lewis acid sites were suggested to be located on the outer surface of the zeolite and binder. The decrease in the amount of Lewis acid sites could subsequently be correlated to an interaction of the Extra-Framework aluminium species on the surface. Additionally, it was shown that the concentration of Brønsted acid sites in the zeolite-binder mix was comparable to the zeolite. This suggested that the combination of binder and zeolite resulted in the formation of additional Brønsted acid sites, which was confirmed by literature.^[28,29,138] The increased concentration of Brønsted acid sites was corroborated by an increase in intensity of the Brønsted peaks in the ¹H-NMR spectrum of the binder-zeolite mix.

In the ²⁷Al MQ-MAS NMR spectrum of the zeolite-binder mix, a decrease in distortion of the peak affiliated with penta-coordinated aluminium species was correlated to the decreased concentration of the strong Lewis acid sites. Moreover, the conservation of the peak at 30,35 ppm (F1,F2) was associated with the residual medium Lewis acid sites in the binder-zeolite mix. It can therefore be concluded that the increase in homogeneity around the penta-coordinated aluminium nuclei results in a decrease in the amount of strong Lewis acid sites. It is therefore postulated that the Lewis acid sites originate from penta-coordinated EFAl groups, located on the outer surface of the binder and zeolite. The shift of the peaks affiliated with octahedrally coordinated aluminium to lower ppm values is subsequently correlated to the decrease in the amount of medium Lewis acid sites.

In the ²⁷Al MQ-MAS NMR spectrum of the binder-zeolite mix, the tetrahedral aluminium coordination of the zeolite appeared to be vanished in the binder-zeolite mix. However, a slight elongation in the F2 direction towards higher ppm values was observed in the zeolite-binder mix, which was associated with more confined aluminium species. The same peak was affiliated with medium Brønsted acid sites in chapter 5. This confirms the conservation of Brønsted acid sites, based on the preservation of this aluminium coordination. It can therefore be concluded that the Brønsted acid sites in the binder-zeolite mix are more confined, compared to the Brønsted acid sites in the zeolite. Additionally, it can be concluded that the increased concentration of medium Brønsted acid sites is affiliated with an increase of the tetrahedral coordination at 80,90 ppm (F1,F2). Therefore, it can be concluded that mixing of the binder-zeolite resulted in more confined Brønsted acid sites.

To conclude: mixing of the binder and zeolite results in an increased concentration of Brønsted acid sites. Additionally, mixing of the binder and zeolite results in a decrease in the amount of Lewis acid sites. The Lewis acid sites originate from Extra-Framework aluminium species, which are located on the surface of the binder and zeolite.

7.2 Binder-Clay

As described in chapter 6, the incorporation of clay resulted in a decrease of the overall acidity in the FCC catalyst. Therefore, a mix of binder with clay was studied.

The acidity was determined with CO and pyridine based infrared (FT-IR) spectroscopy. Additionally, magic angle- nuclear magnetic resonance (MAS-NMR) spectroscopy was used, to study the environment around the aluminium nuclei in a 1D-, and 2D multiple quantum- MAS NMR experiment. (^{27}Al MAS-NMR and ^{27}Al MQ-MAS NMR). Furthermore, proton MAS-NMR (^1H MAS-NMR) was used to study the different protons in the samples.

7.2.1 Acidity

For the FT-IR measurements, the samples were heated to 550 °C for one hour under high vacuum and cooled down, while kept under vacuum, as described in paragraph 3.2.1. All spectra were corrected for the weight of the wafer.

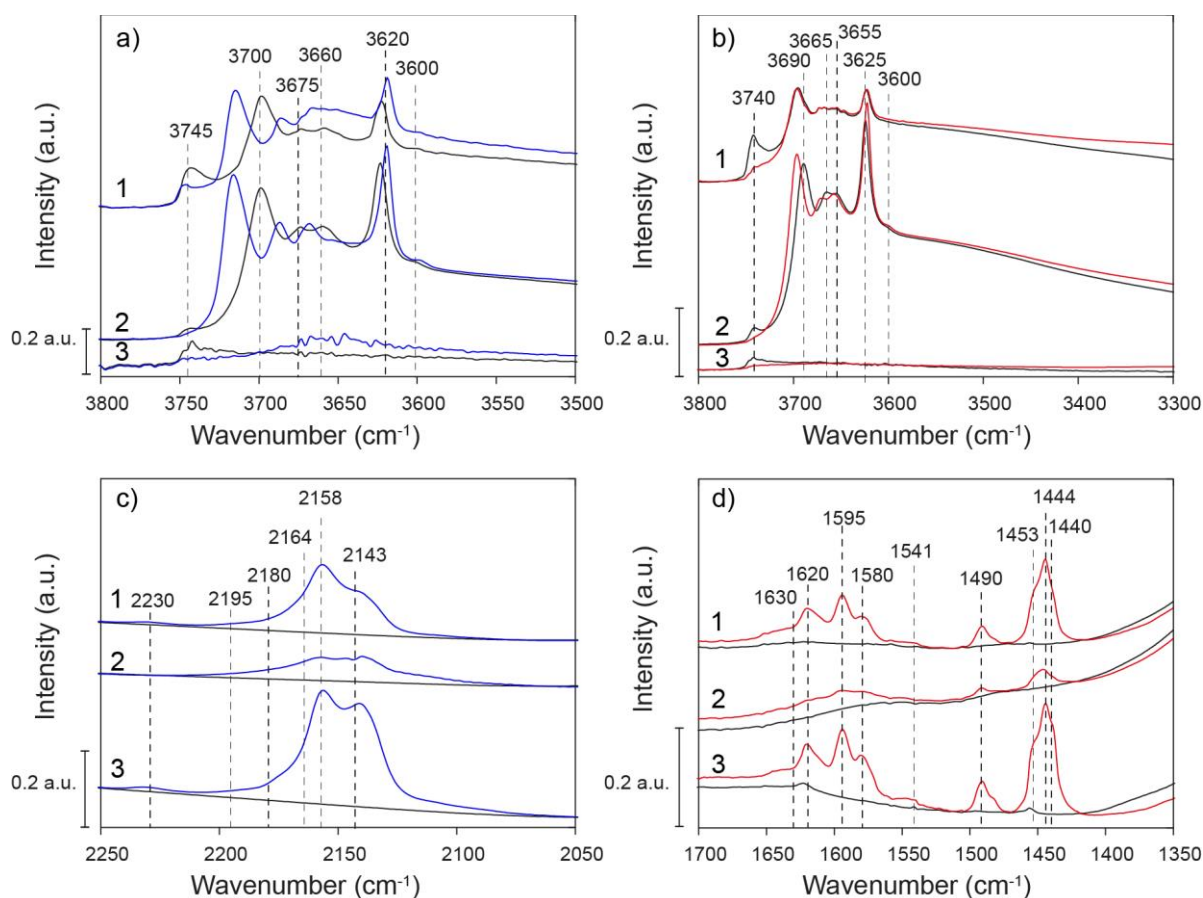


Figure 34 FT-IR spectra of 1. Binder-clay 2. Clay 3. Binder. a)- c) OH vibrational region and CO vibrational region before (black) and after maximal loading with CO(blue) b- d) OH vibrational region and pyridine vibrational region before (black) and after exposed to pyridine vapour for 30 min. (red)

In Figure 34, the FT-IR spectra of the binder-clay mix, clay, and binder is depicted. As described in paragraph 2.4.2, the band positions of the CO stretching vibration and the pyridine ring vibrations are characteristic for the acid type and acid strength, to which the CO or pyridine is attached. [8,16,36,48,82,83,86] Since the spectra are corrected for the weight of the wafer, the intensity of the bands can be compared, which gives information about the amount of the different acid sites in the samples. The FT-IR measurements in Figure 34a and 34c are performed at -188 °C. This results in very defined bands in the

OH vibrational region, which are slight blue shifted, compared to the OH vibrations in Figure 34b, which are taken at room-temperature.^[16,48]

In the CO vibrational region (Figure 34c) of the binder-clay mix, a decreased intensity of bands affiliated with CO on non-acidic hydroxyl groups (2158 cm^{-1}) and liquid like CO (2143 cm^{-1}) can be observed compared to the binder.^[23,36,82] This is confirmed in the pyridine ring vibrational region (Figure 34d) where a decreased intensity of the bands affiliated with physisorbed pyridine (1580 and 1440 cm^{-1}) and pyridine hydrogen bonded to non-acidic hydroxyl groups (1595 and 1444 cm^{-1}) can be observed in the binder-clay mix compared to the binder.^[23,36,50,82,89,103] The decrease of the bands affiliated with physisorbed pyridine and CO could indicate a decrease of the surface area. The intensity of the band at 3745 cm^{-1} (Figure 34a) appears to have an increased intensity in the binder-clay mix compared to the binder and clay. This band is affiliated with non-acidic silanol groups.^[21,36,58,91] This could indicate that mixing of the clay and binder results in a decreased accessibility of the hydroxyl groups.

In the CO vibrational region (Figure 34c), a decreased intensity of the bands affiliated with CO on a Lewis acid site (2230 - 2195 cm^{-1}) and CO on a Brønsted acid site (2195 - 2164 cm^{-1}) can be observed in the binder-clay mix compared to the binder.^[15,23,36,48,50,82,83,86,93,97] This is confirmed by the pyridine measurements in Figure 34d: A decreased intensity of the bands affiliated with pyridine on a Lewis acid site (1620 and 1453 cm^{-1}) and pyridine on a Brønsted acid site (1630 and 1541 cm^{-1}) can be observed.^[22,23,50,82,83,86,89,93,98] The decreased intensity indicates a decreased concentration of the acid sites. This can be ascribed to the mixing with the clay, which contains almost no acid sites. Unlike the binder-zeolite samples, the band affiliated with CO on strong Lewis acid sites (2230 cm^{-1}) is still present upon mixing of the binder and clay.^[15,23,48,50,93,97] This suggests that the clay does not interact with the Lewis acid sites.

To study the origin of the strong Lewis acid sites in the binder-clay mix, the strongest acid sites were studied. Figure 35 depicts the FT-IR spectra of the samples after minimal CO loading and remaining pyridine at 550 °C . The first CO loading is experimentally to give rise to bands which are associated with the strongest acid sites in the samples. The FT-IR spectra in Figure 35d show the residual pyridine which is still attached to acid sites after heating the sample to 550 °C and are therefore associated with the strongest acid sites.

In Figure 35a and 35d, a decreased intensity of the bands affiliated with CO on a strong Lewis acid site (2230 cm^{-1}) and pyridine on a Lewis acid site (1615 and 1453 cm^{-1}) can be observed.^[22,23,50,82,89,93,98] In Figure 35a, a blue shift of all the characteristic OH bands of the clay can be observed in the FT-IR spectrum of the binder-clay mix. As shown in chapter 6, the blue shift of the characteristic clay vibrations is not affiliated with Lewis acid sites. It can therefore be assumed that the Lewis acid sites originate from the binder. The decrease of the blue shift corroborates the idea that the OH surface groups in the clay are hindered, due to the mixing with the binder. In Figure 35b, a decrease of all the OH vibrations between 3720 - 3600 cm^{-1} can be observed in the FT-IR spectrum of the binder-clay mix. No shift of the OH bands is observed in the binder-clay FT-IR spectrum (Figure 35b). This confirms that the OH groups are confined due to the mixing of the binder and clay. Both in Figure 35a and 35b, the OH bands show little to no decrease in intensity upon interaction of CO or pyridine with a Lewis acid site. This shows that the origin of the strong Lewis acid sites in the binder and binder-clay mix could originate from a direct interaction with aluminium species, as was postulated in chapter 5.^[58,89,93,116,139]

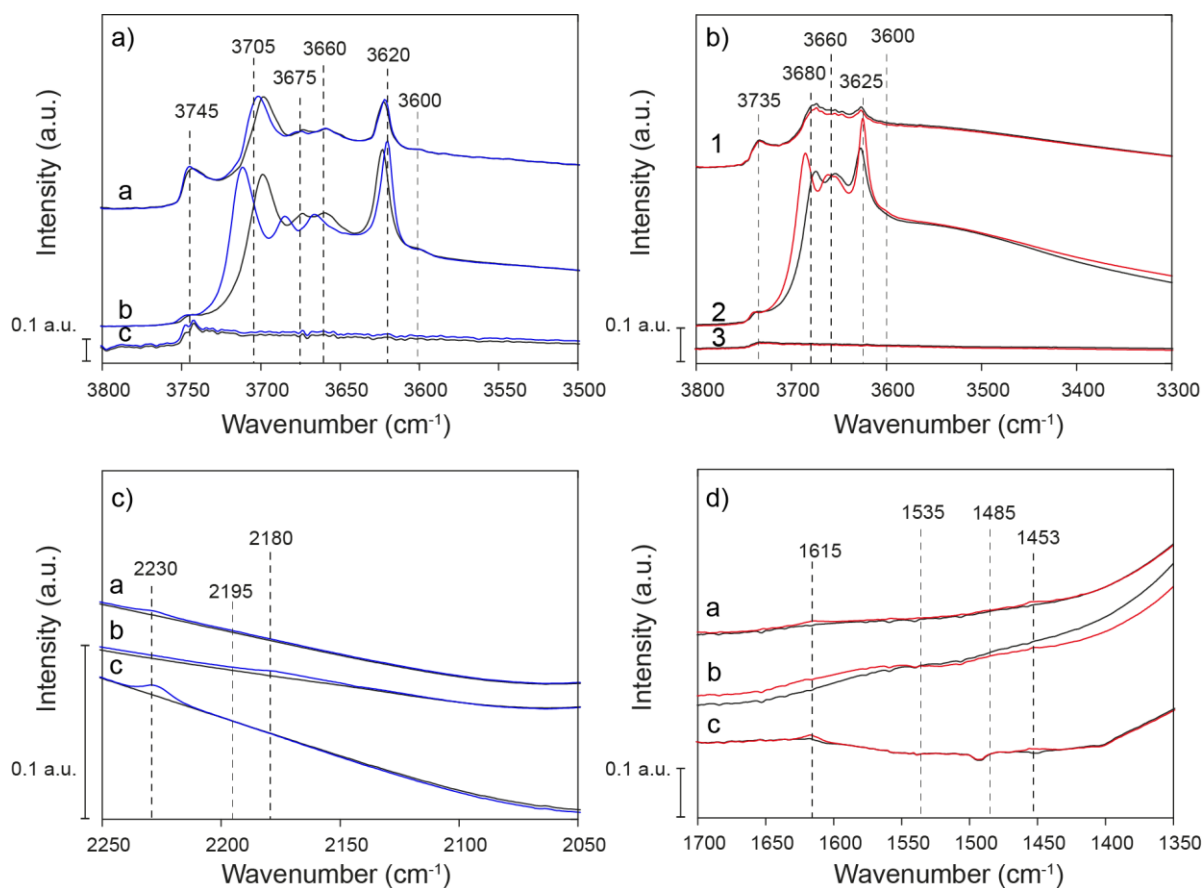


Figure 35 FT-IR spectra of 1. Binder-clay mix 2. Clay 3. Binder. a)- c) OH vibrational region and CO vibrational region before (black) and after minimal loading with CO(blue). b- d) OH vibrational region and pyridine vibrational region under vacuum at 550 550 °C (black) and after being exposed to pyridine vapour for 30 min. and heated to 550 °C (red) as described in paragraph 3.2.1.

To confirm that a decreased acidity is due to hindering of the surface hydroxyl groups, $^1\text{H-NMR}$ was employed to detect the change in surface hydroxyl groups upon mixing of the binder with clay. In Figure 36, the OH vibrational region of the FT-IR spectra (a) is shown with the corresponding $^1\text{H-NMR}$ spectrum (b). The $^1\text{H-NMR}$ spectra are not corrected for the weight of the samples, but equal volume amounts were used. Differences in intensity of similar peaks between the samples can therefore not be assigned to a change in the amount, since differences in sample density result in a changed amount of hydroxyl groups. Differences in peak ratios can however be used to get a better idea about the ratio of different protons within a sample.

The intensity of the peaks in the $^1\text{H-NMR}$ spectrum of the binder-clay mix is comparable to the peaks in the binder. This shows that mixing of binder and clay does not result in a large decrease in the amount of surface hydroxyl groups. The FT-IR measurements showed however that mixing of the binder and clay resulted in a decreased amount of hydrogen bonded pyridine and CO. Therefore, it can be assumed that mixing of the binder and clay results in blockage of the pores, which makes the hydroxyl groups no longer accessible. The A large increase of the peak at 6.1 ppm can be observed in the $^1\text{H-NMR}$ spectrum of the binder-clay mix. This peak is affiliated with water on a Lewis acid site. ^[43,106,112] Based on the FT-IR measurements, it was concluded that mixing of binder and clay resulted in a decreased amount of the Lewis acidity. The increase of the peak at 6.1 ppm could therefore partially originate from water confined in micropores. This confirms the assumption that mixing clay and binder results in a decreased accessibility, due to blockage of the pores.

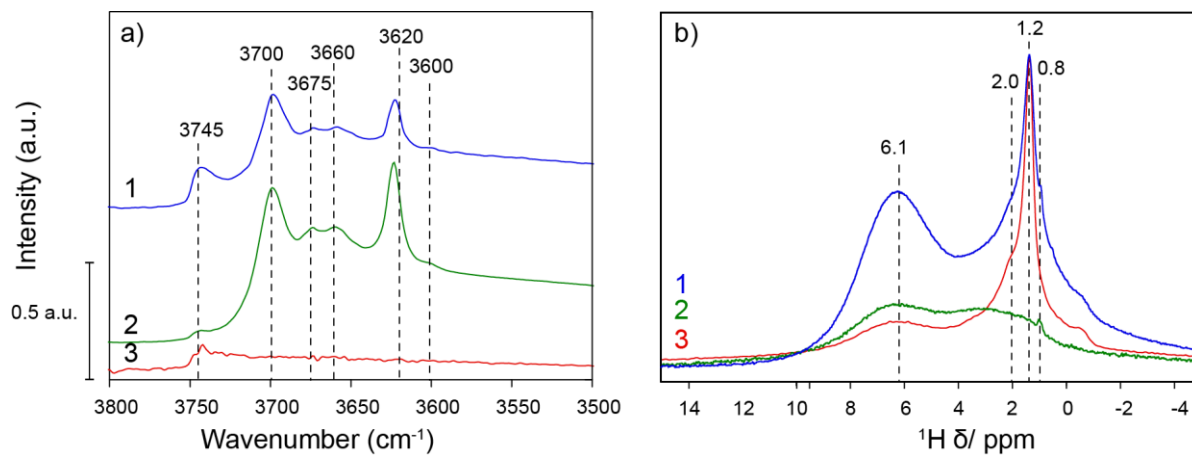


Figure 36 a) FT-IR spectrum of the OH vibrational region under vacuum at -188 °C and b) ¹H-NMR spectrum of 1. Binder-clay mix 2. Clay 3. Binder* * The intensity of the binder in the ¹H-NMR spectrum is divided by 2.

7.2.2 Structure

Mixing of the binder and clay resulted in a decreased concentration of the acid sites. This was partially ascribed to blocking of the pores, due to the incorporation of clay. To see if this hypothesis is true, the aluminium coordination in both the mixed sample and the individual components was studied with ^{27}Al MQ-MAS and ^{27}Al MAS NMR spectroscopy. All the samples were heated to 538 °C for one hour under a nitrogen flow of 100 mL/min, as described in paragraph 3.2.2. The ^{27}Al MAS- and ^{27}Al MQ-MAS NMR spectra are not corrected for the weight of the samples, but equal volume amounts were used. Differences in intensity of similar peaks between the samples can therefore not directly be assigned to a change in the amount, since differences in sample density result in a changed absolute amount of aluminium. Differences in peak ratios can however be used to get a better idea about the ratio of different aluminium coordinations within a sample.

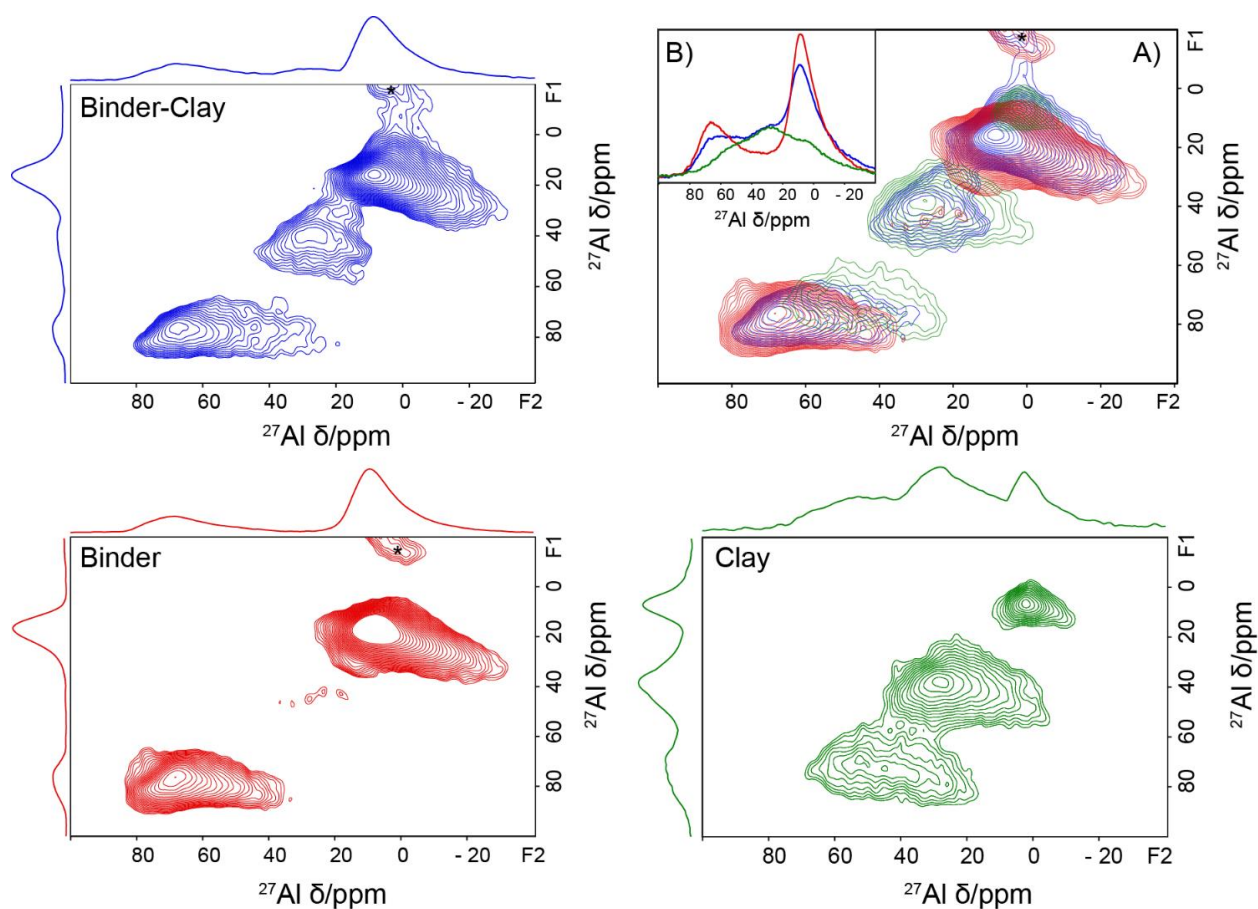


Figure 37 ^{27}Al MQ-MAS of the binder-clay mix and individual components with the projections on the F1 and F2 axis. In the top right an overlay of the ^{27}Al MQ-MAS is shown along with an overlay of the ^{27}Al MAS spectrum. **Blue: Binder-clay, Red: Binder, Green: Clay.** The *asterisk indicates spinning side-bands and are therefore not considered to be real peaks.

As explained in paragraph 2.4.1, in MQ-MAS NMR spectra, the F1 axis depicts the isotropic chemical shift, where the F2 axis shows the anisotropic chemical shift. The peak position along the F1 axis therefore gives information about the coordination of the aluminium nucleus. The peak in the F2 direction is largely affected by the second order quadrupolar coupling. A broadening along the F2 direction thus provides information about the strength of the quadrupolar coupling constant, and therefore about the symmetry and environment around the aluminium nucleus. [35,41,114,115] As described

in paragraph 2.4.1, three regions can be distinguished in the ^{27}Al MQ-MAS NMR spectra: 0-30 ppm, 20-50 ppm and 40-90 ppm, which are ascribed to octahedral, penta- coordinated and tetrahedral aluminium coordinations respectively.^[35,41,114,115]

In the ^{27}Al MAS-NMR spectrum (Figure 37B), a relative high intensity of the peak affiliated with penta-coordinate aluminium (30 ppm) can be observed in the binder-clay mix. This is confirmed by the intense peak at 40,30 ppm (F1,F2) in the ^{27}Al MQ-MAS NMR spectrum of the binder-clay mix. This peak is affiliated with strong Lewis acid sites, in chapter 4 and 5. The presence of this aluminium coordinations therefore suggests that it is no longer accessible upon mixing with the clay. Furthermore, an additional peak at 30,20 ppm in the F1, F2 direction is formed in the binder-clay mix. This peak is also present in the binder. Penta- coordinated and octahedrally coordinated aluminium species are almost always attributed to Lewis acidic EF aluminium species.^[15,53,116,126,131,140] This shows that the amount of Lewis acid sites is possibly conserved in the binder-clay mix. The relatively high intensity of this peak confirms that the incorporation of clay does not result in the removal of Lewis acid sites but reduces the accessibility.

The tetrahedral peak at 70,75 ppm in the ^{27}Al MQ-MAS NMR spectrum of the binder, appears to be vanished in the binder-clay mix. However, a slight tailing can be observed at 75,70 ppm (F1,F2) in the ^{27}Al MQ-MAS NMR spectrum of the binder-clay mix. This peak was attributed to medium Brønsted acid sites in chapter 5. The decreased intensity of this peak can therefore be correlated to the decrease in the amount of Brønsted acid sites. Additionally, the broadening along the F2 direction of the tetrahedral aluminium coordination in the clay (75,50 ppm in the F1,F2 direction) is largely diminished in the clay-binder mix. This could be affiliated with the stabilizing interaction between the binder and clay.

7.2.3 Summary and Conclusion

As described in paragraph 7.2.1, mixing of binder with clay resulted in an overall decreased concentration of acid sites. This was partially ascribed to a diluted concentration of acid sites, due to the incorporation of the clay. Additionally, it was postulated that mixing of the binder and clay resulted in blocking of the pores. Furthermore, a large increase in intensity of the peak at 6 ppm in the $^1\text{H-NMR}$ measurements showed that the mixing of binder and clay results in confinement of water in the pores.

In the ^{27}Al MAS-NMR spectrum of the binder-clay mix, a high intensity of the peak affiliated with penta-coordinated aluminium, was observed. This was linked to the preservation of the strong Lewis acid sites. The decreased amount of strong Lewis acid sites in the FT-IR measurements supported the suggestion that the incorporation of clay results in a decreased accessibility of the acid sites. A decreased intensity of the tetrahedral peak in the ^{27}Al MAS-NMR spectrum could be observed in the binder-clay mix, which was affiliated to the mixing of the two components. The decrease of the tetrahedral aluminium species was associated with a decrease in the amount of Brønsted acid sites.

Overall it can be concluded that mixing of the binder and clay results in blocking of the pores. Additionally, the mixing binder and clay results in a decrease in the amount of Brønsted acid sites. Furthermore, the incorporation of clay results in an increase in the amount of water, which is confined in the pores.

7.3 FCC versus mixed components

In paragraph 7.1 it was concluded that mixing of the zeolite and binder resulted in a decrease of the Lewis acidity but preservation of the Brønsted acid sites. In paragraph 7.2 it was concluded that the incorporation of clay resulted in blocking of the pores and a decrease in the amount of Brønsted acid sites. To confirm these conclusions, the mixed components were compared to the acidity and structure of the FCC catalyst.

The acidity was determined with CO and pyridine based infrared (FT-IR) spectroscopy. Additionally, magic angle- nuclear magnetic resonance (MAS-NMR) spectroscopy was used, to study the environment around the aluminium nuclei in a 1D-, and 2D multiple quantum- MAS NMR experiment. (^{27}Al MAS-NMR and ^{27}Al MQ-MAS NMR). Furthermore, proton MAS-NMR (^1H MAS-NMR) was used to study the different protons in the samples.

7.3.1 Acidity

For the FT-IR measurements, the samples were heated to 550 °C for one hour under high vacuum and cooled down, while kept under vacuum, as described in paragraph 3.2.1. All spectra were corrected for the weight of the wafer.

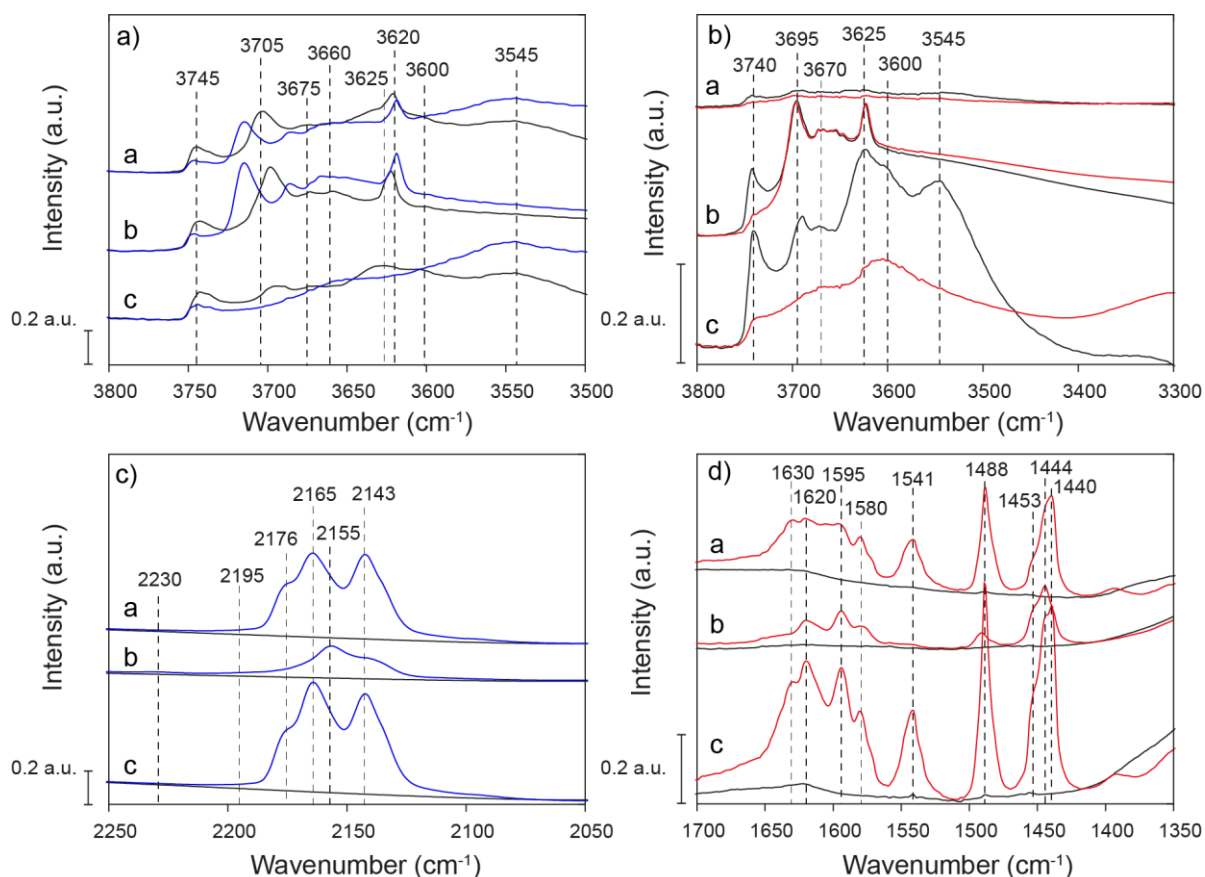


Figure 38 FT-IR spectra of 1. FCC catalyst 2. Binder-clay mix 3. Binder-zeolite mix*. a)- c) OH vibrational region and CO vibrational region before (black) and after maximal loading with CO(blue) b- d) OH vibrational region and pyridine vibrational region before (black) and after exposed to pyridine vapour for 30 min. (red)* The intensity of the Binder-zeolite mix in the pyridine spectra are divided by 2, since the intensity was too high.

In Figure 38, the FT-IR spectra of the FCC, binder-clay mix, and binder-zeolite mix are shown. As described in paragraph 2.4.2, the band positions of the CO stretching vibration and the pyridine ring vibrations are characteristic for the acid type and acid strength, to which the CO or pyridine is attached.

[8,16,36,48,82,83,86] Since the spectra are corrected for the weight of the wafer, the intensity of the bands can be compared, which gives information about the amount of the different acid sites in the samples. The FT-IR measurements in Figure 38a and 38c are performed at -188 °C. This results in very defined bands in the OH vibrational region, which are slight blue shifted, compared to the OH vibrations in Figure 38b, which are taken at room-temperature.^[16,48]

In Figure 38c, the overall intensity of the bands in the FT-IR spectrum of the FCC is comparable to the binder-zeolite mix. The intensity of the bands at 2176 and 2165 cm^{-1} is decreased in the FCC, compared to the bands in the FT-IR spectrum of the zeolite-binder mix. These bands are affiliated with CO on a strong and medium Brønsted acid site.^[15,36,82,91,93,98] In the pyridine ring vibrational region (Figure 38d), a decreased intensity of all the bands can be observed in the FT-IR spectrum of the FCC, compared to the zeolite-binder mix. This confirms that the incorporation of clay results in a decrease of the amount of Brønsted acid sites.

Additionally, a decreased intensity of the bands at 1620 cm^{-1} and 1453 cm^{-1} can be observed, in the FT-IR spectrum of the FCC catalyst. These bands are associated with pyridine on a Lewis acid site.^[36,82,91] This indicates that the amount of Lewis acid sites decreases due to the mixing of all the components.

To study the decrease of the strong acid sites upon mixing of all the components in the FCC, the strongest acid sites were studied. Figure 39 depicts the FT-IR spectra of the samples after minimal CO loading and remaining pyridine at 550 °C. The first CO loading is experimentally to give rise to bands which are associated with the strongest acid sites in the samples. The FT-IR spectra in Figure 39d show the residual pyridine which is still attached to acid sites after heating the sample to 550 °C and are therefore associated with the strongest acid sites.

In the CO vibrational region (Figure 39c), a decreased intensity of the bands affiliated with CO on a medium Lewis acid site (2195 cm^{-1}) can be observed in the FT-IR spectrum of the FCC catalyst compared to the binder-zeolite mix.^[15,23,48,50,93,97] This is confirmed by the decreased intensity of the bands at 1615 and 1453 cm^{-1} (Figure 39d), which are attributed to pyridine on a Lewis acid site.^[22,23,50,82,89,93,98] Moreover, a decreased intensity of the band at 1535 cm^{-1} can be observed in the FCC catalyst, compared to the binder-zeolite mix. This band is associated with pyridine on a Brønsted acid site.^[15,36,82,91,93,98] The decrease in the amount of Brønsted acid sites could be affiliated with the incorporation of clay. In Figure 39c, the intensity of the band at 2230 cm^{-1} appears to be comparable in the FCC catalyst, compared to the binder-clay mix. This band is associated with CO on a strong Lewis acid site.^[15,23,48,50,93,97] This suggests that mixing with clay does not result in a significant decrease in the amount of strong Lewis acid sites.

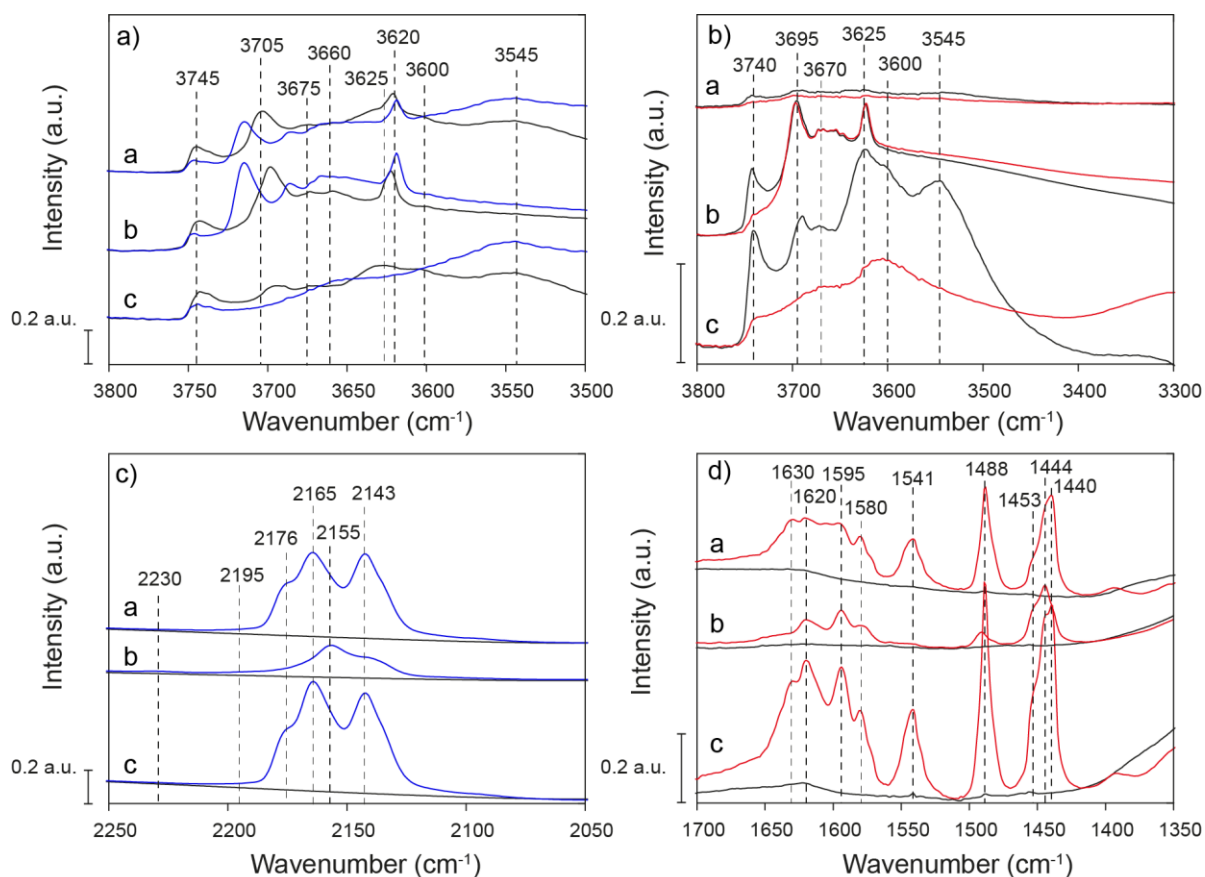


Figure 39 FT-IR spectra of 1. FCC catalyst 2. Binder-clay mix 3. Binder-zeolite mix*. a)- c) OH vibrational region and CO vibrational region before (black) and after minimal loading with CO (blue). b- d) OH vibrational region and pyridine vibrational region under vacuum at 550 °C (black) and after being exposed to pyridine vapour for 30 min. and heated to 550 °C (red) as described in paragraph 3.2.1. * The intensity of the Binder-zeolite mix in the pyridine spectra are divided by 2, since the intensity was very high.

To test whether the decrease in Brønsted acidity is due to interaction of all the components, or due to blockage of the pores, $^1\text{H-NMR}$ spectroscopy was employed, to detect changes in the concentration of the surface hydroxyl groups. In Figure 40 the OH vibrational region of the FT-IR spectra (a) is shown with the corresponding $^1\text{H-NMR}$ spectrum (b). The $^1\text{H-NMR}$ spectra are not corrected for the weight of the samples, but equal volume amounts were used. Differences in intensity of similar peaks between the samples can therefore not be assigned to a change in the amount, since differences in sample density result in a changed amount of hydroxyl groups. Differences in peak ratios can however be used to get a better idea about the ratio of different protons within a sample.

In the $^1\text{H-NMR}$ spectrum of the FCC, a shift of the peak at 3.4 to 2.9 ppm can be observed, compared to the spectrum of the binder-zeolite mix. The peak at 2.9 ppm is associated with the OH band at 3600 cm^{-1} (Figure 40a) and associated with medium Brønsted acid sites. The peak at 3.4 ppm is associated with the OH band at 3625 cm^{-1} in the FT-IR spectrum (Figure 40a) and associated with strong Brønsted acid sites in the super cage.^[96,109] The shift of the peak from 3.4 to 2.9 ppm can thus be associated with the slight decreased intensity of the band at 3625 cm^{-1} in the FT-IR spectrum of the FCC, compared to the FT-IR spectrum of the binder-zeolite mix. When the ratio of the peaks at 4.1 and 2.9 ppm in the FCC $^1\text{H-NMR}$ spectrum are compared to the ratio of the peaks at 4.1 and 3.4 ppm in the zeolite $^1\text{H-NMR}$ spectrum, the peak at 4.1 ppm appears to decrease less. The peak at 4.1 ppm is ascribed to Brønsted acid sites in a sodalite cage. This was also observed in paragraph 7.1 and ascribed to the accessibility of the

Brønsted acid site. The relative decreased intensity of the peak at 2.9 ppm in the FCC suggests that the incorporation of clay results in a decrease of the Brønsted acid sites in the super cage.

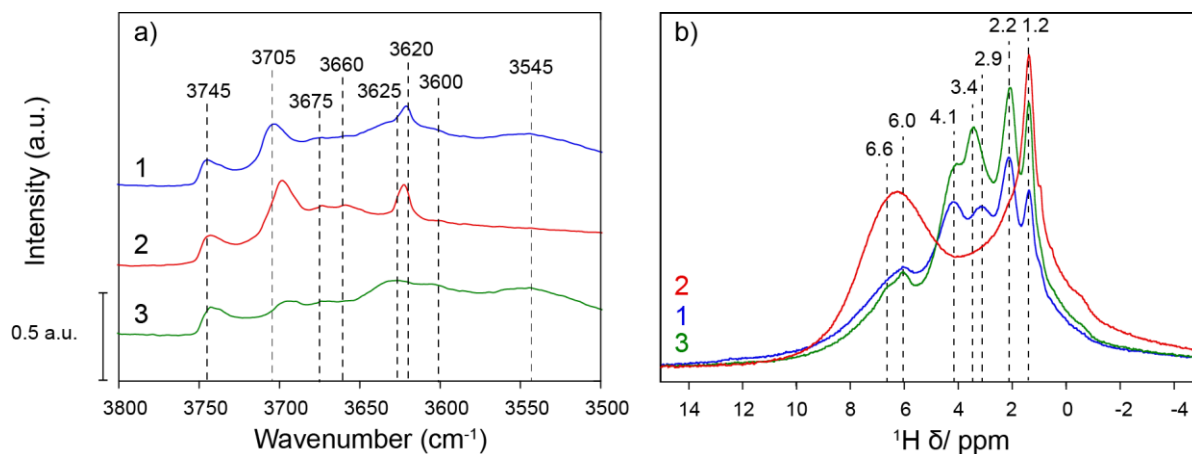


Figure 40 a) FT-IR spectrum of the OH vibrational region under vacuum at -188 °C and b) ¹H-NMR spectrum of 1. FCC catalyst 2. Binder-clay mix 3. Binder-zeolite mix

In the ¹H-NMR spectrum of the FCC the intensity of the peak at 6 ppm appears to be increased compared to the zeolite-binder mix. This peak is associated with water on a Lewis acid site.^[40,41,71,112,114] However, based on the FT-IR measurements, the FCC contained less Lewis acid sites compared to the binder-zeolite mix. The increase can therefore be associated with an increase in the amount of water confined in the pores, which is caused by the incorporation of clay.

7.3.2 Structure

The samples were measured with ^{27}Al MQ-MAS and ^{27}Al MAS NMR spectroscopy, to study the structural changes upon mixing of all the components. All the samples were heat treated as described in paragraph 3.2.2, for one hour at 538 °C under nitrogen. All the samples were heated to 538 °C for one hour under a nitrogen flow of 100 mL/min, as described in paragraph 3.2.2. The ^{27}Al MAS- and ^{27}Al MQ-MAS NMR spectra are not corrected for the weight of the samples, but equal volume amounts were used. Differences in intensity of similar peaks between the samples can therefore not directly be assigned to a change in the amount, since differences in sample density result in a changed absolute amount of aluminium. Differences in peak ratios can however be used to get a better idea about the ratio of different aluminium coordinations within a sample.

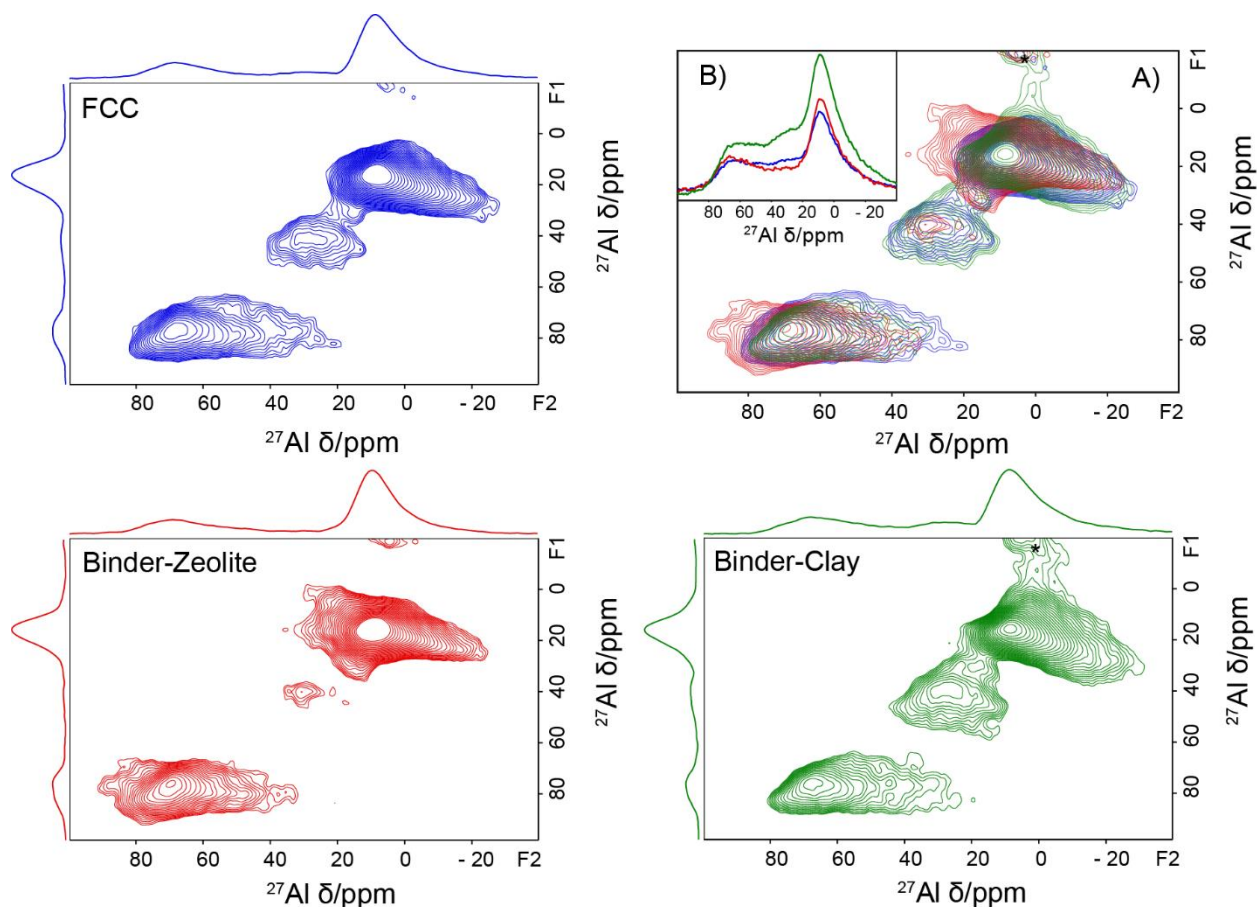


Figure 41 ^{27}Al MQ-MAS of the FCC and mixed components with the projections on the F1 and F2 axis. In the top right an overlay of the ^{27}Al MQ-MAS (A) is shown along with an overlay of the ^{27}Al MAS spectrum (B). Blue: FCC catalyst, Red: Binder-zeolite, Green: Binder-clay. The *asterisk indicates spinning side-bands and are therefore not considered to be real peaks.

As explained in paragraph 2.4.1, in MQ-MAS NMR spectra, the F1 axis depicts the isotropic chemical shift, where the F2 axis shows the anisotropic chemical shift. The peak position along the F1 axis therefore gives information about the coordination of the aluminium nucleus. The peak in the F2 direction is largely affected by the second order quadrupolar coupling. A broadening along the F2 direction thus provides information about the strength of the quadrupolar coupling constant, and therefore about the symmetry and environment around the aluminium nucleus. [35,41,114,115] As described in paragraph 2.4.1, three regions can be distinguished in the ^{27}Al MQ-MAS NMR spectra: 0-30 ppm, 20-50 ppm and 40-90 ppm, which are ascribed to octahedral, penta- coordinated and tetrahedral aluminium coordinations respectively. [35,41,114,115]

In the ^{27}Al MAS NMR spectrum (Figure 41B), the intensity of the peaks in the FCC appear to be most comparable to the zeolite-binder mix. However, in the ^{27}Al MQ-MAS NMR spectrum, the peaks in the FCC appear to be most similar to the peaks in the binder-clay mix.

In the ^{27}Al MQ-MAS NMR spectrum of the FCC, a shift towards lower ppm values in the F2 direction can be observed for the peak affiliated with tetrahedrally coordinated aluminium (70ppm). In chapter 6, it was shown that this shift matched the tetrahedral aluminium coordination of the zeolite. The peak at 75,80 was associated with medium Brønsted acid sites in the binder, as shown in chapter 5. In paragraph 7.1 the shift of the tetrahedral peak to 75,80 (F1,F2) was associated with an increase in the amount of medium Brønsted acid sites. The decrease of the peak at 75,80 ppm (F1, F2) in the FCC can therefore be affiliated to the decrease in the amount of medium Brønsted acid sites.

Additionally, the peak affiliated with penta-coordinated aluminium (40 ppm) in the ^{27}Al MQ-MAS NMR spectrum of the FCC catalyst appears to be almost identical to the binder-clay mix. This confirms the preservation of the strong Lewis acid sites in the FCC catalyst. The peak at 35,20 ppm (F1, F2) in the FCC appears to have a decreased intensity, compared to the binder-clay mix and the binder-zeolite mix. In chapter 5 and 7, this peak was associated with medium Lewis acid sites. The decreased of this coordination can subsequently be correlated to the decreased amount of Lewis acid sites.

In Figure 41A, the peak associated with octahedrally coordinated aluminium (10 ppm) appears to be more symmetrical in the FCC catalyst compared to the mixes. The decrease in distortion of this coordination could originate from the mixing of the different components, which result in stabilization of the aluminium species. The decrease in heterogeneity can subsequently be associated with a decrease in the amount of medium Lewis acid sites.

7.3.3 Summary and Conclusion

In paragraph 7.3.1 a decrease of the medium Lewis acid sites and both strong and medium Brønsted acid sites was observed upon mixing of all the components. Additionally, a decrease of the Brønsted acid sites in the super cage of the zeolite was observed upon mixing. The Brønsted acid sites in the sodalite cages were little affected by the mixing of the components. This was affiliated with the accessibility of these Brønsted acid sites, since the sodalite cage is the smallest cage in the zeolite. ^[66] Furthermore, the incorporation of clay resulted in an increased amount of water confined in the pores. This suggested that the incorporation of clay blocks the pores.

In the ²⁷Al MQ-MAS NMR spectrum of the FCC, a decreased intensity and a shift of the tetrahedral peak to lower ppm values along the F2 axis was associated with the decrease in the amount of medium Brønsted acid sites. In the ²⁷Al MQ-MAS NMR spectrum of the FCC a high amount of penta-coordinated aluminium species could be observed. This indicates the conservation of the Lewis acid sites. The decrease in the amount of Lewis acid sites based on the FT-IR measurements can therefore be ascribed to blocking of the acid sites by the incorporation of clay.

Overall, it can be concluded that the addition of the clay reduces the Brønsted acidity. This is associated with a decrease in the amount of tetrahedral aluminium species. The Brønsted acid sites in the sodalite cages are little affected by the mixing, due to the confinement of the sodalite cage. Additionally, the incorporation of clay results in blocking of the pores.

Chapter 8. The Effect of Heating

All the samples described in the previous chapters were subjected to a heat treatment, to mimic the conditions of the FCC reactor.^[2] The amount of time a FCC catalyst is subjected to the heat-treatment result in differences in acid strength and structure.^[1,2,7,37,38,141,142] Therefore, the change in acidity and aluminium structure upon heating of the FCC was studied.

The acidity was determined with CO and pyridine based infrared (FT-IR) spectroscopy. Additionally, magic angle- nuclear magnetic resonance (MAS-NMR) spectroscopy was used, to study the environment around the aluminium nuclei in a 1D-, and 2D multiple quantum- MAS NMR experiment. (²⁷Al MAS-NMR and ²⁷Al MQ-MAS NMR). Furthermore, proton MAS-NMR (¹H MAS-NMR) was used to study the different protons in the samples.

8.1 Acidity

For the FT-IR measurement, the FCC catalyst was heated to 550 °C for 15 min. and 60 min., under high vacuum, and cooled down, while kept under vacuum, as described in paragraph 3.2.1. All spectra were corrected for the weight of the wafer.

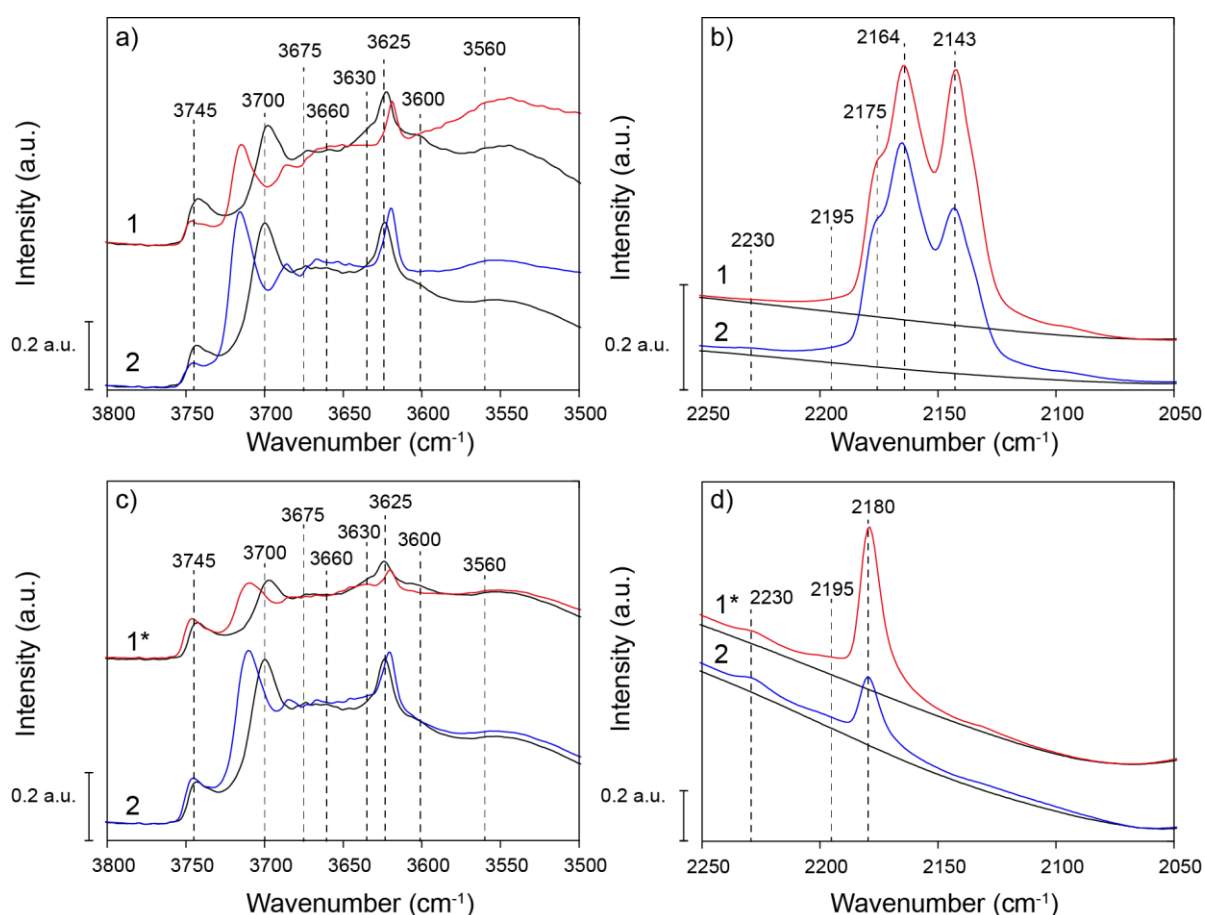


Figure 42 FT-IR spectra of the FCC catalyst heated for: 1. 60 min (red) 2. 15 min. (blue) a)- b) OH vibrational region and CO vibrational region before (black) and after maximal loading with CO c)-d) OH vibrational region and CO vibrational region before (black) and after minimal loading with CO (blue-red). * is a new measurement with a FCC catalyst heated for 60 min., to take a closer look at minimal loading.

In Figure 42 the FT-IR spectra of the FCC catalyst heated for 60 min. and 15 min. is depicted. As described in paragraph 2.4.2, the band positions of the CO stretching vibration is characteristic for the acid type and acid strength, to which the is attached. ^[8,16,36,48,82,83,86] Since the spectra are corrected for

the weight of the wafer, the intensity of the bands can be compared, which gives information about the amount of the different acid sites in the samples.

In Figure 42 b, a decreased intensity of the bands at 2164 and 2175 cm^{-1} can be observed, upon prolonged heating of the FCC catalyst. These bands are attributed to CO on a medium and strong Brønsted acid site respectively.^[36,48,82,83,86] This is confirmed by a decreased intensity of the bands affiliated with Brønsted acid sites in super cages (3630 and 3600 cm^{-1}) (Figure 42a).^[30,54] Additionally, prolonged heating of the FCC catalyst results in an increase of the band at 2195 cm^{-1} . This band is affiliated with CO on medium Lewis acid sites.^[15,23,48,50,93,97] Prolonged heating is reported to result in the formation of Lewis acidic Extra Framework (EF) aluminium species.^[43] The increased Lewis acidity could therefore be affiliated with the formation of EF aluminium species. In chapter 4 it was shown that the aluminium center of the aluminol groups and Brønsted acid sites could act as a Lewis acid site. Therefore, it can also be postulated that the increase in Lewis acidity could originate from the dehydroxylation of the Brønsted acid sites.

To get a better understanding about the increase in the Lewis acidity and the decrease in Brønsted acidity, $^1\text{H-NMR}$ was employed to detect changes in acidity, by comparing the chemical shift of the proton in the $^1\text{H-NMR}$ measurement with the IR bands in the OH vibrational region (4000-3000 cm^{-1}) In Figure 43, the FT-IR spectra of the OH vibrational region (a) and the corresponding $^1\text{H-NMR}$ spectra (b) are shown. The $^1\text{H-NMR}$ spectra are not corrected for the weight of the samples, but equal volume amounts were used. Differences in intensity of similar peaks between the samples can therefore not be assigned to a change in the amount, since differences in sample density result in a changed amount of hydroxyl groups. Differences in peak ratios can however be used to get a better idea about the ratio of different protons within a sample.

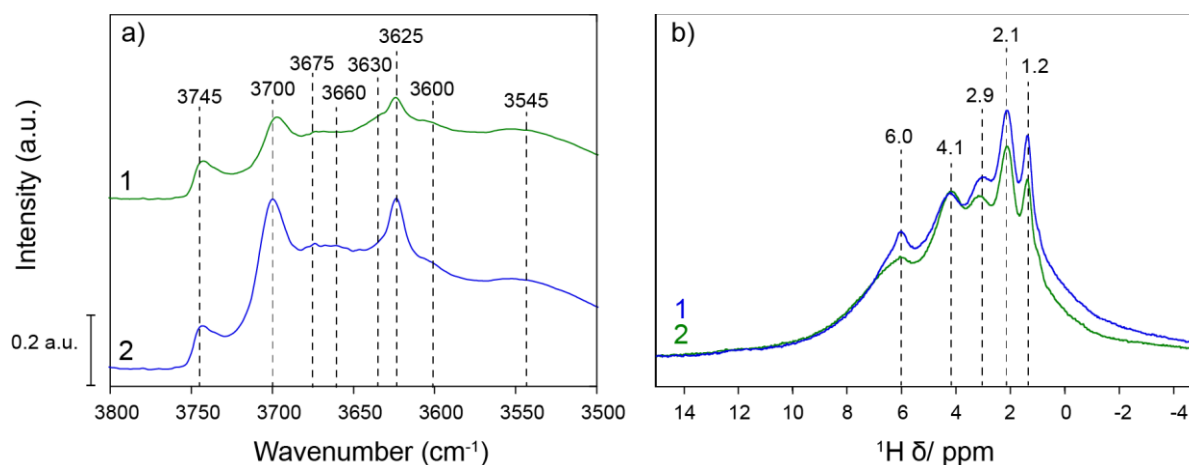


Figure 43 a) FT-IR spectrum of the OH vibrational region under vacuum at $-188\text{ }^\circ\text{C}$ and b) $^1\text{H-NMR}$ spectrum of 1. FCC heated for 15 min. 2. FCC heated for 60 min.

In the OH vibrational region (Figure 43a), a decrease in intensity can be observed for almost all the bands, upon prolonged heating of the FCC catalyst. This is confirmed by a decrease of all the peaks in $^1\text{H-NMR}$ spectrum (Figure 43b), except for the peak at 4.1 ppm. This peak is correlated to the band around at 3545 cm^{-1} and attributed to Brønsted acid sites in a sodalite cage.^[23,36,40,96,129,143] The sodalite cage is the smallest cage in the zeolite.^[66] The minimal decrease of this hydroxyl group could therefore be ascribed to the confinement of this hydroxyl group in the sodalite cage. The peak at 2.9 ppm is associated with medium Brønsted acid sites, based on the results of chapter 4. The decreased intensity of the peak at 2.9 ppm thereby confirms the decrease in Brønsted acidity as determined with CO FT-IR.

8.2 Structure

To see if the heat-treatment had any effect on the aluminium coordination, the sample was measured both before and after heating for 15 min., and 60 min. at 538 °C. To understand the decrease in Lewis and Brønsted acidity in the FCC, the samples were measured with ^{27}Al MQ-MAS and ^{27}Al MAS NMR spectroscopy. Two FCC catalysts were heated to 538 °C for 15 min. and 60 min. under a nitrogen flow of 100 mL/min, as described in paragraph 3.2.2. The ^{27}Al MAS- and ^{27}Al MQ-MAS NMR spectra are not corrected for the weight of the samples, but equal volume amounts were used. Differences in intensity of similar peaks between the samples can therefore not directly be assigned to a change in the amount, since differences in sample density result in a changed absolute amount of aluminium. Differences in peak ratios can however be used to get a better idea about the ratio of different aluminium coordinations within a sample.

As explained in paragraph 2.4.1, in MQ-MAS NMR spectra, the F1 axis depicts the isotropic chemical shift, where the F2 axis shows the anisotropic chemical shift. The peak position along the F1 therefore gives information about the coordination of the aluminium nucleus. The anisotropic chemical shift in the F2 direction is largely affected by the second order quadrupolar coupling. A broadening along the F2 direction thus provides information about the strength of the quadrupolar coupling constant, and therefore about the symmetry and environment around the aluminium nucleus. [35,41,114,115] As described in paragraph 2.4.1, three regions can be distinguished in the ^{27}Al MQ-MAS NMR spectra: 0-30 ppm, 20-50 ppm and 40-90 ppm, which are ascribed to octahedral, penta- coordinated and tetrahedral aluminium coordinations respectively. [35,41,114,115]

Figure 44 displays the overlay of the ^{27}Al MQ-MAS and ^{27}Al MAS NMR spectra of the FCC catalyst before heating, and after heating for 15, and 60 minutes.

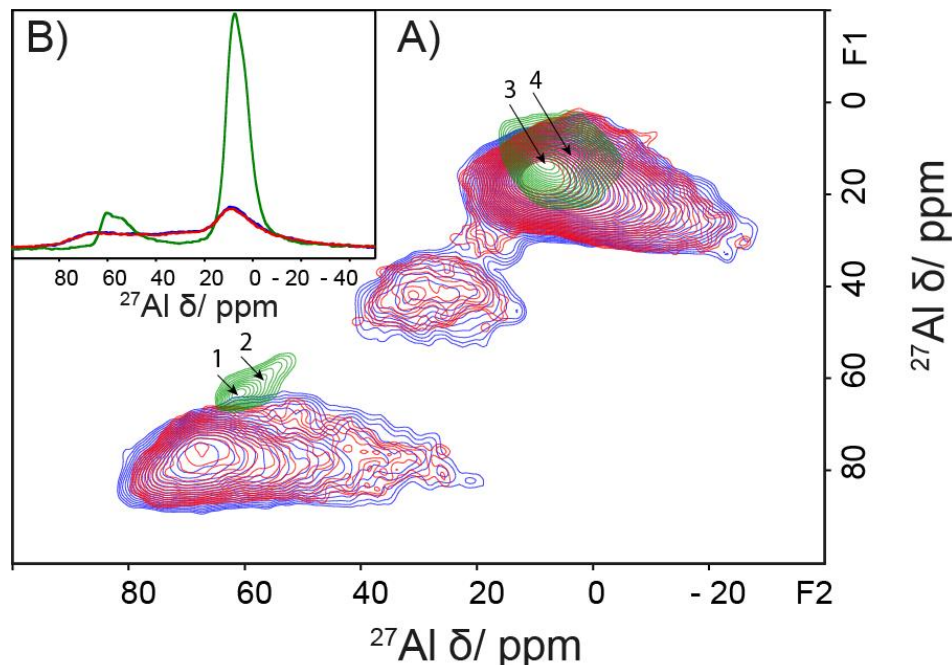


Figure 44 ^{27}Al MQ-MAS (A) and ^{27}Al MAS (B) spectra overlay of the FCC catalyst with different heat treatments. Blue: FCC catalyst treated for 60 min. at 538 °C, Red: FCC catalyst treated for 15 min. at 538 °C, Green: FCC catalyst without heat treatment.

Two distinct peaks in both the tetrahedral and octahedral region can be observed in the ^{27}Al MQ-MAS NMR spectra of the FCC catalyst, before heating. The peaks 1-4 can each be affiliated with a different

component in the FCC, as shown in the appendix paragraph 13.2.2. Peak number 1 originates from the tetrahedral zeolite coordination. Peak 2 and 3 are ascribed to framework aluminium species in the binder. Peak 4 is associated with the clay. As shown in chapter 6, the individual components are not clearly distinguishable in the ^{27}Al MQ-MAS NMR spectrum of the heated FCC. The clear distinction of the individual components before heating indicates that the different aluminium species did not interact before the heat-treatment. This shows that heating of the components results in reorganization and interactions between the different aluminium coordinations.

Furthermore, heating of the FCC catalyst results in the formation of the peak affiliated with penta-coordinated aluminium.^[35] Since this coordination is not present before the heating, this aluminium coordination thus be ascribed to the formation of Extra-Framework (EF) aluminium species.

Additionally, heating of the FCC catalyst results in a shift of the tetrahedral peaks (70 ppm) to higher ppm values. Moreover, heating results in a broadening of the peaks along the F2 direction, which indicates a more distorted environment around the aluminium nuclei.^[35,79,80] The shift in the F1 and F2 direction indicates that the aluminium species are largely affected by the change in local environment.^[35,75,76,79,80] This suggests that the tetrahedral aluminium structures are located close to the surface and are therefore largely affected by the heat-treatment.^[21] The relative position of the octahedral peaks (10 ppm) does not seem to change much upon heating of the FCC catalyst. This suggests that the octahedral coordination originate from framework aluminium which is little affected by the heat-treatment.

The ^{27}Al MAS NMR spectra of the FCC catalyst heated for 15 and 60 min. shows no very significant changes in the intensity of the peaks. In the ^{27}Al MQ-MAS NMR spectra, an increased broadening along the F2 axis can be observed, upon prolonged heating of the FCC catalyst. This can be affiliated with the dehydroxylation of the surface hydroxyl groups, which results in an increased distortion occurs around the aluminium nuclei.^[15,43,92,98,116,142] The increase in Lewis acidity could therefore be correlated to the increase in the distortion of all the aluminium coordinations. This confirms that a decrease in distortion results in a decrease of Lewis acidity, as was postulated in chapter 6 and 7. The peaks affiliated with the penta- and tetrahedrally coordinated aluminium species show the largest broadening along the F2 direction.

To confirm that the structural changes are not only occurring in the environment around the aluminium nuclei, XRD measurements and TEM measurements were performed on the FCC catalysts before and after heating the catalyst for 15 and 60 min. at 538 °C under a nitrogen flow of 100 mL/min.

In the XRD diffractogram (Figure 45a), a collapse in the crystallinity of the binder and clay can be observed, upon heating the FCC catalyst. The not heated FCC catalyst contains all the components in their crystalline form. This is confirmed by the XRD diffractogram of the individual components, which can be found in appendix 13.2.1. The crystallinity of the zeolite does not decrease upon prolonged heating of the FCC catalyst. The formation of EFAl species, therefore, does not affect the crystallinity of the zeolite. The decrease in crystallinity of the binder is affiliated with the change in crystal structure of the boehmite which has also been reported in literature. The clay is known to transform to amorphous meta-kaolinite upon heating to 500 °C.^[46,54,55,124,126,135,136,144–146] The changes in aluminium coordinations can therefore partially be ascribed to the change in crystallinity of the binder and clay.

The TEM images (Figure 45b, 45c and 45d) show the morphology of the FCC catalyst before heating and after heating for 15 min. and 60 min. respectively. In appendix 13.2.3, the TEM images of the individual components is shown. The silica can be distinguished by its grain like structure and the zeolite can be distinguished by the mesopores, which appear in the structure. The TEM image of the FCC before

the heat-treatment displays some rod like structures, which are affiliated to the boehmite. The TEM images of the heated FCC catalysts appear to have an increased in homogeneity of the morphology. The increase in homogeneity could be an indication of the fusing of the different components. An alternative explanation is the formation of an amorphous phase which is formed due to the structural collapse of the clay and binder. The silica appears to be present as silica islands, which has been reported in literature.^[68] However, due to similar contrast of aluminium and silicon, the formation of silica islands is not unambiguous.

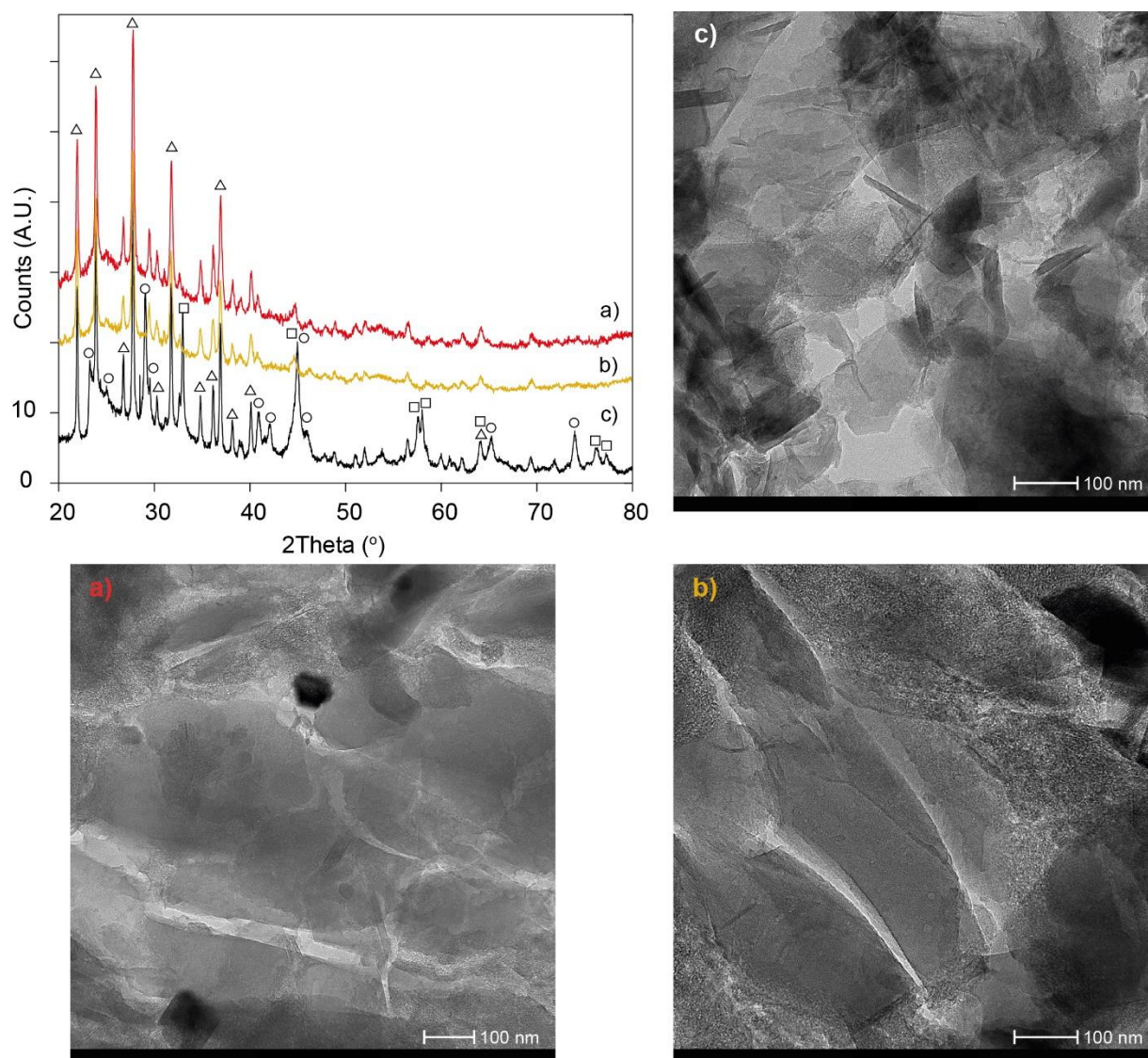


Figure 45 Top left: XRD diffractogram. Top right and bottom two: TEM images. a) FCC catalyst without heat treatment b) FCC catalyst heated for 15 min. at 538 °C c) FCC catalyst heated for 60 min. at 538 °C. Δ Zeolite HY \square Binder \circ Clay

8.3 Summary and Conclusion

In paragraph 8.1, it was observed that prolonged heating of the FCC catalyst resulted in a decreased amount of Brønsted acid sites and a minimal increase in the amount of the medium Lewis acid sites. The decrease in Brønsted acid sites was confirmed by a decrease of the Brønsted peaks in the $^1\text{H-NMR}$ spectrum. In the $^1\text{H-NMR}$ spectrum, the peak at 4.1 ppm did not appear to decrease as much compared to the other peaks. The peak at 4.1 ppm is affiliated with Brønsted acid sites in sodalite cages.^[96,109] The minimal decrease was therefore ascribed to confinement of the Brønsted acid site in the small sodalite cage, which results in hindering of the desorption.^[66] The increase in the amount of medium Lewis acid sites was additionally postulated to originate from the dehydroxylated Brønsted acid sites.^[25]

The ^{27}Al MQ-MAS NMR measurements showed a slight increase in the distortion around all the aluminium coordinations, upon prolonged heating of the FCC catalyst. The increased distortion around the aluminium nuclei was subsequently be linked to the increase in medium Lewis acid sites. It was however unclear if the increase in the concentration of medium Lewis acid sites was correlated to the decrease in Brønsted acid sites or to an increased concentration of Extra-Framework aluminium species.

The aluminium coordination of the FCC before heat-treatment showed large changes in coordinations compared to the heated FCC samples. The tetrahedrally coordinated aluminium species showed an increased broadening along the F2 direction and the shift towards lower ppm values in the F1 direction. This indicated an increased distortion and more electron withdrawing environment. The tetrahedrally coordinated aluminium species were therefore postulated to be located close to the surface of the components, since the peak were largely affected by heating of the FCC catalyst. Additionally, the formation of penta-coordinated aluminium could be observed upon heating of the FCC catalyst. The formation of penta-coordinated aluminium species could therefore be ascribed to the formation of EF aluminium species. The octahedral peak showed little change in position, which could indicate that the octahedral structure originates from framework aluminium and is therefore little affected by the heat-treatment. Since the tetrahedral and penta-coordinated aluminium species change the most in structure, the change in Brønsted and Lewis acidity could be coupled to the change of these structures respectively.

Additionally, it was postulated that the different aluminium coordinations interact upon heating of the FCC catalyst.

The large structural changes in aluminium coordination upon heating of the FCC catalyst were confirmed with XRD measurements. In the XRD diffractogram, a collapse of the crystallinity of the binder and clay could be observed. The zeolite was the only component which remained crystalline during the heat treatment, which showed that the crystallinity is not affected by the formation of Extra-Framework (EF) aluminium species.

The TEM measurements showed an increased homogeneity of the morphology upon heating of the FCC catalyst. The loss of the crystallinity was therefore correlated to an increase in the homogeneity, due to the formation of an amorphous phase. The silica did not seem to fuse together with the other components, but seemed to form silica islands.

Overall, it can be concluded that prolonged heating results in dehydroxylation of the Brønsted acid sites. Furthermore, heating of the FCC catalyst results in the formation of Lewis acidic EF aluminium species.

Chapter 9. Conclusions

Systematic analysis of the Fluid Catalytic Cracking (FCC) catalyst provided new insights into the origin of the acid sites. A better understanding about the nature and structure of the acid sites is essential, to understand the catalytic activity of the FCC catalyst. The acidity was determined with CO and pyridine based infrared (FT-IR) spectroscopy. Additionally, the environment around the aluminium nuclei was studied with ^{27}Al MAS- and ^{27}Al MQ-MAS NMR spectroscopy. Furthermore, ^1H MAS-NMR spectroscopy was used to study the different protons in the samples.

Using probe molecule-based FT-IR spectroscopy and ^1H MAS-NMR spectroscopy, a correlation between the chemical shift in the ^1H -NMR spectra and the frequency in the OH vibrational region in FT-IR spectra, was obtained. ^1H -NMR proved to be a useful technique to analyse the change in the acidity of the Brønsted acid sites. Moreover, by employing $\{^1\text{H}-^{27}\text{Al}\}$ CP NMR and $\{^{27}\text{Al}-^1\text{H}\}$ CP NMR spectroscopy, the different protons are correlated to specific aluminium coordinations.

By correlating the changes in Brønsted acidity with the tetrahedral coordinations in the ^{27}Al MQ-MAS NMR spectra, it is concluded that the Brønsted acid sites originate from tetrahedrally coordinated aluminium, which is located close to the surface. In the binder, the Brønsted acid sites originated from bond formation between silica and alumina. Moreover, a shift of the tetrahedral aluminium coordination in the ^{27}Al MAS-NMR spectra to higher ppm values is associated with localization of the negative charge induced by the aluminium. The localization of the negative charge results in the formation of strong Brønsted acid sites.

Based on the FT-IR measurements, it is confirmed that the acidity of the FCC originates primarily from the zeolite. Moreover, it was shown that the acidity of the active matrix originates from the binder. Therefore, the binder is ascribed to be the component active component of the active matrix.

By studying the acidic and structural properties of mixes of two individual components, interactions between the single components were elucidated. Based on the obtained results it is concluded that mixing of binder and zeolite results in an increased amount of Brønsted acid sites. Additionally, the incorporation of clay results in blocking of the pores and a decrease in the amount of Brønsted acid sites.

Additionally, through studying of the OH vibrational region in the CO FT-IR measurements, it was shown that the aluminium center of the Brønsted acid sites and aluminol groups, acts as a Lewis acid site, to which CO could coordinate. Based on these results and the correlation between the ^1H -NMR and the ^{27}Al MAS-NMR spectra, it is concluded that tetrahedral and octahedral aluminium can act as a Lewis acid site.

Furthermore, it was shown that heating of the FCC catalyst results in the formation of Extra-Framework (EF) penta-coordinated aluminium species. The penta-coordinated aluminium is therefore assigned to the formation of EF aluminium species. Based on an increased amount of Lewis acid sites, it is concluded that the EF aluminium species are Lewis acidic. Moreover, by studying the change in Lewis acidity with FT-IR and the change in the environment around the EF aluminium species with ^{27}Al MQ-MAS NMR, an increased heterogeneity of the penta-coordinated aluminium species was associated with an increase of the Lewis acid strength. Additionally, it was shown that mixing in the FCC resulted in a decrease in the amount of Lewis acid sites. Therefore it is concluded that EF aluminium species are located on the outer surface of the components.

Chapter 10. Outlook and Recommendations

In this chapter a few additional experiments are recommended to confirm the conclusions of chapter 9.

First, it was postulated that the incorporation of clay resulted in blockage of the pores. Additionally, the incorporation of clay resulted in an increase of the peak at 6 ppm in the ^1H -NMR spectrum which was correlated to an increase in the amount of water confined in pores, acid sites and possibly an increased confinement of water in micropores. To see if these postulations are true, nitrogen physisorption and temperature programmed desorption (TPD) experiments should be performed on the clay containing samples. The nitrogen physisorption gives insight in the amount of micro-, meso- and macro- pores. TPD measurements shows how much weight loss occurs upon heating and thus provides information about the amount of water in the sample.^[16]

Additionally, it was proposed that the decrease in the amount of Brønsted acid sites results in the formation of Lewis acid sites. Prolonged heating of zeolite HY could confirm whether the removal of Brønsted acid sites results in the formation of additional Lewis acid sites, since this sample contains primarily Brønsted acid sites.

As described in chapter 4, discrepancies in the determination of the amount of acid sites based on the CO FT-IR and pyridine FT-IR measurements were observed. The use of a NMR active probe molecule could help to elucidate the acidity of the samples. In literature trimethyl-phosphine (TMP) and trimethyl-phosphine oxide (TMPO) are often used as a probe molecule to detect different Lewis and Brønsted acid sites.^[103,105,113,122,139,147–152] TMP is known to interact with Lewis acid sites, which result in very defined shift in the ^{31}P NMR spectrum. TMPO is known to interact primarily with Brønsted acid sites. Phosphorous 31 is a naturally abundant NMR active nucleus and is very sensitive, which makes it an ideal nucleus for NMR experiments.^[76] A $\{^{31}\text{P}-^{27}\text{Al}\}$ CP experiment with TMP or TMPO could give information about the strength and origin of the different acid sites, by correlating the aluminium coordinations with the phosphorus chemical shift. An experiment with TMP was attempted, but due fast oxidation of the TMP to trimethyl-phosphine oxide (TMPO), the experiments were hindered. The use of TMPO is known to interact less strongly with the Lewis acid sites and has a less defined region for the different Lewis acid strengths.^[103,105,113,122,139,147–152] TMPO could however still be used to detect both Lewis and Brønsted acid sites.

Furthermore, in order to elucidate the local environment around the aluminium nuclei, it would be interesting to investigate the samples with MQ-HETCOR NMR spectroscopy. As described in paragraph 2.4.1, the use of MQ HETCOR NMR spectroscopy can give information about the proximity of two different nuclei. In a MQ-HETCOR experiment, a 2D spectrum is obtained in which the enhances signals appear as cross-peaks in the NMR spectrum. Thus, when two nuclei are in close proximity, a cross-peak appears in the NMR spectrum. It can therefore directly be deduced which nuclei are in close proximity to each other, by looking at the cross-peaks. However, a MQ HETCOR experiment was attempted for the FCC heated for 60 min., but the signal was too low for a MQ HETCOR experiment. Additionally, a MQ-HETCOR experiment was performed on Zeolite HY Si/Al 7, which is shown in appendix 13.5. Due to a lack of time, the MQ-HETCOR could not be studied in detail.

Moreover, the exact environment around the different aluminium nuclei was not elucidated in this thesis. The use of density functional theory (DFT) calculations can help with the determination of the local structure around the aluminium nuclei. To the best of our knowledge, no DFT calculations have been performed to elucidate the aluminium structure of the on the FCC catalyst. In the work of Deng et al, multiple DFT calculations were performed to elucidate the structure around the aluminium nuclei in zeolite HY.^[42,43,148] This illustrates the possibility to couple DFT calculations with NMR spectroscopy.

Finally, it would be interesting to study more samples, like steam deactivated FCC catalysts and equilibrium catalysts. With the obtained correlations, the deactivation process of the FCC catalyst could be studied. This would help to understand the FCC cracking mechanism and the deactivation.

Chapter 11. Acknowledgements

First, I would like to thank professor Bert Weckhuysen for providing this interesting research. Professor, you were very critical but it kept us sharp to look at what was truly interesting. You provided us with feedback which proved to be very helpful. I would also like to thank you for providing me with an internship in Stanford. This was an opportunity of which I never even dared dream of, so to be able to go to Stanford is a dream come true.

Secondly, I would like to thank Marjolein Velthoen as my daily supervisor. Marjolein, I'd like to thank you for your optimism and interest in all the results we booked. Your positive attitude made the project fun and kept me motivated to give a 110%. Our weekly meetings with Frédérique Broers, were a really nice addition to the whole project. They motivated us and provided a moment to speculate about the data. Though the interpretation of the data could be very difficult, you were always prepared to sit down and talk everything through until we were satisfied. You provided a difficult project, but you always believed that we could make it work. You told me: "You are going to be the NRM expert and teach me about the technique." I really hope I taught you something, because you taught me a lot, and I'm very grateful for that.

Thirdly, I'd like to thank Alessandra Lucini Paioni, for helping me with all the NMR measurements and for helping me to understand the NMR techniques. Alessandra, we could not have done this project without you. You helped with the measurements and the contact between ICC and NMR. We relied on you for the measuring time and you never let us down. You were very always very interested in our project and motivated to help us with the interpretation and explanation of the NMR data.

I also want to thank the following people for helping me with measurements, or in general by providing support and explanations when I did not know what to do: Klaartje Houben, Paul Pletcher, Fouad Soulimani, Marjan Versluijs-Helder, Ad van Eeden, Oscar Kerkenaar, Herrick Schaink, Lars van der Wal, Petra Keijzer and Jochem Wijten.

Lastly, I want to thank some of my friends and fellow master students who supported me and were there when times got tough. You were there when I needed someone to let off steam with. An extra special thanks to Lotte Geerlings and Mark Slagter. You were always near when I wanted to talk. You provided a listening ear and a hug when needed and you'll always be my dearest friends.

Chapter 12. Bibliography

- [1] M. Rigutto, in *Zeolites Catal. Synth. React. Appl.* (Eds.: J. Čejka, A. Corma, S. Zones), Wiley-VCH Verlag, Weinheim, **2010**, pp. 547–584.
- [2] E. T. C. Vogt, B. M. Weckhuysen, *Chem. Soc. Rev.* **2015**, *44*, 7342–7370.
- [3] Y. V. Kissin, *J. Catal.* **1996**, *163*, 50–62.
- [4] S. E. Tung, E. Mcininch, *J. Catal.* **1964**, *3*, 229–238.
- [5] A. Corma, V. Fornes, *Appl. Catal.* **1990**, *61*, 175–185.
- [6] C. L. Thomas, *Ind. Eng. Chem.* **1949**, *41*, 2564–2573.
- [7] I. L. C. Buurmans, J. Ruiz-Martínez, W. V. Knowles, D. van der Beek, J. A. Bergwerff, E. T. C. Vogt, B. M. Weckhuysen, *Nat. Chem.* **2011**, *3*, 862–867.
- [8] A. W. Chester, E. G. Derouane, *Zeolite Chemistry and Catalysis*, Springer Netherlands, Dordrecht, **2009**.
- [9] “The Clean Air Act,” can be found under <https://www.epw.senate.gov/envlaws/cleanair.pdf>, **2004**.
- [10] UNFCCC, “Paris Agreement,” **2015**.
- [11] G. A. Olah, *Angew. Chemie Int. Ed.* **2005**, *44*, 2636–2639.
- [12] J. Edmonds, J. Reilly, *Energy* **1982**, *8*, 419–432.
- [13] S. Shafiee, E. Topal, *Energy Policy* **2009**, *37*, 181–189.
- [14] H. H. Rogner, *Annu. Rev. Energy Env.* **1997**, *22*, 217–262.
- [15] G. Crépeau, V. Montouillout, A. Vimont, L. Mariey, T. Cseri, F. Maugé, *J. Phys. Chem. B* **2006**, *110*, 15172–15185.
- [16] S. A. Bradley, R. W. Broach, T. M. Mezza, S. Prabhakar, W. Sinkler, in *Zeolites Ind. Sep. Catal.* (Ed.: S. Kulprathipanja), Wiley-VCH Verlag, Weinheim, **2010**, pp. 85–171.
- [17] P.-J. Cbu, V. A. De Mallmann, J. H. Lunsford, *J. Phys. Chem* **1991**, *95*, 7362–7368.
- [18] M. Hunger, in *Zeolite Charact. Catal. A Tutor.* (Eds.: A.W. Chester, E.G. Derouane), Springer Science, **2010**, pp. 1–358.
- [19] A. Corma, J. Planelles, J. Sánchez-Marín, F. Tomás, *J. Catal.* **1984**, *93*, 30–37.
- [20] A. Corma, A. V. Orchillés, *Microporous Mesoporous Mater.* **2000**, *3536*, 21–30.
- [21] E. G. Derouane, J. C. Védrine, R. R. Pinto, P. M. Borges, L. Costa, M. A. N. D. A. Lemos, F. Lemos, F. R. Ribeiro, *Catal. Rev.* **2013**, *55*, 454–515.
- [22] M. Hunger, in *Zeolites Catal.*, Wiley-VCH Verlag, Weinheim, Germany, **2010**, pp. 493–546.
- [23] T. K. Phung, G. Busca, *Appl. Catal. A Gen.* **2015**, *504*, 151–157.
- [24] A. Primo, H. Garcia, *Chem. Soc. Rev.* **2014**, *43*, 7548–7561.
- [25] P. Y. Bruice, *Organic Chemistry: Pearson International Edition*, Pearson Education Limited, Harlow, **2013**.
- [26] J. N. Brönsted, *Chem. Rev.* **1927**, *5*, 231–338.
- [27] I. L. C. Buurmans, *Catalyst Particles for Fluid Catalytic Cracking Visualized at the Individual Particle Level by Micro-Spectroscopy*, **2011**.
- [28] G. T. Whiting, A. D. Chowdhury, R. Oord, P. Paalanen, B. M. Weckhuysen, *Faraday Discuss.* **2016**, *188*, 369–386.
- [29] G. T. Whiting, F. Meirer, M. M. Mertens, A.-J. Bons, B. M. Weiss, P. A. Stevens, E. de Smit, B. M. Weckhuysen, *ChemCatChem* **2015**, *7*, 1312–1321.
- [30] T.-J. Rong, J.-K. Xiao, *Mater. Lett.* **2002**, *57*, 297–301.
- [31] Z. Yunsheng, S. Wei, L. Zongjin, *Appl. Clay Sci.* **2010**, *47*, 271–275.
- [32] S. C. Lim, C. Gomes, M. Zainal, A. A. Kadir, *Int. J. Electrochem. Sci* **2013**, 11429–11447.
- [33] J. G. Miller, W. Linwood Haden, T. Dixon Oulton, in *Twelfth Natl. Conf. Clays Clay Miner.*, **n.d.**
- [34] W. Letzsch, *Handbook of Petroleum Processing*, Springer International Publishing, Cham, **2015**.
- [35] G. Engelhardt, D. Michel, *High-Resolution Solid-State NMR of Silicates and Zeolites*, Wiley-VCH, Chichester, **1987**.
- [36] S. Bordiga, C. Lamberti, F. Bonino, A. Travert, F. Thibault-Starzyk, *Chem. Soc. Rev.* **2015**, *44*, 7262–7341.

- [37] B. Xu, S. Bordiga, R. Prins, J. A. van Bokhoven, *Appl. Catal. A Gen.* **2007**, *333*, 245–253.
- [38] H. S. S. Cerqueira, G. Caeiro, L. Costa, F. Ramôa Ribeiro, *J. Mol. Catal. A Chem.* **2008**, *292*, 1–13.
- [39] L. F. Isernia, *Mater. Res.* **2013**, *16*, 792–802.
- [40] F. Deng, Y. Yue, C. Ye, *Solid State Magn. Reson.* **1998**, *10*, 151–160.
- [41] F. Deng, Y. Yue, C. Ye, *J. Phys. Chem. B* **1998**, *102*, 5252–5256.
- [42] Z. Yu, A. Zheng, Q. Wang, L. Chen, J. Xu, J.-P. Amoureux, F. Deng, *Angew. Chemie Int. Ed.* **2010**, *49*, 8657–8661.
- [43] S. Li, A. Zheng, Y. Su, H. Fang, W. Shen, Z. Yu, L. Chen, F. Deng, *Phys. Chem. Chem. Phys.* **2010**, *12*, 3895.
- [44] S. Li, A. Zheng, Y. Su, H. Zhang, L. Chen, J. Yang, C. Ye, F. Deng, *J. Am. Chem. Soc.* **2007**, *129*, 11161–11171.
- [45] Z. Yu, Q. Wang, L. Chen, F. Deng, *Chinese J. Catal.* **2012**, *33*, 129–139.
- [46] A. Boumaza, L. Favaro, J. Lédion, G. Sattonnay, J. B. Brubach, P. Berthet, A. M. Huntz, P. Roy, R. Tétot, *J. Solid State Chem.* **2009**, *182*, 1171–1176.
- [47] T. H. Ballinger, J. T. Yates, *Langmuir* **1991**, *7*, 3041–3045.
- [48] K. I. Hadjiivanov, G. N. Vayssilov, *Adv. Catal.* **2002**, *47*, 305–511.
- [49] A. Corma, M. S. Grande, V. Gonzalez-Alfaro, A. V Orchilles, *J. Catal.* **1996**, *159*, 375–382.
- [50] J. N. Kondo, R. Nishitani, E. Yoda, T. Yokoi, T. Tatsumi, K. Domen, *Phys. Chem. Chem. Phys.* **2010**, *12*, 11576.
- [51] M. W. Tamele, *Discuss. Faraday Soc.* **1950**, *8*, 270–279.
- [52] G. Busca, in *Adv. Catal.*, Elsevier Inc., **2014**, pp. 319–404.
- [53] S. Chandrasekhar, *Clay Miner.* **1996**, *31*, 253–261.
- [54] B. Fabbri, S. Gualtieri, C. Leonardi, *Appl. Clay Sci.* **2013**, *73*, 2–10.
- [55] M. R. Wang, D. C. Jia, P. G. He, Y. Zhou, *Mater. Lett.* **2010**, *64*, 2551–2554.
- [56] G. Kakali, T. Perraki, S. Tsivilis, E. Badogiannis, *Appl. Clay Sci.* **2001**, *20*, 73–80.
- [57] M. Gábor, M. Tóth, J. Kristóf, G. Komáromi-Hiller, *Clays Clay Miner.* **1995**, *43*, 223–228.
- [58] M. Caillot, A. Chaumonnot, M. Digne, J. A. van Bokhoven, *J. Catal.* **2014**, *316*, 47–56.
- [59] D. Goyvaerts, J. A. Martens, P. J. Grobet, P. A. Jacobs, *Prep. Catal.* **1991**, *5*, 381–395.
- [60] B. A. Williams, S. M. Babitz, J. T. Miller, R. Q. Snurr, H. H. Kung, *Appl. Catal. A Gen.* **1999**, *177*, 161–175.
- [61] H. S. Cerqueira, G. Caeiro, L. Costa, F. Ramôa Ribeiro, *J. Mol. Catal. A Chem.* **2008**, *292*, 1–13.
- [62] D. Wallenstein, T. Roberie, T. Bruhin, *Catal. Today* **2007**, *127*, 54–69.
- [63] J. Shen, A. Auroux, in *Stud. Surf. Sci. Catal.*, **2004**, pp. 35–70.
- [64] B. S. Greensfelder, H. H. Voge, G. M. Good, *Ind. Eng. Chem.* **1949**, *41*, 2573–2584.
- [65] S. Kortel, H. Knözinger, B. C. Gates, *Microporous Mesoporous Mater.* **2000**, *35–36*, 11–20.
- [66] P. D. Hopkins, J. T. Miller, B. L. Meyers, G. J. Ray, R. T. Roginski, M. A. Kuehne, H. H. Kung, *Appl. Catal. A Gen.* **1996**, *136*, 29–48.
- [67] G. E. Maciel, J. F. Haw, I.-S. Chuang, B. L. Hawkins, T. A. Early, D. R. McKay, L. Petrakist, *J. Am. Chem. Soc.* **1983**, *105*, 5529–5535.
- [68] A. A. Gurinov, Y. A. Rozhkova, A. Zukal, J. Čejka, I. G. Shenderovich, *Langmuir* **2011**, *27*, 12115–12123.
- [69] R. H. Crabtree, *The Organometallic Chemistry of the Transition Metals*, John Wiley & Sons Inc, New York, **2014**.
- [70] J. Guan, X. Li, G. Yang, W. Zhang, X. Liu, X. Han, X. Bao, *J. Mol. Catal. A Chem.* **2009**, *310*, 113–120.
- [71] D. Freude, H. Ernst, I. Wolf, *Solid State Nucl. Magn. Reson.* **1994**, *3*, 271–286.
- [72] J. C. C. Chan, *Solid State NMR*, Springer Berlin Heidelberg, Heidelberg, **2012**.
- [73] D. Freude, J. Kärger, in *Handb. Porous Solids*, Wiley-VCH Verlag, Weinheim, **2008**, pp. 465–505.
- [74] L. F. Gladden, M. Lutecki, J. McGregor, in *Charact. Solid Mater. Heterog. Catal.*, Wiley-VCH Verlag, Weinheim, **2012**, pp. 289–342.
- [75] C. A. Fyfe, *Solid State NMR for Chemists*, C.F.C Press P. O Box 1720, Ontario, **1983**.
- [76] H. Friebolin, *Basic One- and Two-Dimensional NMR Spectroscopy*, Wiley-VCH Verlag,

- Einheim, **2013**.
- [77] J. C. Edwards, "Principles of NMR," can be found under <http://www.process-nmr.com/nmr1.htm>, **2008**.
- [78] A. Goldbourt, P. K. Madhu, *Monatshefte für Chemie Cematical Mon.* **2002**, *133*, 1497–1534.
- [79] L. Frydman, D. M. Grant, R. K. Harris, in *Encycl. Nucl. Magn. Reson. Vol. 9 Adv. NMR*, John Wiley & Sons Ltd, Chichester, **2002**, pp. 262–274.
- [80] P. P. Man, in *Encycl. Anal. Chem.* (Ed.: R.A. Meyers), John Wiley & Sons Ltd, Chichester, **2000**, pp. 12224–12265.
- [81] W. O. J. Parker, *Comments Inorg. Chem* **2000**, *1–2*, 31–73.
- [82] A. Vimont, "IR probe molecules for acidic sites," **2016**.
- [83] H. Knözinger, in *Handb. Heterog. Catal.*, Wiley-VCH Verlag, Weinheim, Germany, **2008**, pp. 1135–1162.
- [84] "Handbook of Chemistry and Physics 98th Edition," can be found under http://hbcponline.com/faces/documents/10_23/10_23_0001.xhtml?search=true, **n.d.**
- [85] G. N. Lewis, *Am. Chem. Soc.* **1924**, *43*, 17–170.
- [86] M. I. Zaki, H. Knözinger, *Mater. Chem. Phys.* **1987**, *17*, 201–215.
- [87] J. Clayden, N. Greeves, S. Warren, P. Wothers, *Organic Chemistry*, Oxford University Press, Oxford, **2012**.
- [88] C. H. Kline, J. Turkevich, *J. Chem. Phys.* **1944**, *12*, 300–309.
- [89] C. Morterra, G. Magnacca, *Catal. Today* **1996**, *27*, 497–532.
- [90] M. I. Zaki, M. A. Hasan, F. A. Al-Sagheer, L. Pasupulety, *Colloids Surfaces A Physicochem. Eng. Asp.* **2001**, *190*, 261–274.
- [91] S. Khabtou, T. Chevreau, J. C. Lavalley, *Microporous Mater.* **1994**, *3*, 133–148.
- [92] C. Pecharrmán, I. Sobrados, J. E. Iglesias, T. González-Carreño, J. Sanz, *J. Phys. Chem. B* **1999**, *103*, 6160–6170.
- [93] K. Góra-Marek, M. Derewiński, P. Sarv, J. Datka, *Catal. Today* **2005**, *101*, 131–138.
- [94] V. C. Farmer, J. D. Russell, *Spectrochim. Acta* **1964**, *20*, 1149–1173.
- [95] G. Garralón, A. Corma, V. Fornés, *Zeolites* **1989**, *9*, 84–86.
- [96] D. Freude, M. Hunger, H. Pfeifer, W. Schwieger, *Chem. Phys. Lett.* **1986**, *128*, 62–66.
- [97] T. K. Phung, L. Proietti Hernández, A. Lagazzo, G. Busca, *Appl. Catal. A Gen.* **2015**, *493*, 77–89.
- [98] S. M. C. Menezes, V. L. Camorim, Y. L. Lam, R. A. S. San Gil, A. Bailly, J. P. Amoureux, *Appl. Catal. A Gen.* **2001**, *207*, 367–377.
- [99] N. Sergent, P. Gélin, L. Périer-Camby, H. Praliaud, G. Thomas, *Phys. Chem. Chem. Phys.* **2002**, *4*, 4802–4808.
- [100] K. S. W. Singh, J. Rouquerol, G. Bergeret, P. Gallezot, M. Vaarkamp, D. C. Koningsberger, A. K. . Datye, J. W. Niemantsverdriet, T. Butz, G. Engelhardt, et al., in *Handb. Heterog. Catal.*, Wiley-VCH Verlag, Weinheim, Germany, **1997**, pp. 427–582.
- [101] J. W. Ward, *J. Catal.* **1970**, *17*, 355–358.
- [102] A. Zecchina, G. Spoto, S. Bordiga, *Phys. Chem. Chem. Phys.* **2005**, *7*, 1627.
- [103] A. Zheng, S.-B. Liu, F. Deng, *Solid State Nucl. Magn. Reson.* **2013**, *55–56*, 12–27.
- [104] M. Hunger, S. Ernst, S. Steuernagel, J. Weitkamp, *Microporous Mater.* **1996**, *6*, 349–353.
- [105] M. Hunger, *Catal. Rev.* **1997**, *39*, 345–393.
- [106] M. Müller, G. Harvey, R. Prins, *Microporous Mesoporous Mater.* **2000**, *34*, 281–290.
- [107] B. Gil, S. I. Zones, S.-J. Hwang, M. Bejblova, J. Čejka, *J. Phys. Chem. C* **2008**, *112*, 2997–3007.
- [108] U. Lohse, E. Löffler, M. Hunger, J. Stöckner, V. Patzelová, *Zeolites* **1987**, *7*, 11–13.
- [109] E. Brunner, H. G. Karge, H. Pfeifer, *Zeitschrift für Phys. Chemie* **1992**, *176*, 173–183.
- [110] N. Malicki, P. Beccat, P. Bourges, C. Fernandez, A. A. Quoineaud, L. J. Simon, F. Thibault-Starzyk, in *From Zeolites to Porous MOF Mater.*, Elsevier, **2007**, pp. 762–770.
- [111] E. Brunner, H. Ernst, D. Freude, M. Hunger, H. Pfeifer, *J. Catal.* **1991**, *127*, 34–41.
- [112] M. Hunger, D. Freude, H. Pfeifer, *J. Chem. Soc., Faraday Trans.* **1991**, *87*, 657–662.
- [113] S. Lang, M. Benz, U. Obenaus, R. Himmelmann, M. Hunger, *ChemCatChem* **2016**, *8*, 2031–2036.
- [114] D. Freude, J. Kljnowski, H. Hamdan, *Chem. Phys. Lett.* **1988**, *149*, 355–362.

- [115] E. Lam, A. Comas-Vives, C. Copéret, *J. Phys. Chem. C* **2017**, *121*, 19946–19957.
- [116] J.-P. Gilson, G. C. Edwards, A. W. Peters, K. Rajagopalan, R. F. Wormsbecherp, T. G. Roberie, M. P. Shatlockb, R. F. Wormsbecher, T. G. Roberie, M. P. Shatlock, *J. Chem. Soc. Chem. Commun.* **1987**, *949*, 91–92.
- [117] L. Mafra, J. Klinowski, in *eMagRes*, John Wiley & Sons, Ltd, Chichester, UK, **1996**, pp. 89–108.
- [118] J. Klinowski, J. M. Thomas, C. A. Fyfe, G. C. Gobbi, J. S. Hartman, *Inorg. Chem.* **1983**, *22*, 63–66.
- [119] J. A. van Bokhoven, N. Danilina, in *Zeolites Catal.*, Wiley-VCH Verlag, Weinheim, Germany, **2010**, pp. 283–300.
- [120] J. A. van Bokhoven, A. L. Roest, D. C. Koningsberger, J. T. Miller, G. H. Nachttegaal, A. P. M. Kentgens, *J. Phys. Chem. B* **2000**, *104*, 6743–6754.
- [121] M. Caillot, A. Chaumonnot, M. Digne, J. A. Van Bokhoven, *ChemCatChem* **2013**, *5*, 3644–3656.
- [122] E. F. Rakiewicz, A. W. Peters, R. F. Wormsbecher, K. J. Sutovich, K. T. Mueller, U. V Park, V. Pennsylv, *J. Phys. Chem. B* **1998**, *102*, 2890–2896.
- [123] N. Cardona-Martínez, J. A. Dumesic, *J. Catal.* **1990**, *125*, 427–444.
- [124] S. J. Wilson, *J. Solid State Chem.* **1979**, *30*, 247–255.
- [125] R. Tettenhorst, D. A. Hofmann, *Clays Clay Miner.* **1980**, *28*, 373–380.
- [126] J. J. Fitzgerald, G. Piedra, S. F. Dec, M. Seger, G. E. Maciel, *J. Am. Chem. Soc.* **1997**, *119*, 7832–7842.
- [127] G. Paglia, C. E. Buckley, A. L. Rohl, R. D. Hart, K. Winter, A. J. Studer, B. A. Hunter, J. V Hanna, *Chem. Mater.* **2004**, *16*, 220–236.
- [128] T. K. Phung, C. Herrera, M. Á. Larrubia, M. García-Diéguez, E. Finocchio, L. J. Alemany, G. Busca, *Appl. Catal. A Gen.* **2014**, *483*, 41–51.
- [129] H.-M. Kao, C. P. Grey, *J. Phys. Chem.* **1996**, *100*, 5105–5117.
- [130] C. a. Fyfe, J. M. Thomas, J. Klinowski, G. C. Gobbi, *Angew. Chemie Int. Ed. English* **1983**, *22*, 259–275.
- [131] A. P. M. Kentgens, *Geoderma* **1997**, *80*, 271–306.
- [132] C. A. Fyfe, K. C. Wong-Moon, Y. Huang, H. Grondey, K. T. Muellert, *J. Phys. Chem* **1995**, *99*, 8707–8716.
- [133] E. F. Rakiewicz, K. T. Mueller, T. P. Jarvie, K. J. Sutovich, *Microporous Mater.* **1996**, *7*, 81–88.
- [134] V. C. Farmer, *Clay Miner.* **1998**, *33*, 601–604.
- [135] R. L. Frost, A. M. Vassallo, *Clays Clay Miner.* **1996**, *44*, 635–651.
- [136] A. A. B. Maia, R. S. Angélica, R. Neves, H. Pöllmann, C. Staub, K. Saalwächter, *Appl. Clay Sci.* **2014**, *87*, 189–196.
- [137] V. M. Mastikhin, I. L. Mudrakovsky, A. V. Nosov, *Prog. Nucl. Magn. Reson. Spectrosc.* **1991**, *23*, 259–299.
- [138] N. Hosseinpour, Y. Mortazavi, A. Bazyari, A. A. Khodadadi, *Fuel Process. Technol.* **2009**, *90*, 171–179.
- [139] D. Coster, A. L. Blumenfeld, J. J. Fripiat, *J. Phys. Chem* **1994**, *98*, 6201–6211.
- [140] P. J. Grobet, H. Geerts, M. Tielen, J. A. Martens, P. A. Jacobs, in *Zeolite as Catal. Sorbents Deterg. Build.*, **1989**, pp. 721–734.
- [141] J. A. van Bokhoven, D. C. Koningsberger, P. Kunkeler, H. van Bekkum, A. P. M. Kentgens, *J. Am. Chem. Soc.* **2000**, *122*, 12842–12847.
- [142] E. Guillon, A. A. Quoineaud, T. Armaroli, S. Lacombe, S. Gautier, *Stud. Surf. Sci. Catal.* **2004**, *154*, 1539–1546.
- [143] E. Brunner, *J. Mol. Struct.* **1995**, *355*, 61–85.
- [144] Q. Liu, D. A. Spears, Q. Liu, *Appl. Clay Sci.* **2001**, *19*, 89–94.
- [145] T. Tsukada, H. Segawa, A. Yasumori, K. Okadab, *J. Mater. Chem.* **1999**, *8*, 549–553.
- [146] K. J. D. Mackenzie, J. Temuujin, M. E. Smith, P. Angerer, Y. Kameshima, *Thermochim. Acta* **2000**, *359*, 87–94.
- [147] Q. Luo, F. Deng, Z. Yuan, J. Yang, M. Zhang, Y. Yue, C. Ye, *J. Phys. Chem. B* **2003**, *107*, 2435–2442.

- [148] A. Zheng, S.-J. Huang, S.-B. Liu, F. Deng, *Phys. Chem. Chem. Phys. Phys. Chem. Chem. Phys* **2011**, *13*, 14889–14901.
- [149] H.-M. Kao, H. Liu, J.-C. Jiang, S.-H. Lin, C. P. Grey, *J. Phys. Chem. B* **2000**, *104*, 4923–4933.
- [150] J. H. Lunsford, *Top. Catal.* **1997**, *4*, 91–98.
- [151] Y. Chu, Z. Yu, A. Zheng, H. Fang, H. Zhang, S.-J. Huang, S.-B. Liu, F. Deng, *J. Phys. Chem. C* **2011**, *115*, 7660–7667.
- [152] J. H. Lunsford, P. N. Tutunjian, P. J. Chu, E. B. Yeh, D. J. Zaleski, *J. Phys. Chem.* **1989**, *93*, 2590–2595.

Appendix

Content

13.1	FCC model component	105
13.1.1	Acidity.....	105
13.1.2	Structure	107
13.2	Single Components	108
13.2.1	XRD	108
13.2.2	²⁷ Al MQ-MAS NMR Spectrum	113
13.2.3	TEM Single Components	114
13.3	Clay and Zeolite	116
13.3.1	Acidity.....	116
13.3.2	Structure	118
13.4	Effect of heat treatment on individual components	119
13.5	²⁷ Al-NMR spectra of the zeolites	122
13.6	FT-IR spectra low crystalline boehmite.....	125
13.6.1	High and low crystalline boehmite.....	125
13.6.2	Washed and not washed clay.....	125
13.7	¹ H-NMR Spectra	126

13.1 FCC model component

In this section the FCC catalyst versus the model component of the FCC is studied to see if the model component was comparable to the real FCC. The acidity and overall structure were studied with CO based FT-IR spectroscopy and XRD respectively. For the FT-IR measurement, the samples were heated to 550 °C for one hour under high vacuum, as described in paragraph 3.2.1. All the spectra were corrected for the weight of the wafer.

13.1.1 Acidity

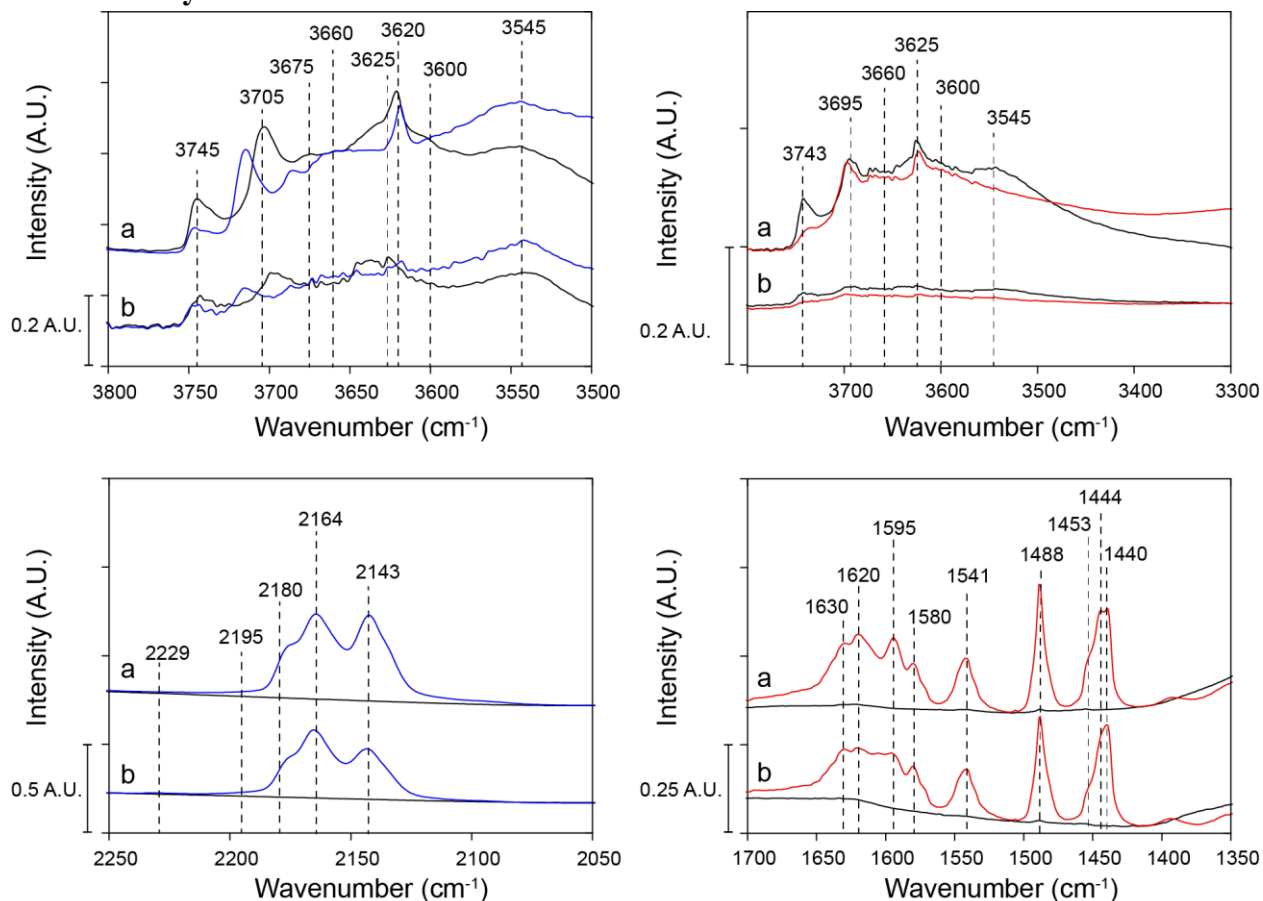


Figure 46 FT-IR spectra of: a. FCC model component, and b. FCC catalyst. The left spectra show the OH (top) and CO (bottom) vibrational region after maximal loading with CO (blue) versus the cooled vacuum spectrum (black). The spectra on the right show the OH (top) and pyridine (bottom) region after being exposed to pyridine vapour for 30 min. (red) versus the cooled vacuum spectrum (black).

In Figure 46 the FT-IR spectra of the FCC catalyst and the real FCC are shown. The OH vibrational region of the real FCC catalyst looks a lot more distorted compared to the real FCC catalyst. The bands in the CO and pyridine vibrational region appear to be almost identical. This shows that both catalysts have a similar acidity. The distortion in the OH vibrational region might be due to the incorporation of additional components to prevent and minimize the deactivation of the FCC catalyst.^[2] The OH vibrations attributed to clay in chapter 6 are not as pronounced in the real FCC, compared to the model component. The overall consumption of the OH peaks seems to be similar in both samples, though it is difficult to identify the OH bands which is consumed.

Figure 47 depicts the FT-IR spectra of the samples after minimal CO loading and remaining pyridine at 550 °C. The first CO loading is experimentally to give rise to bands which are associated with the strongest acid sites in the samples.

Both the CO and pyridine measurement confirm that also the amount acid sites are comparable for the FCC catalysts. The positive shift of the clay peak at 3700 cm^{-1} is visible in the CO-OH vibrational region, indicating that most likely similar interactions are present in the real FCC compared to the model component.

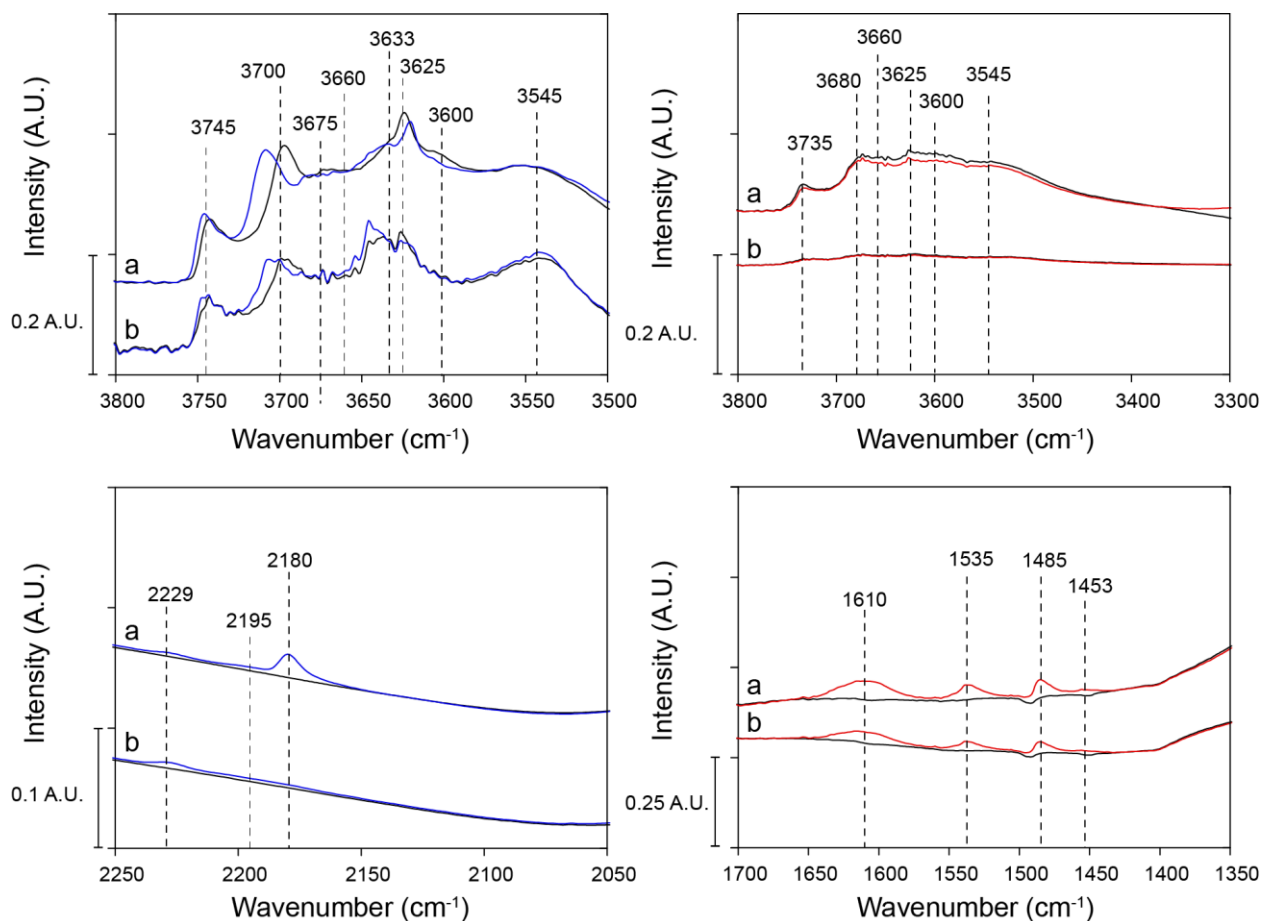


Figure 47 FT-IR spectra of: a. FCC model component b. FCC catalyst. The left spectra show the OH (top) and CO (bottom) vibrational region after minimal loading with CO (blue) versus the vacuum cooled spectra (black). The spectra on the right show the OH (top) and pyridine (bottom) region after being exposed to pyridine vapour for 30 min. and subsequently heating the samples to 550 °C (red) versus the vacuum spectrum at 550 °C (black) as described in paragraph 3.2.1.

Overall the acidity seems to be very alike for the two FCC catalysts. This proves that the model component is a good representation of the real FCC.

13.1.2 Structure

To further verify that the FCC model component is a good representation of the real FCC the structure was determined with XRD. The FCC catalysts were not heated before measuring the XRD, since the binder and clay lose their crystallinity when heated to 550 °C, as shown in chapter 8. Figure 48 displays the diffractogram of both the FCC and the model component.

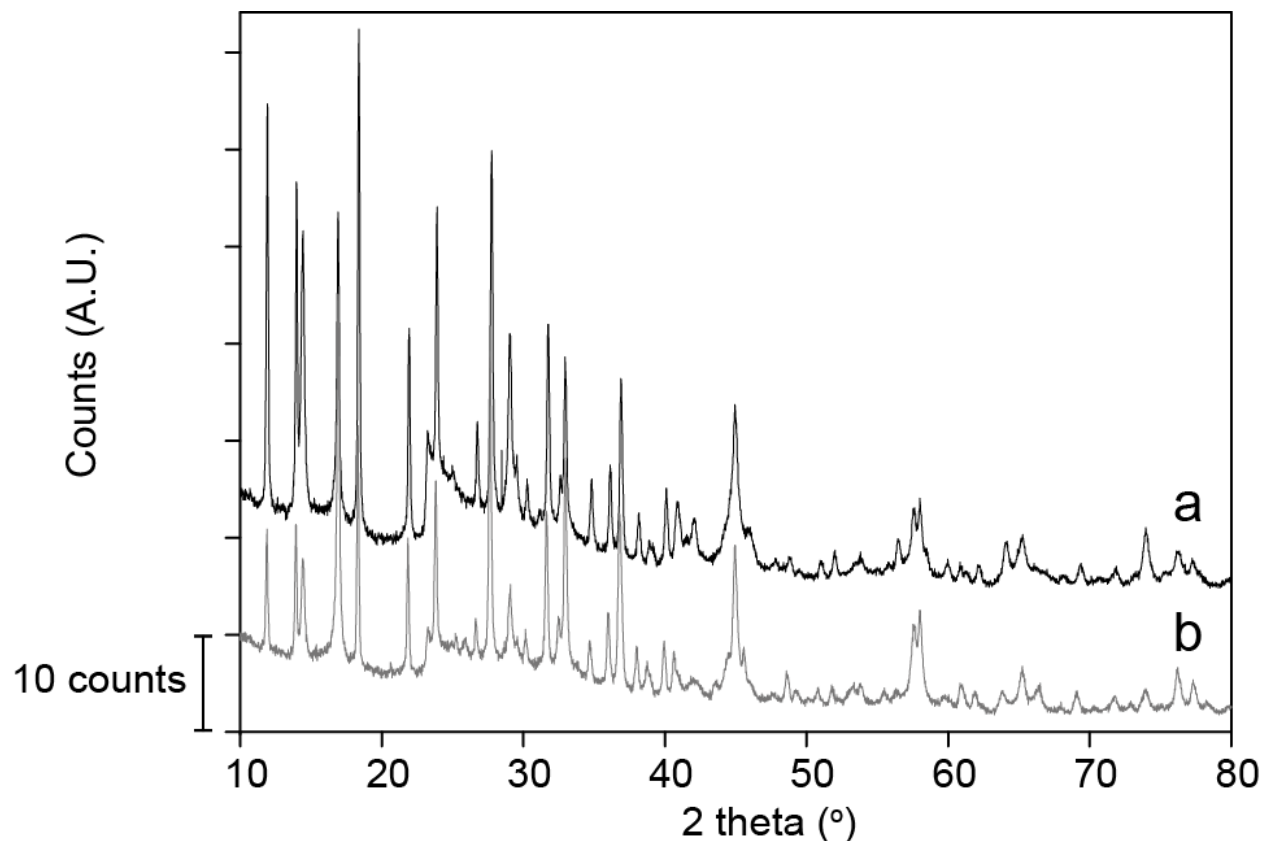


Figure 48 XRD diffractogram displaying the crystallinity of: a. FCC catalyst b. Real FCC catalyst with additional components. Though the intensity of the peaks might not exactly be the same the overall composition is similar, proving that the model component is indeed a good model component for the FCC.

It is clear from Figure 48 that there are no clear differences in crystallinity of the different FCC catalysts. The slight differences in peak intensities could be due to slight changes in the unit cell, which might be an effect of the preparation.

13.2 Single Components

13.2.1 XRD

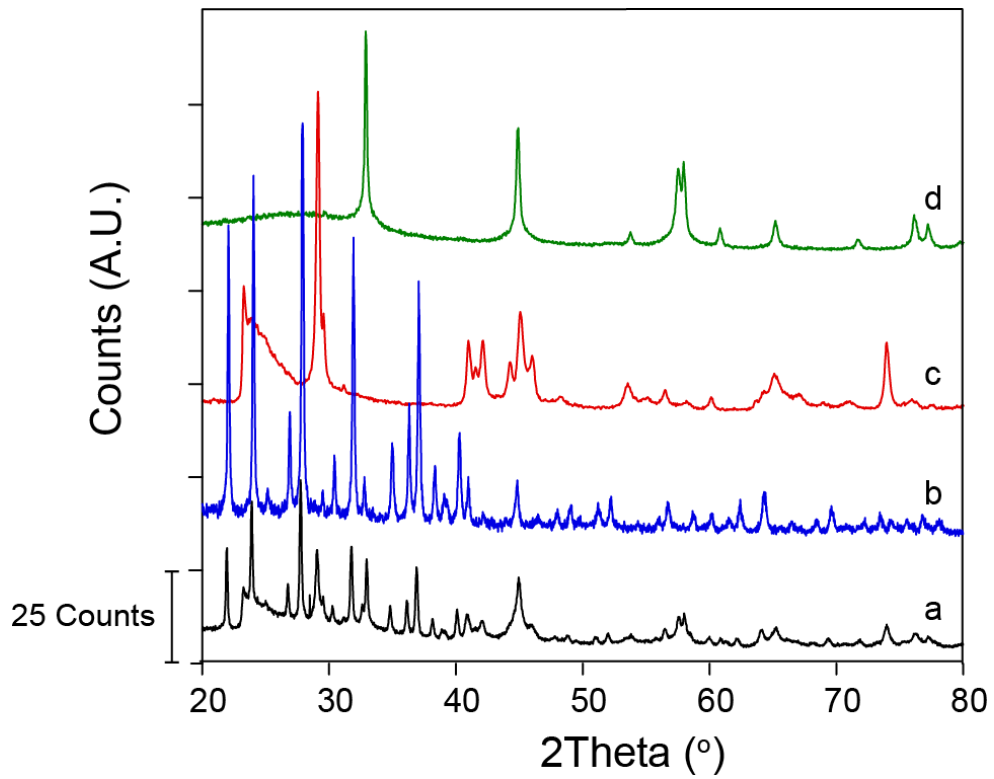


Figure 49 XRD diffractograms of all the components in the FCC, before heating. a. FCC catalyst b. Zeolite HY Si/Al 7 c. Clay d. Binder.

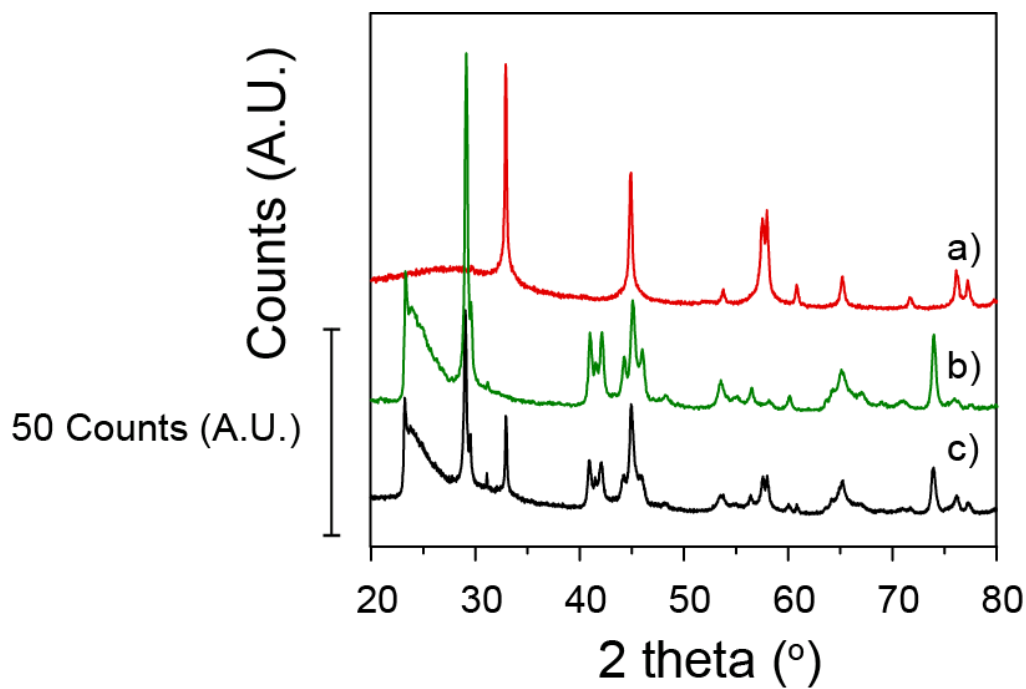


Figure 50 XRD diffractograms of a. Binder b. Clay c. Binder-clay mix

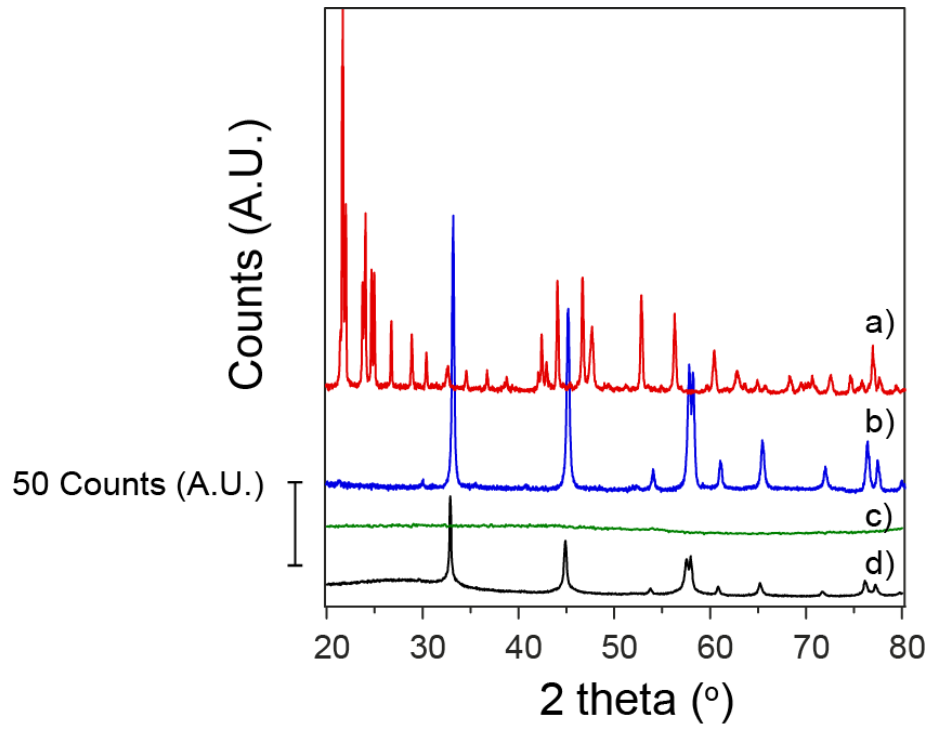


Figure 51 XRD diffractograms of a. *Low crystalline boehmite* b. *High crystalline boehmite* c. *Alumina* d. *Binder*

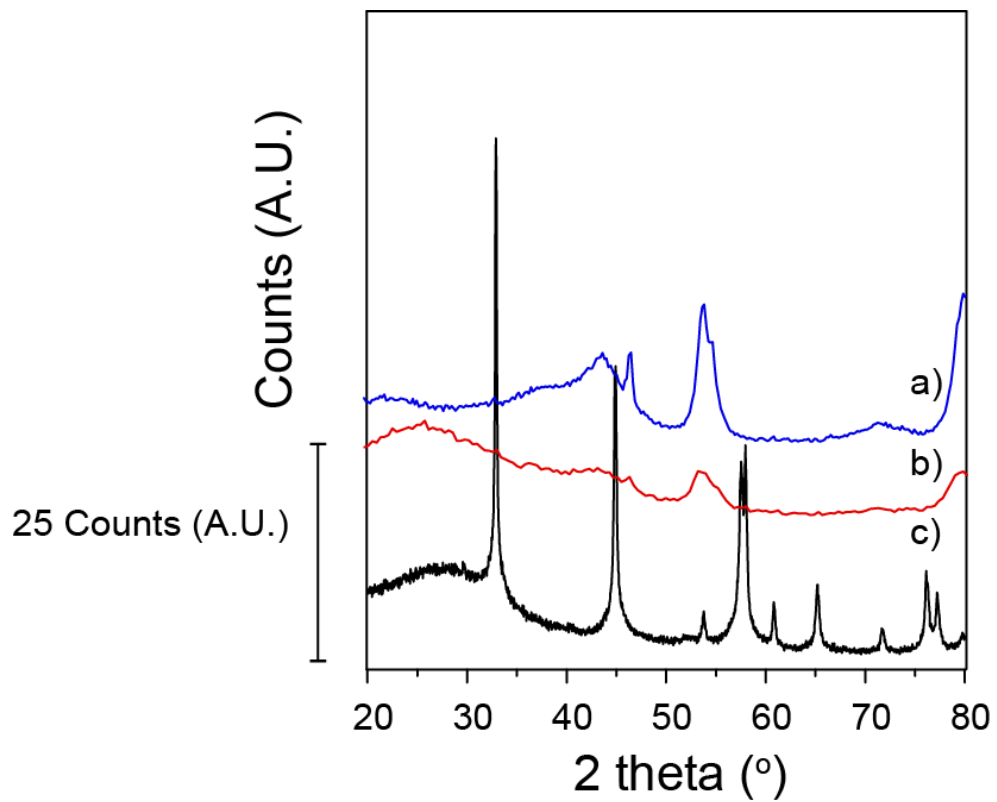


Figure 52 XRD diffractograms of a. *Heated boehmite* b. *Heated binder* c. *Binder*

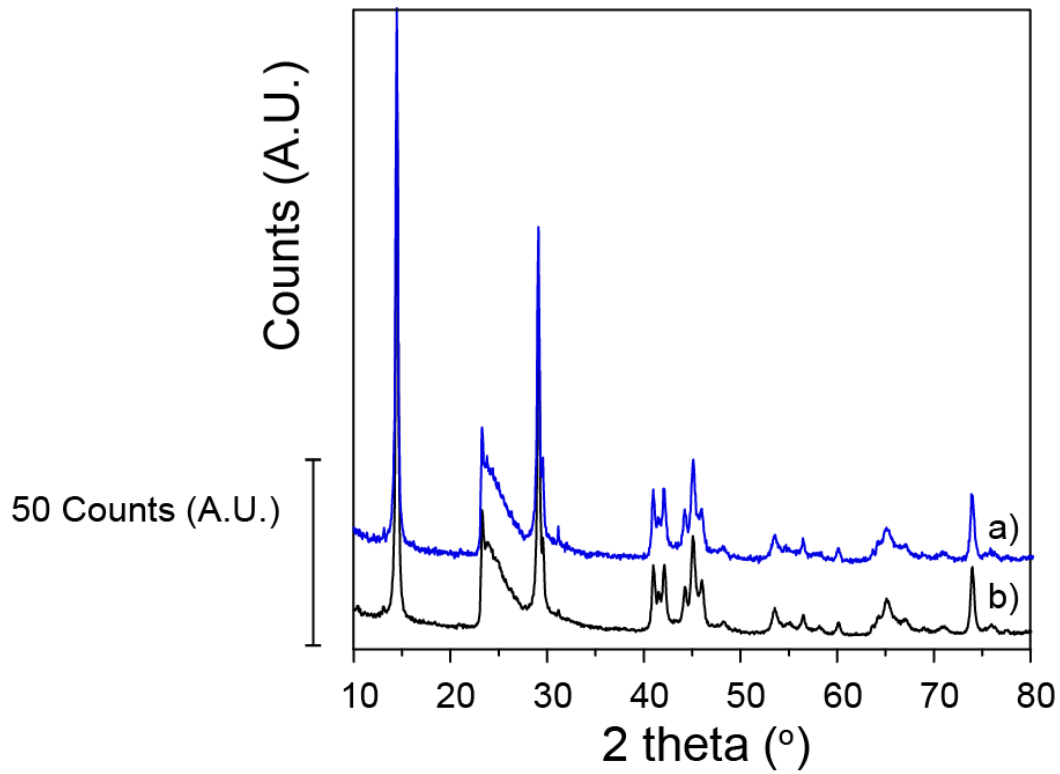


Figure 53 XRD diffractograms of a. Washed clay b. Not-washed clay

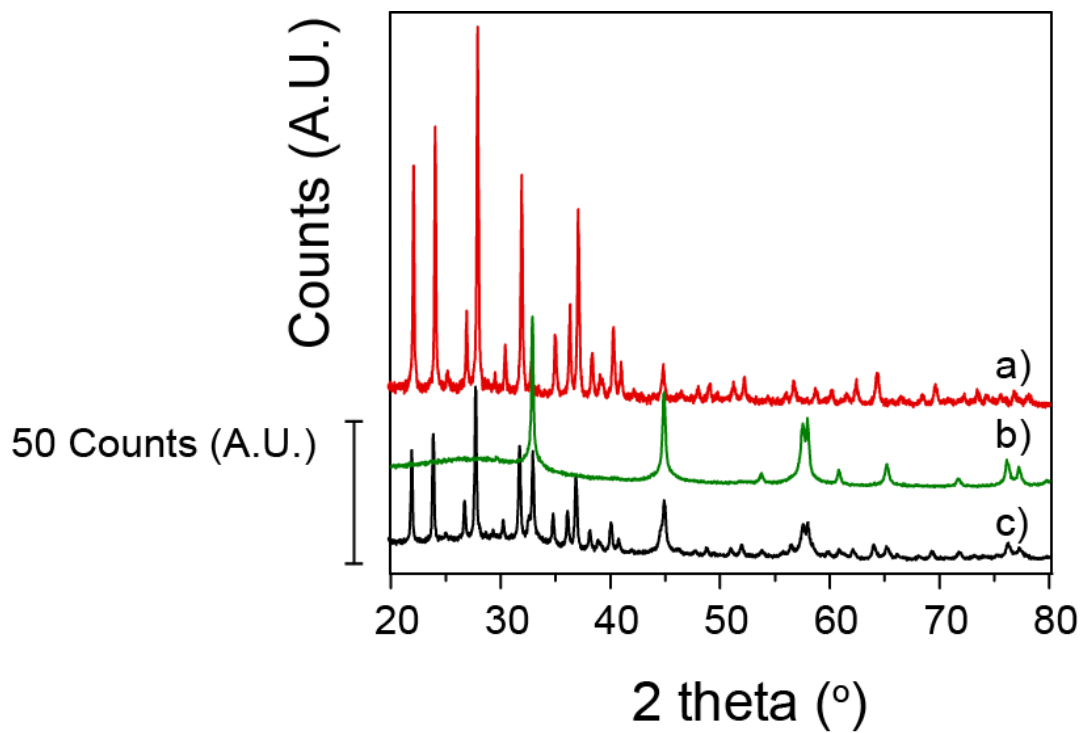


Figure 54 XRD diffractograms of a. Zeolite HY Si/Al 7 b. Binder c. Binder-zeolite mix

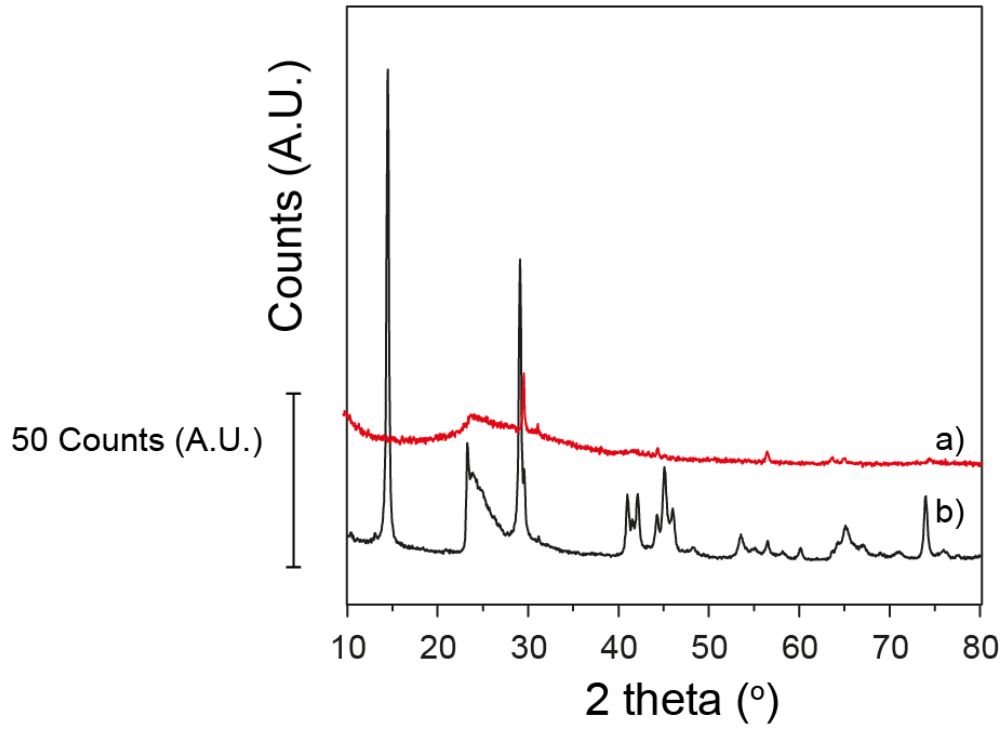


Figure 55 XRD diffractograms of *a. Heated clay* *b. Not-heated clay*

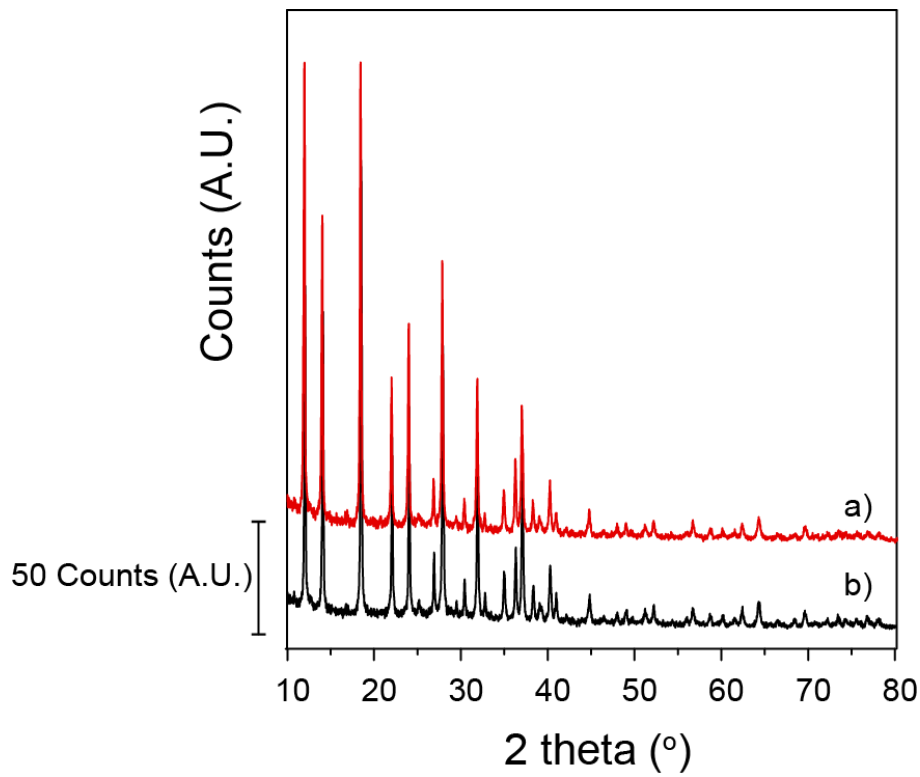


Figure 56 XRD diffractograms of *a. Heated Zeolite HY Si/Al 7* *b. Not-heated Zeolite HY Si/Al 7*

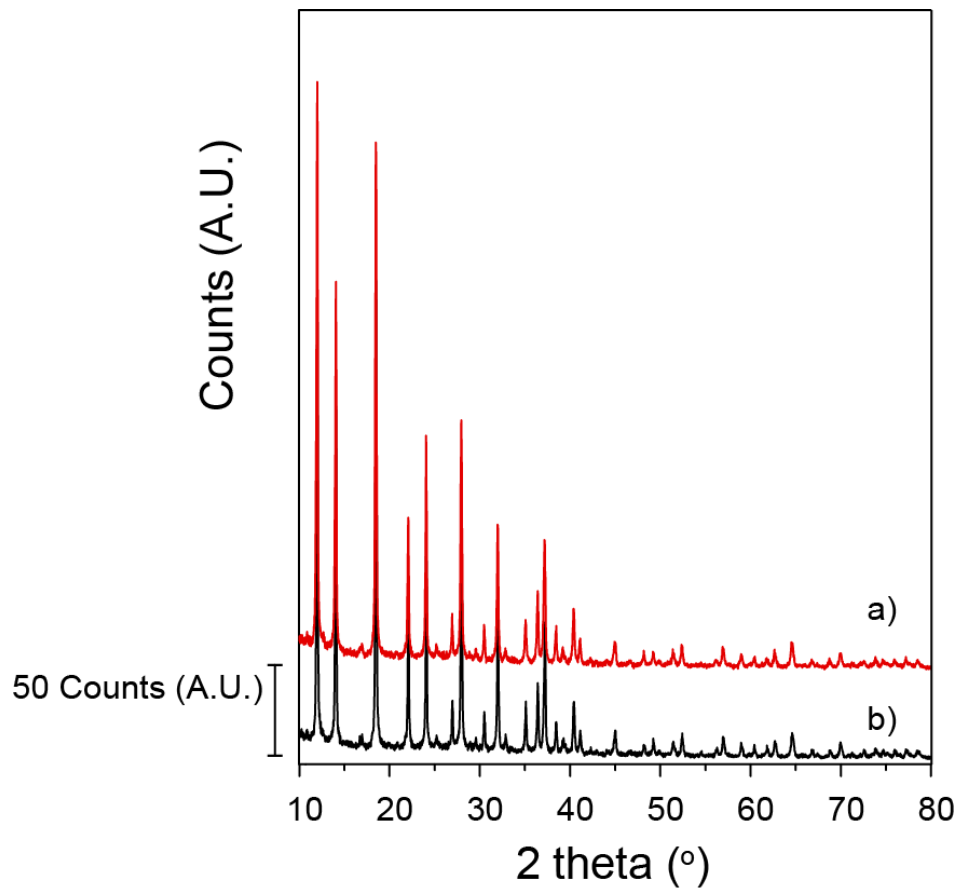


Figure 57 XRD diffractograms of *a. Heated Zeolite HY Si/Al 30* *b. Not-heated Zeolite HY Si/Al 30*

13.2.2 ^{27}Al MQ-MAS NMR Spectrum

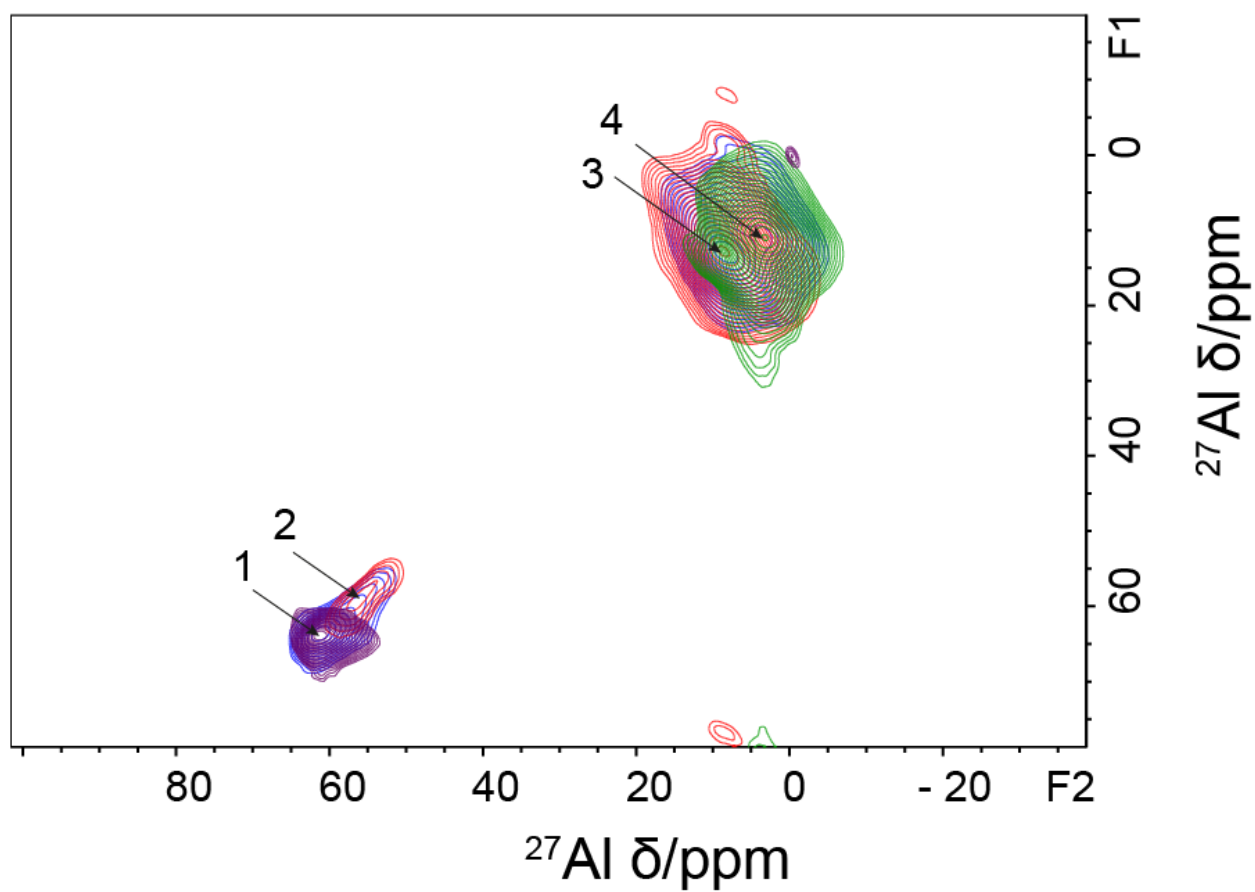


Figure 58 ^{27}Al MQ-MAS of the FCC and individual components before heating. *Blue: FCC, Green: Clay, Red: Binder, Purple: Zeolite HY Si/Al 30*

13.2.3 TEM Single Components

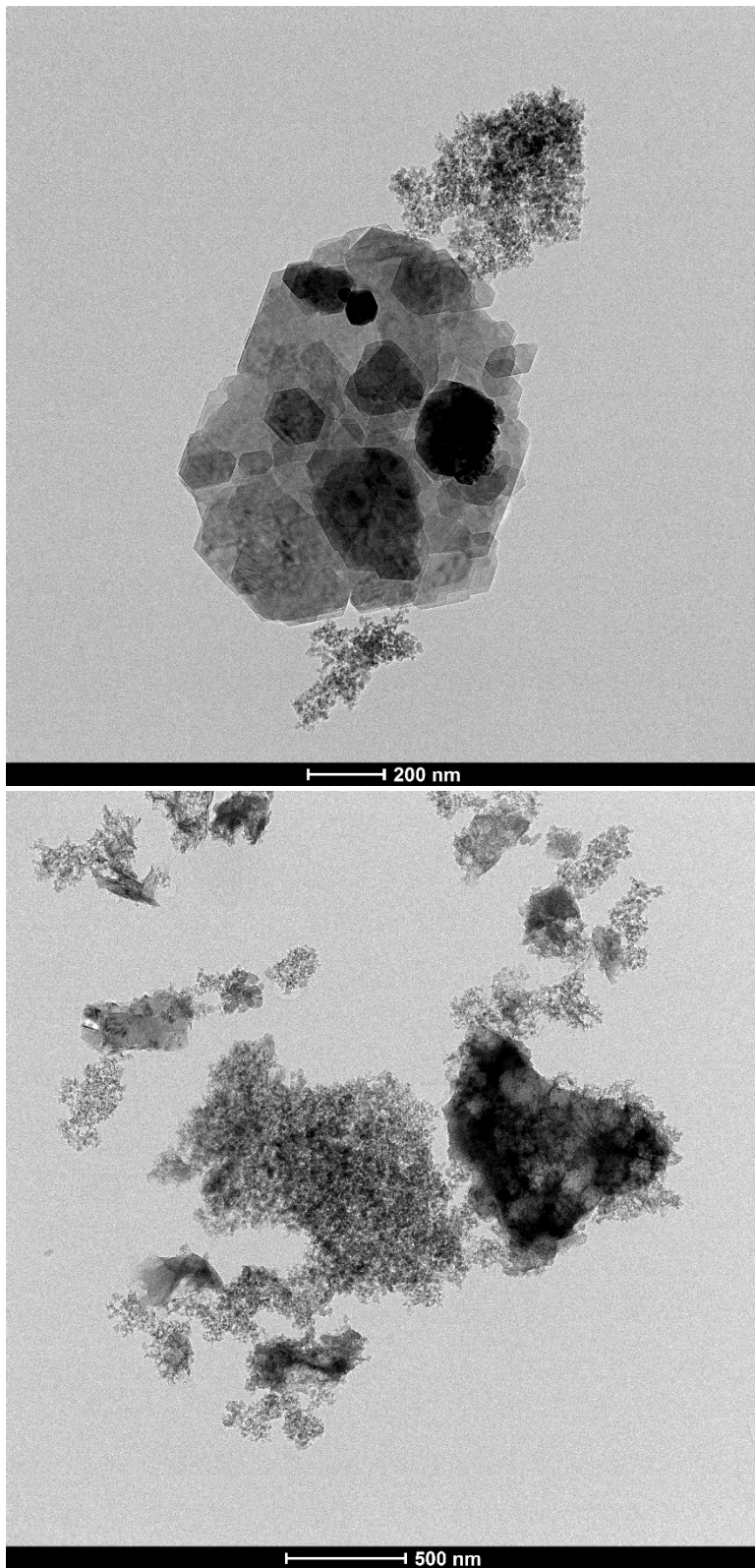


Figure 59 TEM images of the binder before heating. The small spherical parts above and below are silica. The big crystals originates from the high crystalline boehmite, whereas the rod like structures in the bottom image are low crystalline boehmite. The grain like structure originates from the silica.

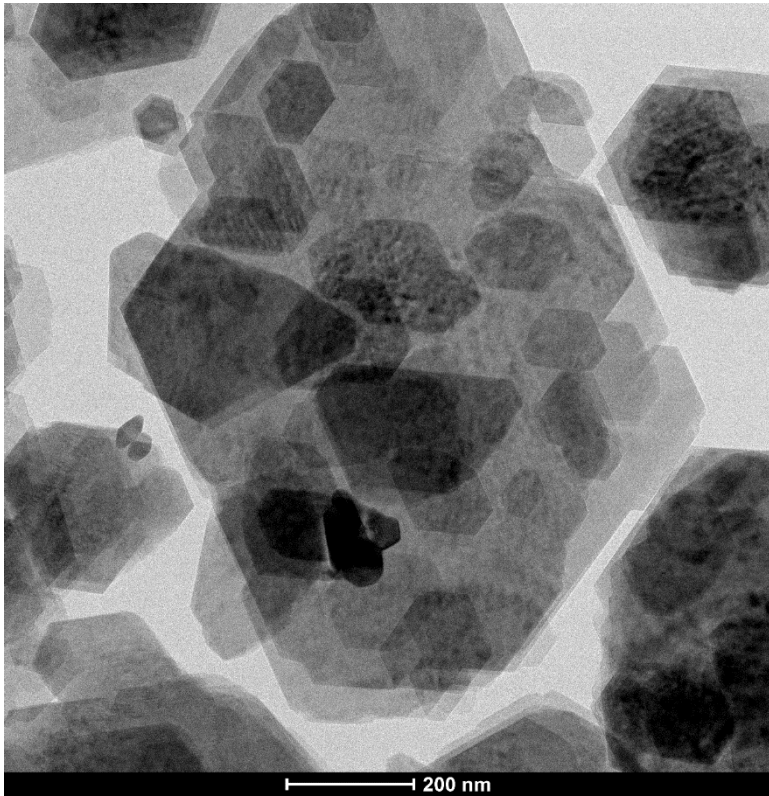


Figure 60 TEM image of the clay before heating, showing the crystalline structure of the kaolinite.

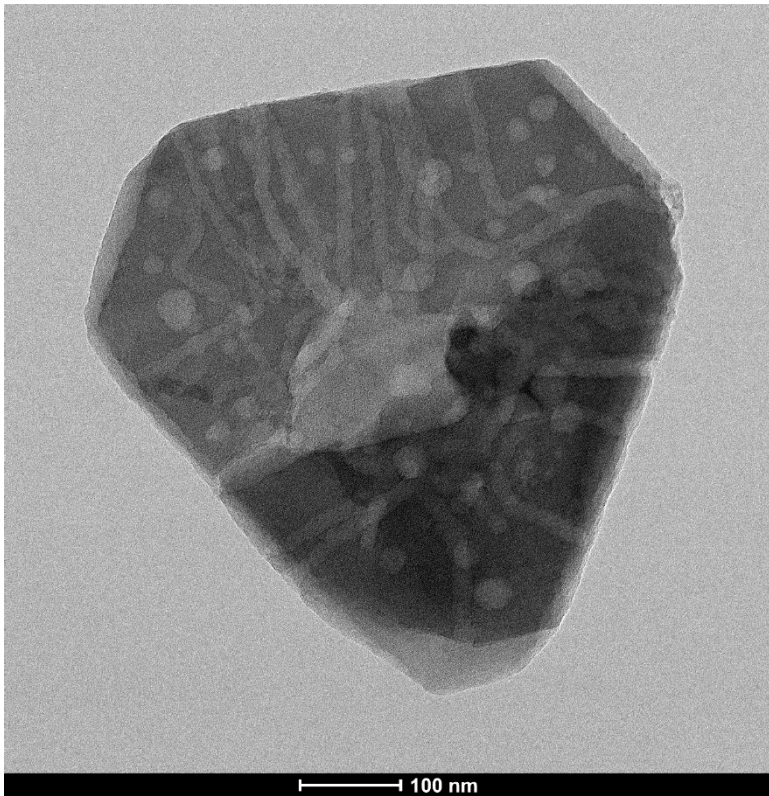


Figure 61 TEM image of one zeolite crystal before heating. the structure shows some clear mesopores.

13.3 Clay and Zeolite

A physical mixture of Zeolite HY Si/Al 30 and the clay was made by grinding equal amounts of clay and zeolite together. The acidity and overall structure were studied with CO based FT-IR and ^{27}Al MQ-MAS respectively. For the FT-IR measurement, the samples were heated to 550 °C for one hour under high vacuum, as described in paragraph 3.2.1. All the spectra were corrected for the weight of the wafer.

14.3.1 Acidity

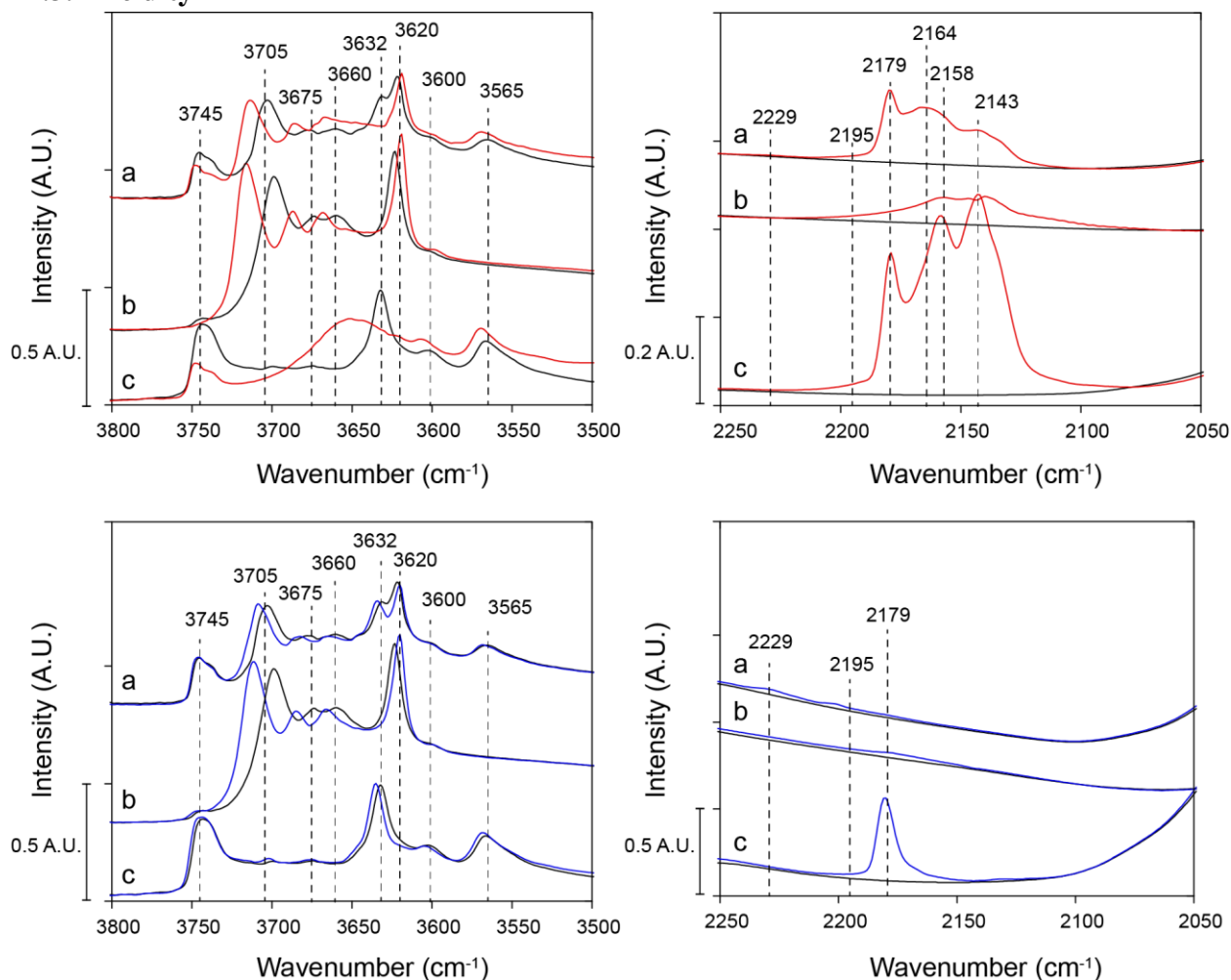


Figure 62 FT-IR spectra of: a. Clay-zeolite mixt, b. Clay, c. Zeolite HY Si/Al 30. The top spectra show the OH (left) and CO (right) vibrational region after maximal loading with CO (blue) versus the cooled vacuum spectrum (black). The bottom two spectra show the OH (left) and CO (right) vibrational region after minimal loading with CO (blue) versus the vacuum cooled spectra (black).

A slight increase in Lewis acidity is found in the CO measurements, along with a very strong decrease of the amount of Brønsted acid sites. In the OH vibrational region a perfect addition of the two components is visible.

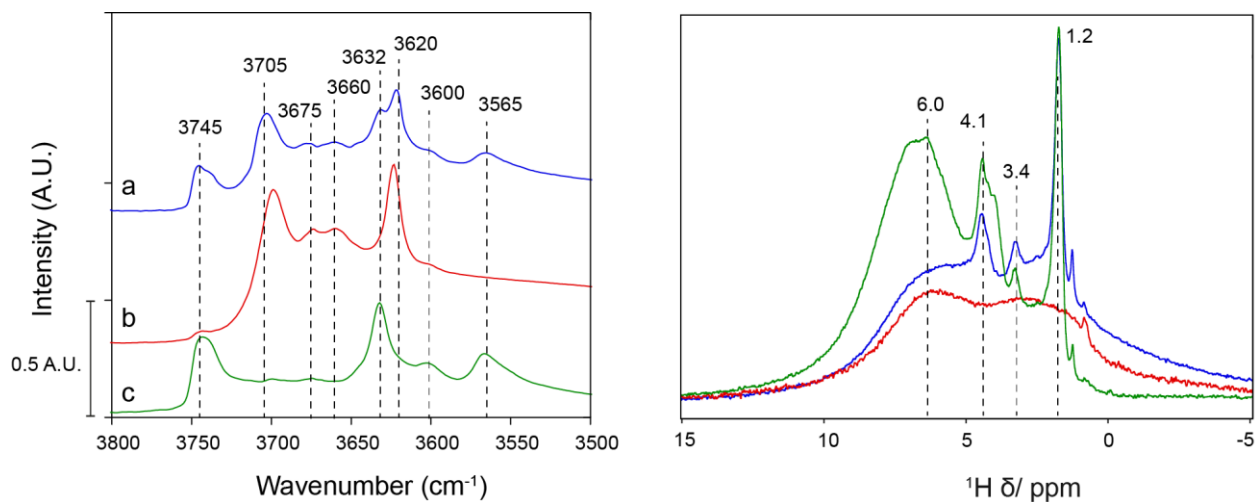


Figure 63 Left: IR spectrum of the OH region under vacuum at $-188\text{ }^{\circ}\text{C}$. Right: $^1\text{H-NMR}$ of the heat-treated samples. 1. Zeolite-clay 2. Clay 3. Zeolite HY Si/Al 30

In Figure 63 the OH vibrational region and $^1\text{H-NMR}$ spectra of the zeolite-clay mix are depicted along with the single components. a very strong decrease of the peaks at 6 ppm can be observed, along with a decrease of the Brønsted acidic peaks at 4.1 and 3.4 ppm. This indicates that indeed the clay diminishes the overall acidity of the zeolite.

13.3.2 Structure

The samples were heated for one hour at 538 °C, as described in paragraph 3.2.2.

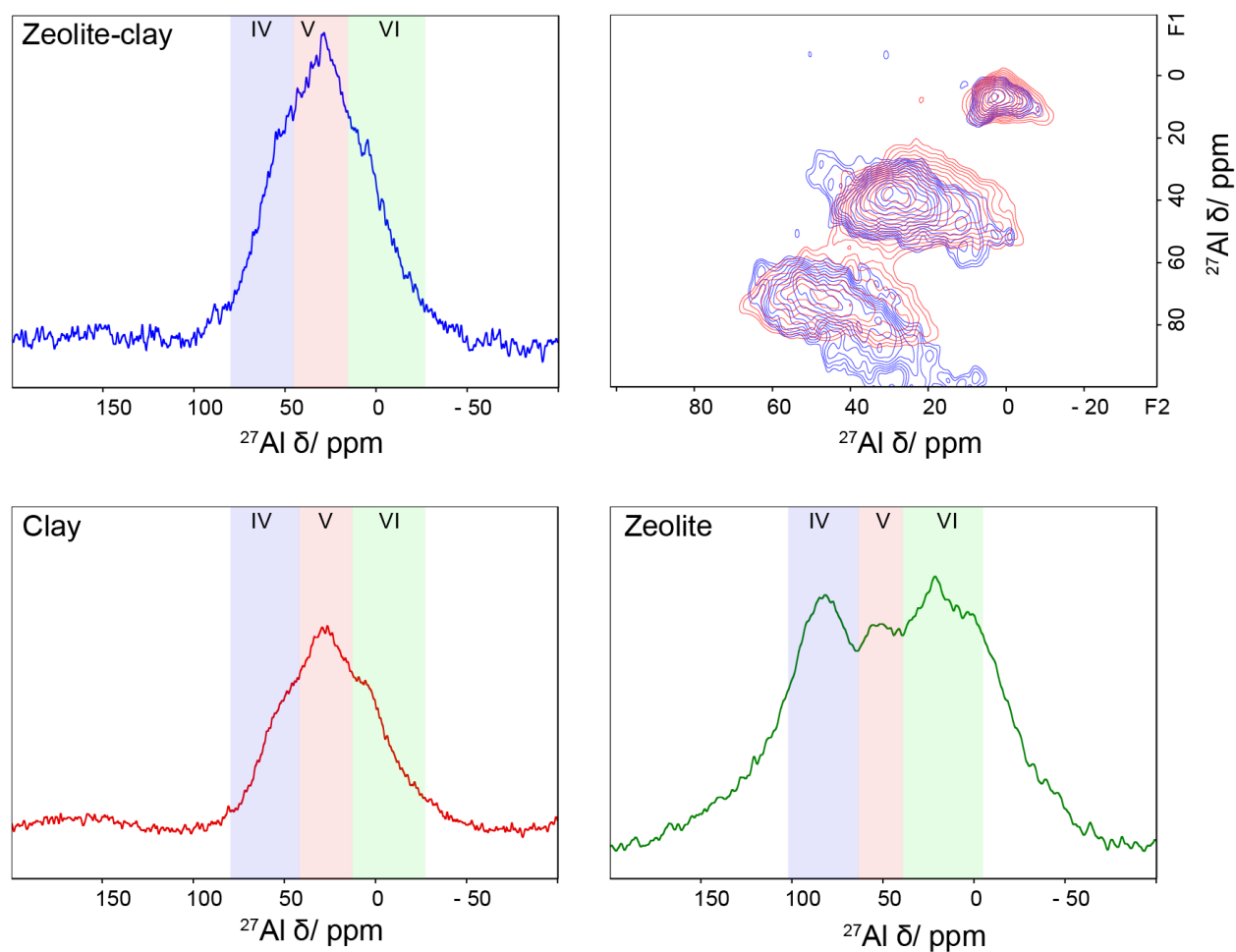


Figure 64 ^{27}Al MAS spectra of the zeolite-clay mix and the individual components. *Blue: Zeolite-clay, Red: Clay, Green: Zeolite HY Si/Al 30* Top right: ^{27}Al MQ-MAS overlay of the zeolite-clay mix and the clay.

The aluminium coordinations present in the zeolite-clay mix are most similar to the clay, based on the ^{27}Al MAS spectra. This is probably due to the relatively low concentration of aluminium in the zeolite.

13.4 Effect of heat treatment on individual components

In this section the different ^{27}Al MQ-MAS spectra of several samples are shown before and after heating. Most often the octahedral peak remains in approximately the same region, whereas large changes occur for the tetrahedral region. None of the samples contain a penta-coordinated peak before heating and can therefore exclusively be ascribed to EF aluminium species.

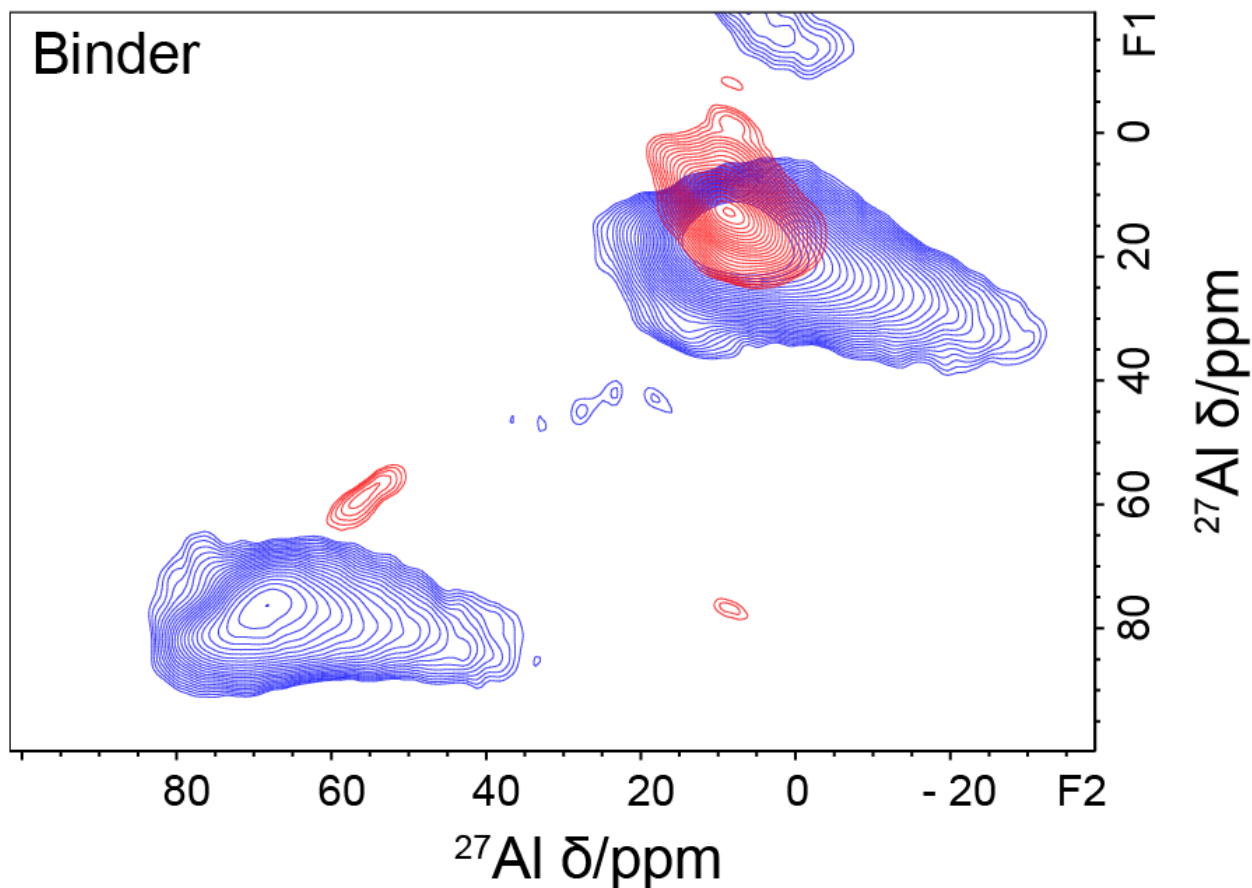


Figure 65 ^{27}Al MQ-MAS of the binder *before* (red) and *after heating* (blue)

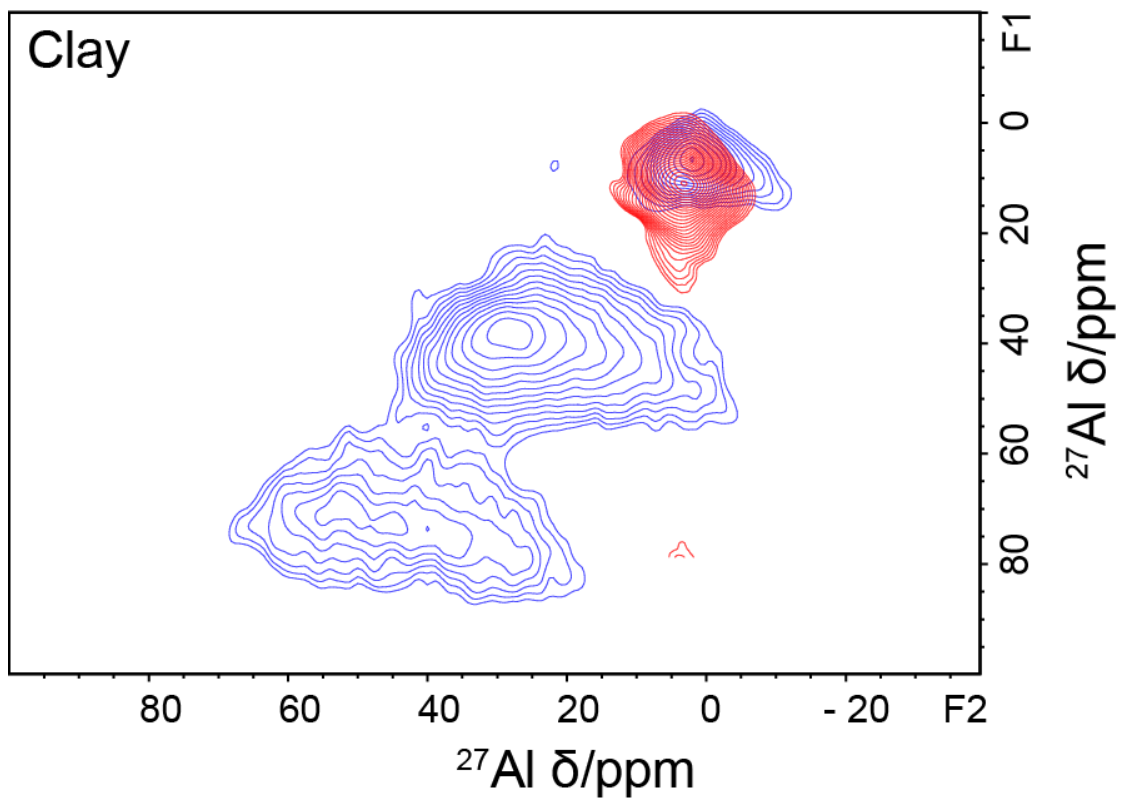


Figure 66 ^{27}Al MQ-MAS of the clay *before* (red) and *after heating* (blue)

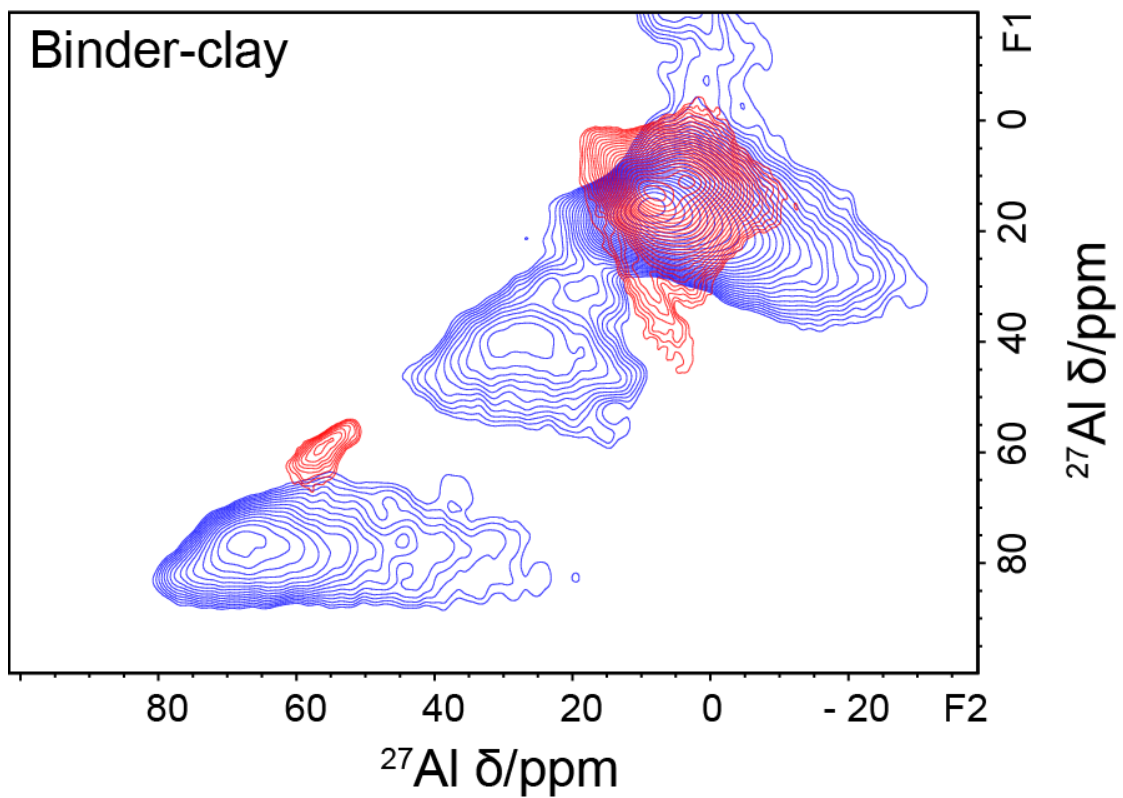


Figure 67 ^{27}Al MQ-MAS of the binder-clay mix *before* (red) and *after heating* (blue)

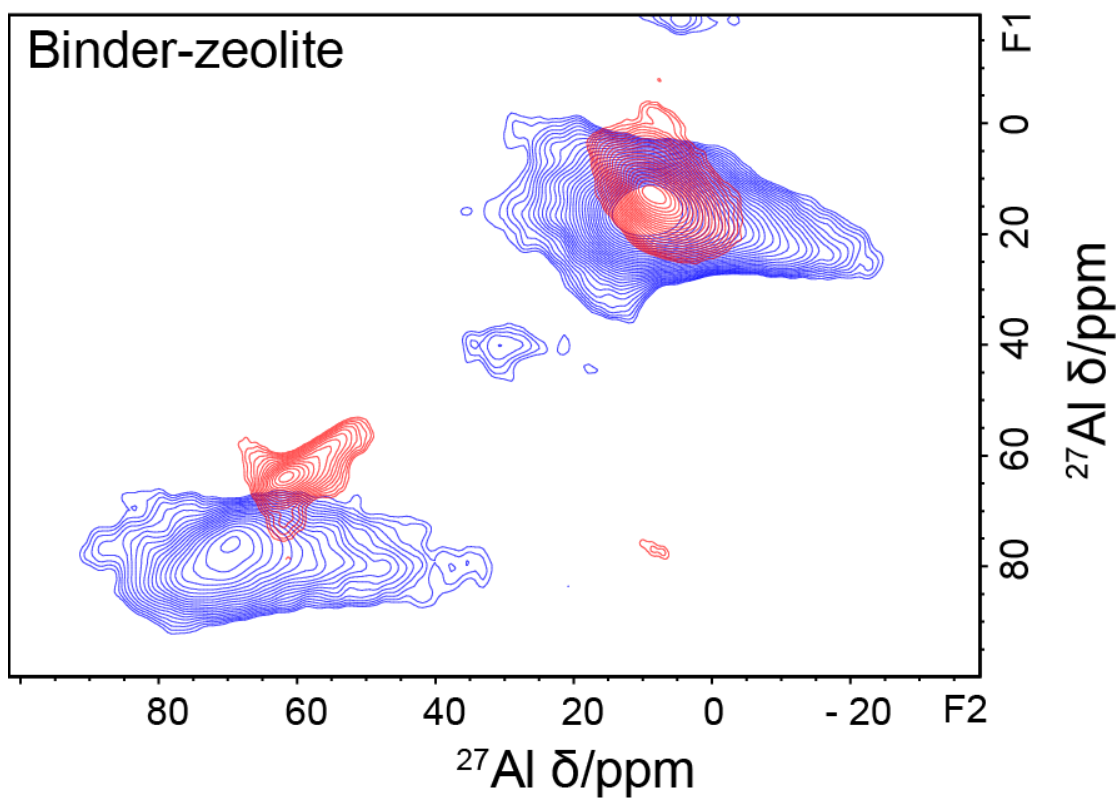


Figure 68 ^{27}Al MQ-MAS of the binder-zeolite mix before (red) and after heating (blue)

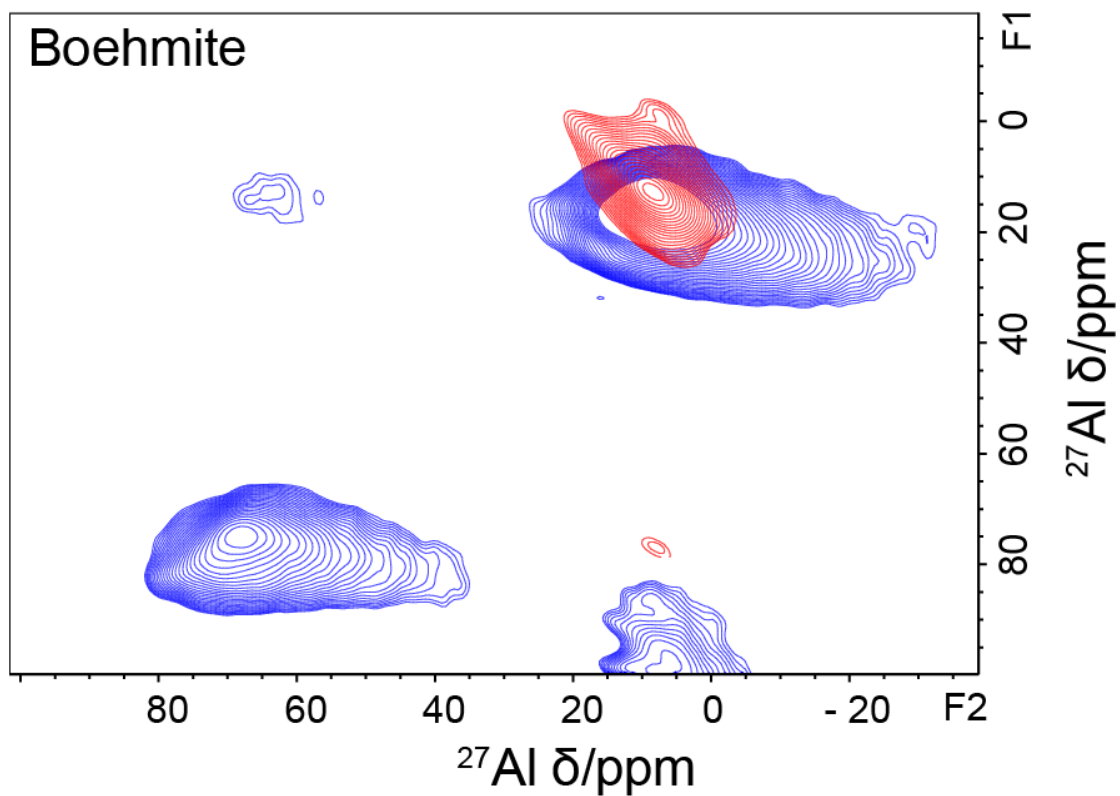


Figure 69 ^{27}Al MQ-MAS of the boehmite mix before (red) and after heating (blue)

13.5 ^{27}Al -NMR spectra of the zeolites

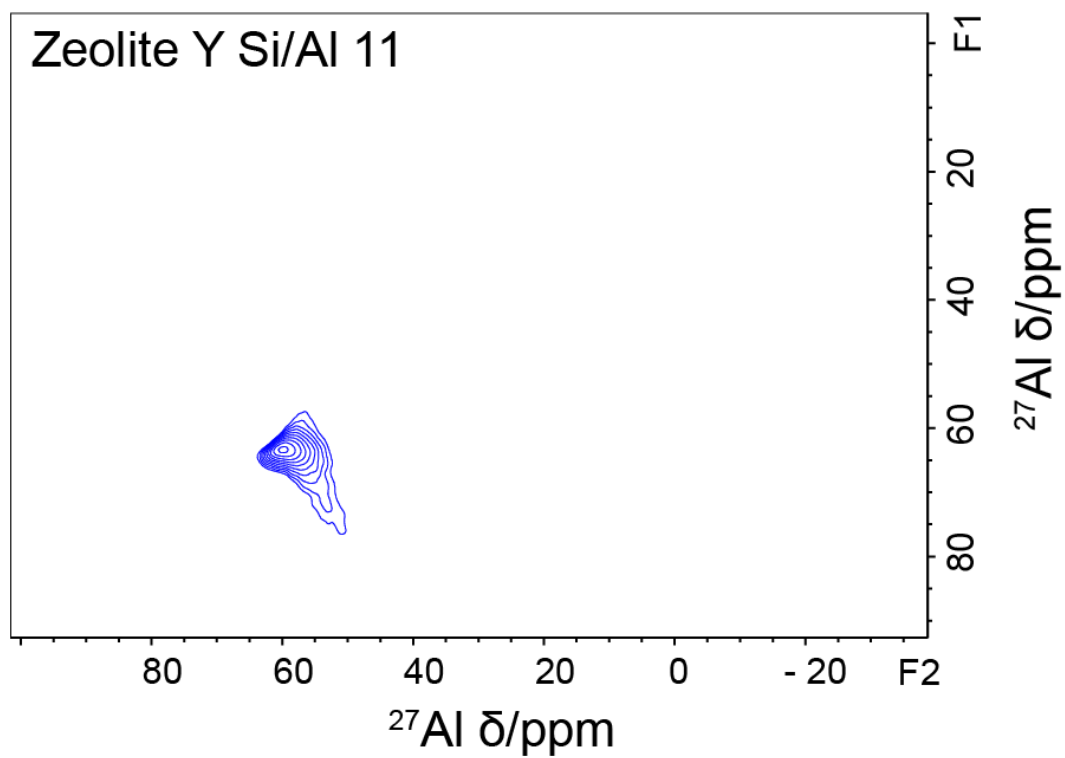


Figure 70 ^{27}Al MQ-MAS of zeolite HY Si/Al 11

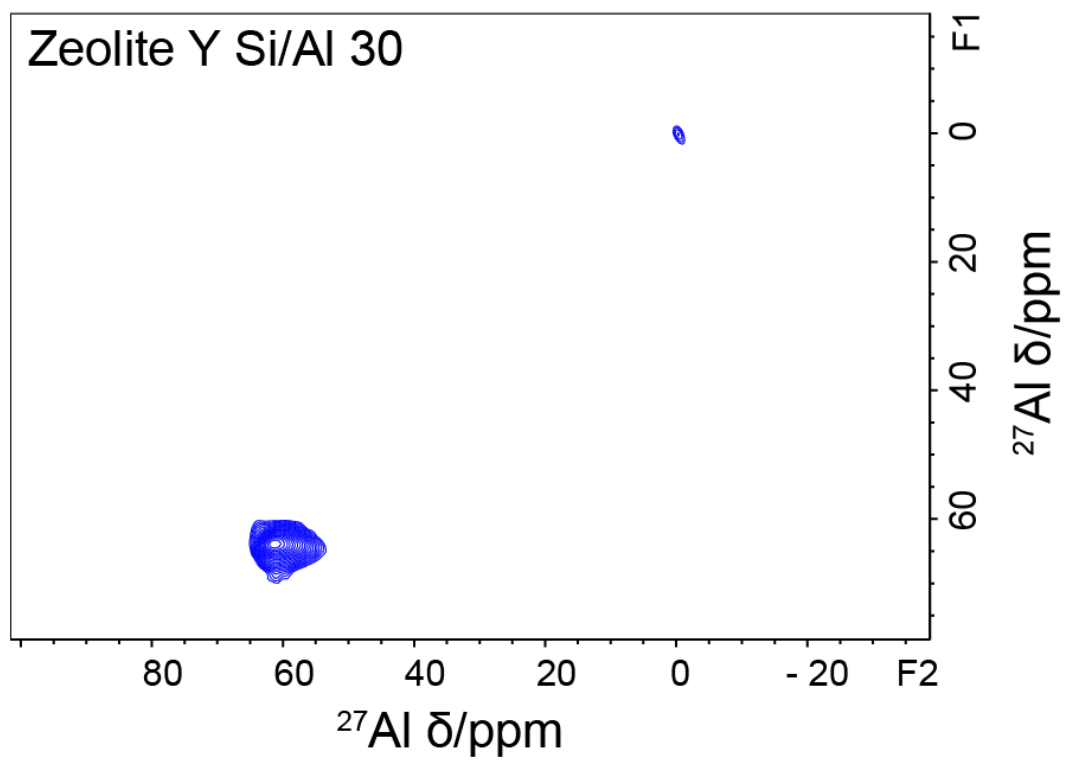


Figure 71 ^{27}Al MQ-MAS of zeolite HY Si/Al 30

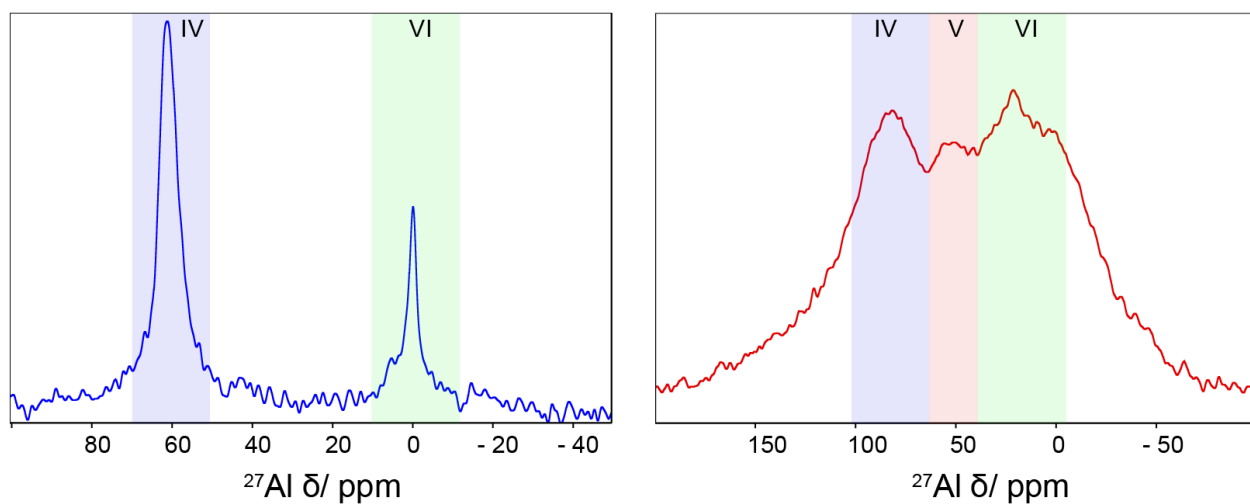


Figure 72 ^{27}Al MAS of zeolite HY Si/Al 30 *before* (left) and *after heating* (right)

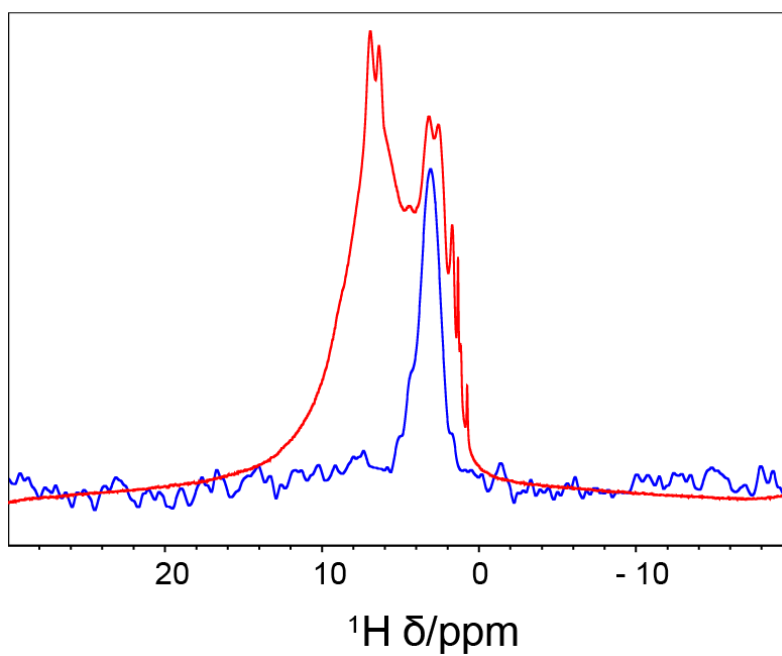


Figure 73 ^1H -NMR spectrum (red) and $\{^{27}\text{Al}-^1\text{H}\}$ NMR spectrum (blue) of Zeolite Si/Al 7. The intensity is normalized with respect to the most intense peak in the $\{^{27}\text{Al}-^1\text{H}\}$ NMR spectrum

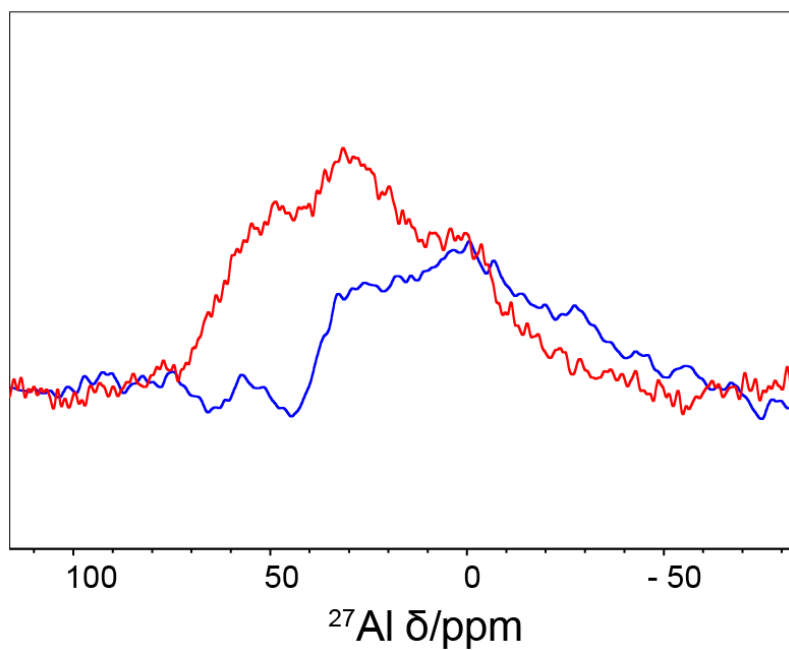


Figure 74 ^{27}Al -NMR spectrum (red) and $\{^1\text{H}-^{27}\text{Al}\}$ NMR spectrum (blue) of Zeolite Si/Al 7. The intensity is normalized with respect to the most intense peak in the $\{^1\text{H}-^{27}\text{Al}\}$ NMR spectrum

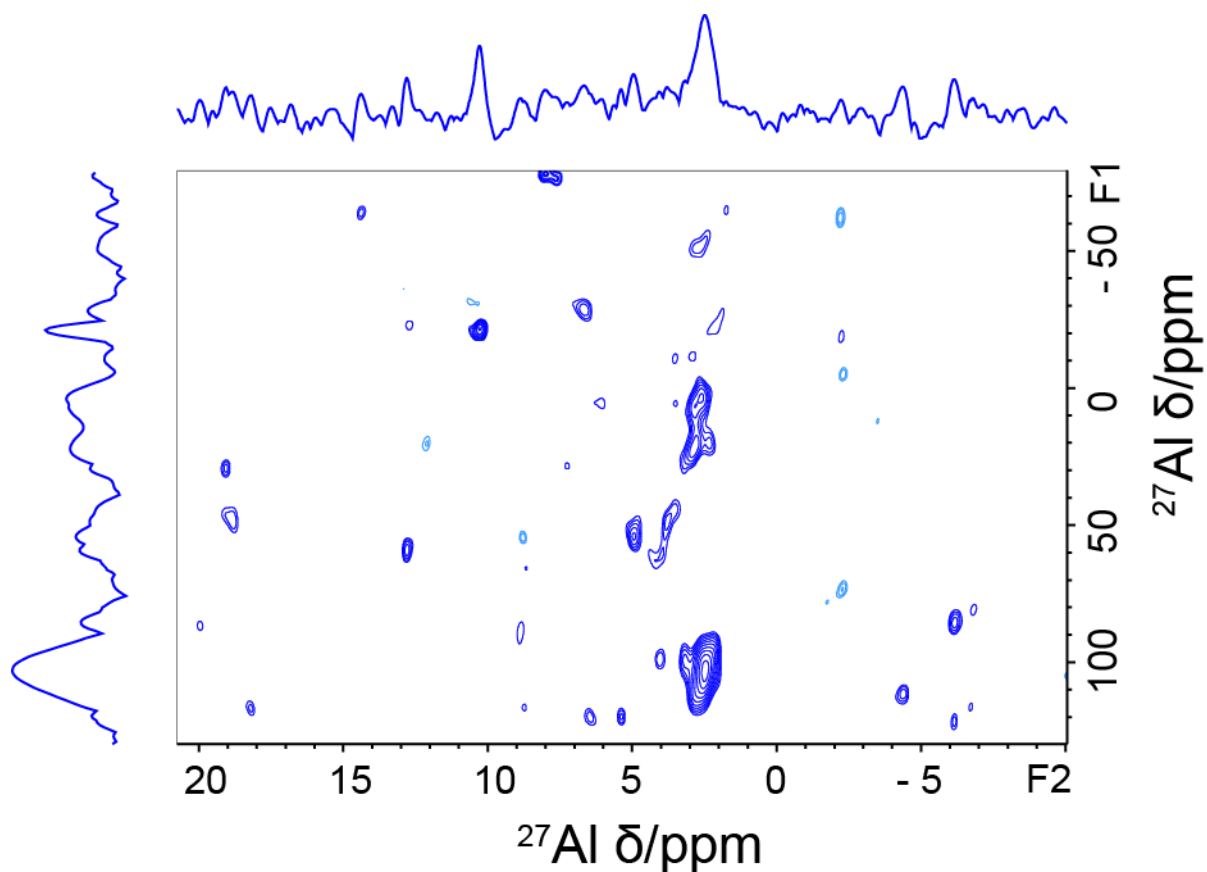


Figure 75 MQ-HETCOR spectrum of zeolite HY Si/Al 7. On the F1 axis is the ^{27}Al MAS-NMR spectrum. On the F2 axis is the ^1H -NMR spectrum.

13.6 FT-IR spectra low crystalline boehmite

13.6.1 High and low crystalline boehmite

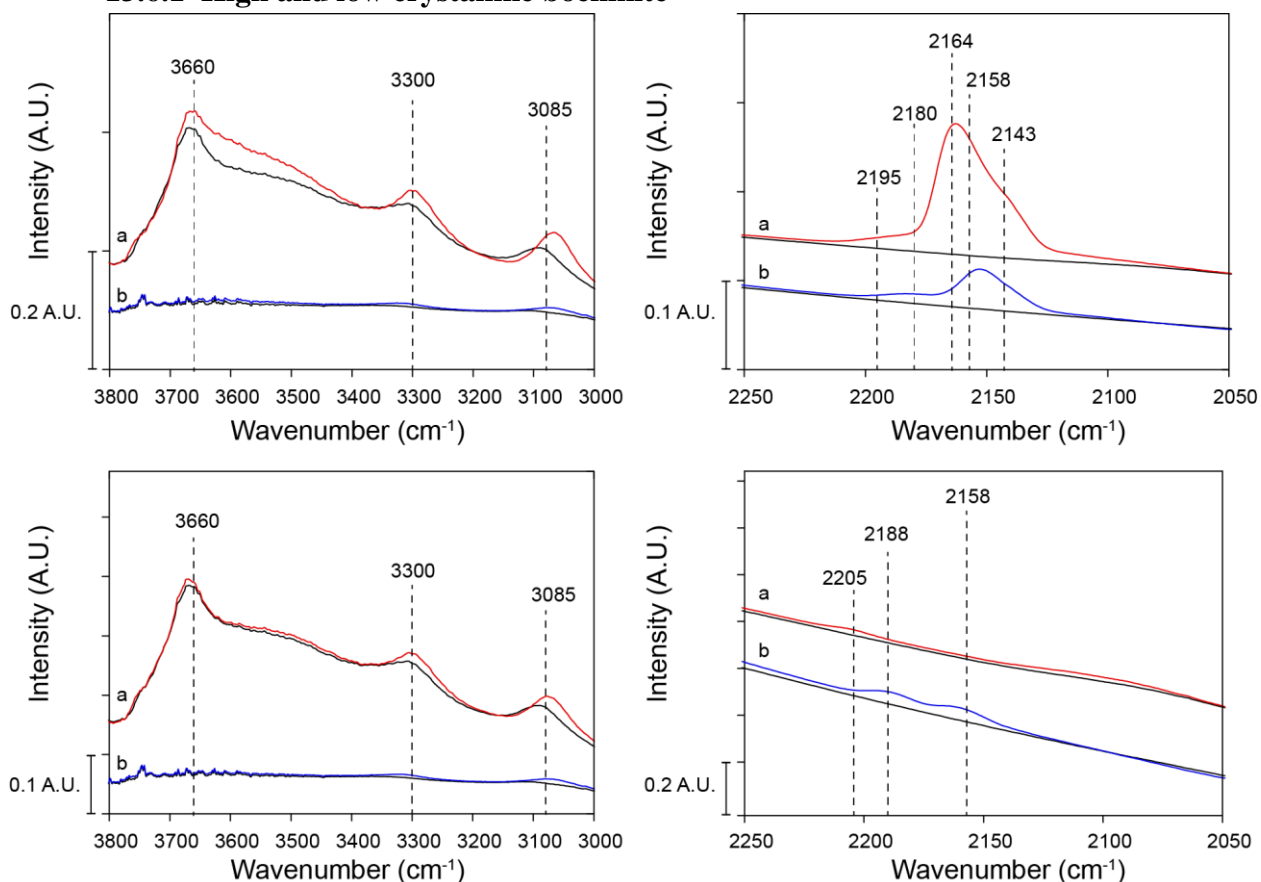


Figure 76 FT-IR spectra of high crystalline boehmite (a) and low crystalline boehmite (b). The left spectra show the OH (top) and CO (bottom) vibrational region after maximal loading with CO (red) versus the cooled vacuum spectrum (black). The right two spectra show the OH (top) and CO (bottom) vibrational region after minimal loading with CO (red) versus the vacuum cooled spectra (black).

13.6.2 Washed and not washed clay

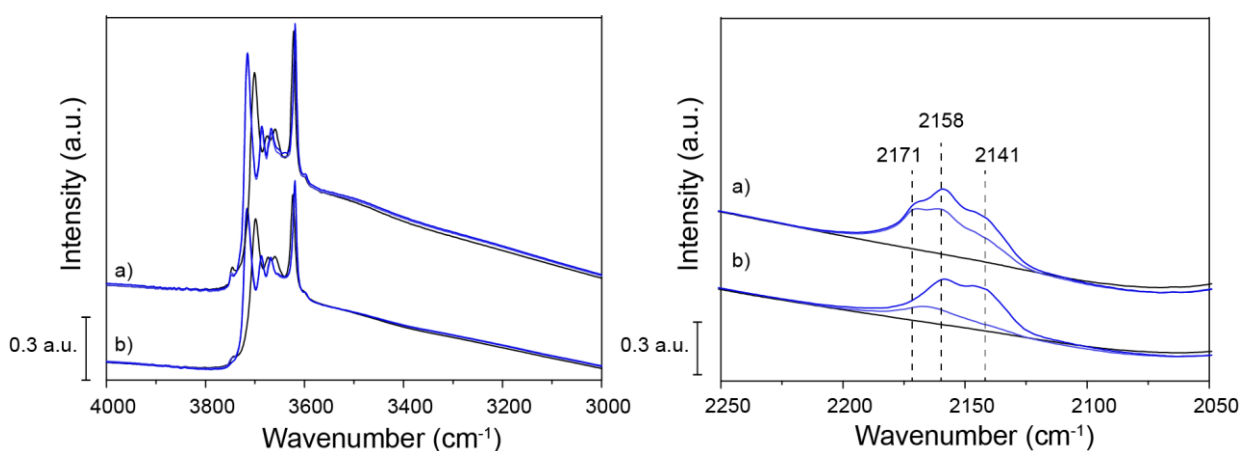


Figure 77 FT-IR spectra of washed clay (a) and not washed clay (b). The left spectra show the OH vibrational region. The right spectra show the CO vibrational region upon increasing loading of CO.

13.7 ^1H -NMR Spectra

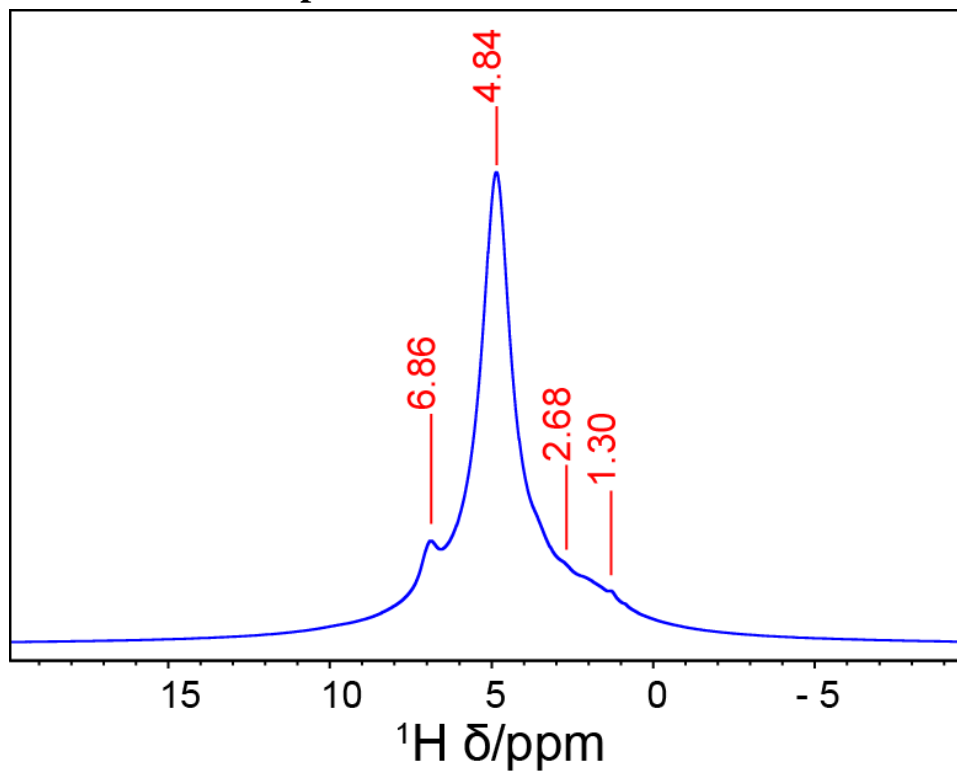


Figure 78 ^1H -NMR spectrum of the FCC catalyst before the heat-treatment

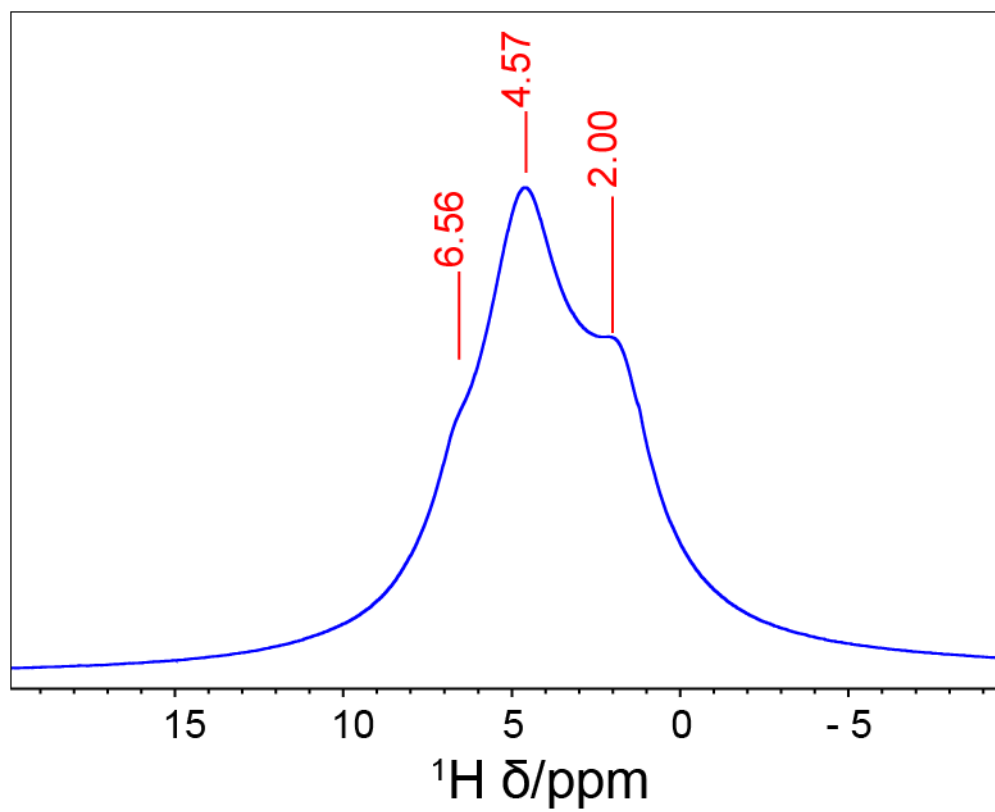


Figure 79 ^1H -NMR spectrum of the binder-clay mix before the heat-treatment

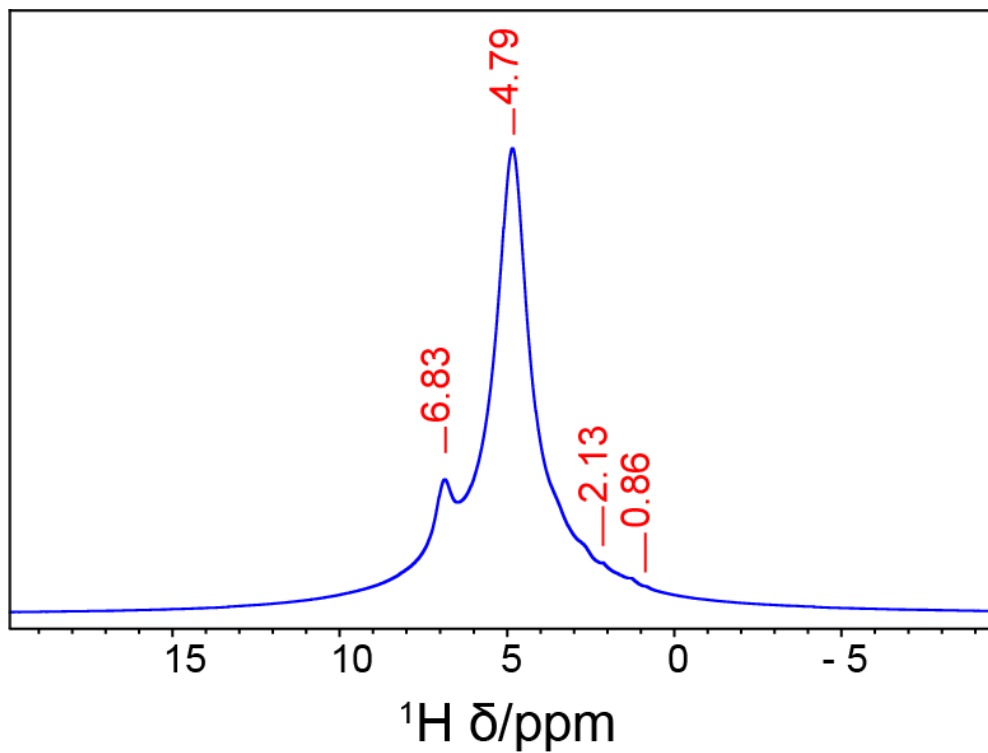


Figure 80 ^1H -NMR spectrum of the binder-zeolite mix before the heat-treatment

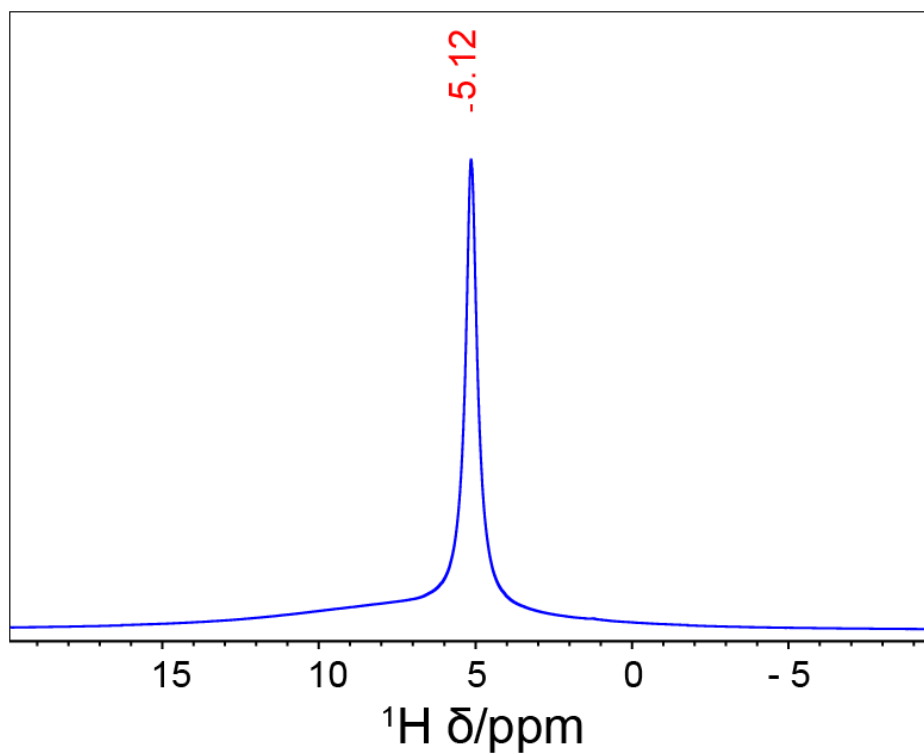


Figure 81 ^1H -NMR spectrum of the boehmite before the heat-treatment

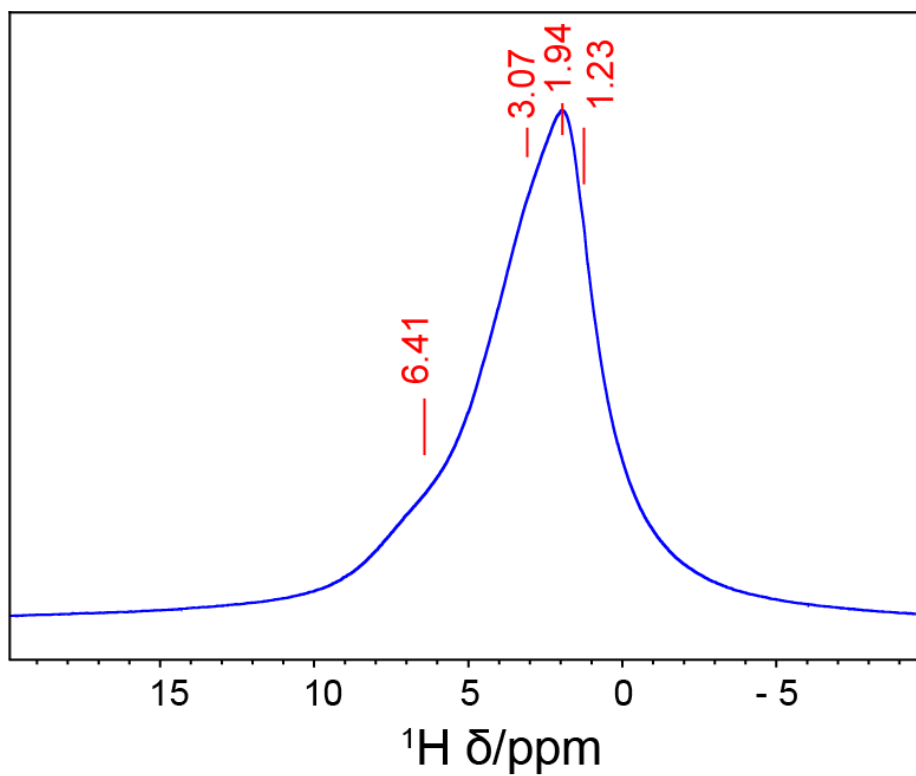


Figure 82 ^1H -NMR spectrum of the clay before the heat-treatment

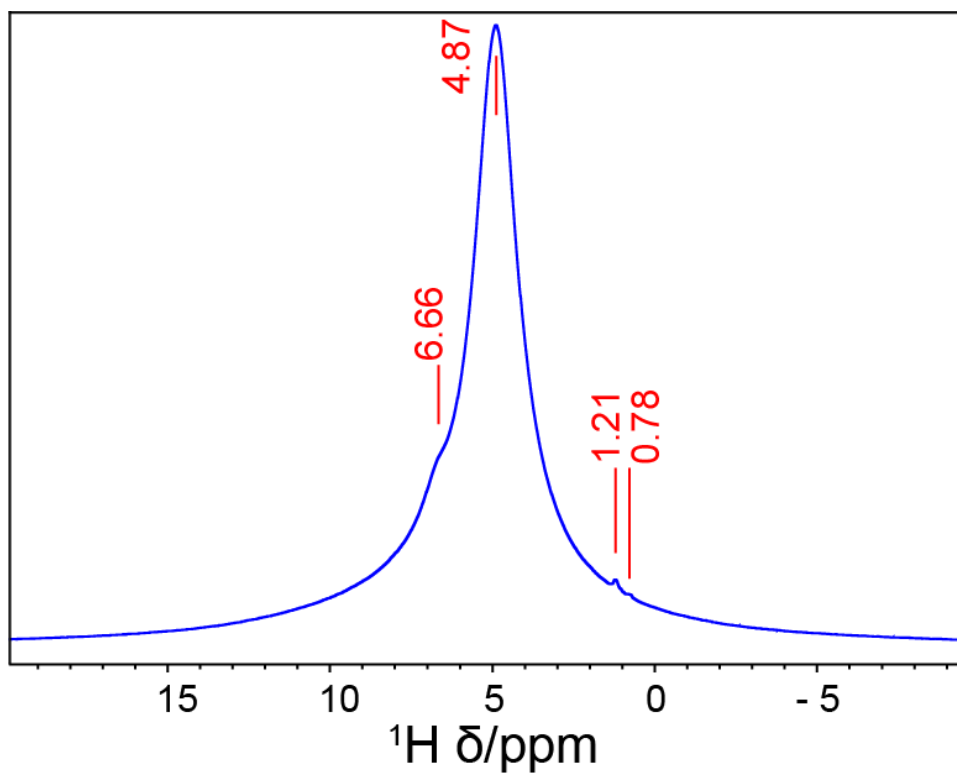


Figure 83 ^1H -NMR spectrum of the binder before the heat-treatment

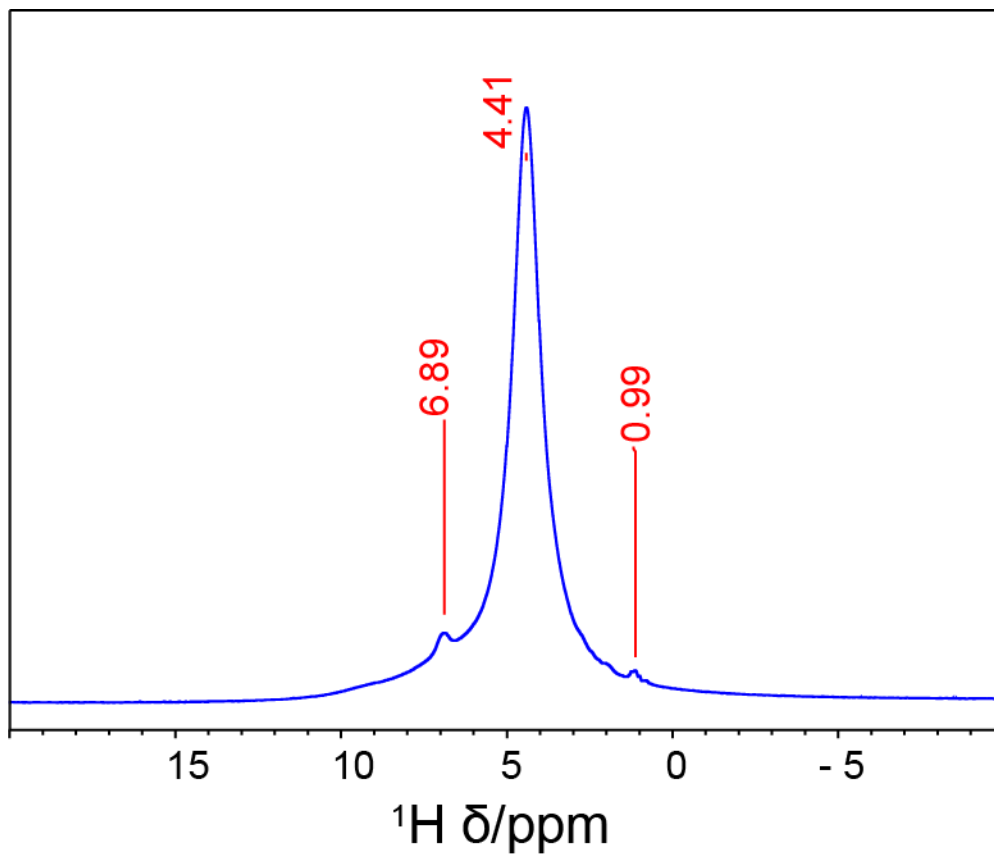


Figure 84 ^1H -NMR spectrum of zeolite HY Si/Al 30 before the heat-treatment

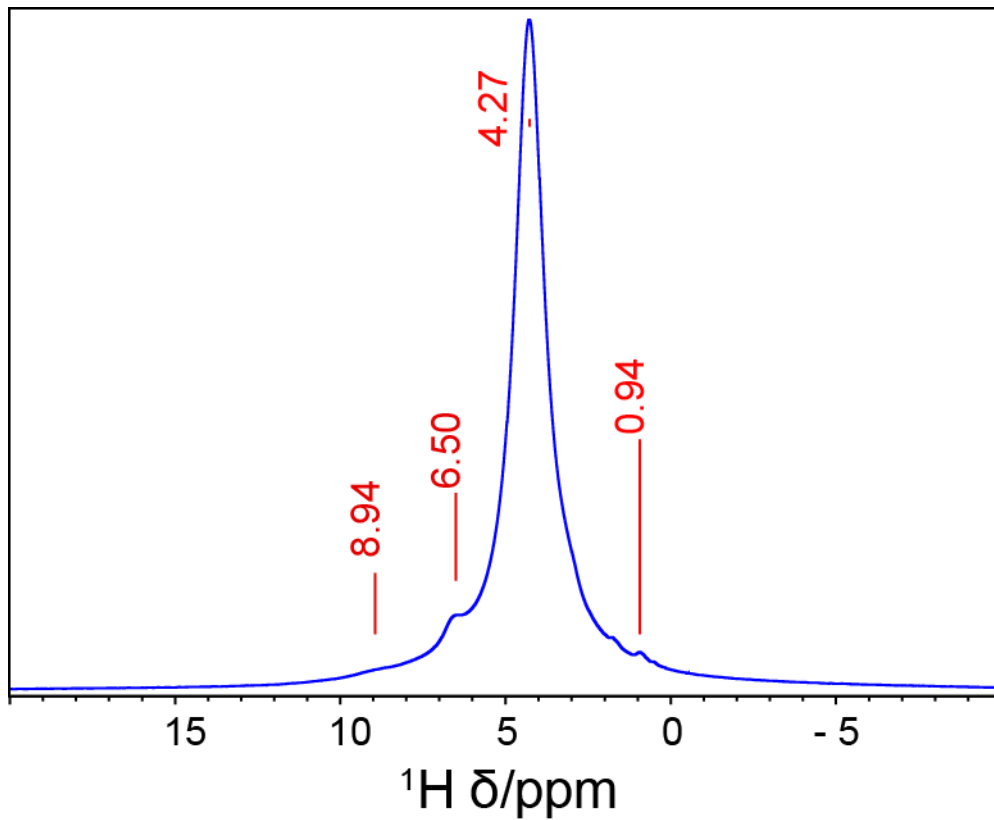


Figure 85 ^1H -NMR spectrum of zeolite HY Si/Al 11 before the heat-treatment